

2008-04-21

Response of A Small, Two-Strait Semi-Enclosed Sea to External Forcings

Xinglong Wu

University of Miami, xwu@rsmas.miami.edu

Follow this and additional works at: https://scholarlyrepository.miami.edu/oa_dissertations

Recommended Citation

Wu, Xinglong, "Response of A Small, Two-Strait Semi-Enclosed Sea to External Forcings" (2008). *Open Access Dissertations*. 84.
https://scholarlyrepository.miami.edu/oa_dissertations/84

This Open access is brought to you for free and open access by the Electronic Theses and Dissertations at Scholarly Repository. It has been accepted for inclusion in Open Access Dissertations by an authorized administrator of Scholarly Repository. For more information, please contact repository.library@miami.edu.

UNIVERSITY OF MIAMI

RESPONSE OF A SMALL, TWO-STRAIT SEMI-ENCLOSED SEA TO
EXTERNAL FORCINGS

By

Xinglong Wu

A DISSERTATION

Submitted to the Faculty
of the University of Miami
in partial fulfillment of the requirements for
the degree of Doctor of Philosophy

Coral Gables, Florida

May 2008

UNIVERSITY OF MIAMI

A dissertation submitted in partial fulfillment of
the requirements for the degree of
Doctor of Philosophy

RESPONSE OF A SMALL, TWO-STRAIT SEMI-ENCLOSED SEA TO
EXTERNAL FORCINGS

Xinglong Wu

Approved:

Dr. Christopher N.K. Mooers
Professor of Applied Marine Physics

Dr. Terri A. Scandura
Dean of the Graduate School

Dr. George R. Halliwell, Jr.
Research Associate Professor
of Meteorology and Physical Oceanography

Dr. Mohamed Iskandarani
Research Associate Professor
of Meteorology and Physical Oceanography

Dr. William E. Johns
Professor
of Meteorology and Physical Oceanography

Dr. John D. Wang
Professor of Applied Marine Physics

WU, XINGLONG
Response of a Small Two-Strait
Semi-Enclosed Sea to External Forcings

(Ph.D., Applied Marine Physics)
(May 2008)

Abstract of a dissertation at the University of Miami.
Dissertation supervised by Professor Christopher N.K. Mooers.

No. of pages in text. (215)

Located at the northern edge of the Northern Gulf of Alaska (NGOA), Prince William Sound (PWS) is a small, two-strait semi-enclosed sea. The general ocean circulation pattern inside PWS is significantly affected by external forcings, for instance, the large-scale circulation in NGOA, atmospheric pressure and surface winds, surface heating/cooling, runoff, and tides. Motivated by multi-year experience with a well-validated, quasi-operational ocean circulation nowcast/forecast system for PWS (*viz.*, Extended PWS Nowcast/Forecast System (EPWS/NFS)), the present study addresses some aspects of the PWS response to various external forcings, via numerical simulations.

Based on the Princeton Ocean Model (POM), four numerical implementations have been examined, *viz.*, PWS-POM, Extended PWS-POM (EPWS-POM), Idealized PWS-POM (IPWS-POM), and a 2-D tidal model. These implementations are used to simulate physical processes with various spatial and temporal scales in PWS. A series of numerical simulations are conducted, driven by various external forcings ranging from large scale and mesoscale circulation in NGOA represented by the Global Navy Coastal Ocean Model (NCOM), to atmospheric pressure observed by National Data Buoy Center (NDBC) buoys and mesoscale winds predicted by Regional Atmospheric Modeling System (RAMS), and to tides simulated by the 2-D tidal model.

These simulations, along with analysis from a Helmholtz resonance model, demonstrate and help interpret some phenomena in PWS; for instance, barotropic Helmholtz resonance in coastal sea levels, and volume transports through the two PWS straits, and a dominant cyclonic gyre in the Central Sound in August and September. The simulation results are used to study a wide range of oceanic phenomena in PWS; *e.g.*, two-layer/three-layer baroclinic transports through the straits, a “transition band” in the coherence pattern between volume transports through the two straits, mesoscale circulation in the Central Sound, the deep water circulation, and the annual tidal energy budget.

Acknowledgments

First of all, I would like to express my deep appreciation to my advisor, Prof. Christopher N.K. Mooers, whose careful and far-sighted guidance, rigorous scholarship, and scientific attitude always give me strength and confidence to persist in my study and research.

I thank Dr. Wang, Dr. Halliwell, Dr. Johns, and Dr. Iskandarani for serving on the committee, and providing invaluable discussions and beneficial suggestions. I also thank Dr. Inkweon Bang, whose sincere and sharp suggestions gave me valuable experience during this work.

Fellowship support for my first year from the Rosentiel School of Marine and Atmospheric Science (RSMAS), and for my subsequent six years from the Oil Spill Recovery Institute (OSRI), of Cordova, Alaska, are greatly appreciated.

Finally, love from my parents, my wife, Ping, and my son, William always encourage me to pursue my dreams in the world of science.

Contents

List of Figures	viii
1 Introduction	1
1.1 Semi-enclosed Sea <i>vis-a-vis</i> Open Ocean	3
1.2 Prince William Sound <i>vis-a-vis</i> Northern Gulf of Alaska	6
1.3 Prince William Sound In Focus	14
1.3.1 Oceanic Observations	15
1.3.2 Results of Previous Numerical Studies	17
1.4 PWS/NFS and EPWS/NFS	19
1.4.1 Modeling System	20
1.4.2 Global-NCOM, RAMS Forcing	25
1.4.3 Performance of EPWS/NFS vs. PWS/NFS	27
1.4.4 Application of EPWS/NFS	46
1.4.5 Summary of PWS/NFS and EPWS/NFS	70
1.5 Purpose of Dissertation	72
2 Numerical Ocean Circulation Model	74

2.1	Princeton Ocean Model	74
2.2	Model Configuration	77
2.2.1	High-Resolution Topography in POM	79
2.3	One-way Coupling	80
2.3.1	From Global-NCOM to EPWS-POM	81
2.3.2	From EPWS-POM to PWS-POM	84
2.4	Internal Pressure Gradient Error/Hydrostatic Inconsistency	88
2.4.1	Sensitivity Studies	89
2.5	Model Initialization	90
2.5.1	EPWS-POM Initialization	91
2.5.2	Comments on Computation Time	93
2.6	Summary	94
3	Response of PWS to Large-Scale Circulation (LSC)	96
3.1	Methodology	96
3.1.1	Verification of NCOM Performance in NGOA	98
3.2	Annual-mean LSC Response	103
3.3	Synoptic LSC Response	107
3.3.1	Synoptic LSC Response in PWS-POM	114
3.4	Summary and Discussion	127
4	Response of PWS to Surface Atmospheric Forcing	129
4.1	Introduction	129
4.2	Observed and EPWS/NFS Simulated Response	131

4.3	Barotropic Helmholtz Resonance	135
4.3.1	Helmholtz Resonance in Musical Acoustics	135
4.3.2	Barotropic Helmholtz Resonance in Semi-enclosed Seas	136
4.3.3	Mean Sea Level Response of A Barotropic Semi-enclosed Sea	140
4.3.4	Discussion on Barotropoc Helmholtz Resonance	144
4.4	Numerical Experiments	145
4.4.1	Reference Experiment	145
4.4.2	Effects of Density Stratification and Rotation Experiments	152
4.4.3	Effect of Domain Geometry Experiments	155
4.4.4	Effect of Forcing Functions Experiments	158
4.4.5	Summary of Numerical Experiments	158
4.5	Summary and Discussion	159
5	Response of Prince Willam Sound to Surface Winds	161
5.1	Methodology	161
5.1.1	Verification of RAMS Surface Winds	162
5.2	Response to RAMS Surface Winds	164
5.2.1	Wind-Driven Mesoscale Circulation in PWS	174
5.3	Summary and Discussion	178
6	Response of Prince William Sound to Tides	181
6.1	Methodology	182
6.2	Response of PWS to Tides	184
6.3	Tidal Energy Flux and Dissipation	191

6.4	Baroclinic Tidal Energy Flux	197
6.5	Summary and Discussion	199
7	Summary and Conclusions	201
	Bibliography	208

List of Figures

1.1	Location of Prince William Sound (PWS) and Gulf of Alaska (GOA). Three coastal cities around PWS, Cordova, Seward, and Valdez, are also shown. (courtesy of Google Maps)	2
1.2	Main geometric features and observing system in PWS, along with PWS/NFS and EPWS/NFS bottom topography. EPWS/NFS and PWS/NFS model domains are represented by outer and inner rectangles, respectively. The open boundaries for PWS/NFS are placed near the southern ends of MS and HE. KEY: HE, Hinchinbrook Entrance; MS, Montague Strait; BH, Black Hole; Cordova, Seward, and Veldez are locations of three tide gauges; 46060, 46061, 46076 and 46081 are locations of four NDBC meteorological buoys; 1, 2, 3, and 4, representing MS1, MS3, HE1 and HE3, respectively, are four ADCP mooring locations during JUN to SEP 2005; GAK1 is the location of a 30-year monthly CTD mooring measurement. Isobath contour interval = 100 <i>m</i>	7
1.3	MODIS sea surface temperature at 02 AUG 2004	8
1.4	Major circulation system in GOA (courtesy of Reed and Schumacher, 1986)	13

1.5	NDBC buoys observed and RAMS simulated wind velocities: (a) eastward and (b) northward velocity at 46060; (c) eastward and (d) northward velocity at 46061	26
1.6	Power spectra (DOF=10) for NDBC observed (red) and RAMS simulated (blue) (a, c) eastward and (b, d) northward wind velocities at 46060 (in Central Sound) and 46061 (outside HE)	28
1.7	Coherence function (DOF=10) between observed eastward wind velocity between 46060 and 46061: (a) magnitude and (b) phase. For comparison, results from nowcast eastward wind velocity are also shown: (c) magnitude and (d) phase.	29
1.8	Monthly-mean depth-averaged zonal velocity at the eastern (upper) and western (bottom) boundaries of EPWS/NFS during March 2005 - March 2006, as well as the corresponding annual-mean depth-averaged velocity (right panels). The bottom topography at boundaries is also shown (left panels); notice that the different depth scales are used for the plot of bottom topography and depth-averaged velocities, respectively, at the eastern and western boundaries.	30
1.9	Monthly-mean depth-averaged meridional velocity (b) at the southern boundary of EPWS/NFS during March 2005 - March 2006, as well as the corresponding annual-mean depth-averaged velocity (c). The bottom topography at the southern boundary is also shown (a)	31
1.10	One-month comparisons of PWS/NFS nowcast (green), EPWS/NFS nowcast (blue) and observed coastal sea levels at (a) Cordova; (b) Valdez; and (c) Seward	32

1.11	One-year comparisons of 40-hr low-passed PWS/NFS nowcast (green), EPWS/NFS simulated (blue) and adjusted observed (red) coastal sea levels at (a) Cordova; (b) Valdez; and (c) Seward	33
1.12	Power spectra (DOF=10) of one-year PWS/NFS simulated (green), EPWS/NFS simulated (blue) and observed coastal sea levels at (a) Cordova; (b) Valdez; and (c) Seward	35
1.13	Coherence (a) and phase (b) of EPWS/NFS nowcast (blue) and observed (red) detided CSLs between Cordova and Valdez (DOF=10). For comparison, coherence and phase of PWS/NFS nowcast detided CSLs are also shown (c, d)	37
1.14	Comparisons between observed (red) and EPWS/NFS nowcast (blue) SST time series at: (a) NOS tide gauge Valdez; (b) NOS tide gauge Cordova; (c) NDBC buoy 46060; (d) NDBC buoy 46061; (e) NDBC buoy 46081; (f) NDBC buoy 46076	38
1.15	Comparisons between observed (red), EPWS/NFS (blue) and PWS/NFS (green) nowcast (blue) SST at 46060	39
1.16	Observed (upper) and nowcast (bottom) monthly-mean temperature at various depths at GAK1. Observed monthly climatology is based on 30-year CTD measurements. Nowcast monthly mean is provided by EPWS/NFS from MAR2005 through FEB2006, and for the purpose of direct comparisons with observed values, monthly-means for the first two months are based on EPWS/NFS data in 2006 while for the remaining ten months, EPWS/NFS data in 2005 are used. Notice that the water depth is different between GAK1 (<i>ca.</i> 250 <i>m</i>) and the corresponding model location (<i>ca.</i> 140 <i>m</i>)	40

1.17	Amplitude (solid line) and phase (dashed line) of eight tidal constituents for six-month ADCP observed (star) and EPWS/NFS nowcast (solid circle) eastward velocities at buoy 46060 at three depths: (a) 28 m; (b) 186 m; (c) 368 m (Mooers <i>et al.</i> , 2007).	42
1.18	Amplitude (solid line) and phase (dashed line) of eight tidal constituents for six-month ADCP observed (star) and EPWS/NFS nowcast (solid circle) northward velocities at buoy 46060 at three depths: (a) 28 m; (b) 186 m; (c) 368 m. (on courtesy of Mooers <i>et al.</i> , 2007)	43
1.19	(a) Magnitude and (b) phase of anti-clockwise component of M2 tidal current at buoy 46060: ADCP observed (solid line), PWS/NFS nowcast (dashed line) and EPWS/NFS nowcast (dot-dashed line). Results for (c, d) clockwise component of M2 tide are also shown (Mooers <i>et al.</i> , 2007).	44
1.20	(a) Temporal mean and (b) standard deviations of six-month ADCP observed (solid line), PWS/NFS nowcast (dashed line) and EPWS/NFS nowcast (dot-dashed line) baroclinic eastward velocity profiles at buoy 46060. Results for (c, d) baroclinic northward velocities are also shown (Mooers <i>et al.</i> , 2007).	45
1.21	Three-month (15 JUN to 15 SEP 2005) observed (solid line) and nowcast (dot-dashed line) velocity (m/s) vertical profiles at HE1 mean eastward (a) and northward (b), plus standard deviation eastward (c) and northward (d)	47
1.22	Three-month (15 JUN to 15 SEP 2005) observed (solid line) and nowcast (dot-dashed line) velocity (m/s) vertical profiles at MS1 mean eastward (a) and northward (b), plus standard deviation eastward (c) and northward (d)	48

1.23	EPWS/NFS one-year (MAR 2005 thru FEB 2006) nowcast volume transports (Sv: Sverdrup= $10^6 m^3/s$) through HE (blue) and MS (red): (a) original; (b) detided	50
1.24	EPWS/NFS power spectra (DOF=10) of one-year (MAR 2005 thru FEB 2006) nowcast volume transports through HE (a) and MS (b): original (blue) and detided (red)	51
1.25	EPWS/NFS coherence squared and phase (DOF=10) of one-year nowcast volume transports between HE and MS: original [(a) magnitude; (b) phase]; detided [(c) magnitude; (d) phase]. The transition band (marked as yellow solid circle) of the coherence function is defined by the frequencies for which the coherence squared is generally less than 0.9.	52
1.26	One-month comparison among observed (blue), EPWS/NFS nowcast (red) spatial mean sea level rate-of-change over PWS, and EPWS/NFS nowcast net transports (green) through HE and MS. The correlation at zero lag (linear regression coefficient) between observed and nowcast mean sea level rate-of-change is 0.3 (0.6), and between nowcast net transport and nowcast mean sea level rate-of-change is 0.9 (1.0).	53
1.27	Point-by-point annual-mean (blue star), as well as the corresponding standard deviations (dashed red), volume transports through HE, based on one-year EPWS/NFS nowcasts. Locations of one-point ADCP observation (red circle) and two-point ADCP emulation (black circle) at HE are indicated; the bottom topography (gray) along the cross section of HE is superposed.	54

1.28	Monthly-mean volume transport through HE: (1) EPWS/NFS nowcast (solid red), (2) one-point ADCP estimated (dashed green; as in Vaughan et al. 1997), (3) one-point ADCP emulated (partial depth; dashed cyan), (4) one-point ADCP emulated (full depth; dashed magenta), and (5) two-point ADCP emulated (full depth; dashed black). EPWS/NFS nowcast (6) monthly-mean volume transport through MS is also shown (solid blue).	55
1.29	EPWS/NFS annual mean northward velocity (m/s) transects at MS and HE (a, b), and the corresponding standard deviation (STD; c, d).	57
1.30	EPWS/NFS monthly mean northward velocity (m/s) transects at HE . . .	59
1.31	EPWS/NFS monthly mean northward velocity (m/s) transects at MS . . .	60
1.32	EPWS/NFS monthly mean temperature ($^{\circ}C$) transects at HE	62
1.33	EPWS/NFS monthly mean salinity (<i>ppt</i>) transects at HE	63
1.34	EPWS/NFS monthly mean density (σ_t) transects at HE	64
1.35	(upper) EPWS/NFS topography and selected locations (red asterisks; 1, 2, 3) to examine across-strait (HE) density gradient. (lower) EPWS/NFS monthly-mean across-strait (HE) density gradient (solid lines) and corresponding northward velocity profiles (dot-dashed lines) based on thermal-wind dynamics in JUN 2005: between the locations 1 and 2 (red), and between the locations 2 and 3 (blue).	66
1.36	EPWS/NFS nowcast surface current on (a) 01MAR, (b) 15MAR and (c) 30MAR2005. The background color indicates the current speed (m/s). . . .	68
1.37	EPWS/NFS nowcast surface current on 10AUG and 20 AUG 2005. The background color indicates the current speed (m/s).	69

1.38	EPWS/NFS nowcast vertical profiles of daily-averaged temperature (a), salinity (b), and σ_t in Central Sound between MAR 2005 and MAR 2007	70
1.39	EPWS/NFS nowcast vertical profiles of daily-averaged temperature (a), salinity (b), and σ_t in the BH between MAR 2005 and MAR 2007	71
2.1	EPWS-POM (upper) and PWS-POM (bottom) grids	78
2.2	EPWS-POM (left), PWS-POM (middle) grid represented topography and coastline in the northeast PWS. For comparison, the satellite image (right) indicates the realistic coastline features in the same region (courtesy of Google Maps).	80
2.3	EPWS-POM (upper), PWS-POM (lower) grid represented topography and coastline in the east PWS, without (left) or with (middle) coastline refinement to remove the spurious “lakes”. For comparison, the satellite image (right) indicates the realistic coastline features in the same region (courtesy of Google Maps).	81
2.4	Global-NCOM topography in PWS, as well as on the continental shelf outside PWS (upper) with the superposition of EPWS-POM southern boundary (red solid line). Global-NCOM topography (lower) along the EPWS-POM southern boundary (blue sold line), via the simple 2-D interpolation, is greatly different from the local, high-resolution EPWS-POM topography (red asterisks).	82
2.5	Diagram mapping Global-NCOM vertical profile to EPWS-POM σ -levels . . .	83
2.6	Diagram on coupling grids in an embedded C-Grid with a ratio of 1:3 . . .	85

2.7	EPWS-POM spin-up: (a) total kinetic energy; (b) volume transport through HE and MS; time-depth plots of temperature in (c) BH and (d) Central Sound	94
3.1	(upper) Two-year comparison of three-hourly Global-NCOM nowcast (blue) with 40-hr low-passed observed (red) coastal sea level at Seward. (lower) Comparison with observed adjusted sea level is also shown.	99
3.2	Two-year comparison of Global-NCOM nowcast (blue) and observed (red) sea surface temperature at Seward, NDBC buoy 46061, 46076 and 46082	100
3.3	One-year comparison of Global-NCOM nowcast (upper) and observed (lower) temperature/salinity profiles at GAK1 between MAY05 and JUN06. Observed GAK1 T/S plots are directly obtained from GAK1 website and colors indicate nominal depth level: Near surface (blue & cyan), 60m (red), 100m (green), 150m (black), 200m (magenta) and 250m (yellow).	101
3.4	Two-year NCOM nowcast SST at EPWS/NFS eastern, western, and southern boundary	102
3.5	Two-year mean and <i>std</i> of eastward flow profile along the EPWS/NFS eastern boundary	103
3.6	EPWS-POM simulated 1-yr sea levels at various locations (upper), along with SSH (bottom left) and surface current speed (bottom right) in DEC 2006	104
3.7	EPWS-POM simulated 1-yr volume transports through HE and MS (upper), along with annual-mean northward velocity at MS (bottom left) and HE (bottom right)	105
3.8	EPWS-POM simulated 1-yr time-depth plots temperature at (a) BH, (b) 46060, (d) MS, and (e) 46061, along with (c) map of SST in DEC 2006	106

3.9	EPWS-POM simulated 1-yr sea levels at various locations	107
3.10	EPWS-POM simulated 1-yr (a) volume transports through HE (red) and MS (blue), as well as the net transport (green); (b) corresponding power spectra (DOF=10); (c) coherence squared between volume transports through HE and MS; and (d) phase. The transition band (solid yellow dots) of the co- herence function is indicated. KEY: H, Helmholtz resonance period for PWS (<i>ca.</i> 6 hrs); I, inertial period (13.8 hrs).	108
3.11	EPWS-POM simulated monthly-mean SSH	110
3.12	EPWS-POM simulated monthly-mean SST	111
3.13	EPWS-POM simulated monthly-mean northward velocity transect through HE	112
3.14	EPWS-POM simulated monthly-mean northward velocity transect through MS	113
3.15	EPWS-POM simulated 1-yr time-depth plots of temperature at (a) BH, (b) 46060, (d) MS, and (e) 46061, along with (c) annual-mean SST	115
3.16	PWS-POM simulated SSH and surface current after 15 days, as well as the corresponding EPWS-POM fields at the same time	117
3.17	PWS-POM simulated SST and SSS after 15 days, as well as the corresponding EPWS-POM fields at the same time	118
3.18	PWS-POM simulated temperature and normal velocity section in Central Sound after 15 days, as well as the corresponding EPWS-POM field during the same time	119

3.19	PWS-POM simulated surface current and vorticity in Central Sound. The example is randomly selected from PWS-POM simulations. The red dot marks the center of the CG. Notice that locations with negative vorticity have not been visualized for clarity.	121
3.20	PWS-POM determined CG center and its path in AUG. Blue and green triangle marks indicate the initial and final positions of the CG center, respectively, and arrows are numbered to follow the movement of the CG center.	122
3.21	PWS-POM simulated SST at the same time as the surface current shown in Fig. 3.19	123
3.22	Histogram of PWS-POM simulated CG radius and eccentricity in AUG	124
3.23	Comparison of the CG meridional and zonal movement with HE surface inflow velocity	125
3.24	Comparison of CG (a) coverage area, (b) eccentricity, and (c) max. current speed with HE surface inflow and temperature	126
4.1	Power spectra, along with spectrograms, of 10-year observed local AP and AP difference over PWS. The spectrograms are obtained via a 512-point FFT window with a total of 328 degrees-of-freedom.	132
4.2	Spectrograms of 10-year observed CSL gain magnitude in Cordova to local AP (left) and AP difference (right)	133

4.3	Gain magnitude and phase (DOF=10) of EPWS/NFS simulated volume transports to AP difference: HE (red), MS (blue), and net (sum of HE and MS transports; green). KEY: H, barotropic Helmholtz resonance period for IPWS (<i>ca.</i> 2.5 hrs); I, inertial period (13.8 hrs). Magenta dots indicate the location of transition band in coherence pattern between EPWS/NFS simulated HE and MS volume transports (Fig. 1.25).	134
4.4	Schematic of a simple Helmholtz resonator (courtesy of http://www.phys.unsw.edu.au/jw/Helmholtz.html)	136
4.5	Schematic of simple oceanic Helmholtz resonator in a semi-enclosed sea . . .	137
4.6	Schematic of Helmholtz resonance in a barotropic ocean	141
4.7	Response of mean sea level response to AP: a barotropic HR model ($\lambda = 1.0 \times 10^{-4}$)	144
4.8	IPWS Reference Case model domain (IPWS) for an idealized PWS, open ocean, and two straits connecting them. For convenience, the lefthand strait is named as IMS, and the righthand strait as IHE.	146
4.9	Atmospheric forcing for 100 days (1 JAN thru 10 APR 2005): (a) atmospheric pressure and (b) eastward wind stress at NDBC buoy 46060 (blue) and 46061 (red). The atmospheric pressure difference between 46060 and 46061 is indicated by green line in (a).	148

4.10	IPWS barotropic case: (a) simulated 10-day volume transports through IHE (red) and IMS (blue), as well as difference between IHE and IMS transport (green); (b) power spectra (DOF=10) for IHE (red), IMS (blue), and net volume transports (green); (c) coherence squared between volume transports through IHE and IMS; and (d) phase. KEY: H, barotropic Helmholtz resonance period for IPWS (<i>ca.</i> 2.5 hrs); I, inertial period (13.8 hrs).	149
4.11	IPWS Reference Case: simulated 100-day (a) volume transports through IHE (red) and IMS (blue), as well as the net transport (green); (b) corresponding power spectra (DOF=10); (c) coherence squared between volume transports through IHE and IMS; and (d) phase. The transition band of the coherence function (solid magenta dots) is defined where the coherence squared is generally less than 0.9, and the minimum coherence squared (magenta star) is inside the transition band.	150
4.12	IPWS Reference Case: response of IHE (red), IMS (blue), and net (green) volume transports to atmospheric pressure forcing: gain (a) magnitude and (b) phase (DOF=10). The transition band (solid magenta dots) of the coherence function between IHE and IMS volume transports is indicated.	151
4.13	IPWS Reference Case 100-day mean northward velocity transect (m/s) at IMS and IHE (a, b), and the corresponding standard deviation transect (STD; c, d).	152

4.14	Normalized (by inertial period) upper and lower period bounds of transition band versus normalized (by strait length) baroclinic Rossby radius of deformation for the experiments documented in Table 4.3. The slopes of least-square fitted curves for the upper and lower period bounds are -1.01, and -1.09, respectively.	155
5.1	One-year (2006) comparison between RAMS simulated and NDBC buoy observed wind velocities at buoy 46060	163
5.2	Monthly histogram on buoy observed and RAMS simulated zonal winds at 46060	164
5.3	Weekly histogram on buoy observed and RAMS simulated zonal winds at 46060	165
5.4	EPWS-POM simulated 1-yr sea levels at various locations (upper), along with annual-mean SSH (bottom left) and surface current speed (bottom right)	166
5.5	EPWS-POM simulated monthly mean SSH	167
5.6	EPWS-POM simulated 1-yr (a) volume transports through HE (red) and MS (blue), as well as the net transport (green); (b) corresponding power spectra (DOF=10); (c) coherence squared between volume transports through HE and MS; and (d) phase. The transition band (solid yellow dots) of the coherence function is indicated. KEY: H, Helmholtz resonance period for PWS (<i>ca.</i> 6 hrs); I, inertial period (13.8 hrs).	169
5.7	EPWS-POM simulated monthly mean northward velocity transect at MS .	170
5.8	EPWS-POM simulated monthly mean northward velocity transect at HE .	171
5.9	EPWS-POM simulated monthly mean SST	172

5.10	EPWS-POM simulated 1-yr temperature time-depth plots at (a) BH, (b) 46060, (d) MS, and (e) 46061, along with (c) annual-mean SST	173
5.11	RAMS surface winds at 46060 between 11 MAR and 16 MAR, and between 14 SEP and 23 SEP	175
5.12	EPWS-POM simulated surface current in Central Sound between 11 MAR and 16 MAR	176
5.13	EPWS-POM simulated meridional section across Central Sound: (a) temperature and (b) zonal velocity	177
5.14	EPWS-POM simulated simulated surface current in Central Sound between 14 SEP and 19 SEP	179
5.15	EPWS-POM simulated simulated surface current in Central Sound between 20 SEP and 23 SEP	180
6.1	Domain of the 2-D tidal model (red lines) and locations of available tidal constituents (green stars) based on a North Pacific tidal model. For comparison, EPWS-POM domain is also indicated (blue lines).	183
6.2	One-month comparisons of EPWS-POM simulated (blue) and tide gauge observed (red) CSLs at Cordova, Valdez and Seward	185
6.3	One-month (24 JUL to 23 AUG) comparisons of EPWS-POM simulated (blue) and ADCP observed (red) eastward velocity at 46060: (a) 25 m; (b) 200 m; and (c) 368m. Observed velocity is obtained from ADCP deployment during the same month in 2005	187

6.4	One-month (24 JUL to 23 AUG) comparisons of EPWS-POM simulated (blue) and ADCP observed (red) northward velocity at 46060: (a) 25 m; (b) 200 m; and (c) 368m. Observed velocity is obtained from ADCP deployment during the same month in 2005	188
6.5	EPWS-POM simulated 1-yr temperature time-depth plots at (a) BH, (b) 46060, (d) MS, and (e) 46061, along with (c) annual-mean SST	189
6.6	EPWS-POM simulated 1-yr (a) volume transports through HE (red) and MS (blue), as well as the net transport (green); (b) corresponding power spectra (DOF=10); (c) coherence squared between volume transports through HE and MS; and (d) phase. KEY: H, Helmholtz resonance period for PWS (<i>ca.</i> 6 hrs); I, inertial period (13.8 hrs).	190
6.7	EPWS-POM simulated annual-mean northward velocity transect at MS and HE	191
6.8	EPWS-POM simulated surface current in PWS on 11 AUG 2006	192
6.9	EPWS-POM simulated annual-mean tidal energy dissipation	196
6.10	Ratio between EPWS-POM simulated annual-mean baroclinic and barotropic tidal energy flux	198

Chapter 1

Introduction

The coastal ocean, including the continental shelf and slope seas, ranges from the coastline to 200 nautical miles offshore, where it is several kilometers deep. Due to its significant societal and economic importance, the coastal ocean is the most important region of the world ocean, even though it occupies only a small portion of the ocean's water area and volume. The physical processes occurring there are complex and involve temporal scales ranging from a few seconds to years in time, and spatial scales ranging from a few meters to hundreds of kilometers. The superposition and interaction of these different physical processes, as well as the chaotic nature of the oceanic system, imposes great difficulties on establishment of a universal analytical model for studying coastal oceanography. Instead, numerical models have become the most reliable and efficient tools; while in some particular circumstances, analytical models can be used to shed light on the fundamental underlying physical mechanisms, or serve to provide insight into the numerical simulation results. One of these many coastal ocean studies, focusing on the dynamical response of a semi-enclosed sea, indicates how the understandings of oceanic processes can be greatly enhanced by numerical simulations.

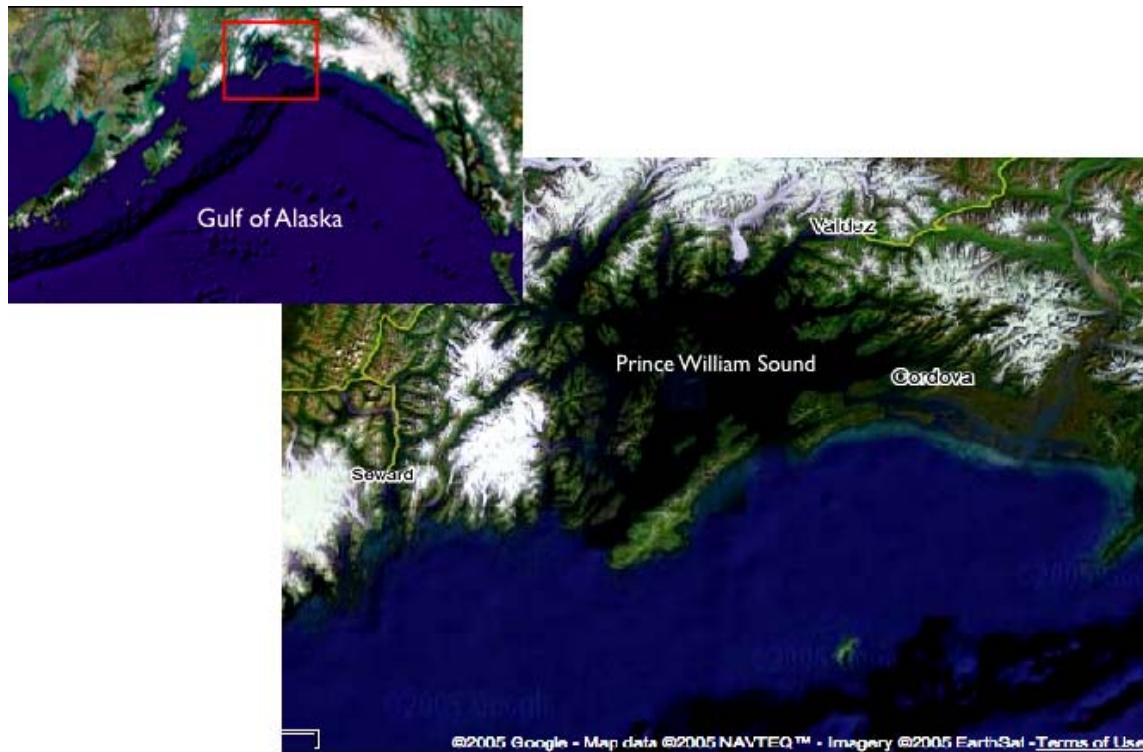


Figure 1.1: Location of Prince William Sound (PWS) and Gulf of Alaska (GOA). Three coastal cities around PWS, Cordova, Seward, and Valdez, are also shown. (courtesy of Google Maps)

The present study was initially motivated by several years of experience with continuously monitoring the synoptic, seasonal, and inter-annual variability of a small coastal ocean, Prince William Sound (PWS; Fig. 1.1), Alaska, through a real-time, daily-updated, Internet-broadcasted, ocean circulation prediction system for PWS (Mooers et al, 2007). This system, called Extended-PWS Nowcast/Forecast System (EPWS/NFS¹), provides the oceanographic modeling backbone supporting biological, chemical, and societal applications

in PWS, and simultaneously poses a demand for better understanding of the dominant physical processes and underlying mechanisms.

1.1 Semi-enclosed Sea *vis-a-vis* Open Ocean

A semi-enclosed sea, often appearing in contrast with the open ocean, is loosely referred to as a small-scale coastal ocean, which may be as large as the Yellow Sea, Japan/East Sea, South China Sea, Black Sea, Mediterranean Sea, Caribbean Sea, Gulf of Mexico, or a much smaller sea like Prince William Sound (PWS; *ca.* 100 km diameter and *ca.* 400 m deep) located at the northern edge of the Gulf of Alaska (GOA). All these seas are dynamically similar in that they are large enough in terms of the internal radius of deformation (R_{bc} ; *ca.* 5 (50) km for winter (summer) in PWS (Bang *et al.*, 2005)) to develop a geostrophically balanced circulation. Consisting of only a very small portion of the global ocean, most of these regional oceans are relatively shallow, connected with the open ocean via one or more straits/channels with underwater sills often guarding the entrance, and bounded by complex coastline shapes. Inside these regions, waters are impacted by oceanic, atmospheric, topographic, and terrestrial influences, as well as human activities. To further confound the topic, most of the coastal oceans also service fragile ecosystems which are inseparable habitats of many valuable and endangered species in the marine environment. On the other hand, since most significant societal and economic activities nowadays occupy land areas within 200 km of the coastlines, any related environmental change would greatly impact our lives; hence, studies of coastal oceans are extremely important. Each of these considerations may force us to focus our investigations on coastal oceans in addition to the

¹Web access: <http://epws-nfs.rsmas.miami.edu>

open ocean to understand phenomena on a smaller spatial scale and a shorter temporal scale, and with a deeper physical insight. The fact that coastal ocean regions are greatly impacted by more complicated geographical settings; more intense interactions among the three-phase environment of oceanic, atmospheric, and terrestrial phenomena and processes; and a more fragile ecological balance requires careful estimation with high-resolution (*ca.* 1 *km*, horizontally; *ca.* 5 *m*, vertically; *ca.* 10 *min*, temporally) of the detectable response due to variations in the forcing functions. Examples of such approaches include a growing number of scientific projects in US, Europe, and East Asia to build coastal ocean monitoring systems; such as, BOOS², COMPS³, COTS⁴, EFSIS⁵, IAS/NFS⁶, MedGOOS⁷, NEAR-GOOS⁸, SEACOOS⁹, while in the open ocean because dynamical space and time scales are generally larger and longer, respectively, this high-resolution description¹⁰, including observations and modeling, is not feasible at present¹¹.

In this dissertation, the oceanic response of PWS to dominant forcings, *e.g.*, atmospheric pressure, surface winds, tides, and prevailing flow structures at the offshore (open) boundaries, will be addressed. The synoptic and general circulation patterns will be reconstructed

²Baltic Operational Oceanographic System; See <http://www.boos.org>

³Coastal Ocean Monitoring and Prediction System, University of South Florida; See <http://comps.marine.usf.edu/info.html>

⁴NOAA Coastal Observation System; See <http://www.csc.noaa.gov/cots/>

⁵East Florida Shelf Information System, University of Miami; See <http://efsis.rsmas.miami.edu>

⁶Intra-Americas Sea Ocean Nowcast/Forecast System, Naval Research Laboratory; See http://www7320.nrlssc.navy.mil/IASNFS_WWW/

⁷Mediterranean Global Ocean Observing System; See <http://www.medgoos.net>

⁸North-East Asian Regional Global Ocean Observing System; See <http://ioc.unesco.org/goos/NearGOOS/neargoos.htm>

⁹Southeast Atlantic Coastal Ocean Observing System; See <http://www.seacoos.org/>

¹⁰*ca.* 1*km* resolution is considered adequate for now (*Earth Science Vision 2030*, NASA report, 2004)

¹¹Global observing systems do exist, like ARGO (the broad-scale global array of temperature/salinity profiling floats), VOS (Volunteer Observing Ships) profile data, and GCOS/GOOS (Global Climate Observing System/Global Ocean Observing System) including surface drifters, moored buoys, hydrographic profiles, and remotely sensed data, but, observations from them are sparsely distributed throughout the open ocean.

according to their relative importance. However, the relative contribution of different forcings in driving the ocean circulation is still unsettled. For instance, recent studies question the relative importance of thermohaline circulation, or buoyancy forcing, suggesting that it is likely not as significant as previously regarded for the general ocean circulation (Wunsch and Ferrari, 2004). Instead, in contrast to the conventional viewpoint that tides are dissipated almost entirely on the continental shelf where the tidal energy input would be irrelevant to the general circulation, a more important role is played by tides as an energy source in driving the ocean circulation than has been previously postulated (*ibid.*). Since forced tidal motion of a stratified fluid over the topographic gradient in the ocean generates internal waves at tidal period, and since these internal tides can transmit their energy over long distances, they are detectable in satellite altimeter data for sea surface height due to their characteristically shorter wavelengths than those of the barotropic tides (Ray and Mitchum, 1997; Egbert and Ray, 2000). These waves are ubiquitous and have small surface amplitudes (3 to 5 *cm* near some large ridge systems, such as, the Hawaiian Ridge, and 1*cm* elsewhere in the open ocean, but they have a vertical displacement of 10 to 50 *m* or more in the thermocline), and apparently are more effective at mixing the ocean than previously thought. They mix the fluid remote from the generation region through further encounters with topographic gradients (Rudnick *et al.*, 2003) that enhance their vertical shears. Up to 30% of the tidal energy input to the ocean at the Hawaiian Ridge is dissipated through internal tides (Egbert and Ray, 2000). Also, in contrast to wind forcing, tidal forcing is introduced throughout depth. Associated with interactions with complex topography, conditions that often occur in shallow water, tides, including barotropic and baroclinic

components, require a careful investigation of their influence on the general circulation in a semi-enclosed sea; e.g., PWS.

1.2 Prince William Sound *vis-a-vis* Northern Gulf of Alaska

Prince William Sound (Fig. 1.1) has been chosen as an illuminating example for the proposed study. PWS, covering a water area¹² of approximately 9,000 km^2 , is a small semi-enclosed sea connected with the Northern Gulf of Alaska (NGOA) via two major passages, Hinchinbrook Entrance (HE) and Montague Strait (MS) (Figs. 1.2). HE is about 10 km wide and no more than 320 m deep, and MS about 20 km wide and no more than 240 m deep. Other passages are sufficiently narrow and shallow to be ignored for the purposes of this circulation study. The Central Basin depth ranges from 400 to 450 m . The maximum water depth is about 800 m in the northwestern basin called the Black Hole, between Naked Island and Perry Island. Exchanges with the NGOA shelf are restricted by sills just outside HE and MS with a depth of about 250 and 150 m , respectively. Much of PWS is surrounded by the Chugach Mountains with an average elevation of about 2000 m and peaks extending to nearly 3000 m . Considering the freshwater/runoff from snowmelt input to the Sound and the shelf/sills guarding the much deeper interior depths from the GOA, PWS has also been classified as a large, complex, fjord-type estuarine system (Schmidt, 1977; Muench and Heggie, 1978). Alternatively, PWS also exhibits characteristics of a small inland sea with substantial horizontal (throughflow) circulation (Niebauer *et al.*, 1994). Basin-scale transient cyclonic or anticyclonic gyres in central PWS occur throughout the year with significant interannual variability, accompanied generally by small scale (*ca.* 5 to 8 km

¹²Source: <http://www.fisheries.ubc.ca/Projects/PWSound/AlaskaEco/PWSPOSTS/PWSREP5.HTM>

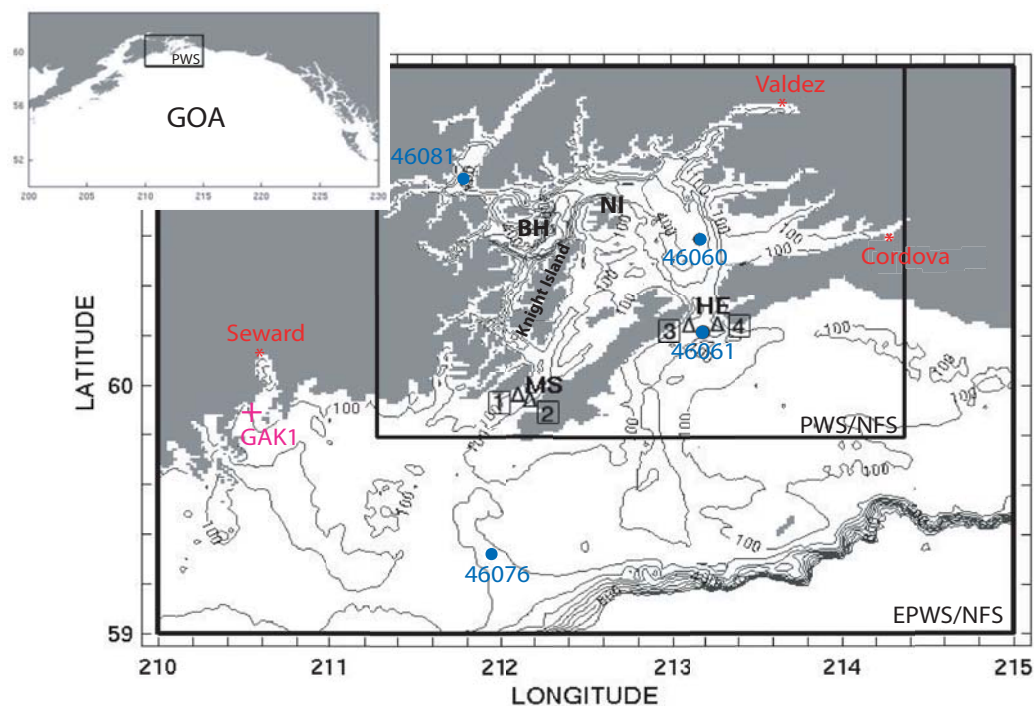


Figure 1.2: Main geometric features and observing system in PWS, along with PWS/NFS and EPWS/NFS bottom topography. EPWS/NFS and PWS/NFS model domains are represented by outer and inner rectangles, respectively. The open boundaries for PWS/NFS are placed near the southern ends of MS and HE. KEY: HE, Hinchinbrook Entrance; MS, Montague Strait; BH, Black Hole; Cordova, Seward, and Valdez are locations of three tide gauges; 46060, 46061, 46076 and 46081 are locations of four NDBC meteorological buoys; 1, 2, 3, and 4, representing MS1, MS3, HE1 and HE3, respectively, are four ADCP mooring locations during JUN to SEP 2005; GAK1 is the location of a 30-year monthly CTD mooring measurement. Isobath contour interval = 100 m.

diameter or submesoscale) eddies. The eddies are usually generated by baroclinic instability of the circulation system due to the vertical shear in the flow field (Vaughan *et al.*, 2001). Through interactions between transient flows at HE and MS with the topography, these basin-scale gyres (*ca.* 30 to 50km diameter or mesoscale eddies) are suggested to be the sources of the submesoscale eddies (Wang *et al.*, 2001). August (Fig. 1.3) and September have been characterized by a strong cyclonic circulation and isopycnal doming in Central Sound, with little year-to-year variability (Cox, 2004; Vaughan *et al.*, 2001).

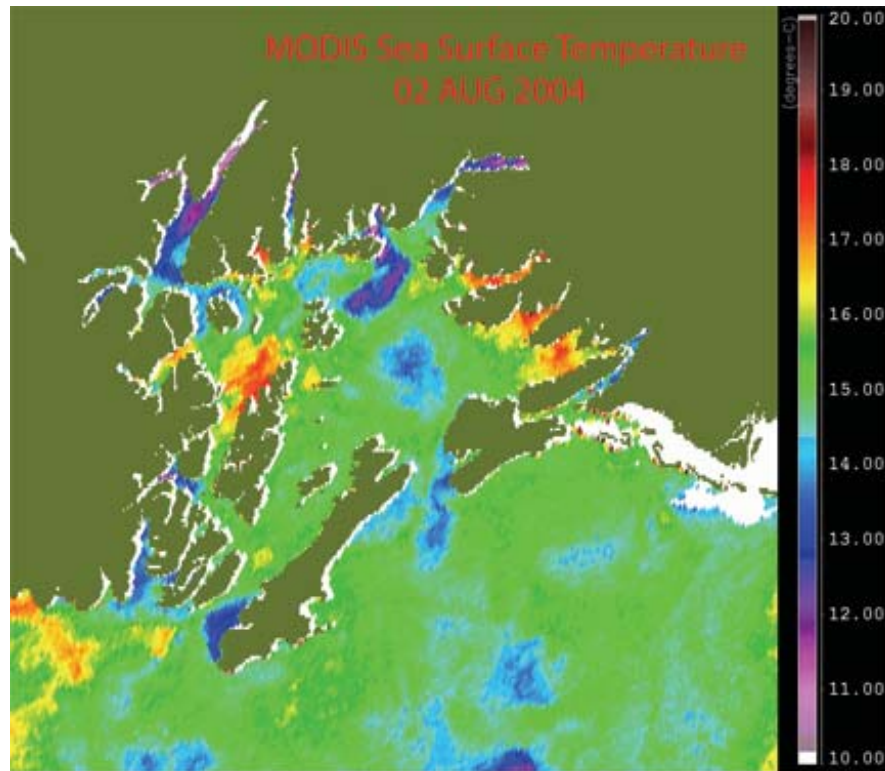


Figure 1.3: MODIS sea surface temperature at 02 AUG 2004

Upper ocean seasonal stratification does not appear simultaneously throughout PWS. In central PWS, it first appears in the north in April, primarily due to freshwater runoff, with an associated surface density front persisting at least through June (Vaughan *et al.*, 2001). Seasonal heating intensifies the stratification through the summer, and seasonal snowmelt persists through October.

Previously, suggested by subsurface-drogued (near a depth of 35 *m*) Lagrangian observations conducted in PWS (Royer *et al.*, 1979) and along the Alaska coast (Royer, 1975), and based on hydrographic, current meter, and ADCP (Acoustic Doppler Current Profiler) data, the general circulation pattern in PWS has been described as a portion of the westward flowing Alaska Coastal Current (ACC) on the GOA shelf that typically enters PWS

through HE and transits the Sound from east to west before exiting through MS and re-joining the ACC, though there is much variation in the transport through HE (Niebauer *et al.*, 1994; Deleersnijder *et al.*, 1998). In July 1976, three satellite-tracked buoys (drogued at 40 m) were deployed in GOA (Royer *et al.*, 1979). These drifters entered PWS through HE and traveled in a cyclonic loop inside. Two of them were entrapped and then grounded in a shallow passage, the third one almost exited through MS but was grounded near Chicken Island in LaTouche Passage. Recent investigations of circulation inside PWS challenge this simple through-flow picture in observations (Vaughan *et al.*, 2001). For instance, at HE alternating inflows and outflows occurred in spring over all depths; during summer through early autumn 1995, in the absence of predominately westward winds, the dominant exchange pattern between PWS and NGOA at HE was outflow above about 150m and inflow below. In summer through early autumn 1996-98, there was also surface (< 20 m) inflow at MS. Northward transport at HE was maximum in late autumn through winter, with inflow above 150m and outflow below when westward winds were dominant. Furthermore, cross-channel flow velocities were large at HE, whereas they were negligible at MS. Moreover, of the 14 drifters deployed at a mean depth of 15m depth released in PWS (two in 1996, three in 1997, and nine in 1998), only five escaped PWS, two of which even exited from HE in August 1996 and re-entered through MS. It seems that the general circulation in the Sound may be more variable than has been assumed.

Over the GOA, three climatologically semipermanent atmospheric features, the Aleutian Low, the East Pacific High and the Siberian High, tend to determine the large-scale atmospheric circulation pattern affecting the northern Gulf of Alaska coast at most times (Putins, 1966; Overland and Hiester, 1980). During the cool season (mid-September to

mid-April), extra-tropical cyclones developing in the central Pacific move eastward along the Aleutian Chain (contributing to the climatological Aleutian Low) into the Gulf. Often these storms lose their individual identities as they reach the northern Gulf and, instead, tend to coalesce, reinforcing a general cyclonic upper ocean flow in the region, generating on-shore ocean surface Ekman transport, and resulting in coastal convergence and coastal downwelling outside PWS. Winds in excess of 30 m/s are common in the winter. During the warm season, the large-scale atmospheric baroclinicity (associated with the meridional temperature gradient) becomes much weaker than in winter and subsequently, the cyclonic atmospheric system is replaced by a weak anticyclonic system (Dodimead *et al.*, 1963), resulting in fewer and weaker storms, slightly offshore ocean surface Ekman transport, coastal divergence, and coastal upwelling in summer, particularly along the northern boundary of the NGOA. As a result, winds over PWS are predominantly westward except during the summer when they may reverse for substantial periods (Bang and Mooers, 2003). Along the NGOA coast, terrain also plays an important role in determining local weather. During the winter, the high terrain of rugged coastal ranges in south central Alaska isolates the cold, dry continental air mass of interior Alaska from the relatively warm, moist maritime air mass typical of the GOA. Even in the absence of a strong temperature difference across the mountain barrier, the local terrain can still have profound impact on the local winds, especially when the mountains are snow-covered or glaciated (Reynolds *et al.*, 2001). This effect of the local terrain may bring significant fluctuations to the general wind-field pattern over PWS as mentioned above. The so-called “barrier winds” and “gap winds” provide good examples demonstrating the terrain-controlled wind pattern. Barrier winds are low-level, mountain-parallel jets, a result of the pressure field created by the damming of stable air as

it is forced up against the steep mountain barrier (Parish, 1982). Barrier winds often occur between 600 to 1500 m in elevation with a speed of 15 to 30 m/s . Barrier winds occur near Wide Bay in Alaska (Bond and Macklin, 1992) and in Antarctica, along the Antarctic Peninsula and Transantarctic Mountains (O'Connor *et al.*, 1994). Gap winds (termed by Reed, 1931) can be defined as a flow of air in a sea level channel which accelerates under the influence of a pressure gradient parallel to the axis of the channel. In an analysis of surface winds which focuses on periods of gap winds in Shelikof Strait in Alaska using observations from two NOAA research flights (Bond and Stabeno, 1998), the prominent terrain bordering Shelikof Strait constrains the low-level winds to accelerate down the local pressure gradient in a direction approximately parallel to the axis of the strait. In a similar study in the vicinity of Prince William Sound (Macklin *et al.*, 1988), strong off-shore directed winds were observed with a research aircraft. These winds are affected by coastal mountains which provide channels that focus and accelerate drainage winds.

The precipitation amount is very high in NGOA, sometimes exceeding 800 $cm/year$ (Wilson and Overland, 1986). The estimated average annual freshwater discharge to GOA integrated along the coastline from the Alaska - British Columbia boundary to Cook Inlet is about 23,000 m^3/s (730 $km^3/year$; Royer, 1982). The major rivers such as the Copper (mean annual discharge of 1050 m^3/s), Fraser (2700 m^3/s) and Columbia (5660 m^3/s ; Roden, 1967) contribute 40% and are not included in the 23,000 m^3/s total¹³. New findings show that line sources (including numerous ungauged small streams and creeks) account for more of the total runoff, about 74%, while point sources (five major rivers, *e.g.*, Susitna,

¹³These major rivers are considered as point sources of freshwater discharge along the coastline of GOA, which are separate from the estimate of line sources of freshwater discharge. The latter, as indicated, is about 23,000 m^3/s .

Copper, Alsek, Taku, and Stikine) account only for 26% (Wang *et al.*, 2004). The seasonality of precipitation and snowmelt along the NGOA coast results in maximum freshwater discharge in the autumn (decreases rapidly after October) and minimum in spring (increases rapidly after May) (Royer *et al.*, 1979; Wang *et al.*, 2004), and are well-correlated with seasonal dynamic height fluctuations in the upper layers ($< 100m$) determined from hydrographic data (Royer, 1979). Surface waters in the GOA undergo a net dilution throughout most of the year since the regional precipitation exceeds evaporation. Thus, except for summer, density stratification in the NGOA depends more on salinity than temperature differences when GOA shelf water temperatures are moderately low (mean annual SST = $7^{\circ}C$) and temperature gradients are generally weak (Weingartner *et al.*, 2001).

The GOA basin scale flow (Fig. 1.4) is characterized by a subarctic cyclonic gyre, and the weak, broad, and shallow Alaska Current is manifested offshore in the eastern basin (Reed and Schumacher, 1986). It becomes the intense, narrow, and deep Alaska Stream in the western basin along the Aleutians. Over the inner continental shelf, the flow is dominated by the wind-driven and buoyancy-driven ACC. The ACC responds strongly and seasonally to both wind forcing and freshwater discharge (Johnson *et al.*, 1988; Schumacher *et al.*, 1990). The mean 0/100 *dbar* baroclinic geostrophic transport of ACC is about 0.2 *Sv* with a seasonal fluctuation of about 0.1 *Sv* (Niebauer, *et al.*, 1994). Current speeds are quite variable but usually while maximum speeds occur in autumn, when they may exceed 1.5 *m/s* (Johnson and Royer, 1986). A portion of the ACC (about 15%; Royer, 1998) typically passes through PWS, with a significant contribution from the discharge of the nearby Copper River. Satellite imagery suggests that sediment-laden Copper River waters sometimes enter PWS through HE (Royer *et al.*, 1990).

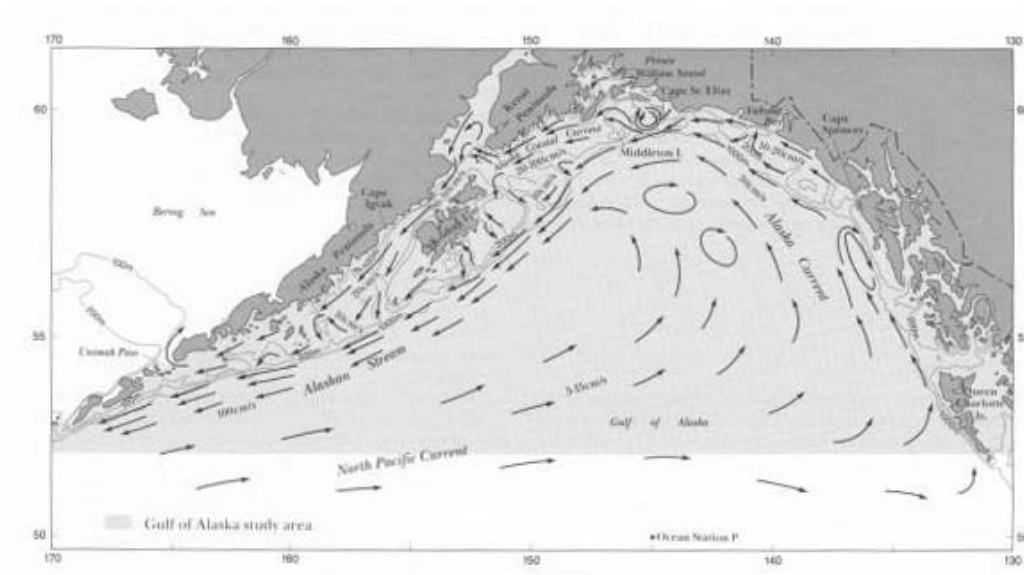


Figure 1.4: Major circulation system in GOA (courtesy of Reed and Schumacher, 1986)

The Alaska Shelf circulation is influenced by the mesoscale (Okkonen *et al.*, 2003), seasonal (Vaughan *et al.*, 2001), and interannual (Bang and Kowalik, 1994) variability of the GOA. Large anticyclonic eddies are abundant in the GOA, such as the recurrent Sitka Eddy (Tabata, 1982; Thomson and Gower, 1998; Melsom *et al.*, 1999; Murray *et al.*, 2001). From altimetric studies, they may remain intact for well beyond one year (Crawford and Whitney, 1999; Okkonen *et al.*, 2001). In NGOA, eddies typically form during fall and winter. They translate southwestward adjacent to the continental shelf in the northwestern GOA (Okkonen, *et al.*, 2003), and westward away from the coast into the central Gulf along the northeastern boundary of GOA (Crawford and Whitney, 1999). This translation alters the structure of the shelf break front (Linder and Gawarkiewicz, 1998) and influences the cross-shelf water exchange. Occasionally, these eddies may penetrate the Alaskan Shelf to influence the variability of ACC.

1.3 Prince William Sound In Focus

PWS is well-known for its high biological productivity and diversity, and as an intersection of diverse cultures, including the resident Chugach Eskimos and Eyak Indians, and Asian and European explorers and pioneers. PWS is also the main commercial route for oil tankers by which the Alaska oil is shipped from Port Valdez. The Exxon Valdez Oil Spill on 24 MAR 1989 is one of the largest manmade environmental disasters ever to occur at sea, seriously affecting marine life in PWS. Several years after the spill, the Sound Ecosystem Assessment (SEA) project¹⁴, financially supported by the EXXON Valdez Oil Spill Trustee Council (EVOS), was launched in 1993 as part of the restoration effort to investigate factors affecting the recovery of pink salmon and Pacific herring in PWS (Cooney *et al.*, 2001). The 7-year program resulted in numerous data sets and various models being incorporated into the EVOS Trustee Council Gulf Ecosystem Monitoring (GEM) program and the Oil Spill Recovery Institute (OSRI¹⁵) Nowcast/Forecast observing and modeling system. All these efforts have led to a larger, Sound-wide observing system¹⁶, including oceanic, atmospheric, and biological components, to enable the detection and prediction of oil-spill related impacts and subsequent recovery. The system also incorporates a regional atmospheric circulation model (RAMS, as explained below), and a coupled ocean circulation model (EPWS/NFS, as explained more below; Fig. 1.2), both of which are able to provide up to a 72-hr forecast. The modeling program is now rapidly evolving toward integration with the Alaska Ocean Observing System (AOOS¹⁷) in order to take better advantage of real-time data streams

¹⁴Web access: <http://www.pwssc.gen.ak.us/sea/sea.html>

¹⁵Web access: <http://www.pws-osri.org>

¹⁶Web access: <http://ak.aos.org/pws/>

¹⁷Web access: <http://www.aos.org>

from satellites, weather stations, and an enhanced observational oceanography program consisting of permanent moored buoys and seasonal hydrographic transects.

1.3.1 Oceanic Observations

PWS has a limited, but expanding, real-time, operational observing system consisting of several coastal tide gauges, and meteorological buoys and land stations. Other than that, ADCP moorings, surface drifters, and CTD (conductivitytemperaturedepth profiler) profiles, and occasional scientific cruises, supplement the operational observed database on an irregular basis. Surface temperature and ocean color based on satellite data (AVHRR¹⁸ and MODIS¹⁹) is occasionally available for PWS domain, but due to the spatial resolution and cloud coverage issues for this small coastal region, these satellite data (the corresponding images) are of limited use.

Observations of coastal sea level (CSL) are based on NOAA/National Ocean Service (NOS)/Center for Operational Oceanographic Products and Services (CO-OPS²⁰) tide gauges, at Cordova, Valdez, and Seward (Fig. 1.2). The first two tide gauges are located inside PWS, while the other one is exposed to the continental shelf near the entrance to MS. The hourly CSL data, available back to the year of 1995, indicate a mixed type of ocean tides inside PWS with the ratio between diurnal and semidiurnal constituent of about 0.5, a strong diurnal inequality, and also a strong spring/neap cycle. The tides are energetic with an amplitude of *ca.* 3 m at the coast and over 1.3 m close to HE and MS. Tidal currents (*ca.* 35 to 150 cm/s) are strong, particularly in channels and nearshore

¹⁸Web access: <http://noaasis.noaa.gov/NOAASIS/ml/avhrr.html>

¹⁹Web access: <http://modis.gsfc.nasa.gov/>

²⁰Web access: <http://tidesonline.nos.noaa.gov/>

regions (Gay and Vaughan, 2001). Associated with the variable bottom topography and stratification in PWS, complex patterns of internal tides are to be expected but have not yet been systematically studied. The NOS tide gauge stations also record hourly sea surface temperature and surface pressure data.

Four NOAA/National Weather Service (NWS)/National Data Buoy Center (NDBC²¹) buoys, 46060, 46061, 46076 and 46081 (Fig. 1.2), provide quality-controlled, hourly SST and surface meteorological data over PWS and the adjacent continental shelf region. Among these buoys, 46060, located in Central Sound, and 46081, in the northwestern Sound, are inside PWS. The position of 46060 was re-established on 6 DEC 2004 at *ca.* 2 *km* north of its previous location. The position of 46061 is *ca.* 40 *km*, south of the position of 46060 on the continental shelf outside the entrance of HE. The data are quality-controlled and temporal gaps are filled by linear interpolation. Buoy 46060 also provided real-time hourly vertical profiles of horizontal velocity through ADCP observations between 22 SEP 2004 and 25 AUG 05. The ADCP covered the water column between 26 and 368 *m* in 18 *m* interval bins in a total water depth of 446 *m*.

There are four other ADCP moorings that were deployed by PWSOOS (PWS Ocean Observing System²²) for nearly one-year (JUN 2005 to MAY 2006), providing time series of velocity profiles at two locations in each strait, viz., HE1 and HE3 in HE and MS1 and MS3 in MS, respectively (Fig. 1.2). At each mooring location, there is an upward looking and a downward looking ADCP, both located at a depth of 100 *m* to provide effective coverage over the full water column. For the upper 100 *m*, the velocity data are recorded from *ca.* 4 *m* below the surface with a constant 4 *m* depth interval. There is a *ca.* 17 *m* gap between

²¹Web access: <http://www.ndbc.noaa.gov>

²²Web access: <http://ak.aos.org/op/data.php?region=PWS>

the upward-looking and downward-looking ADCP measurements at each mooring location. At depths greater than 100 *m*, the velocity data are recorded with a constant 8 *m* depth interval at three of the locations; however, at MS3, the data are recorded with a 4 *m* depth interval. Due to occasional ADCP failures, only *ca.* 90 day (JUN to SEP 2005) of hourly velocity profiles are available for the simultaneous, two-point estimates of observed volume transports through HE and MS.

Another independent dataset, the GAK1 time series²³ (Fig. 1.2), provides a monthly climatology at hydrographic station GAK1 (59°51' *N*, 149°28' *W*) (Weingartner *et al.*, 2005), based on a 30-year record of monthly CTD profiles. GAK1 is located outside PWS at the mouth of Resurrection Bay near Seward with a water depth of 260 *m*. The GAK1 dataset includes *ca.* 300 monthly measurements since 1970. The measurement accuracy for temperature and salinity before the mid-80s was 0.02°C and 0.05 *ppt*, and better than 0.01°C and 0.01 *ppt* since then (Weingartner *et al.*, 2005). Six time series of temperature and salinity are available at standard depths of 25, 50, 100, 150, 200, and 250 *m*.

1.3.2 Results of Previous Numerical Studies

Based on numerical simulations with Princeton Ocean Model (POM²⁴), for strong inflow through HE, the cyclonic circulation in the Sound is vigorous and strongly coupled to offshore influences; for weak inflow through HE, the circulation in the Sound is weakly coupled to offshore influences (Mooers and Wang, 1998). In some other numerical simulations with POM (Wang *et al.*, 2001 and Jin and Wang, 2004), the spring (April - May) circulation pattern is characterized by a weak (maximum current 0.1*m/s*) anticyclonic flow

²³Web access: <http://www.ims.uaf.edu/gak1/>

²⁴Web access: <http://www.aos.princeton.edu/WWWPUBLIC/htdocs.pom/>

over the Central Sound, while the autumn (September - October) circulation is dominated by a basin-scale, cyclonic gyre (maximum current 0.2 m/s) due to the increase of the ACC through-flow and maximum freshwater discharge. Summer is the transition period between the two circulation regimes. Based on model sensitivity studies (Jin and Wang, 2004), salinity is the most important factor determining the Central Sound circulation patterns, while wind has more impact on the mixed layer depth.

Again using POM, the response of the PWS interior circulation to the flow structure at HE and MS under various initial states and forcing configurations was examined (Bang and Mooers, 2003). The flow is layered both at HE and MS under baroclinic conditions with two (four) layers under March (September) stratification conditions. In both stratification conditions, the upper layers typically transport inflow through HE, and a cyclonic eddy develops over Central Sound. Dominant westward (coastal downwelling-favorable) winds enhance the upper layer inflow and the lower layer outflow; when eastward (coastal upwelling-favorable) winds are dominant, the upper layer outflow and the lower layer inflow agree with the observations in the SEA study (Vaughan *et al.*, 2001). Finally, conservation of mass at HE and MS indicates that there is also significant recirculation (outflow) through HE, which is robust evidence to challenge the simple “through-flow circulation” pattern in PWS, *i.e.*, water masses simply entering PWS through HE and then exiting through MS.

More recently, numerical simulations demonstrate the influence of detailed temporal/spatial flow structures at the HE open boundary on the circulation and stratification in PWS (Bang *et al.*, 2005). Hourly winds at a single point alone are not capable of reproducing synoptic variations in the observed temperature and velocity. Further examination of their simulations (thanks for Dr. Bang’s generously providing their simulated model fields) indicates

that with the help of time-dependent baroclinic inflows at HE, the model reproduces a surface heating/cooling cycle beginning from June of 1996 when compared with observed CLAB temperature profile data, and better agreement can be obtained when the dominant tide (M2) is incorporated at the HE and MS open boundaries. The necessity of extending the open boundaries of the model to include the Alaska shelf for avoidance of great uncertainties in the numerical OBCs caused by large variability of the flow structure at HE and MS was recognized as necessary to study more consistently and comprehensively the dynamical interactions between PWS and the NGOA. The first attempt at one-way coupling of this extended-PWS POM, which covers the shelf region offshore PWS, with North Pacific Nowcast/Forecast System (NPACNFS; from Dr. Dong-Shan Ko) from the Naval Research Laboratory (NRL), produced realistic circulation features over the NGOA shelf, but it failed to simulate the seasonal thermohaline variations in the Sound due to the local occurrence of unexpectedly strong mixing (Wu, 2003). Obviously, more work is needed to introduce accurately and evaluate fully the role of surface winds, atmospheric pressure, and flow and mass structures at open boundaries in determining the synoptic (transient) circulation patterns in PWS.

1.4 PWS/NFS and EPWS/NFS

Various coastal ocean nowcast/forecast systems are being developed around the world (Section 1.1), aiming at ocean current, thermohaline structure, and coastal sea level prediction for safe navigation, ecosystem protection, and coastal defense. Typically, the real-time operation of these systems is in need of continuous inputs of surface atmospheric forcing and flow/temperature/salinity forcings at the lateral open boundaries to a coastal ocean model.

A common strategy is off-line coupling from a regional mesoscale atmospheric model at the sea surface, and from a basin-scale or global ocean circulation model and a tidal model at the lateral open boundaries. The real-time implementation of such a system includes model validation and verification, data transfer and management, and output visualization.

One such nowcast/forecast system, named as PWS/NFS (Fig. 1.2), has been running for Prince William Sound, Alaska since early 2001. After further upgrading of PWS/NFS to make use of more realistic Open Boundary Conditions (OBCs) with a larger model domain, EPWS/NFS (Fig. 1.2) has been running continuously since 23 FEB 2005. And PWS/NFS continued to operate until AUG 2006, nearly 1.5 years after the successful operation of EPWS/NFS began, to allow the smooth transition to, and the evaluation of the superiority of, the upgraded system. The EPWS/NFS model parameters, forcings, and outputs are published daily through the Internet along with real-time verifications with observations²⁵.

1.4.1 Modeling System

Based on the Princeton Ocean Model (POM; Mellor, 2002; Blumberg and Mellor, 1987), PWS/NFS is the first-generation coastal ocean prediction system for PWS (Table 1.1). PWS/NFS covers the entire PWS domain (but does not include the continental shelf outside HE and MS) with a horizontal resolution of *ca.* 1 *km* and 26 σ -levels in the vertical. The high-resolution bottom topographic data (*ca.* 300 *m*) from PWSSC (Prince William Sound Science Center²⁶), combined with ETOPO5 (5-minute gridded elevation data) from NGDC (National Geophysical Data Center), are used to obtain PWS/NFS bottom topography. The minimum water depth in PWS/NFS is set to 10 *m* due to the large tidal range.

²⁵Web access: <http://epws-nfs.rsmas.miami.edu>

²⁶Web access: <http://www.pwssc.gen.ak.us/>

PWS/NFS and EPWS/NFS configurations

	PWS/NFS	EPWS/NFS
Domain	59.79 to 61.28N 211.28 to 214.36E	59 to 61.28N 210 to 215E
Grids	155x150x26	251x226x26
Horizontal Resolution (m)	ca. 1100	ca. 1100
Max. Water Depth (m)	846	4420
HORCON	0.2	0.1
TPRNI	1.0	1.0
Tides	8 tidal constituents from Foreman tidal model (Foreman, 2005)	8 tidal constituents from a 2-D tidal model forced by Foreman tidal model (Foreman, 2005)
Surface Winds	RAMS	RAMS
OBCs	tides (elevation only)	hourly Global-NCOM (temperature, salinity, currents) plus tides (elevation and current)
Heating/Cooling	COADS climatology	COADS climatology plus relaxation to Global-NCOM SST
Runoff	Simmons snow melt climatology (Simmons, 1996)	none

The HORCON (non-dimensional factor in the Smagorinsky closure scheme (1963) for horizontal mixing of momentum) and TPRNI (inverse horizontal Prandtl number; *i.e.*, ratio of horizontal diffusivity to horizontal viscosity) parameters are set equal to 0.2, and 1.0, respectively. PWS/NFS starts from rest with the initial temperature/salinity condition interpolated from the observed winter climatology. With its lateral open boundary placed at HE and MS, passive radiation Open Boundary Conditions (OBCs) are applied; *i.e.*, propagating waves inside the model domain are allowed to radiate out of the open boundary, but no throughflow (net transport), is specified.

Surface wind is obtained by the vertical extrapolation of the wind output from RAMS (Pielke *et al.*, 1992; Liu *et al.*, 2006) to 10 *m* height, and then the wind stress is calculated

using the formula by Large and Pond (1981). RAMS is run at the Alaska Experimental Forecast Facility (AEFF) of the University of Alaska Anchorage (UAA) with triply-nested horizontal grids and a stretched sigma vertical coordinate system. The finest horizontal resolution is 4 *km*, covering the entire PWS/NFS (and also EPWS/NFS) domain. RAMS is initialized from the 12Z initialization of the North American-domain National Centers for Environmental Prediction (NCEP) mesoscale Eta model as represented on the 45-km World Meteorological Organization (WMO) 216 grid, and integrated for a 48-hr forecast.

Monthly fresh water flux due to runoff from snowmelt distributed according to the coastal orography is derived from a hydrological model (Simmons, 1996), and it is applied as precipitation at the PWS/NFS surface grid points adjacent to land (Bang and Mooers, 2005). Surface heating and cooling are given by the climatological monthly heat flux from COADS (Comprehensive Ocean and Atmospheric Data Set; Woodruff *et al.*, 1998). Tidal forcing with surface elevation only, consisting of 8 tidal constituents (M2, S2, N2, K2, K1, O1, P1, Q1), is obtained from a tidal model (Foreman *et al.*, 2000) and interpolated into PWS/NFS open boundary points.

Despite its partial success in addressing the circulation in Central Sound, the discovery of the complexity of flow structures at HE and MS, as well as the strong sensitivity of the circulation in Central Sound to the detailed flow structure at HE (Bang and Mooers, 2003), suggests that the simple radiation OBCs at HE and MS for PWS/NFS is inappropriate because it does not allow for the full dynamical interaction between PWS and continental shelf, where the ACC, wind-forcing, and mesoscale variability dominate.

Consequently, in 2005, with the advent of Global-NCOM availability for OBCs, using the same wind and atmospheric pressure forcing and surface heating and cooling, as mentioned

above, a second-generation coastal ocean prediction system, called EPWS/NFS, was implemented expanding the model domain to include the continental margin seaward of PWS (Table 1.1). This approach replaces simple radiation OBCs specified at HE and MS with OBCs specified around the open boundaries of the extended domain based on daily values from Global-NCOM²⁷, plus values from the a 2-D tidal model (explained below). Therefore, the internal dynamics of EPWS/NFS over the Alaskan Shelf and PWS determine the flow and mass field structures at HE and MS.

The availability of the data-assimilative Global-NCOM since 23 FEB 2005, and also the availability of the mesoscale numerical weather prediction model RAMS for PWS since OCT 2004, provide an opportunity to establish a more realistic nowcast/forecast system than before by using one-way coupling from the operational global ocean model fields and the regional mesoscale atmospheric model fields.

Global-NCOM is the $1/8^\circ$ global version of the Naval Research Laboratory (NRL) Navy Coastal Ocean Model (NCOM) with 40 (sigma-z) hybrid vertical levels concentrated toward the surface to maintain a minimum rest thickness of 1m in the uppermost layer, and with sigma coordinates above 130 m depth (i.e., the global average shelf break depth) and z coordinates below (Barron *et al.*, 2006). It is run daily at the Naval Oceanographic Office (NAVOCEANO) with atmospheric forcing from the Navy Operational Global Atmospheric Prediction System (NOGAPS) and assimilation of satellite sea surface temperature (SST) and synthetic temperature and salinity vertical profiles derived from satellite altimetry via the MODAS analysis system. Monthly climatological runoff from nearly 1,000 rivers, including the Copper River immediately upstream of PWS, is incorporated.

²⁷Web access: http://www7320.nrlssc.navy.mil/global_ncom/

EPWS/NFS has a grid size of 1/100th degree in latitude and 1/50th degree in longitude (*ca.* 1.1 km at 60° N), with 26 σ -levels in the vertical direction (4(5) levels with logarithmic distribution at the surface (bottom), and 17 intermediate levels with uniform distribution). The horizontal resolution is sufficient to resolve mesoscale eddies prevailing inside PWS. High-resolution bottom topographic data from PWSSC is applied inside PWS, and ETOPO5 is used outside PWS for EPWS/NFS topography. The HORCON and TPRNI parameters are set equal to 0.1 and 1, respectively. Due to the narrow, steep shelf in PWS, and due to the large tidal amplitude (*ca.* +/- 3 m), the minimum water depth at the coastline is set equal to 5 m since a wetting-and-drying algorithm is not used. Also due to the complex nature of the coastline surrounding PWS, the orthogonal rectilinear grid in EPWS/NFS does not represent well the small-scale details of the coastline, and thus, the minimum water depth in some small inlets or fjords is greater than 5 m.

Instead of the elevation-only tidal forcing applied as the OBCs in PWS/NFS, tidal elevations and current are applied at the (southern) open boundary in EPWS/NFS. They are computed by a density-homogeneous version of EPWS-POM implemented on a slightly larger model domain but with the same grid as in EPWS/NFS. The tidal model is forced by sea level oscillations at the open boundaries, which consist of eight tidal constituents (amplitudes and phases), namely, four major semi-diurnal constituents (M2, S2, N2, K2) and four major diurnal constituents (K1, O1, P1, Q1), and which are obtained from the a tide model (Foreman *et al.*, 2000) and interpolated to the open boundaries of the EPWS-POM tidal model.

The boundary conditions utilized are the modified Flather radiation OBCs (Flather radiation plus Roed local solution, Roed and Smedstad, 1984; Palma and Matano, 2000),

and one-way nesting with three-hourly Global-NCOM fields (temperature/salinity, velocity, sea level) with tides added as described above.

There is no fresh water flux for runoff from snowmelt used in EPWS/NFS. Outside PWS, runoff from the Copper River, which is regarded as the most important source of fresh water on the shelf, has been incorporated into Global-NCOM. An operational hydrological model for fresh water runoff will be considered as a future upgrade option. Surface heating and cooling are given by the climatological monthly heat flux from COADS as in PWS/NFS, and in addition, EPWS/NFS SST is relaxed to Global-NCOM SST with a relaxation time scale of 1 day.

1.4.2 Global-NCOM, RAMS Forcing

Wind velocities for one-year (2005) (Fig. 1.5) are strongly correlated between RAMS predicted and buoy observed winds at NDBC buoys 46060 and 46061: 0.6 and 0.7 (at zero lag) with *rmse* (root-mean-square-error) of 1.4 and 1.2, respectively, for both eastward and northward velocities. Significant synoptic wind events were effectively predicted by RAMS; for instance, a strong northwestward wind event during the first half of March 2005, and another strong northeastward wind event in mid-November. Both events are characterized by a significant wind speed of *ca.* 20 *m/s* for several days in both the predictions and observations.

Power spectra for RAMS predicted and observed winds at both buoy locations agree well, including diurnal peaks (Fig. 1.6), and they have relatively high coherence and are nearly in phase for periods longer than a few days (not shown). Also, the spatial coherence for RAMS predicted and observed surface winds between the two buoy locations (separated

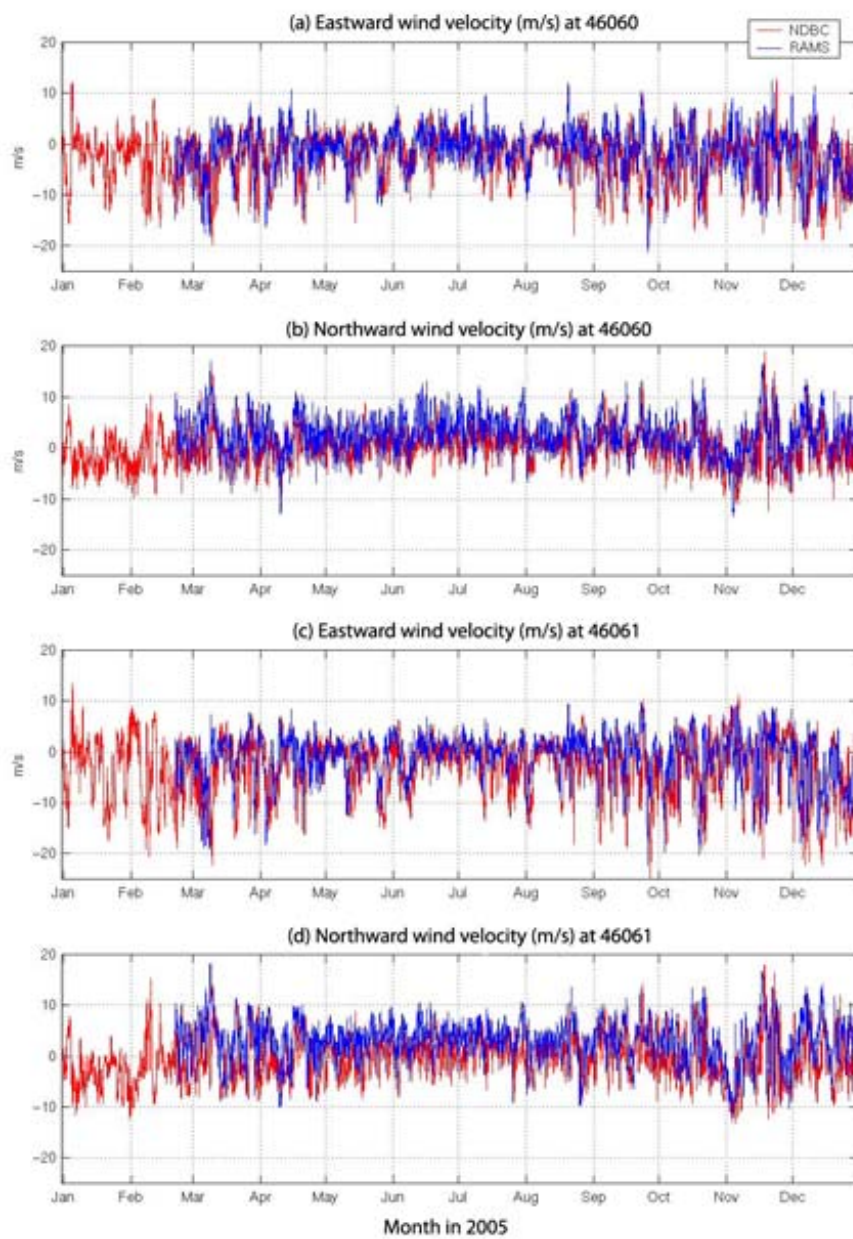


Figure 1.5: NDBC buoys observed and RAMS simulated wind velocities: (a) eastward and (b) northward velocity at 46060; (c) eastward and (d) northward velocity at 46061

by *ca.* 40 *km*) indicates similar structure: highly coherent and in phase for periods longer than *ca.* 20 hours (Fig. 1.7).

In NGOA, Global-NCOM resolves the significant seasonal variability of the ACC. Based on the transition from a westward flow zone to an eastward flow zone near the coast at the EPWS/NFS eastern boundary (Fig. 1.8), the width of the ACC is as broad as 32 *km* in December 2005 and as narrow as 18 *km* in June 2005 and February 2006. Correspondingly, the annual-mean ACC volume transport is estimated as 0.1 *Sv* with a maximum of 0.22 *Sv* and a minimum of 0.04 *Sv*. Further offshore over the shelf, the reversed eastward flow is also weakest and narrowest in December 2005, while broadest and strongest in June 2005 and February 2006. Over the continental slope and the deep water, westward flow dominates throughout the year except during summer 2005 (July, August, and September) and February 2006. At the western boundary (Fig. 1.8), westward flow occurs within a few kilometers of the coast, with eastward (westward) flow dominant during the summer (winter) time further offshore. At the southern boundary (Fig. 1.9), except for the predominantly northward flow in March, April and July 2005, co-occurrence of northward and southward flow during the remaining months indicates complicated eddy variations.

1.4.3 Performance of EPWS/NFS vs. PWS/NFS

Results of EPWS/NFS serve as part of the motivation for this study, and will be utilized in the subsequent analyses. Therefore, it is essential to assess the performance of EPWS/NFS and its improvement over PWS/NFS.

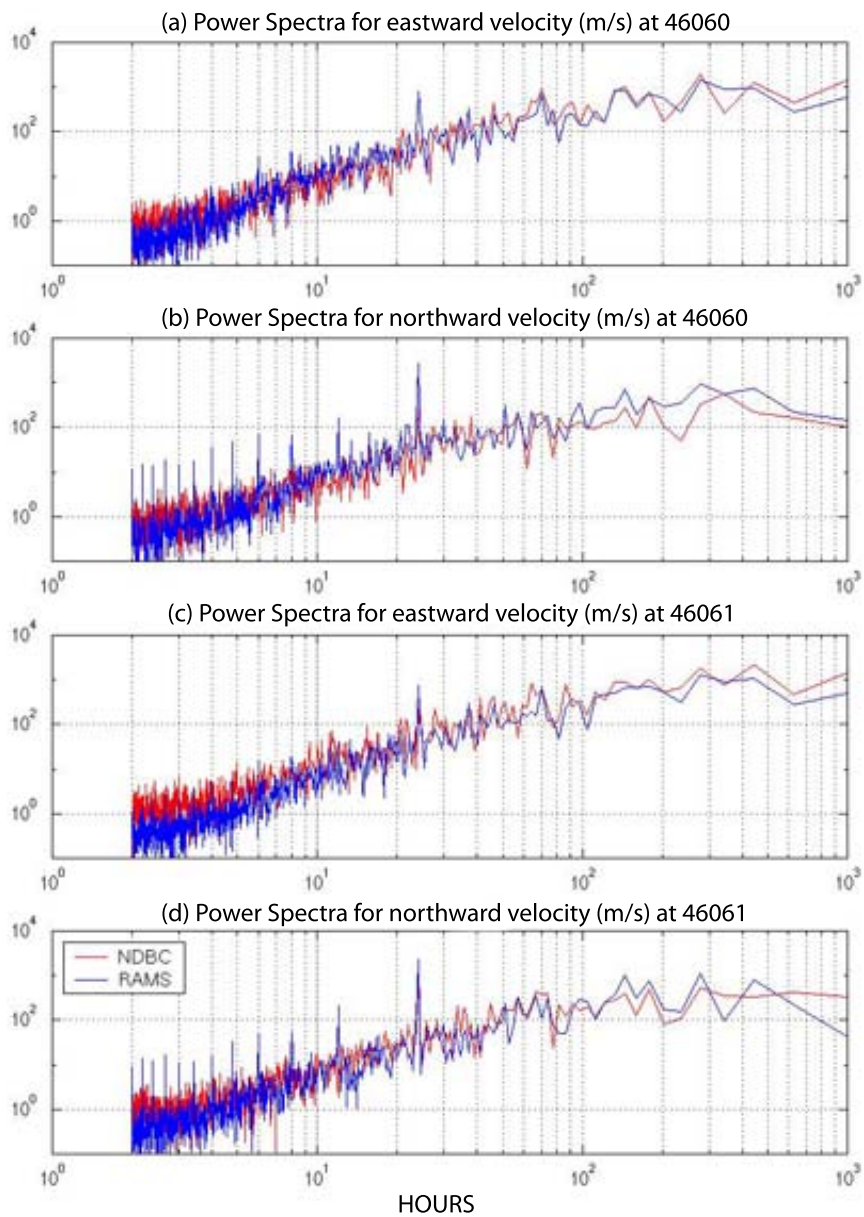


Figure 1.6: Power spectra (DOF=10) for NDBC observed (red) and RAMS simulated (blue) (a, c) eastward and (b, d) northward wind velocities at 46060 (in Central Sound) and 46061 (outside HE)

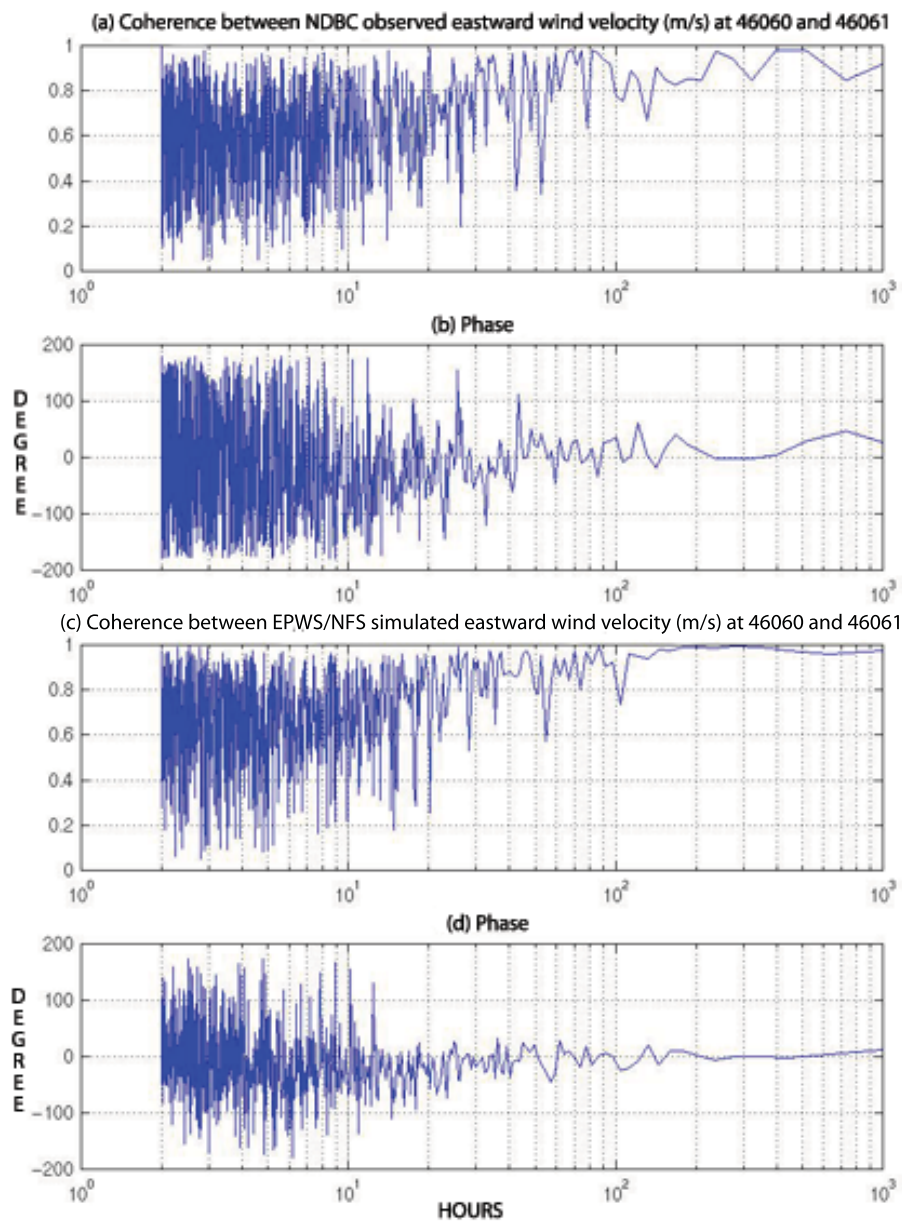


Figure 1.7: Coherence function (DOF=10) between observed eastward wind velocity between 46060 and 46061: (a) magnitude and (b) phase. For comparison, results from nowcast eastward wind velocity are also shown: (c) magnitude and (d) phase.

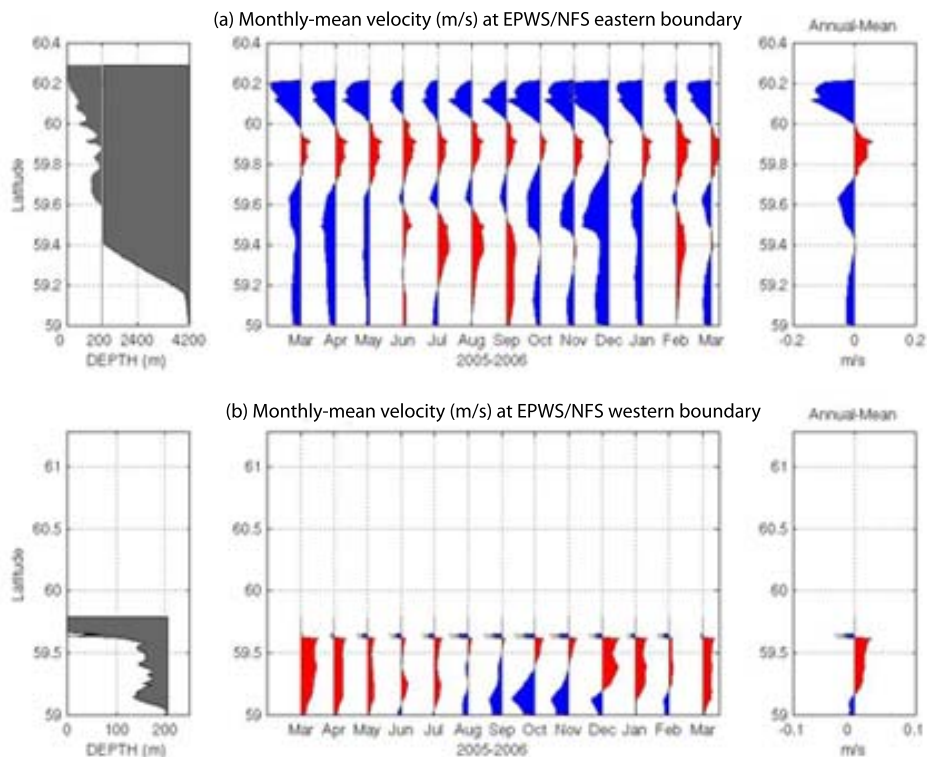


Figure 1.8: Monthly-mean depth-averaged zonal velocity at the eastern (upper) and western (bottom) boundaries of EPWS/NFS during March 2005 - March 2006, as well as the corresponding annual-mean depth-averaged velocity (right panels). The bottom topography at boundaries is also shown (left panels); notice that the different depth scales are used for the plot of bottom topography and depth-averaged velocities, respectively, at the eastern and western boundaries.

Coastal Sea Level

With the one-year (MAR2005 to FEB2006) local mean removed at the three tide gauge stations (Cordova, Seward, and Valdez) from both the simulations and observations, EPWS/NFS nowcasts of CSLs had standard deviations (STDs) of 1.20, 1.16, and 1.02 m , with $rmse$ of 0.76, 0.58, and 0.64 m and cross-correlations of 0.85, 0.85 and 0.84 (zero lag), respectively. In comparison, PWS/NFS nowcasts of CSLs at Cordova and Valdez had STDs of 1.32 and 1.38 m , with $rmse$ of 0.88 and 0.84 m and cross-correlation of 0.68 and 0.67 (zero lag). One-month time series (Fig. 1.10) indicate the characteristics of mixed tides with fortnightly modulation at each station. The difference between observations and PWS/NFS or

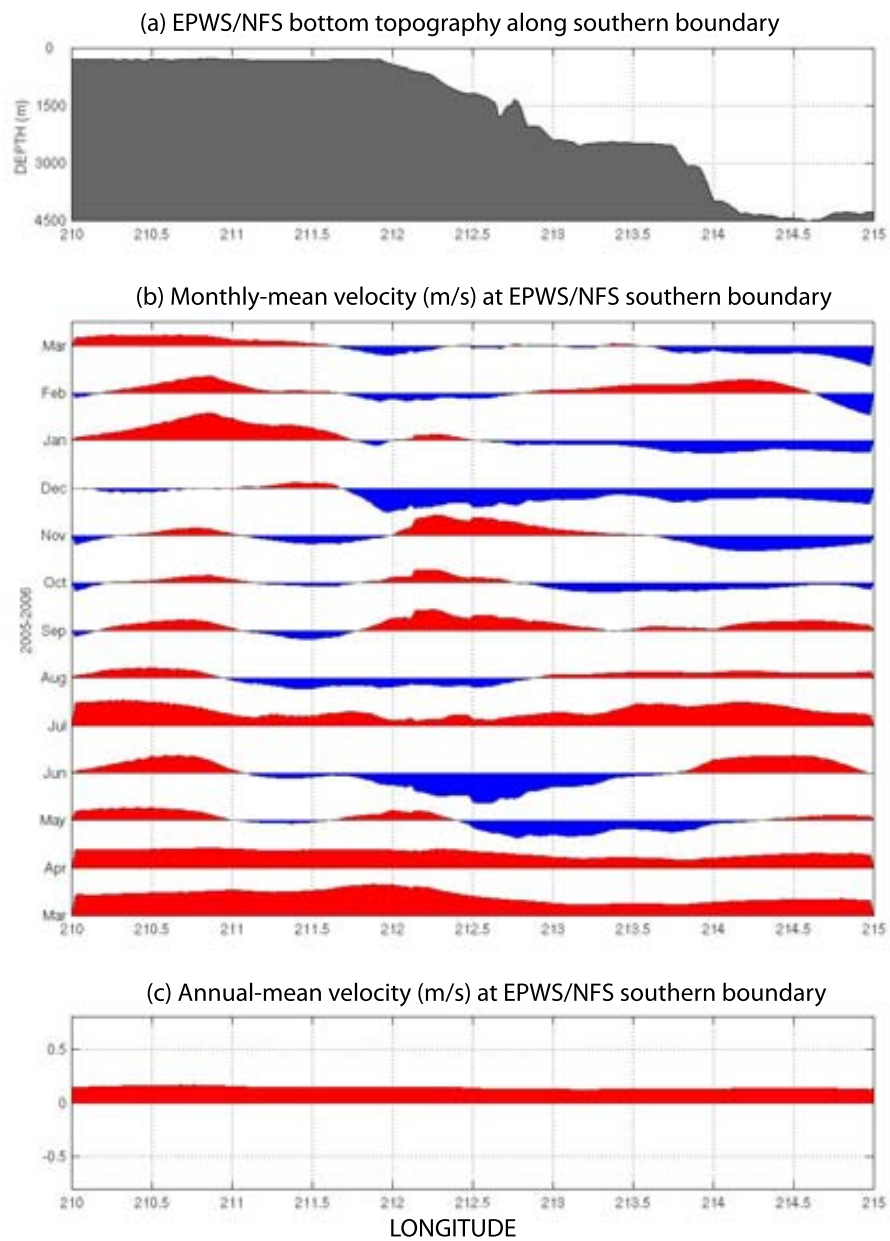


Figure 1.9: Monthly-mean depth-averaged meridional velocity (b) at the southern boundary of EPWS/NFS during March 2005 - March 2006, as well as the corresponding annual-mean depth-averaged velocity (c). The bottom topography at the southern boundary is also shown (a)

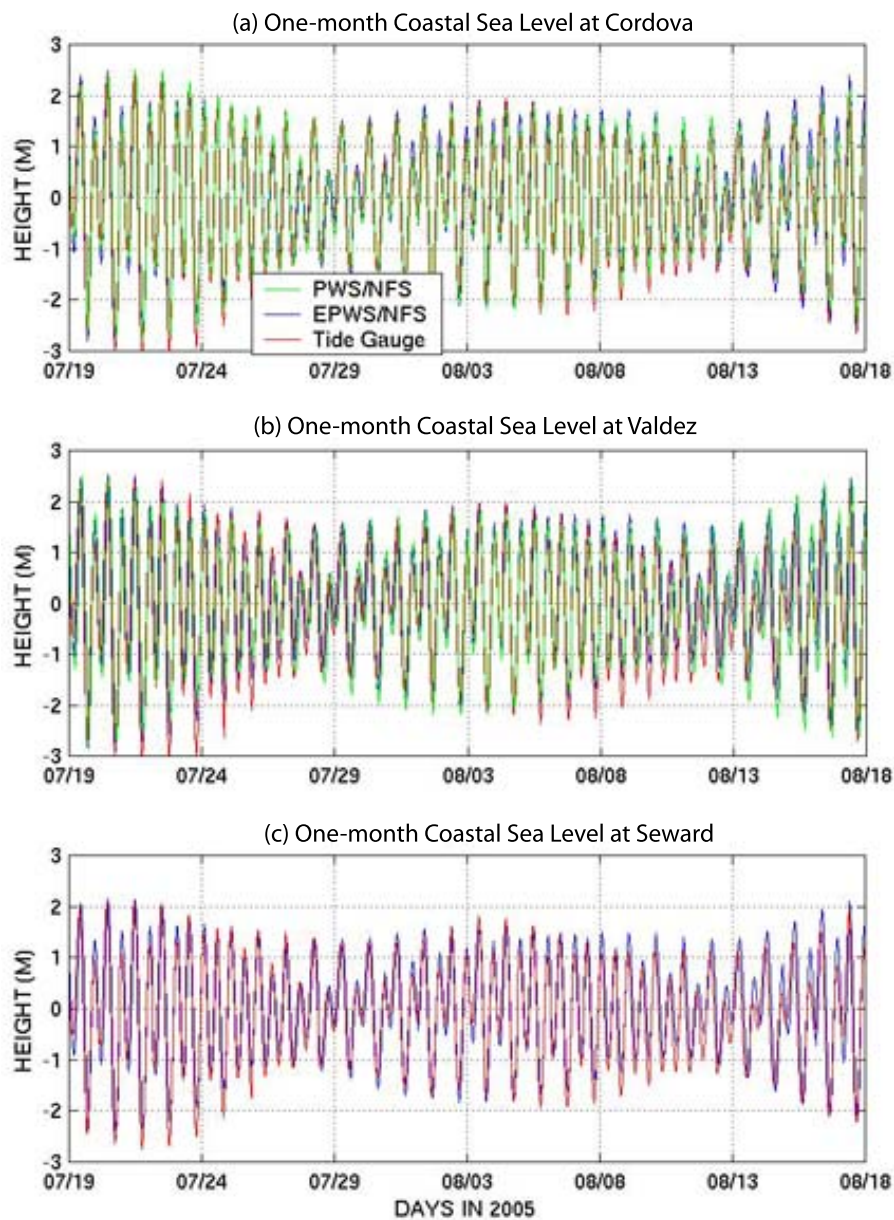


Figure 1.10: One-month comparisons of PWS/NFS nowcast (green), EPWS/NFS nowcast (blue) and observed coastal sea levels at (a) Cordova; (b) Valdez; and (c) Seward

EPWS/NFS nowcasts is usually a few centimeters but sometimes as large as 0.5 *m*, which occurs during spring or neap tides; for instance, on 25 JUL and 14 AUG 2005 at Cordova and Valdez. For the 40-hr low-passed CSL (Fig. 1.11), EPWS/NFS is less energetic than the observations, while PWS/NFS has very weak low-frequency variability.

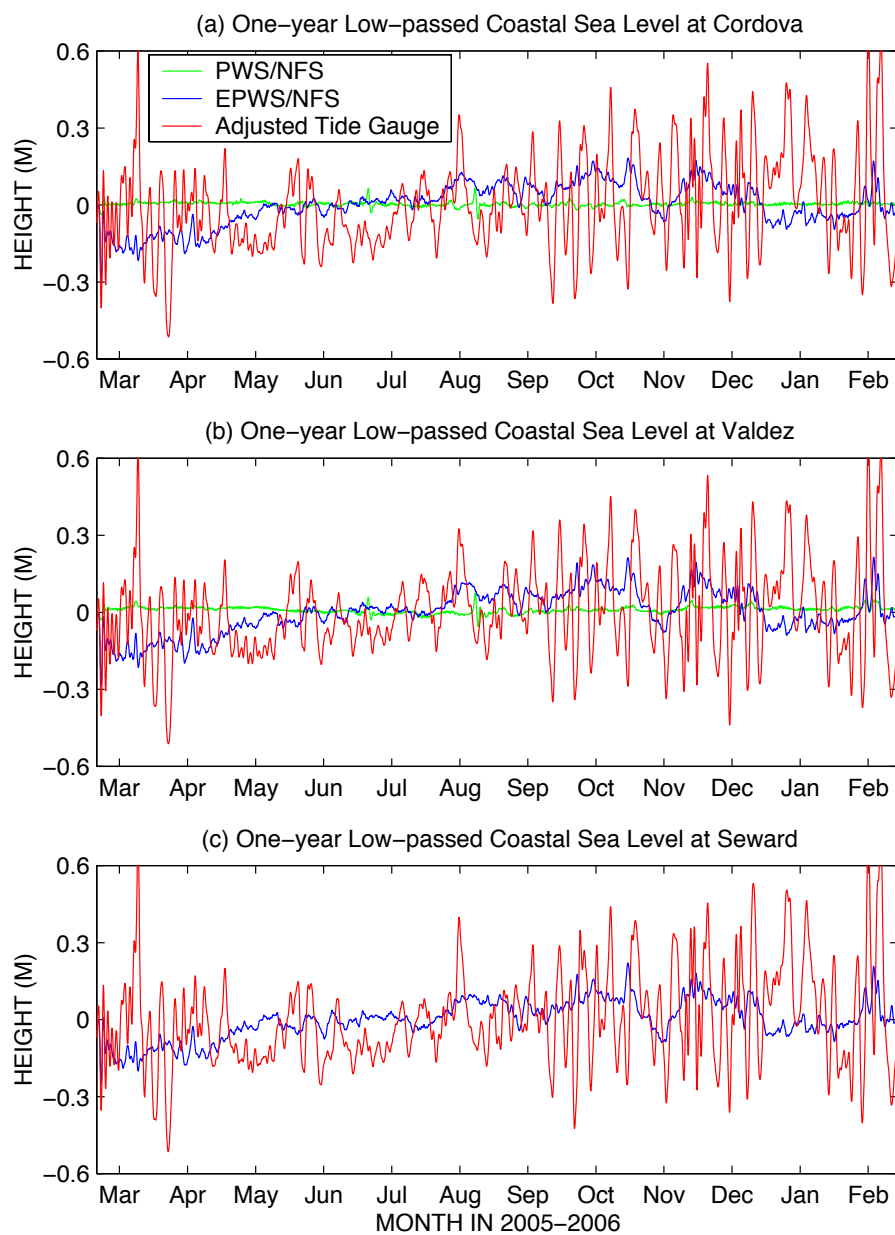


Figure 1.11: One-year comparisons of 40-hr low-passed PWS/NFS nowcast (green), EPWS/NFS simulated (blue) and adjusted observed (red) coastal sea levels at (a) Cordova; (b) Valdez; and (c) Seward

The CSL power spectra (Fig. 1.12) demonstrate the success of tide nowcasts in EPWS/NFS: the most energetic peaks, corresponding to diurnal and semi-diurnal tides, are nearly the same magnitude for the observations and nowcasts, although the peak for diurnal tides is broader in the observations than in the nowcasts. EPWS/NFS tides resemble PWS/NFS results, except that the PWS/NFS semi-diurnal tide is one to two orders of magnitude larger than the observed value. The secondary energetic peaks at 4, 6, and 8 *hrs* represent the shallow-water tidal constituent, but other physical process, such as atmospheric (wind and pressure) forcing, whose power spectra indicate a peak at 8 *hrs* (not shown), and barotropic Helmholtz resonance (Candela, 1991), whose typical period is around 6 hrs for PWS (Mooers *et al.*, 2007), may contribute to the 6 and 8-*hr* peaks, too. Other than for tidal periods, EPWS/NFS usually underestimates the observed CSL variations by an order of magnitude, while in PWS/NFS, for periods longer than 100 *hr*, the nowcast CSL variations differ from the observations by as much as three orders of magnitude, although better agreement is achieved for shorter periods ($< 10hr$). The apparent failure to simulate energetic low-frequency variations in CSLs (although significant improvement has been achieved in EPWS/NFS), probably suggests the lack of some important dynamical information inside PWS from the nowcasts; for instance, atmospheric pressure forcing, or more likely, from the OBCs.

From the coherence of detided CSLs between Valdez and Cordova (Fig. 1.13), PWS/NFS, EPWS/NFS nowcasts and observations are highly coherent and in phase at *ca.* 6 *hr* and for periods longer than 60 *hr*. Compared with both PWS/NFS and EPWS/NFS nowcasts, the relative large fluctuations of the observed phase and coherence relations between periods of 6 and 60 *hr* probably suggest that the effects of sea level response to synoptic atmospheric

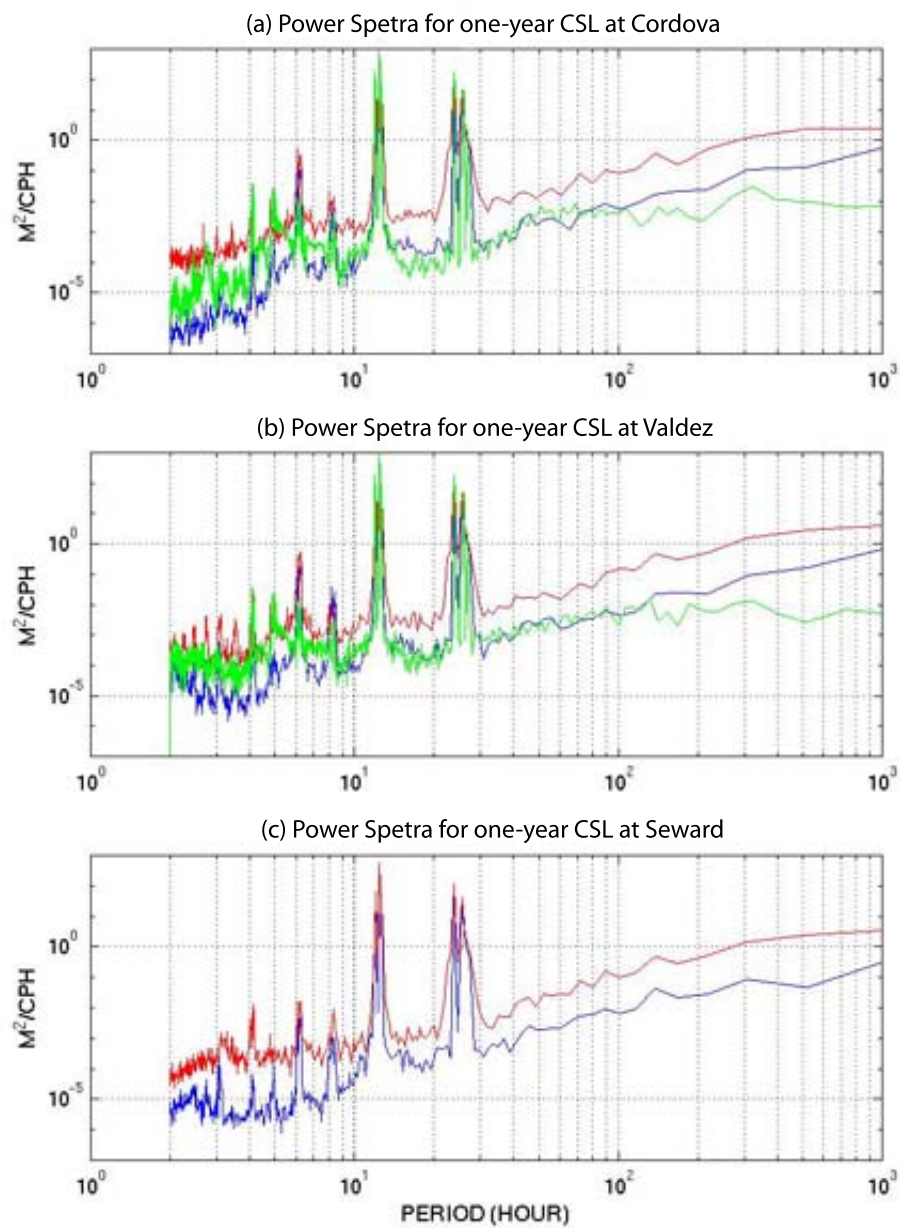


Figure 1.12: Power spectra (DOF=10) of one-year PWS/NFS simulated (green), EPWS/NFS simulated (blue) and observed coastal sea levels at (a) Cordova; (b) Valdez; and (c) Seward

forcing in this transition period band (explained in 6.1) is not well nowcast by both NFSs. For the periods longer than 100 *hr*, EPWS/NFS more closely resembles the coherence pattern and phase relations of the observations; e.g., highly coherent and in-phase, between detided CSLs at the two tide gauges. PWS/NFS nowcasts have somewhat smaller coherence and larger phase fluctuations.

Sea Surface Temperature

Overall, EPWS/NFS agrees with observed seasonal cycles of SST at all NDBC buoys, where water depth is relatively deep ($> 100m$), with the maximum SST in AUG and the minimum SST in MAR (Fig. 1.14). For instance, at NDBC buoy 46061, two adjacent SST peaks, separated by about two weeks in AUG, are nowcast by EPWS/NFS. While at Cordova and Valdez NOS tide gauges located in very shallow water ($< 10m$), EPWS/NFS over-estimates the maximum SST by 4 to 5 C° .

Cross-validation between EPWS/NFS and PWS/NFS at NDBC buoy 46060 (Fig. 1.15), which is located in Central Sound, indicates that although both models describe well the seasonal cycle of surface heating/cooling, PWS/NFS diverged from observed SST after MAY05 with a maximum of 5 C° difference. Starting from JUL 2005, EPWS/NFS accurately nowcast an observed cooling event, which reduced the SST by *ca.* 3 C° for a month. This event, however, was not nowcast by PWS/NFS. Also, for PWS/NFS, the maximum SST lagged observations by nearly two-weeks. During the wintertime, the synoptic time scale SST fluctuations of both EPWS/NFS and PWS/NFS are less energetic than observed. However, in contrast with EPWS/NFS, PWS/NFS SST is nearly 0.5 C° warmer than the observed values. The improved performance of EPWS/NFS compared to PWS/NFS was presumably

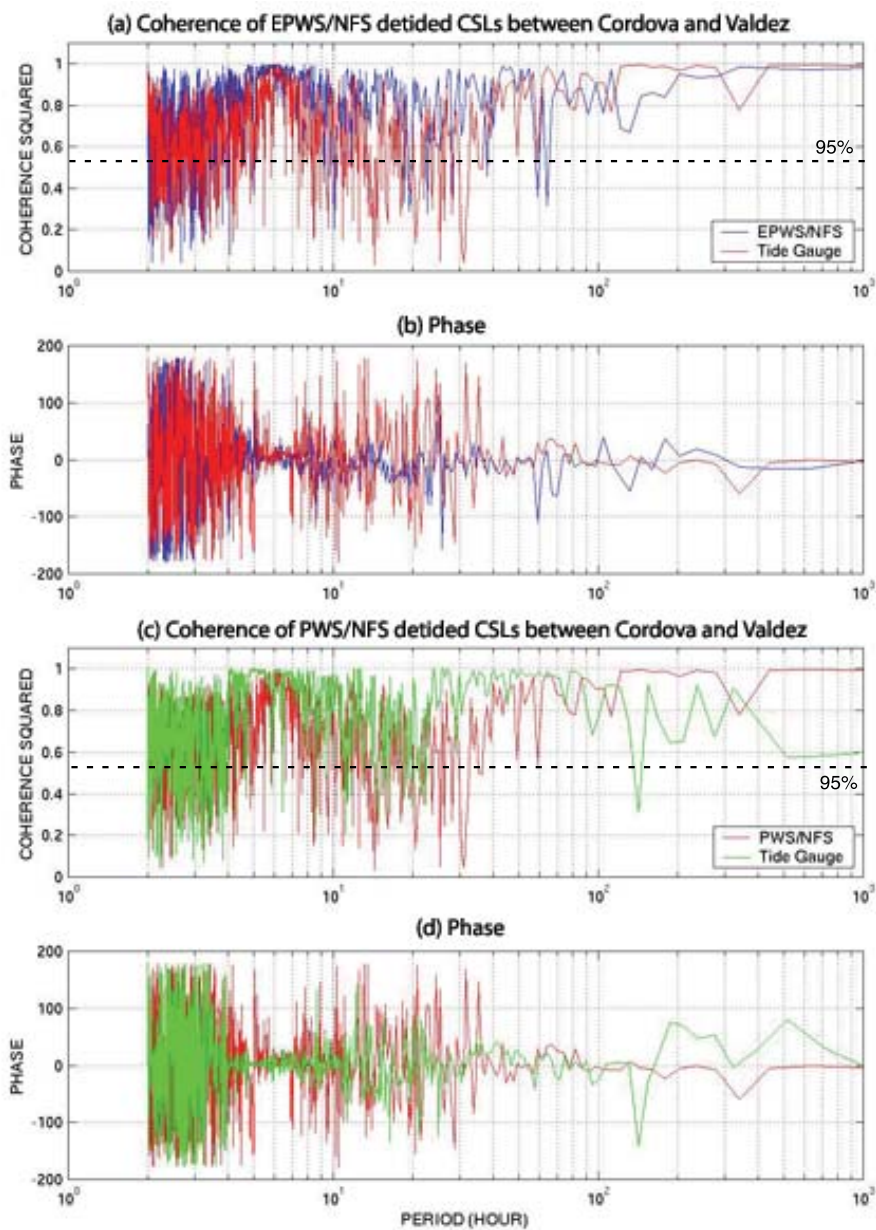


Figure 1.13: Coherence (a) and phase (b) of EPWS/NFS nowcast (blue) and observed (red) detided CSLs between Cordova and Valdez (DOF=10). For comparison, coherence and phase of PWS/NFS nowcast detided CSLs are also shown (c, d)

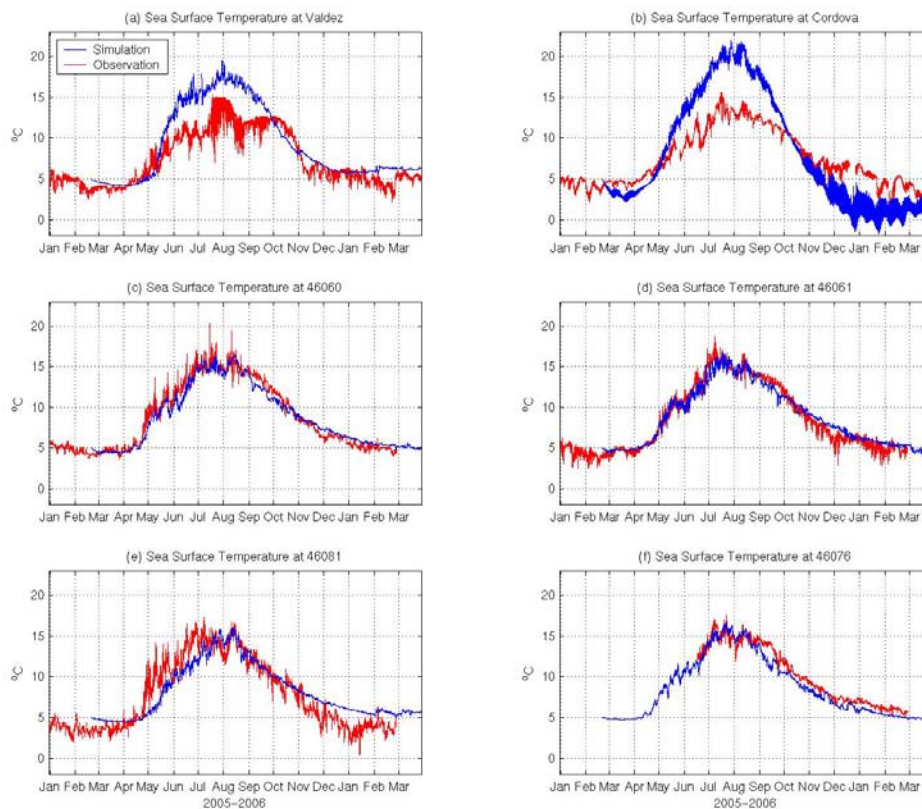


Figure 1.14: Comparisons between observed (red) and EPWS/NFS nowcast (blue) SST time series at: (a) NOS tide gauge Valdez; (b) NOS tide gauge Cordova; (c) NDBC buoy 46060; (d) NDBC buoy 46061; (e) NDBC buoy 46081; (f) NDBC buoy 46076

due to relaxation to the SST field of Global-NCOM, and probably due to improved surface horizontal advection of heat between the Alaska Shelf and PWS.

Seasonal Cycle of the Vertical Temperature Profile at the GAK1 Station on the Alaska Shelf

The monthly-mean SST, as well as the vertical temperature structure, at GAK1 of EPWS/NFS and the observed monthly climatology (Fig. 1.2) are similar for the upper 150 m (Fig. 1.16). Both indicate a of maximum SST of ca 13.5°C in AUG, and the maximum is increasingly delayed with depth; for example, it is delayed until OCT at 50 m

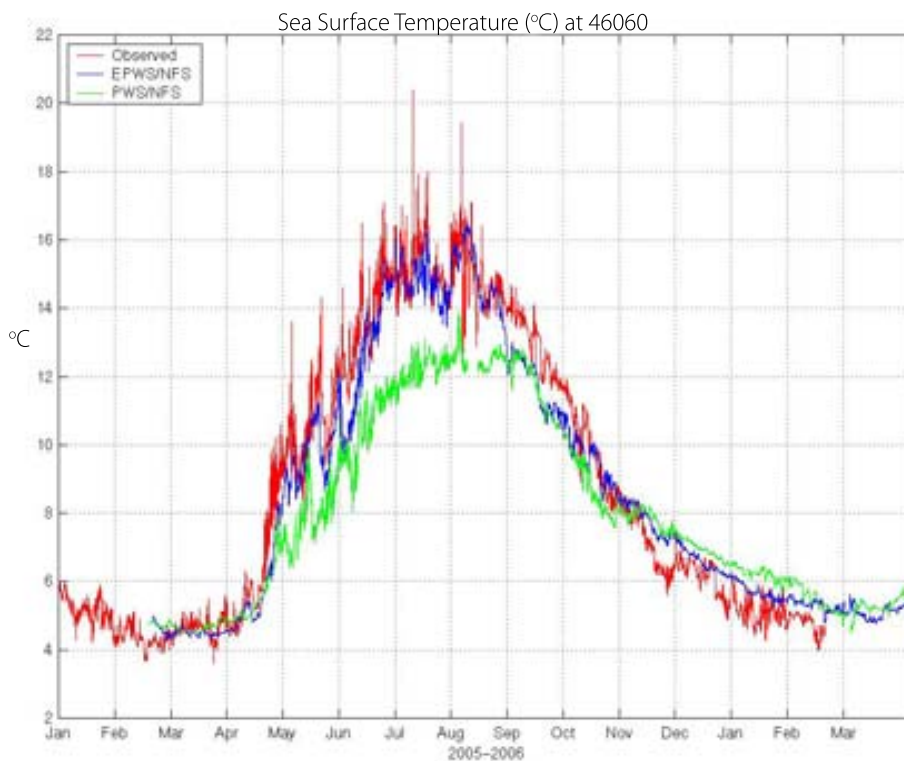


Figure 1.15: Comparisons between observed (red), EPWS/NFS (blue) and PWS/NFS (green) nowcast (blue) SST at 46060

depth. Below 50 *m*, however, the further delay to NOV of the maximum temperature in the monthly climatology is not reproduced by EPWS/NFS, which indicates the maximum temperature in OCT. Starting in the middle of OCT, the temperature at 75 *m* depth is warmer than that above due to the surface cooling, that reaches as low as *ca.* 4°C in MAR, which is well predicted by EPWS/NFS although the detailed structure of temperature variation at other depths is slightly different. This temperature inversion is compensated (not shown) for with freshening in the upper layer that maintains hydrostatic stability, at least on the monthly time scale.

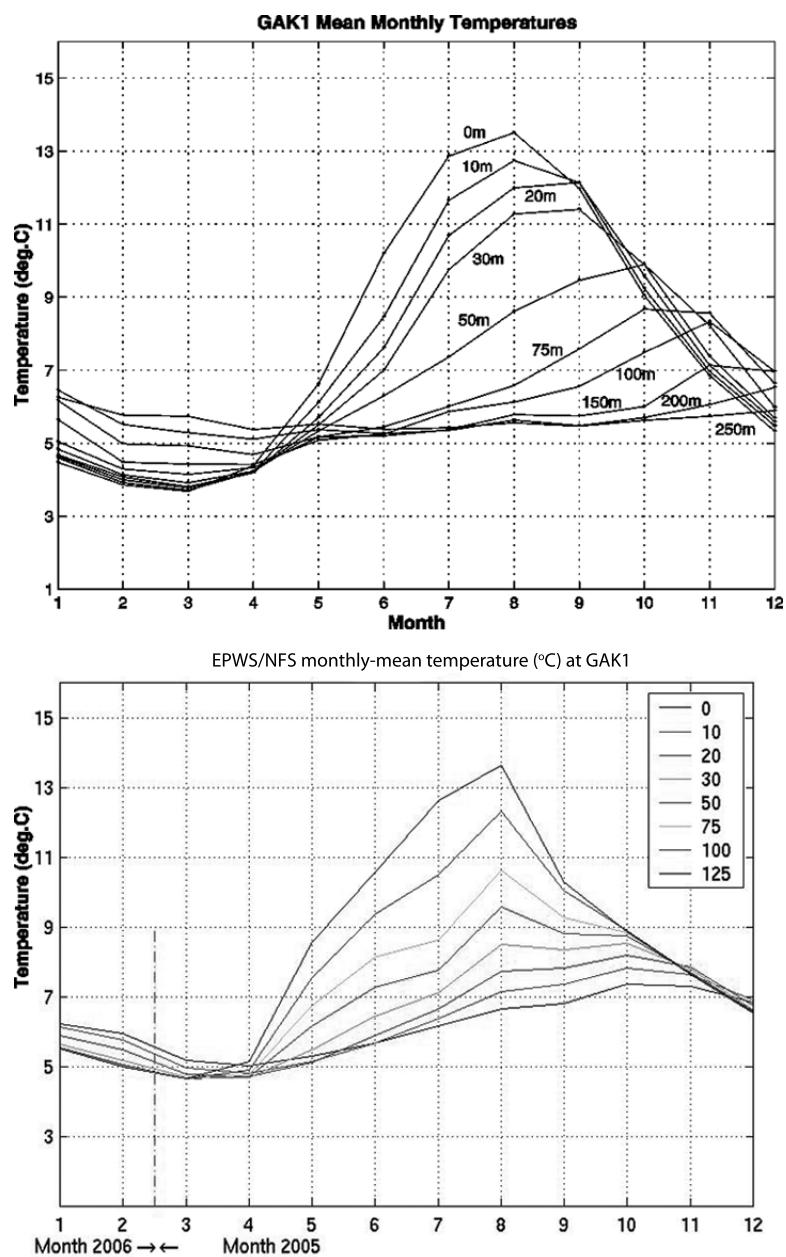


Figure 1.16: Observed (upper) and nowcast (bottom) monthly-mean temperature at various depths at GAK1. Observed monthly climatology is based on 30-year CTD measurements. Nowcast monthly mean is provided by EPWS/NFS from MAR2005 through FEB2006, and for the purpose of direct comparisons with observed values, monthly-means for the first two months are based on EPWS/NFS data in 2006 while for the remaining ten months, EPWS/NFS data in 2005 are used. Notice that the water depth is different between GAK1 (*ca.* 250 *m*) and the corresponding model location (*ca.* 140 *m*)

Vertical Current Profiles

In Central Sound, the ADCP installation on NDBC buoy 46060 operated from 22 SEP 2004 to 25 AUG 2005, allowing comparisons only during the first six months of the EPWS/NFS operation. Based on the six-month comparisons, EPWS/NFS, compared to PWS/NFS, provides rather reliable estimates of vertical profiles of tidal currents based on the comparison between nowcasts and ADCP observations at buoy 46060 (Mooers *et al.*, 2007). For instance, the dominant diurnal and semi-diurnal tidal currents, in both amplitude and phase (Figs. 1.17 and 1.18), are better nowcast by EPWS/NFS, especially for the northward velocity component. Further examination of the observed baroclinic structure (magnitude and phase) of the M2 tidal current, the most energetic tidal constituent in PWS, indicates that EPWS/NFS nearly duplicates the observed amplitude and phase in both anticlockwise and clockwise directions, in contrast to PWS/NFS results (Fig. 1.19). The large vertical variations of observed and EPWS/NFS M2 velocity are indicative of the presence of semi-diurnal internal tides.

Both the observed and nowcast time-depth mean velocities are small compared to their standard deviations, and compared with PWS/NFS, the EPWS/NFS time-mean velocity profile, as well as perturbation velocity profile, has a smaller mean square difference (and also larger correlation) relative to the observed value via a smaller coordinate rotation angle (see Table 3 in Mooers *et al.*, 2007). Except for the EPWS/NFS eastward velocity, PWS/NFS and EPWS/NFS barotropic velocities have a similar degree of temporal variability compared with the observations, although better correlation with the observations is obtained for the EPWS/NFS northward velocity. For the baroclinic velocities, both the observations and EPWS/NFS have similar standard deviation profiles but there are some

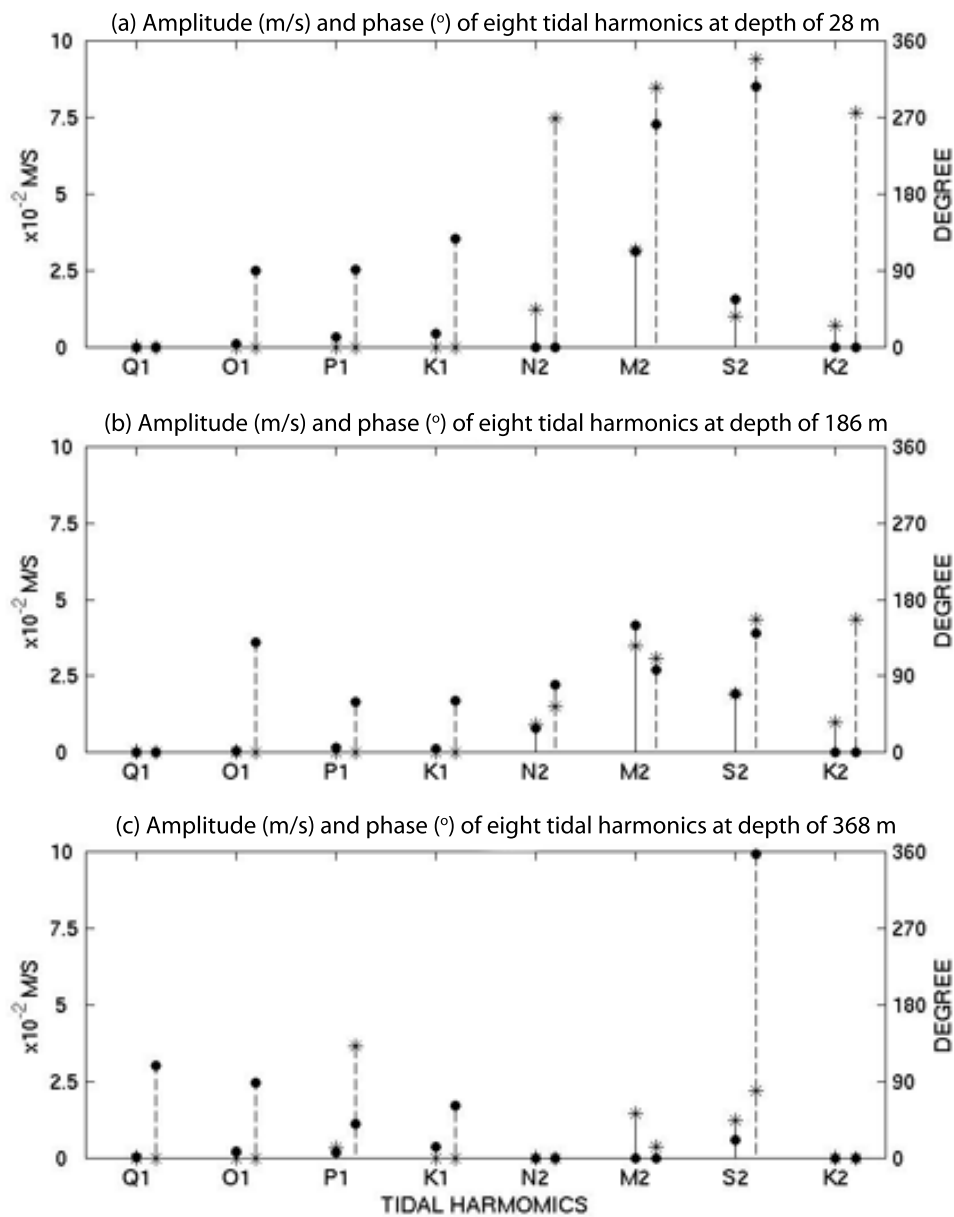


Figure 1.17: Amplitude (solid line) and phase (dashed line) of eight tidal constituents for six-month ADCP observed (star) and EPWS/NFS nowcast (solid circle) eastward velocities at buoy 46060 at three depths: (a) 28 m; (b) 186 m; (c) 368 m (Moore *et al.*, 2007).

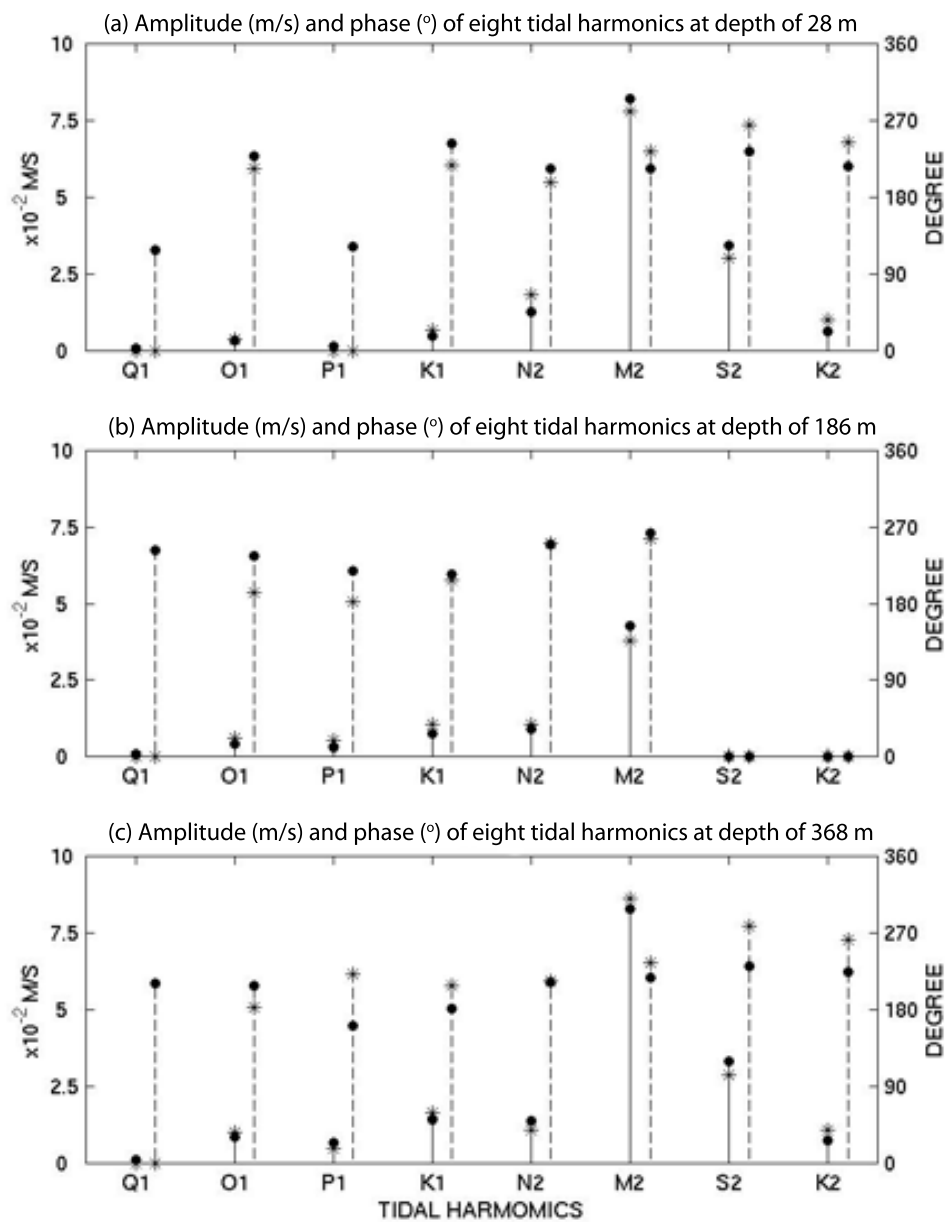


Figure 1.18: Amplitude (solid line) and phase (dashed line) of eight tidal constituents for six-month ADCP observed (star) and EPWS/NFS nowcast (solid circle) northward velocities at buoy 46060 at three depths: (a) 28 m; (b) 186 m; (c) 368 m. (on courtesy of Mooers *et al.*, 2007)

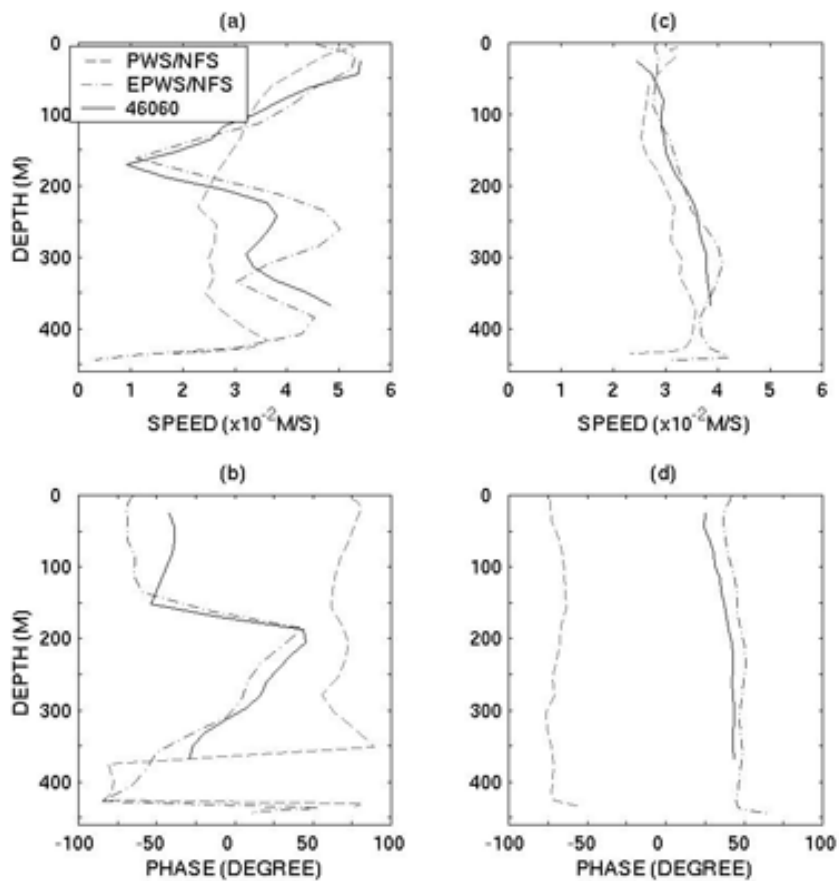


Figure 1.19: (a) Magnitude and (b) phase of anti-clockwise component of M2 tidal current at buoy 46060: ADCP observed (solid line), PWS/NFS nowcast (dashed line) and EPWS/NFS nowcast (dot-dashed line). Results for (c, d) clockwise component of M2 tide are also shown (Mooers *et al.*, 2007).

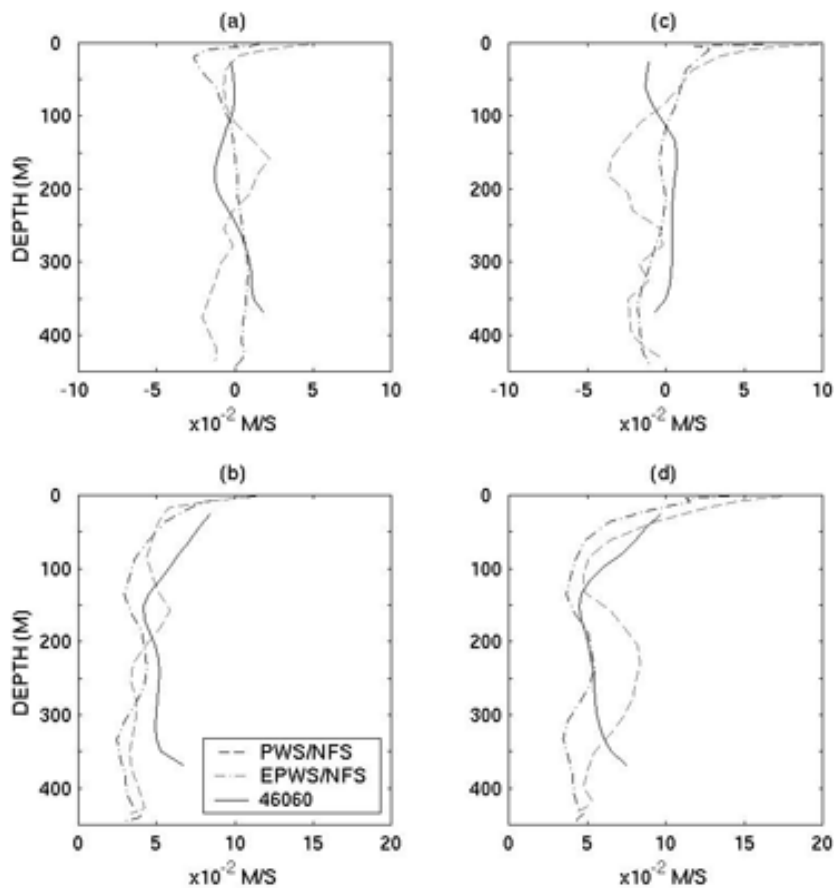


Figure 1.20: (a) Temporal mean and (b) standard deviations of six-month ADCP observed (solid line), PWS/NFS nowcast (dashed line) and EPWS/NFS nowcast (dot-dashed line) baroclinic eastward velocity profiles at buoy 46060. Results for (c, d) baroclinic northward velocities are also shown (Mooers *et al.*, 2007).

serious discrepancies in velocity directions (Fig. 1.20). Except close to the bottom, both models produce similar low-frequency velocity variability compared to that of the observations, while serious discrepancies in directions occurred from time to time.

Comparison of the 90-day mean velocity profile at HE1 with EPWS/NFS nowcast (Fig. 1.21) indicates that although the trend of the observed speed to increase with depth below 180 *m* is followed by EPWS/NFS, there exists a significant difference throughout the water column for the mean eastward velocity. The STD of the eastward velocity, however, is

better nowcast by EPWS/NFS, especially below 100 *m* depth. For the northward velocity, EPWS/NFS correctly simulates the inflow in both the surface and bottom layers, but misses the outflow in the intermediate layer (*ca.* 100 to 200 *m*) at this location for this 90-day period. Compared with the observed value, the EPWS/NFS nowcast STD of the northward velocity is less energetic for the upper 50 *m* and the intermediate depths of 100 to 200 *m*. At MS1 (Fig. 1.22), EPWS/NFS fails to simulate the observed mean eastward velocity profile, but, except close to the surface, the EPWS/NFS northward velocity agrees well with the observed profile. Close to the bottom, both nowcasts and observations indicate very weak mean flow with large temporal variability. Similar validation results are obtained at HE3 and MS3 (not shown).

1.4.4 Application of EPWS/NFS

EPWS/NFS products are analyzed for investigations of different aspects of ocean circulation in PWS. The investigations reveal some interesting new phenomena, directly or indirectly motivating the present dissertation study.

Transports through HE and MS

Previous numerical studies have indicated the importance of horizontal as well as vertical flow structure at HE and MS, with implications for the circulation pattern in Central Sound and elsewhere in PWS (Bang and Mooers, 2005). Since a sustained observing system from surface to bottom and across the entire cross section at HE and MS is not available for determining flow and mass fields, volume and heat transports, *etc.*, the present EPWS/NFS

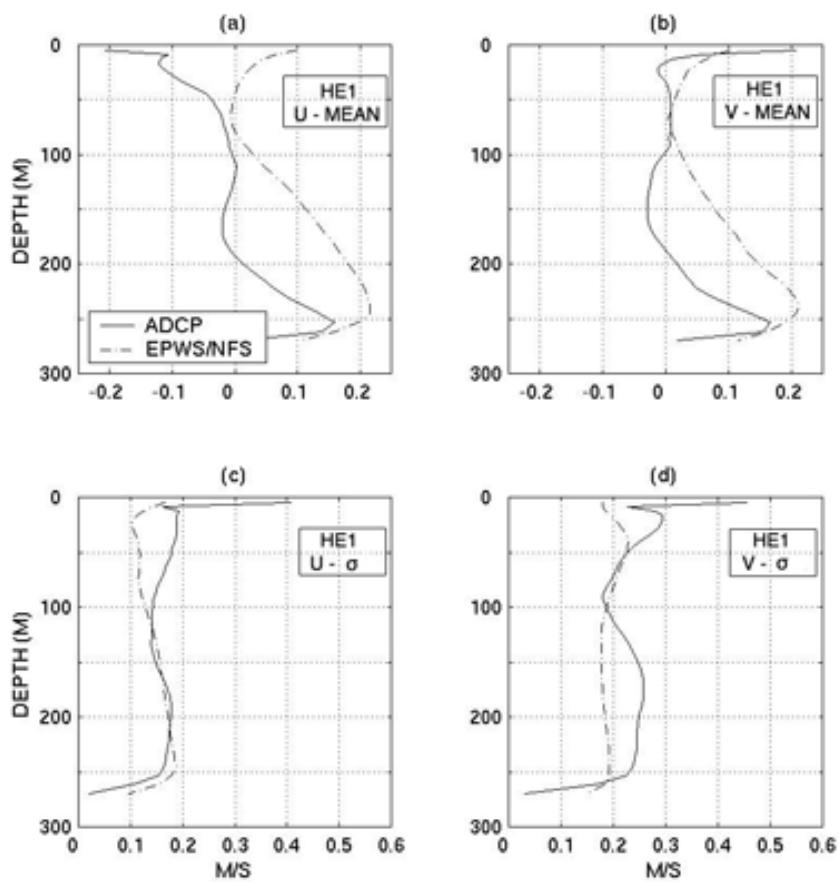


Figure 1.21: Three-month (15 JUN to 15 SEP 2005) observed (solid line) and nowcast (dot-dashed line) velocity (m/s) vertical profiles at HE1 mean eastward (a) and northward (b), plus standard deviation eastward (c) and northward (d)

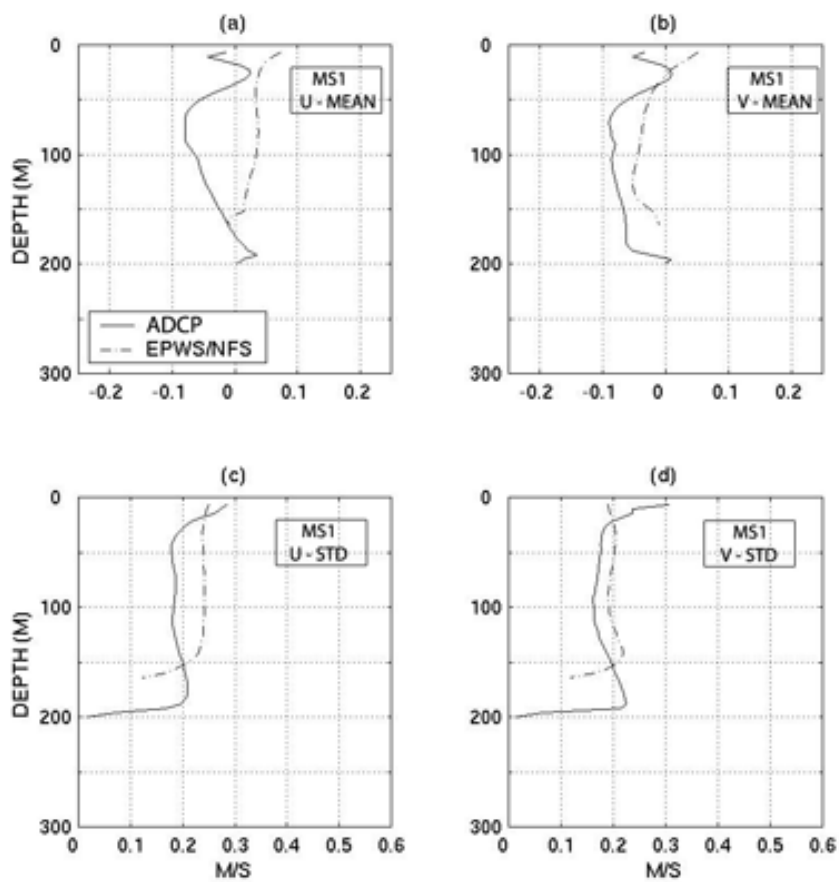


Figure 1.22: Three-month (15 JUN to 15 SEP 2005) observed (solid line) and nowcast (dot-dashed line) velocity (m/s) vertical profiles at MS1 mean eastward (a) and northward (b), plus standard deviation eastward (c) and northward (d)

run provides a useful proxy, and a unique opportunity to investigate how the volume transport through the two straits are related to each other, and what role(s) these two straits play in affecting the variability of circulation patterns inside PWS.

With the four major diurnal and four major semidiurnal tides removed via harmonic analysis, the EPWS/NFS nowcast volume transports at HE and MS (Fig. 1.23) are significantly correlated (maximum COR=-0.84 at zero lag). The throughflow transport occasionally reverses direction. The diurnal and semi-diurnal peaks have been largely removed from the power spectra (Fig. 1.24), yet there are still (though substantially reduced by *ca.* three orders of magnitude) diurnal, semidiurnal/inertial, and quarter-diurnal/HR peaks remaining. The HE and MS transports are highly coherent, generally out of phase, and nearly balanced for periods longer than *ca.* 30 *hr* (Fig. 1.25). At periods shorter than *ca.* 6 *hr*, the HE and MS transports are partially coherent, generally in phase, and balanced by the time rate-of-change of the PWS spatial-mean sea level (Figs. 1.25 and 1.26). For verification, observed coastal sea levels during the same time period from two tide gauges inside PWS, Cordova and Valdez, are used to estimate the mean sea level rate-of-change, which is well-balanced by the nowcast net transport (i.e., the sum of HE and MS volume transports) for the same period band. For intermediate periods between 6 and 30 *hr*, the HE and MS transports are only partially coherent and exhibit an abrupt 180° phase shift. This period band, where the phase between volume transports experiences a transition from in-phase to out-of-phase, is hereafter referred to as the “transition band”.

Based on the nowcast volume transports through HE and MS (Fig. 1.23), the corresponding annual mean (barotropic) transports are 0.024 and -0.023 Sv, respectively. Because EPWS/NFS has 11 cross-channel grid points at HE, a fairly detailed point-by-point

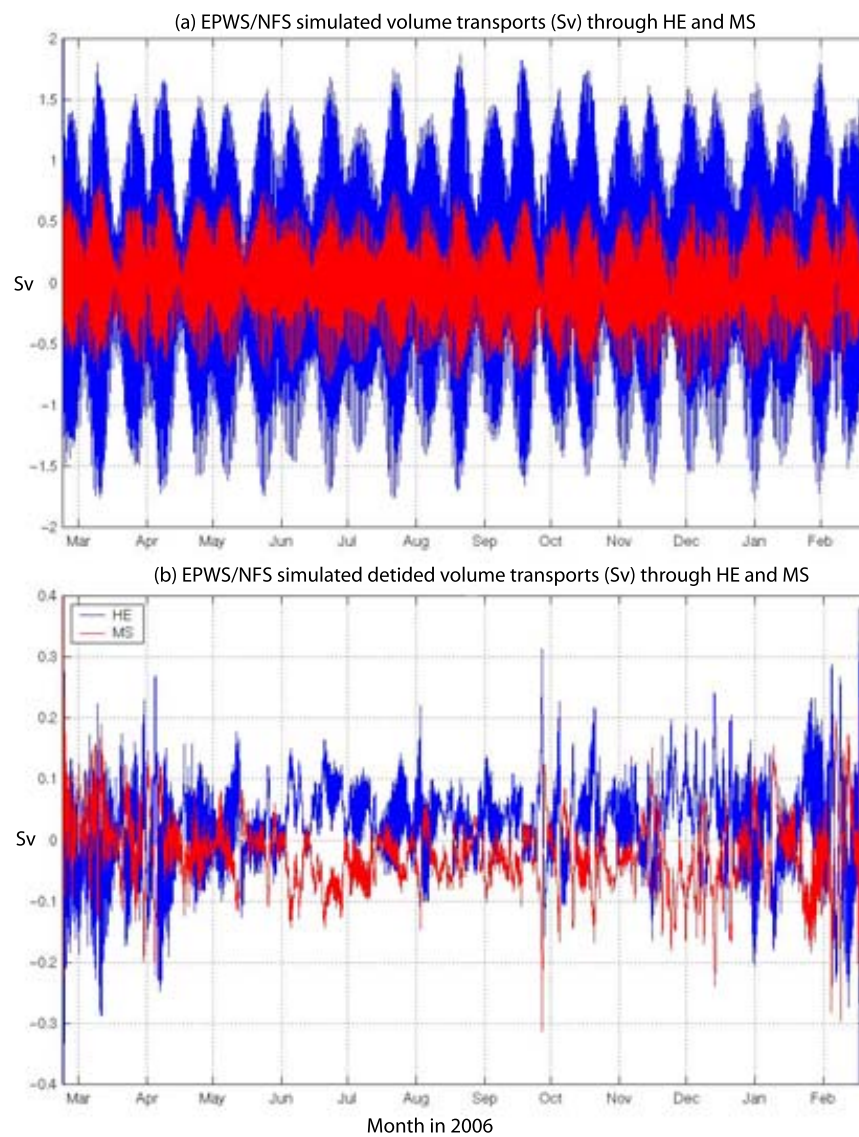


Figure 1.23: EPWS/NFS one-year (MAR 2005 thru FEB 2006) nowcast volume transports (Sv: Sverdrup= $10^6 m^3/s$) through HE (blue) and MS (red): (a) original; (b) detided

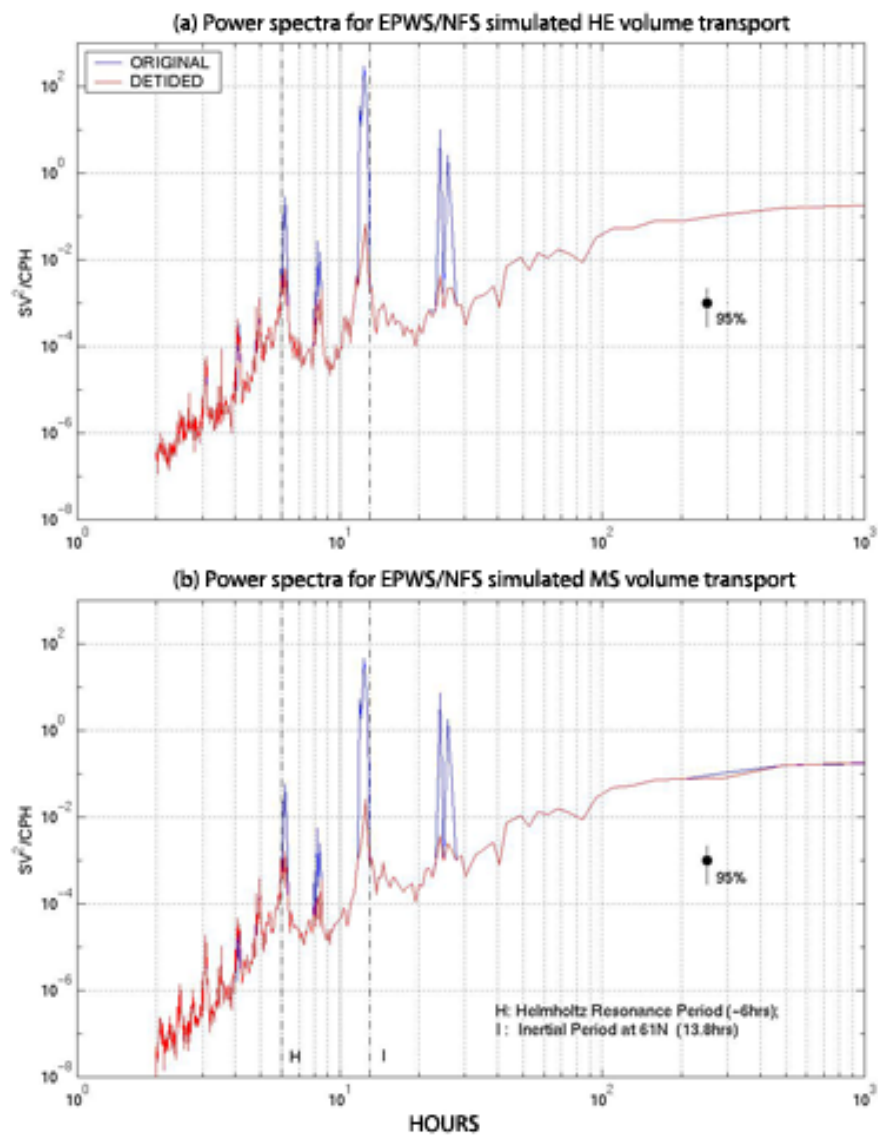


Figure 1.24: EPWS/NFS power spectra (DOF=10) of one-year (MAR 2005 thru FEB 2006) nowcast volume transports through HE (a) and MS (b): original (blue) and detided (red)

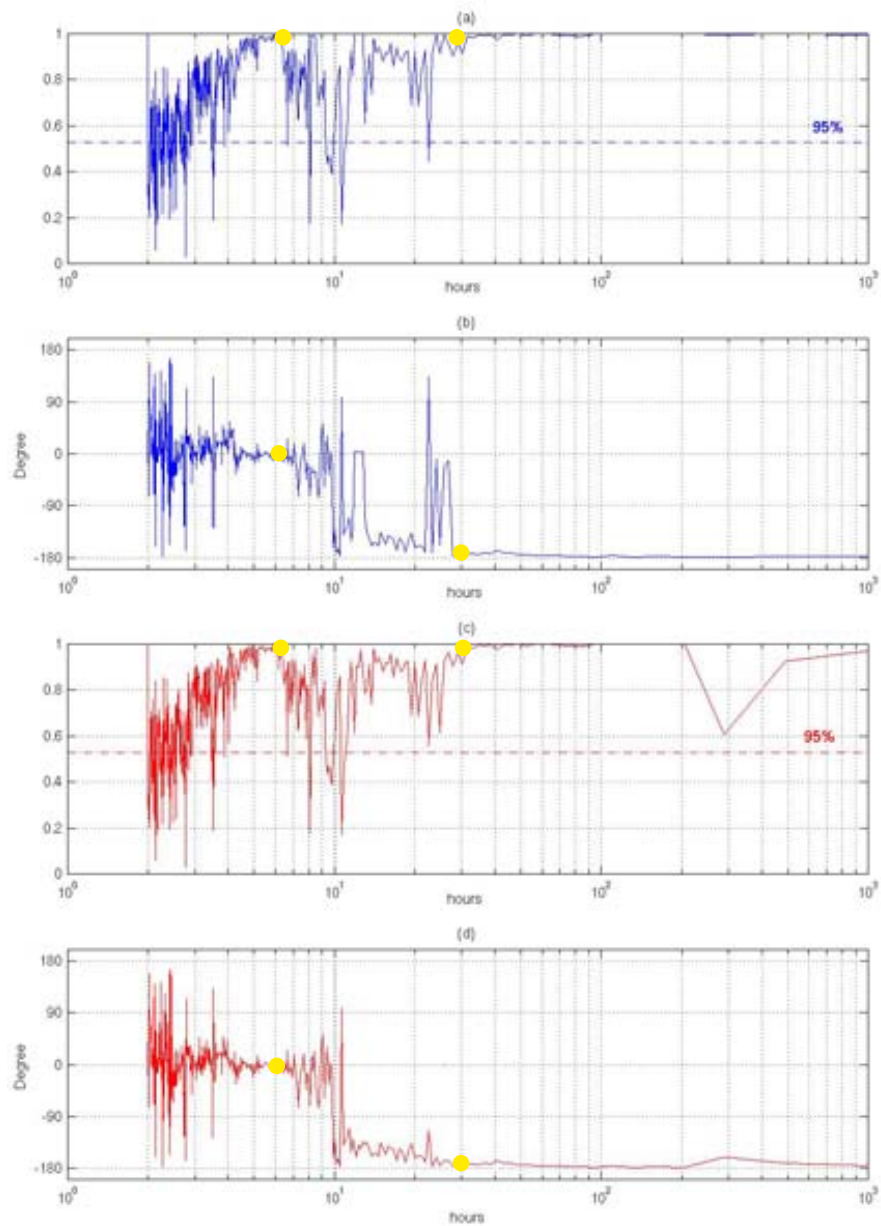


Figure 1.25: EPWS/NFS coherence squared and phase (DOF=10) of one-year nowcast volume transports between HE and MS: original [(a) magnitude; (b) phase]; detided [(c) magnitude; (d) phase]. The transition band (marked as yellow solid circle) of the coherence function is defined by the frequencies for which the coherence squared is generally less than 0.9.

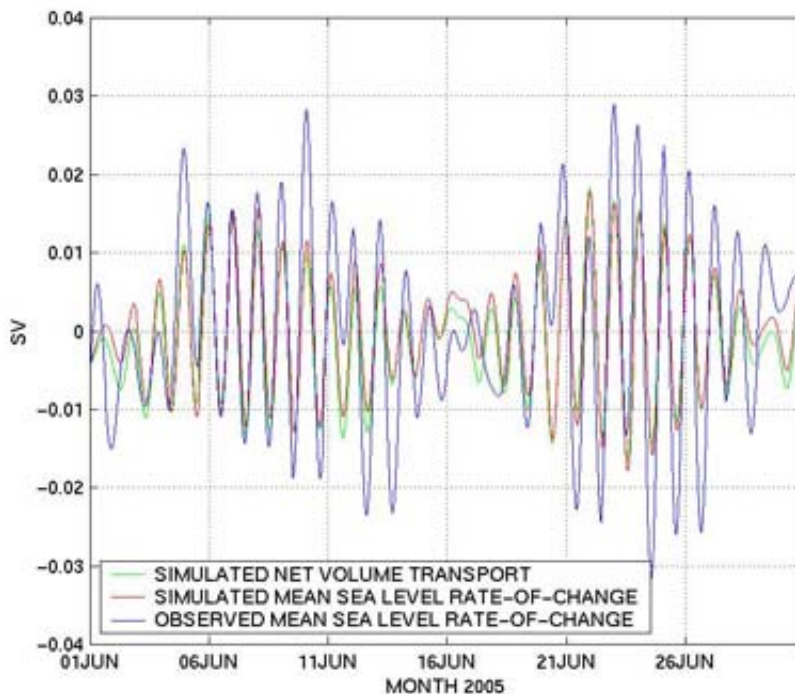


Figure 1.26: One-month comparison among observed (blue), EPWS/NFS nowcast (red) spatial mean sea level rate-of-change over PWS, and EPWS/NFS nowcast net transports (green) through HE and MS. The correlation at zero lag (linear regression coefficient) between observed and nowcast mean sea level rate-of-change is 0.3 (0.6), and between nowcast net transport and nowcast mean sea level rate-of-change is 0.9 (1.0).

annual-mean transport through HE is obtained (Fig. 1.27). The annual-mean inflow (*ca.* $0.05 Sv/m^2$) is along the western side and in the center, and the outflow (*ca.* $0.05 Sv/m^2$) occupies a small section along the eastern side. The primary maximum inflow (*ca.* $0.1 Sv/m^2$) occurs on the westernmost side of HE, with the secondary maximum inflow (*ca.* $0.07 Sv/m^2$) in the center. The corresponding standard deviation (*ca.* $0.05 Sv/m^2$) of the volume transport is remarkably uniform across HE.

HE and MS monthly-mean volume transports are used to examine the seasonal variability. During the first three months (MAR to MAY 2005), the volume transport (Fig. 1.28) is predominantly out of PWS (*ca.* $0.05 Sv$) at HE and into PWS (*ca.* $0.05 Sv$) at MS, and

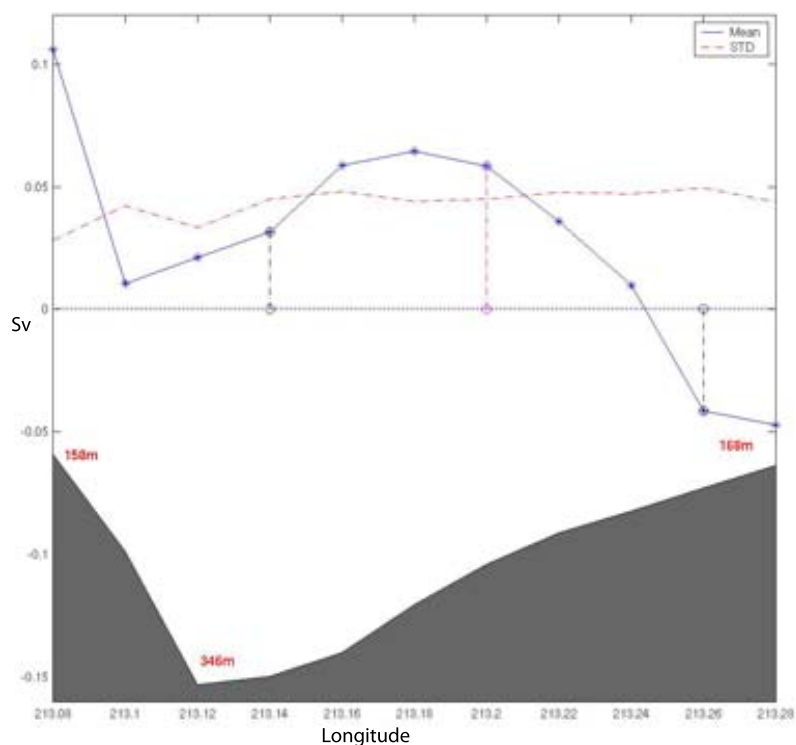


Figure 1.27: Point-by-point annual-mean (blue star), as well as the corresponding standard deviations (dashed red), volume transports through HE, based on one-year EPWS/NFS nowcasts. Locations of one-point ADCP observation (red circle) and two-point ADCP emulation (black circle) at HE are indicated; the bottom topography (gray) along the cross section of HE is superposed.

that pattern is reversed from AUG to DEC 2005. The maximum inflow through HE occurs during SEP and OCT (*ca.* $0.08 Sv$). This seasonal pattern is somewhat different from prior estimates (Vaughan et al., 1997), where the HE volume transport is predominantly into PWS (*ca.* $0.18 Sv$) during MAR, fairly insignificant ($< 0.01 Sv$) during APR and MAY, and out of PWS during JUL and AUG (*ca.* $0.05 Sv$), but the tendency for maximum inflow at HE in the autumn is in common. Further investigation of the monthly-mean transport through MS (Fig. 1.28) confirms that the EPWS/NFS nowcast transport through the two straits is balanced for monthly means.

As an interesting application of EPWS/NFS for examination of observational data requirements to monitor volume transport at HE, nowcasts are used to emulate an ADCP

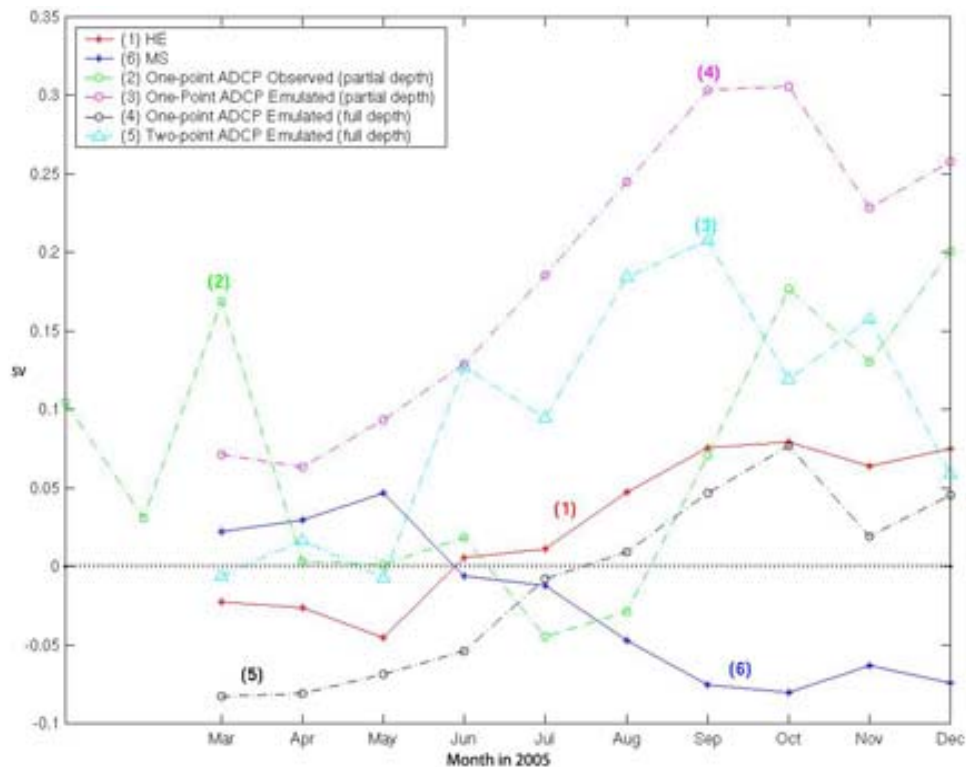


Figure 1.28: Monthly-mean volume transport through HE: (1) EPWS/NFS nowcast (solid red), (2) one-point ADCP estimated (dashed green; as in Vaughan *et al.* 1997), (3) one-point ADCP emulated (partial depth; dashed cyan), (4) one-point ADCP emulated (full depth; dashed magenta), and (5) two-point ADCP emulated (full depth; dashed black). EPWS/NFS nowcast (6) monthly-mean volume transport through MS is also shown (solid blue).

moored at HE near an actual ADCP site (cf. Vaughan *et al.*, 1997) in order to determine how adequately a single ADCP might estimate HE transport. Although the actual ADCP measurements only covered part of the water column, it is convenient for EPWS/NFS to assess the efficiency of a one-point ADCP emulation covering both the full and partial water column. The results (Fig. 1.28, curves 3 and 4) indicate inflow in all months, contrary to the full estimate of HE transport by EPWS/NFS. However, the observed seasonal trend with maximum inflow in the autumn is well captured in the simulation. Obviously, a single-point ADCP cannot be expected to capture this cross-strait flow structure (Fig. 1.27), and caution must be suggested in inferring HE transport from a single ADCP. With EPWS/NFS,

it is feasible to explore estimating the HE transport using various combinations of two or more emulated ADCPs to improve the estimates. For example, an emulation using two ADCPs, at grid points 4 and 10, (Fig. 1.27) significantly improves the estimation accuracy for HE transport (Fig. 1.28, curve 5).

Examination of vertical structure of annual mean baroclinic transports across HE transect (Fig. 1.29) indicates a well-defined three-layered structure in the annual-mean meridional velocity field: strong inflow in both the surface layer (the upper *ca.* 50 *m*) and the bottom layer (the lower *ca.* 70 *m*), and outflow in the intermediate layer (*ca.* 50 to 280 *m* deep). There is substantial horizontal shear in each layer, with maximum inflow on the western and eastern sides of HE in the surface and bottom layers, and maximum outflow on the eastern side of the intermediate layer. Across the eastern side of the MS transect, there is a similar three-layered structure in the annual mean meridional velocity field, with inflow in the surface and bottom layers and outflow in the intermediate layer. However, on the western side, there is a two-layered structure where the average water depth is *ca.* 50 *m*. The corresponding standard deviations of the annual-mean meridional velocity transects at HE and MS are typically five to eight times greater than the speed of the mean velocity field.

The annual mean baroclinic transports at HE are 0.059, -0.124, and 0.065 *Sv* for the three layers from the surface to intermediate to bottom, respectively. Similarly, the annual mean baroclinic transports at MS are 0.016, -0.034, and 0.018 *Sv*. Hence, the magnitude of the mean barotropic and baroclinic transports are comparable at MS, while the mean baroclinic transport at HE is about four times larger than at MS and, thus, about five times

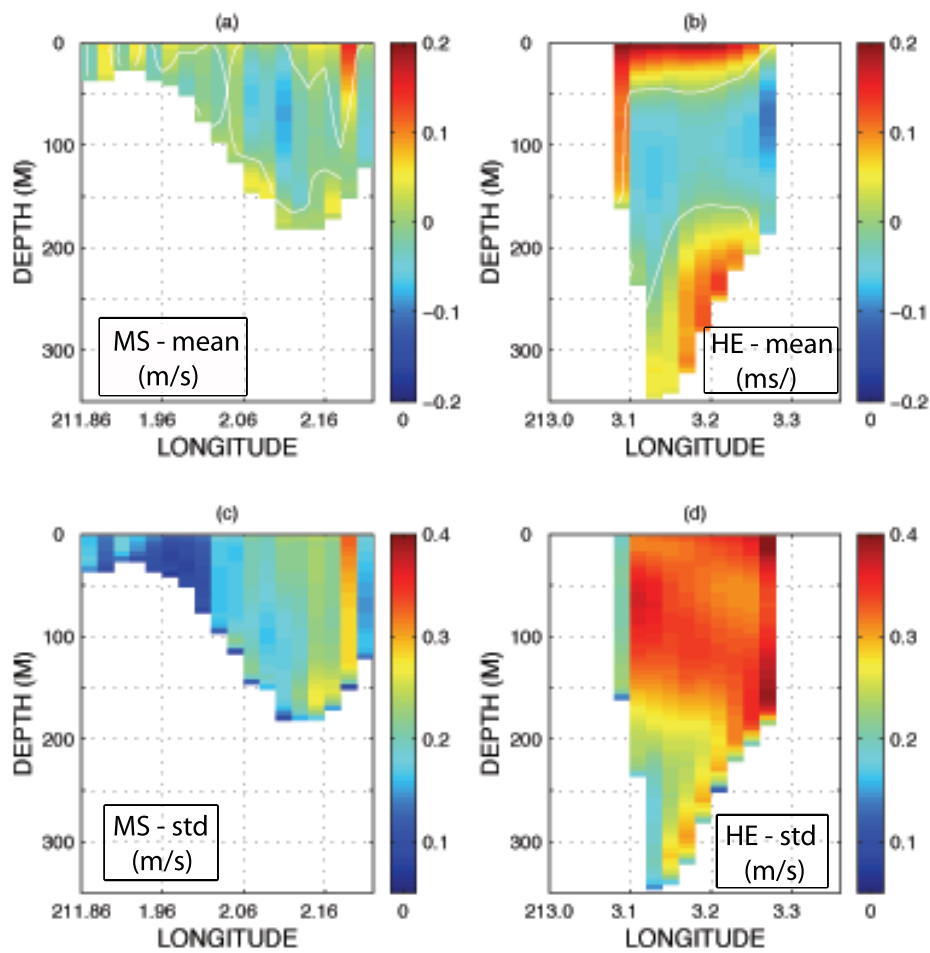


Figure 1.29: EPWS/NFS annual mean northward velocity (m/s) transects at MS and HE (a, b), and the corresponding standard deviation (STD; c, d).

larger than the mean barotropic transport at HE. The strong baroclinic flows through each layer can be anticipated to have significant effects on the circulation inside the Sound.

Further examination of the vertical structure of monthly mean baroclinic transports across HE transect (Fig. 1.30) reveals more details on seasonality of baroclinic flows: during the wintertime (JAN, FEB, MAR and DEC), two-layer flows, with inflow above 150 m depth and outflow below, dominate the HE through-flow; while for the remainder of the year, three-layer baroclinic flows dominate, with inflow near the surface and the bottom and outflow within the intermediate water. Also, inflow is dominant throughout year in the westernmost part of HE. Further investigation of surface and bottom inflow layers indicates that the surface layer inflow starts to develop in APR, reaches a maximum of 0.3 m/s at a depth of 50 m in AUG, and then, weakens and disappears in DEC. Correspondingly, a similar cycle occurs for the bottom layer inflow which is weak in APR, develops and reaches a maximum of 0.3 m/s in SEP, and weakens until NOV. However, with the disappearance of surface layer inflow, the bottom inflow layer again becomes stronger from DEC to FEB. Similar seasonal variability of monthly mean baroclinic transport occurs across MS transect (Fig. 1.31).

The bottom layer inflow at HE was previously observed in monthly-mean current meter-estimates for baroclinic transport through HE (Niebauer *et al.*, 1994). Those estimates indicated that, between the depth of 250 m and the bottom at HE, inflow dominated for six months during a nine-month observational period, and was as strong as 0.12 Sv in JUN. Also, three-layer monthly-mean transport structure; e.g., inflow above 150 m and below 250 m with outflow within the intermediate depth, occurred in AUG and SEP 1978 (Niebauer *et al.*, 1994),

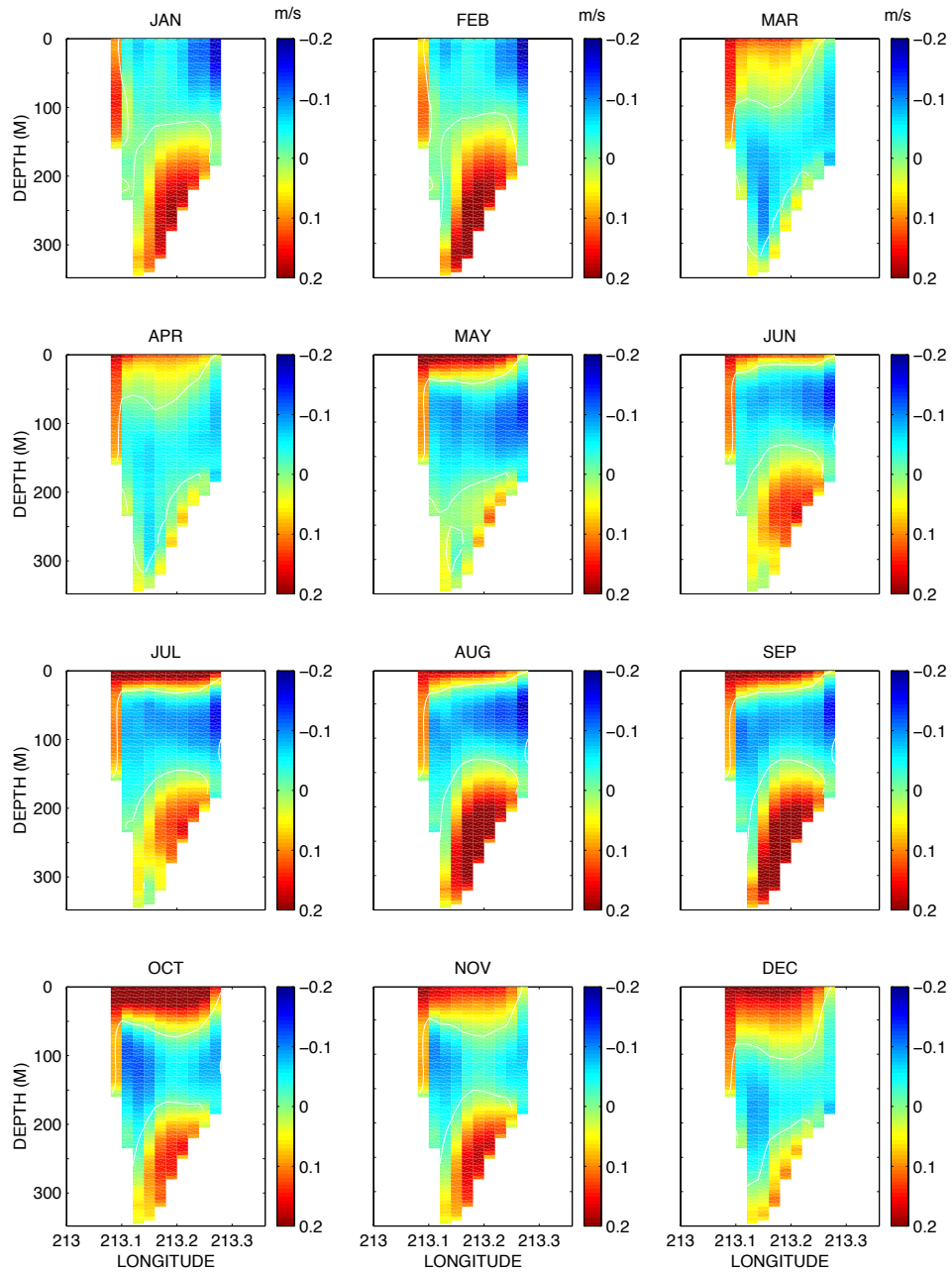


Figure 1.30: EPWS/NFS monthly mean northward velocity (m/s) transects at HE

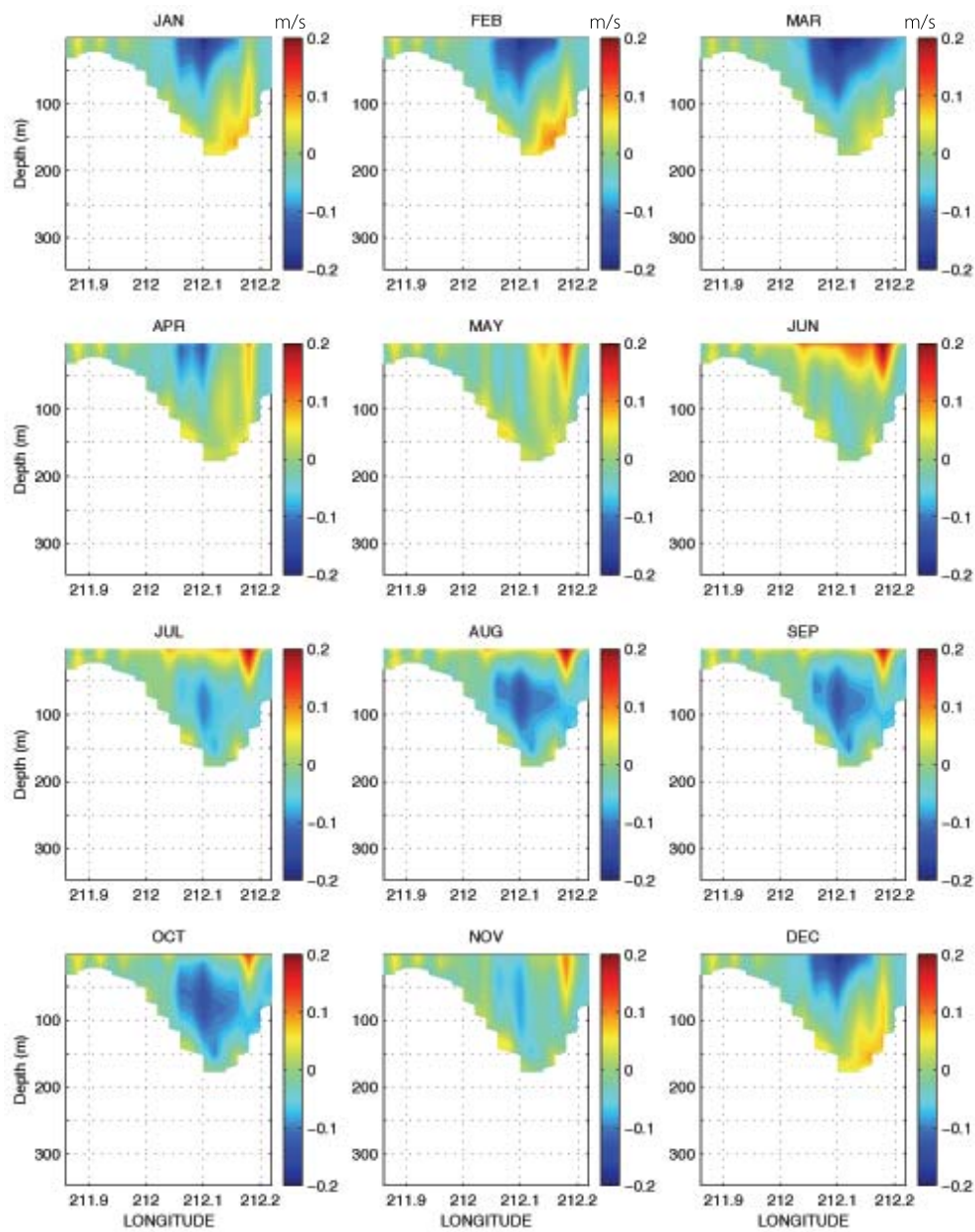


Figure 1.31: EPWS/NFS monthly mean northward velocity (m/s) transects at MS

This two-layer/three-layer flow transition is also observed with the significant seasonality at other straits; for instance, the Bab al Mandab, which connects the Gulf of Aden with the Red Sea (Smeed, 2000). In the wintertime, two-layer exchange flow occurs with surface outflow above dense salty water, while in the summertime, three distinct water masses are observed with an outflow/inflow/outflow pattern. These exchange flows are presumably due to the along-strait pressure gradient, but other mechanisms, *e.g.*, thermal-wind dynamics (Gill, 1982) and geostrophic control (Toulany and Garrett, 1984), may be important too, since the seasonality of these exchange flows is probably associated with the seasonality of across-strait temperature (Fig. 1.32), salinity (Fig. 1.33), and density (Fig. 1.34) field. For instance, the change in sign of the horizontal density gradient at *ca.* 150 *m* depth across HE from negative (positive) to positive (negative) value in MAR (DEC) suggests the corresponding positive (negative) vertical gradient of northward velocity, which is consistent with the cycle of occurrence of surface layer inflow.

Three-Layer Exchange Flow in PWS

Exchange flows through the strait(s) between a semi-enclosed sea and the open ocean often present two-layer structures (Helfrich, 1995; Schmidt; 1977; Sofianos, 2000), while three-layer exchange flows occur, too (Smeed, 2000). It is thus beneficial to further examine the development of layered exchange flows in PWS based on EPWS/NFS nowcasts.

As a typical example, EPWS/NFS monthly-mean baroclinic flow at HE in JUN 2005 (Fig. 1.30) was selected, when intermediate layer outflow existed between the surface layer (above 40 *m*) and bottom layer (below *ca.* 180 *m*) inflow. Across HE, EPWS/NFS monthly-mean density profiles are obtained at three locations (Fig. 1.35) separated by *ca.* 3 *km*, and

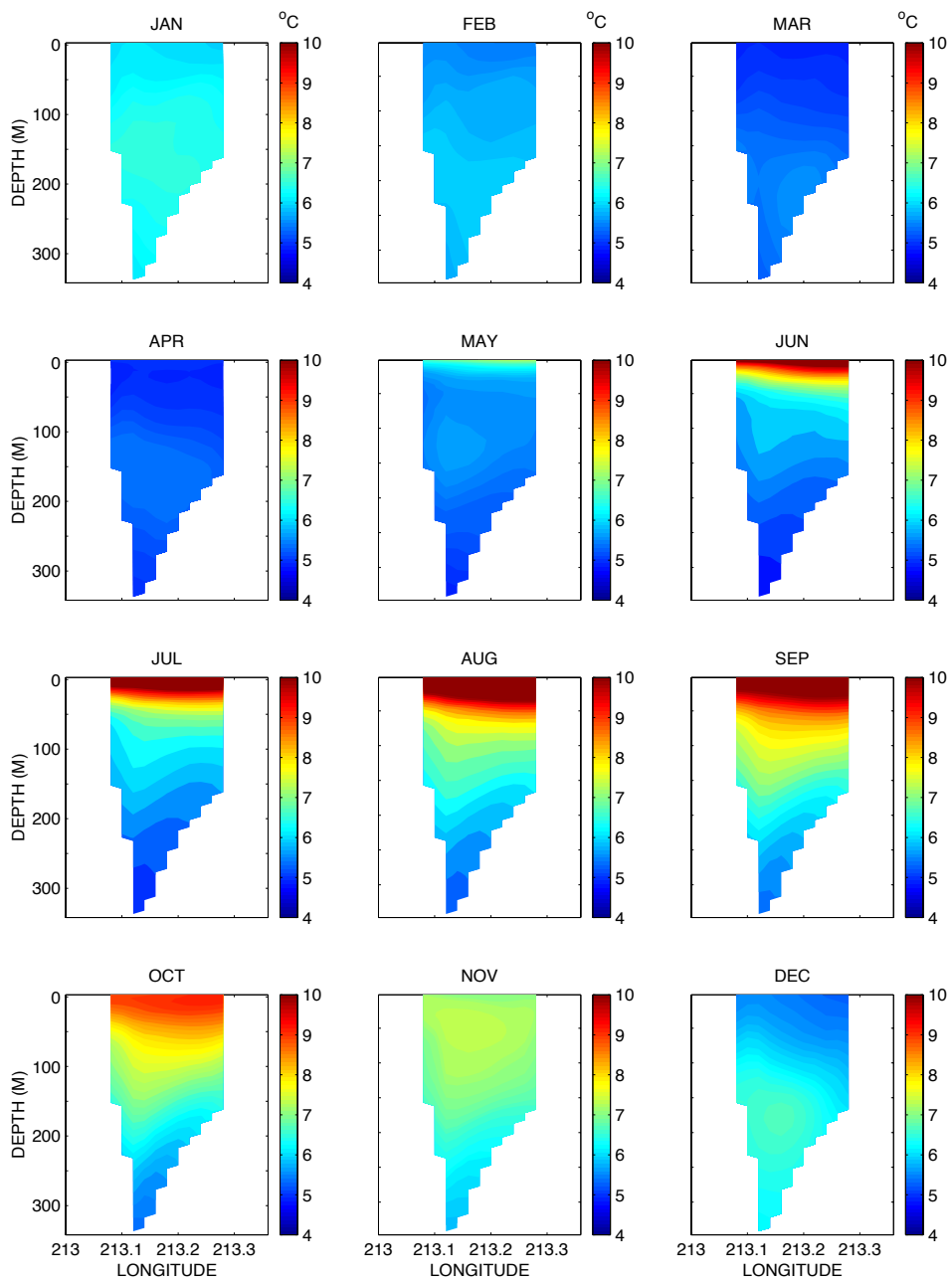


Figure 1.32: EPWS/NFS monthly mean temperature ($^{\circ}\text{C}$) transects at HE

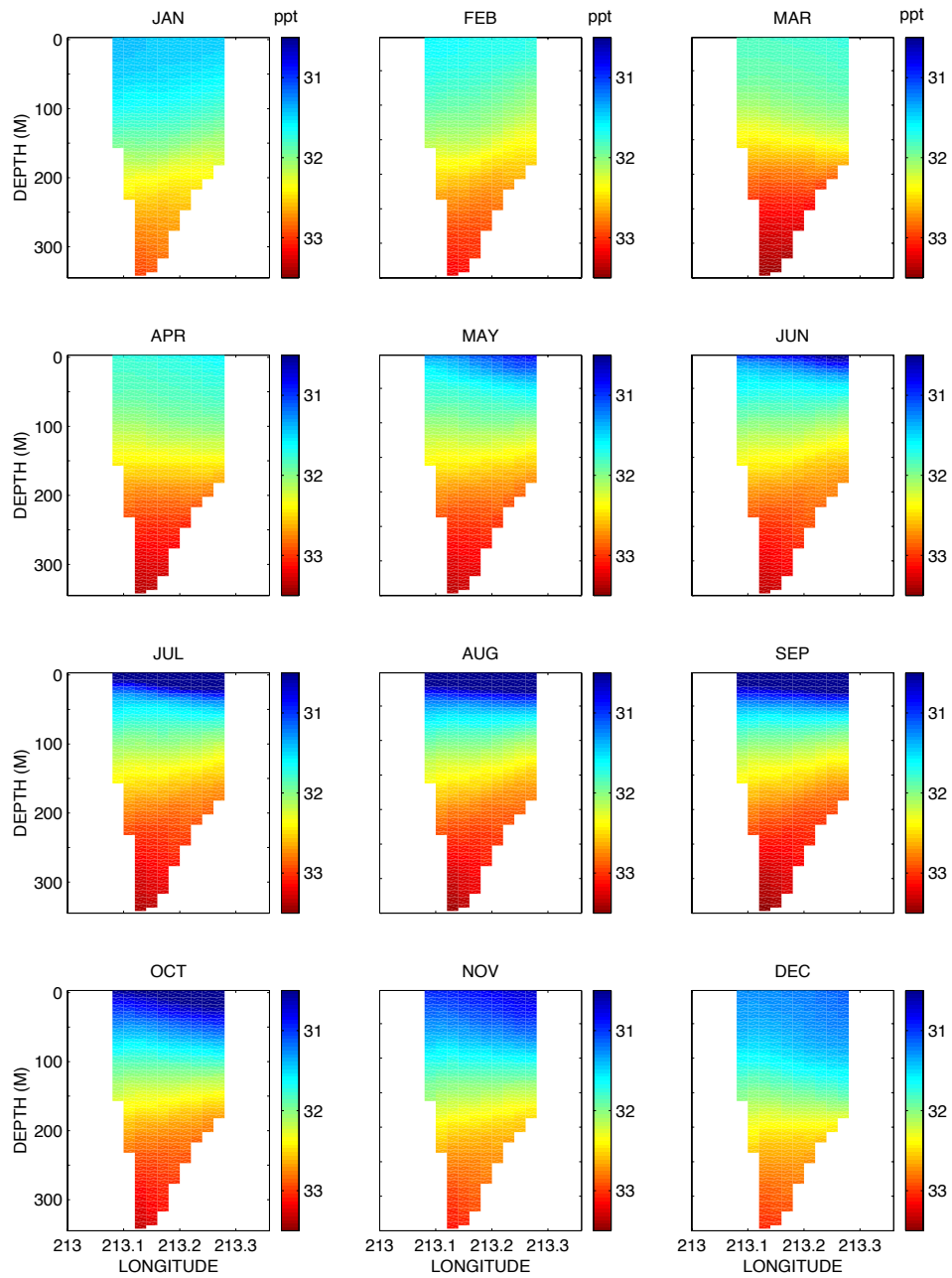


Figure 1.33: EPWS/NFS monthly mean salinity (ppt) transects at HE

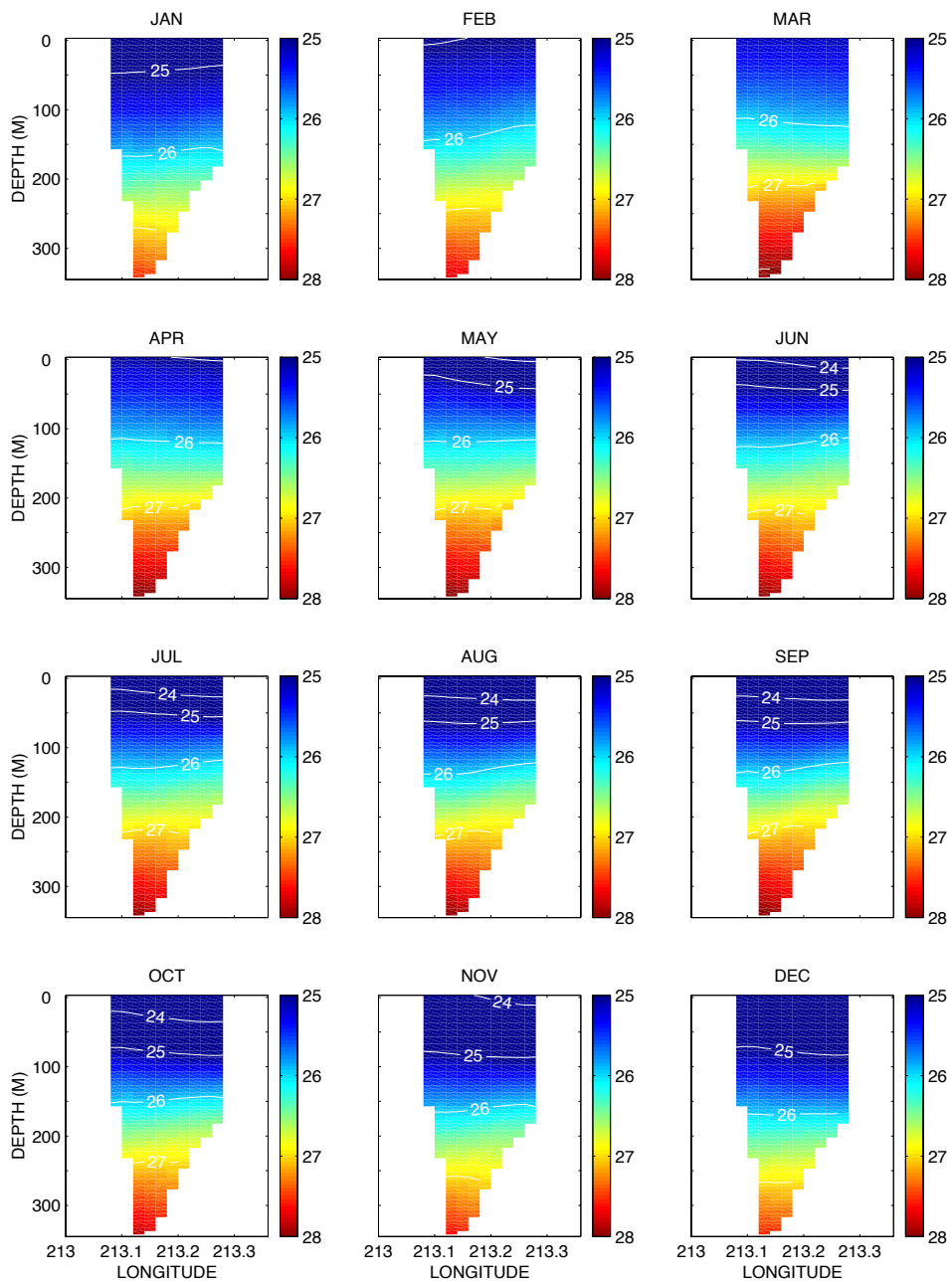


Figure 1.34: EPWS/NFS monthly mean density (σ_t) transects at HE

the across-strait density gradient is computed between adjacent locations with a positive value indicating an eastward increase of density. The result indicates that in JUN 2005, negative gradients were nowcast near the surface and the bottom, and a positive gradient at intermediate depths (Fig. 1.35). Correspondingly, if the thermal-wind relation; *i.e.*, dependence of the vertical velocity gradient ($\frac{\partial v}{\partial z}$) on horizontal density gradient ($\frac{\partial \rho}{\partial x}$), is invoked ($\frac{\partial v}{\partial z} = -\frac{g}{\rho_0 f} \frac{\partial \rho}{\partial x}$) and the bottom velocity is obtained from the EPWS/NFS nowcast, the across-strait density gradient in JUN 2005 implies that along-strait, geostrophic velocity profiles would have a three-layer flow structure on the eastern side of HE: the surface (the upper 25 m) and bottom (below 130 m) inflows and the outflow in the intermediate water; while on the western side of HE, there would be inflow at all depths (Fig. 1.35). Compared with nowcast three-layer baroclinic flow at HE in JUN 2005 (Fig. 1.30), it is thus suggested that layered flow through HE is mainly geostrophic, but the presence of topographic features; *e.g.*, the deep channel and the sill outside HE entrance and across-strait depth variation, may significantly affect the dynamics of along-strait geostrophic flow. Consequently, non-geostrophic flow can develop at HE; for instance, baroclinic flow on the western side of HE in JUN 2005.

The above analysis of EPWS/NFS nowcast along- and across-strait (HE) density gradients in JUN 2005 suggests that the three-layer throughflow at HE is mainly buoyancy-driven, geostrophic flow, and is affected significantly by topography. Therefore, seasonal changes in buoyancy over the shelf and PWS are presumably the dominant factors controlling the seasonal transition of two-layer/three-layer baroclinic flows at HE. In PWS, external forcings; *e.g.*, surface winds, tidal mixing, heating/cooling, freshwater runoff, and ACC all contribute to buoyancy variability in the along-strait direction. Among these forcings, the buoyancy-

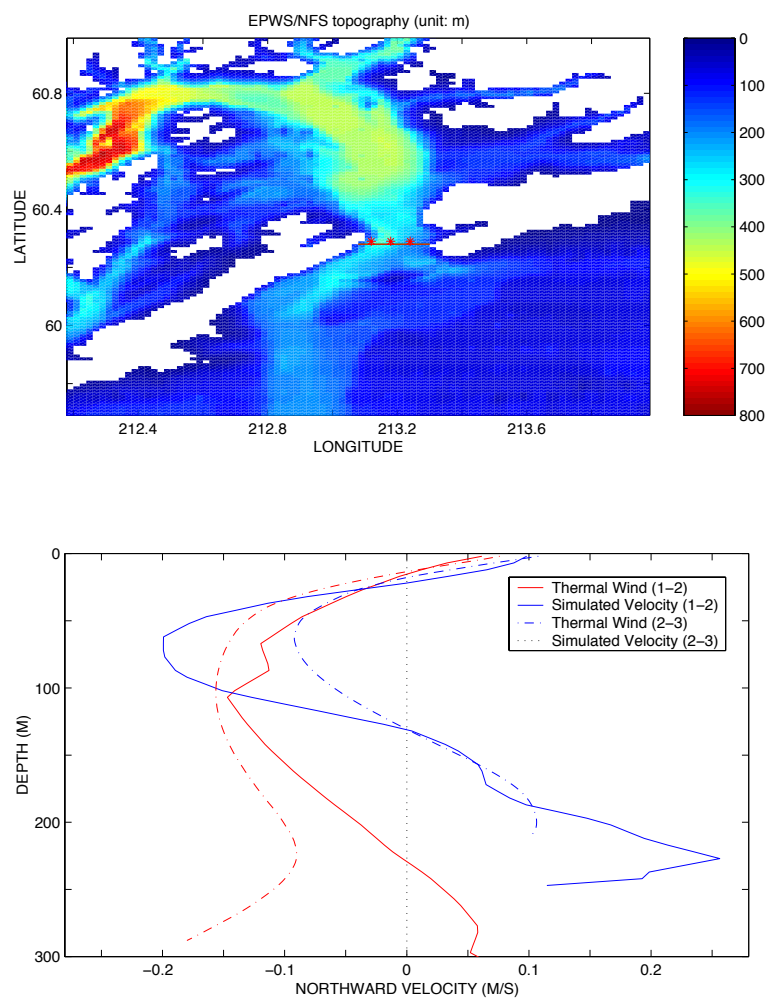


Figure 1.35: (upper) EPWS/NFS topography and selected locations (red asterisks; 1, 2, 3) to examine across-strait (HE) density gradient. (lower) EPWS/NFS monthly-mean across-strait (HE) density gradient (solid lines) and corresponding northward velocity profiles (dot-dashed lines) based on thermal-wind dynamics in JUN 2005: between the locations 1 and 2 (red), and between the locations 2 and 3 (blue).

and downwelling-wind-forced ACC (Williams *et al.*, 2007) is probably the most influential, and along with surface wind, will be investigated more in subsequent studies.

Seasonal Circulation Fields in Central Sound

The EPWS/NFS nowcast surface currents in Central Sound are characterized by a cyclonic gyre (cool and salty water) in MAR2005 (Fig. 1.36) and an anticyclonic gyre (warm and fresh water) in AUG2005 (Fig. 1.37) (Wu *et al.*, 2007). These gyres normally have a life cycle of less than one month, and the centers of the gyres move slowly (*ca.* 2-3 km/day) northward. It is evident that during the summer and winter 2005, Central Sound experiences a transition between two well-defined circulation patterns. Except in JUN 2005, the surface flow is normally weak at MS. At HE, the surface flow structure is stronger and more complicated with significant seasonal variability.

Deep Water in PWS

Geometrically, PWS can be roughly divided into two small regions with respect to the presence of Naked Island: Central Sound (CS) in the east and the Black Hole (BH) in the northwest (Fig. 1.2). The water depth of the BH (*ca.* 800 m) is much deeper than that of CS (*ca.* 400 m), and these two regions are mainly connected via a channel (with a depth of *ca.* 400 m) to the north of Naked Island. The remaining area of PWS is normally shallower than 400 m, and it is thus suggested that deep water in PWS is most probably formed and developed within CS and the BH.

Two-year time-depth plots of temperature/salinity/ σ_t (Fig. 1.38) in CS (near the location of NDBC buoy 46060) and the BH (near the location of deepest water depth) demonstrate that near the bottom of BH, salty (*ca.* 35 ppt) and cool (*ca.* 5° C) water begins to

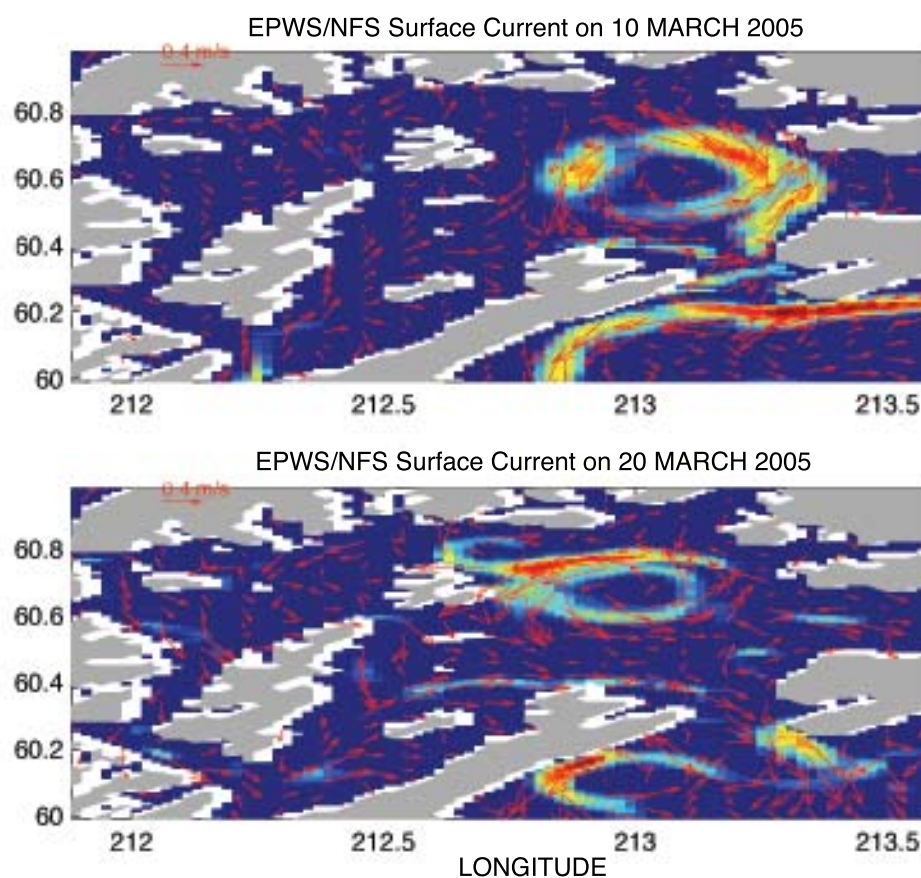


Figure 1.36: EPWS/NFS nowcast surface current on (a) 01MAR, (b) 15MAR and (c) 30MAR2005. The background color indicates the current speed (m/s).

develop in summertime, evolve and retreat until the early winter, while this salty and cool water does not appear in CS. Notice that there is considerable inter-annual variability of the deep water in the BH: in 2005, the deep water is present from MAR until NOV, in contrast to from JUL until OCT in 2006. Considering that EPWS/NFS starts to operate on 22FEB 2005, the initial condition of EPWS/NFS (obtained from PWS winter climatology) likely contributes to this apparent inter-annual variability.

More investigations with EPWS/NFS nowcast monthly-mean temperature/salinity transects at HE and MS indicate that no such heavy water; e.g., characterized by 35 *ppt* and

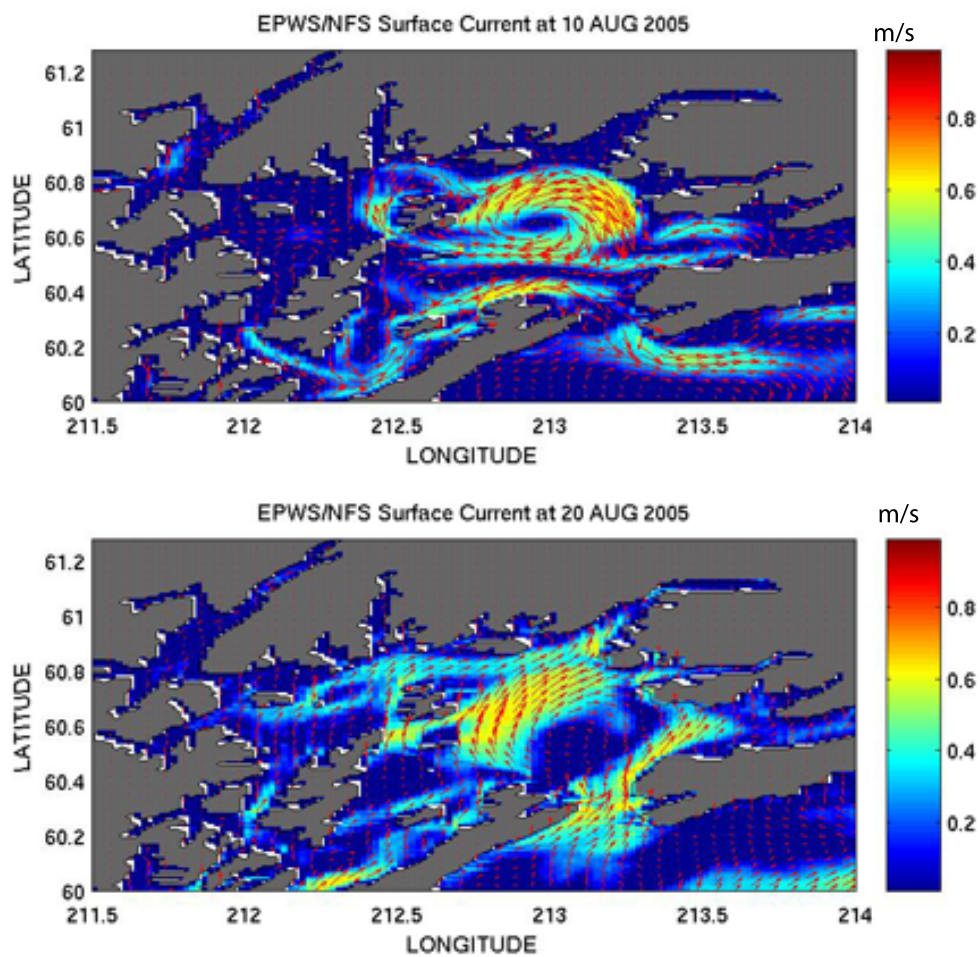


Figure 1.37: EPWS/NFS nowcast surface current on 10AUG and 20 AUG 2005. The background color indicates the current speed (m/s).

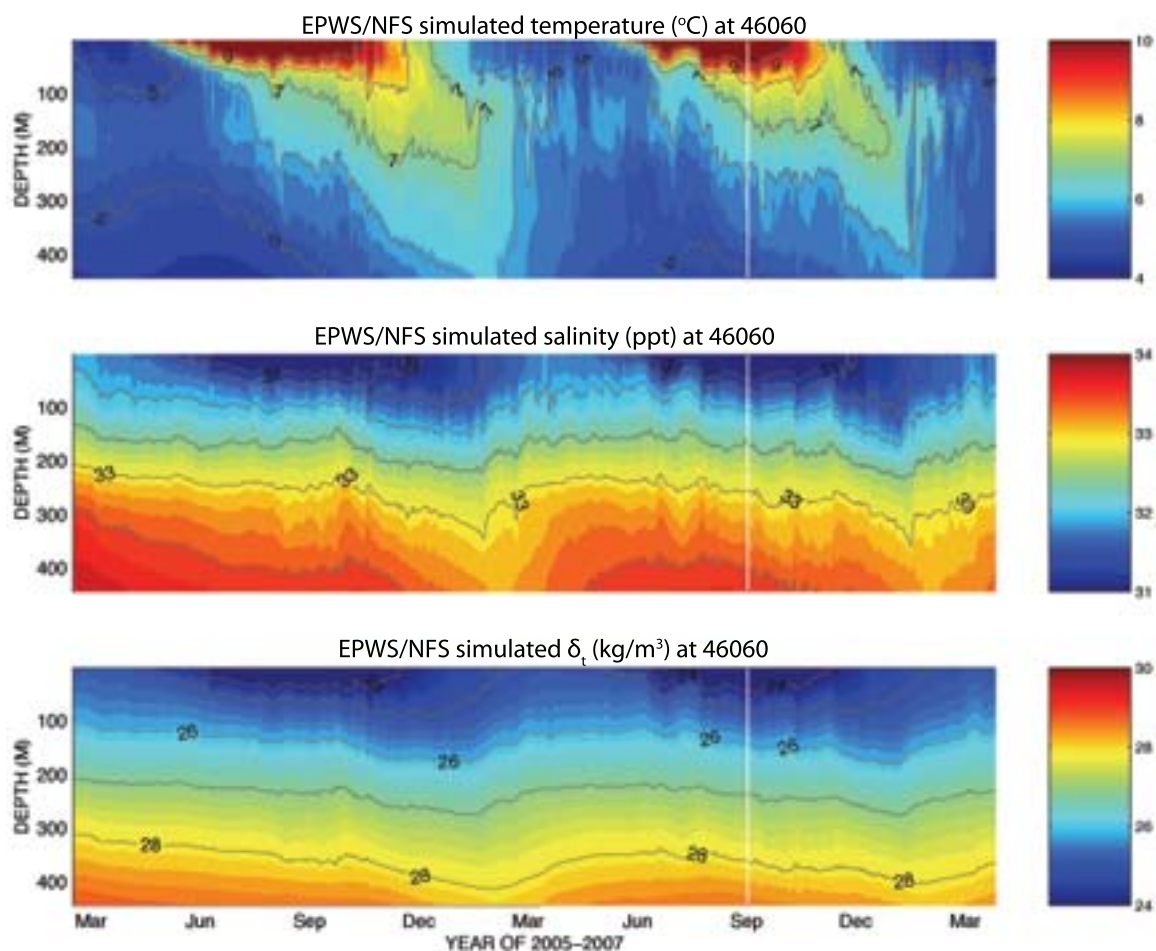


Figure 1.38: EPWS/NFS nowcast vertical profiles of daily-averaged temperature (a), salinity (b), and σ_t in Central Sound between MAR 2005 and MAR 2007

5°C , flows into the Sound. Thus, deep water in the BH is presumably formed within the Sound via wintertime cooling, evaporation, and deep convection.

1.4.5 Summary of PWS/NFS and EPWS/NFS

As the second generation nowcast/forecast system developed for PWS, EPWS/NFS contains several important upgrades, including (1) the extension of the model domain to incorporate the continental shelf outside PWS, (2) the application of a one-way nesting scheme for Global-NCOM forcing at the open boundaries, and (3) better inclusion of tidal forcing

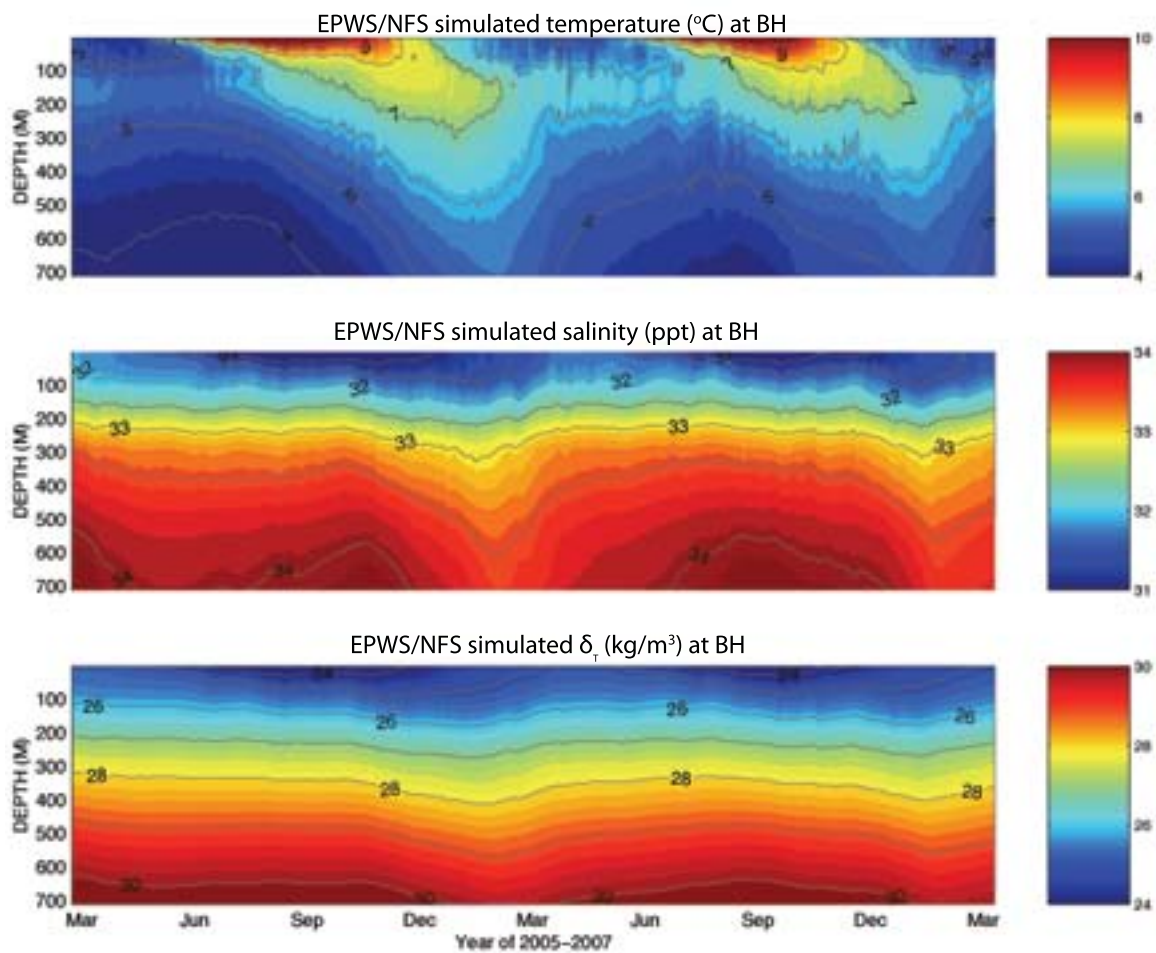


Figure 1.39: EPWS/NFS nowcast vertical profiles of daily-averaged temperature (a), salinity (b), and σ_t in the BH between MAR 2005 and MAR 2007

(elevation and currents) at the open boundary from a separate 2-D tide model. Significant improvements over PWS/NFS have thus been obtained for predicted variables; for instance, CSL, SST, and tidal currents.

New phenomena are revealed, including the so-called transition band in the coherence pattern between HE and MS volume transports, the seasonal change of two-layer to three-layer flows in velocity transects across HE and MS, the transient cyclonic and anticyclonic gyres in CS, and the annual variability of salty, cool water near the bottom of BH. These phenomena are related to various aspects of the dynamic response of an oceanic system; such as, PWS, to external forcings and/or internal instabilities.

On the other hand, the insufficiently energetic subtidal-frequency variations in EPWS/NFS CSL and currents provide challenges for further upgrades.

1.5 Purpose of Dissertation

The quasi-operational EPWS/NFS “opens a window” to continuously monitor the ocean circulation in PWS in real-time, and it enhances our understanding of oceanic processes, on both large/small spatial and long/short temporal scales. On the other hand, it brings overwhelming information about new and challenging phenomena in PWS, waiting for further exploration. Some of these phenomena may be common and applicable in other semi-enclosed seas, while others may be unique to this small, two-strait oceanic system. Some of the scientific questions presented are

- (1) What causes the seasonal change from two-layer mean flow at HE and MS in the wintertime to three-layer mean flow for the remainder of the year?

- (2) Why does a large cyclonic gyre occur in PWS in late summer, while in other seasons the predominant circulation pattern in central PWS may be either cyclonic or anticyclonic?
- (3) Considering that the sills just outside the two main entrances impede the entry of the deeper NGOA coastal waters into PWS, and that the seasonal heating/cooling, freshening/salinification, and stratification of PWS are strong factors, what controls the formation, properties, and variability of the PWS deep water?
- (4) What is the nature of the transient circulation in PWS? For example, what is the nature of the PWS response to synoptic atmospheric forcing? In particular, what is the nature of the flow in the so-called transition band in the coherence and phase patterns between HE and MS volume transports?
- (5) Associated with the complex bottom topography and density stratification, how are the tides dissipated inside PWS? What is the PWS's annual tidal energy budget?

Systematic investigations, primarily via numerical models (Chapter 2) and partially guided by Helmholtz resonance theory (Chapter 4), of the response of PWS to external forcings, including large-scale circulations in NGOA (Chapter 3), atmospheric pressure (Chapter 4), surface winds (Chapter 5), and tides (Chapter 6), are thus conducted in the dissertation. A better understanding is sought of the basic dynamical behavior of PWS circulation, as well as other similar semi-enclosed seas around the world ocean. It may also effectively help the upgrade to a next-generation EPWS/NFS, which in turn, will improve ecological modeling in PWS.

Chapter 2

Numerical Ocean Circulation Model

Numerical ocean circulation models are essential tools for studying physical ocean processes. Various models have thus been developed for coastal ocean circulation, for example, the Princeton Ocean Model (POM), and the Regional Ocean Model System (ROMS²⁸). Both models have a terrain-following vertical coordinate system, which fits naturally the complex features of coastal bottom topography. As in the present study, POM is utilized for a wide range of applications.

2.1 Princeton Ocean Model

POM is a three-dimensional, free-surface, primitive equation ocean model with a sigma (terrain-following) coordinate system in the vertical. The version used in this study is POM2K, downloadable from <http://www.aos.princeton.edu/WWWPUBLIC/htdocs.pom/>.

²⁸Web access: <http://www.myroms.org/>

It incorporates the hydrostatic assumption²⁹ and the Boussinesq approximation³⁰ with respect to density variations. In a Cartesian coordinate system with positive x direction pointing eastward, positive y direction pointing northward, and positive z direction pointing upward, the momentum and continuity equations are

$$\frac{\partial u}{\partial t} + \vec{v} \cdot \nabla u - fv = -\frac{1}{\rho_0} \frac{\partial p}{\partial x} + \frac{\partial}{\partial z} \left(K_M \frac{\partial u}{\partial z} \right) + F_x \quad (2.1)$$

$$\frac{\partial v}{\partial t} + \vec{v} \cdot \nabla v + fu = -\frac{1}{\rho_0} \frac{\partial p}{\partial y} + \frac{\partial}{\partial z} \left(K_M \frac{\partial v}{\partial z} \right) + F_y \quad (2.2)$$

$$0 = -\frac{1}{\rho_0} \frac{\partial p}{\partial z} - \frac{\rho}{\rho_0} g \quad (2.3)$$

$$\nabla \cdot \vec{v} = 0, \quad (2.4)$$

where (u, v, w) are the (x, y, z) components of velocity vector \vec{v} ; ∇ is the vector operator $(\frac{\partial}{\partial x}, \frac{\partial}{\partial y}, \frac{\partial}{\partial z})$; g is acceleration due to gravity; f is the Coriolis parameter; p is the pressure; ρ_0 is the reference density; K_M is the vertical eddy viscosity; and F_x and F_y are the horizontal diffusion terms which depend on the horizontal eddy diffusivity for momentum, A_M . Density is calculated through the nonlinear equation of state, $\rho = \rho(\theta, S)$, where the

²⁹In the vertical momentum equation, the vertical pressure gradient is simply balanced by the gravitational body force; hence, no vertical acceleration, etc., is involved.

³⁰Boussinesq (1903) suggested that for flows satisfying certain conditions; such as, the Mach number of the flow is small, or the vertical scale of the flow is not too large, or the temperature differences in the fluid are small, the effects of density variations in fluids can be neglected, except in the gravitational term where ρ is multiplied by g . The formal justification was given by Spiegel and Veronis (1960).

conservation equations for potential temperature θ (heat) and salinity S are

$$\frac{\partial(\theta, S)}{\partial t} + \vec{v} \cdot \nabla_h(\theta, S) + w \frac{\partial(\theta, S)}{\partial z} = \frac{\partial}{\partial z} (K_H \frac{\partial(\theta, S)}{\partial z}) + F_{(\theta, S)}, \quad (2.5)$$

where ∇_h is the horizontal vector operator $(\frac{\partial}{\partial x}, \frac{\partial}{\partial y})$, K_H is the vertical eddy diffusivity for heat and salinity, and F_θ, F_S are horizontal diffusion terms which depend on the horizontal eddy diffusivity for heat and salinity, A_H . The above equations are then transformed into the vertical σ coordinate to represent topographic variations faithfully.

An embedded second moment, vertical turbulence closure sub-model (Mellor, 1973; Mellor and Yamada, 1982) is included to provide the vertical mixing coefficients. The horizontal mixing coefficients for momentum are calculated by the Smagorinsky (1963) parameterization and, thus, are spatially and temporally dependent on velocity gradient and grid size, with horizontal eddy viscosity, A_M ,

$$A_M = \alpha \Delta x \Delta y \left[\left(\frac{\partial u}{\partial x} \right)^2 + \left(\frac{\partial v}{\partial y} \right)^2 + \frac{1}{2} \left(\frac{\partial u}{\partial y} + \frac{\partial v}{\partial x} \right)^2 \right]^{\frac{1}{2}} \quad (2.6)$$

where Δx and Δy are the local grid size and α is the non-dimensional Smagorinsky coefficient (the so-called HORCON parameter). Another important parameter is the inverse horizontal eddy Prandtl number $(\frac{A_H}{A_M})$, the so-called TPRNI parameter), whose value is generally small as a remedy for the possible situation in POM that sigma coordinates can introduce vertical fluxes even when isotherms and isohalines are level in Cartesian coordinates.

The numerical time-integration scheme used in the horizontal direction is temporally-explicit and spatially-staggered on an Arakawa C-grid; it is temporally-implicit in the vertical.

A leapfrog scheme is employed for time integration, and, in practice, to save computational time it is split into two integration modes: a shorter time-step (external/fast) mode for solving the vertically-integrated, two-dimensional equations of \bar{u} , \bar{v} and elevation η , and a longer time-step (internal/slow) mode for solving the three-dimensional system of equations. The Courant-Friedrichs-Levy (CFL) stability condition limits the maximum possible time steps for both the internal and external modes.

2.2 Model Configuration

POM is the “numerical engine” utilized in the present PWS ocean circulation study. A high-resolution orthogonal curvilinear grid in the horizontal direction covers an extended-PWS domain that includes PWS and the continental shelf with a coast-to-coast, open southern boundary (EPWS-POM; Fig. 2.1). The orthogonal curvilinear coordinate is employed because (1) compared with PWS, it decreases the number of horizontal grid points over the shelf, where a large number of grid points are not necessary to define the dominant coastal currents but would greatly increase computational time during numerical integrations; and (2) it maintains the high-resolution (*ca.* 1 to 2*km*) used inside the Sound and at the two main entrances (HE and MS). The importance of the latter arises when further nesting of the model is required for an even-higher-resolution (*ca.* 100 to 300*m*) numerical study inside the Sound (PWS-POM; Fig. 2.1), which crucially depends on the Open Boundary Conditions (OBCs) at HE and MS. The PWS-POM grid is embedded within EPWS-POM grid with a constant grid size ratio of 1:3, and covers only the PWS domain itself. The embedded grid of PWS-POM with an odd ratio to EPWS-POM grid

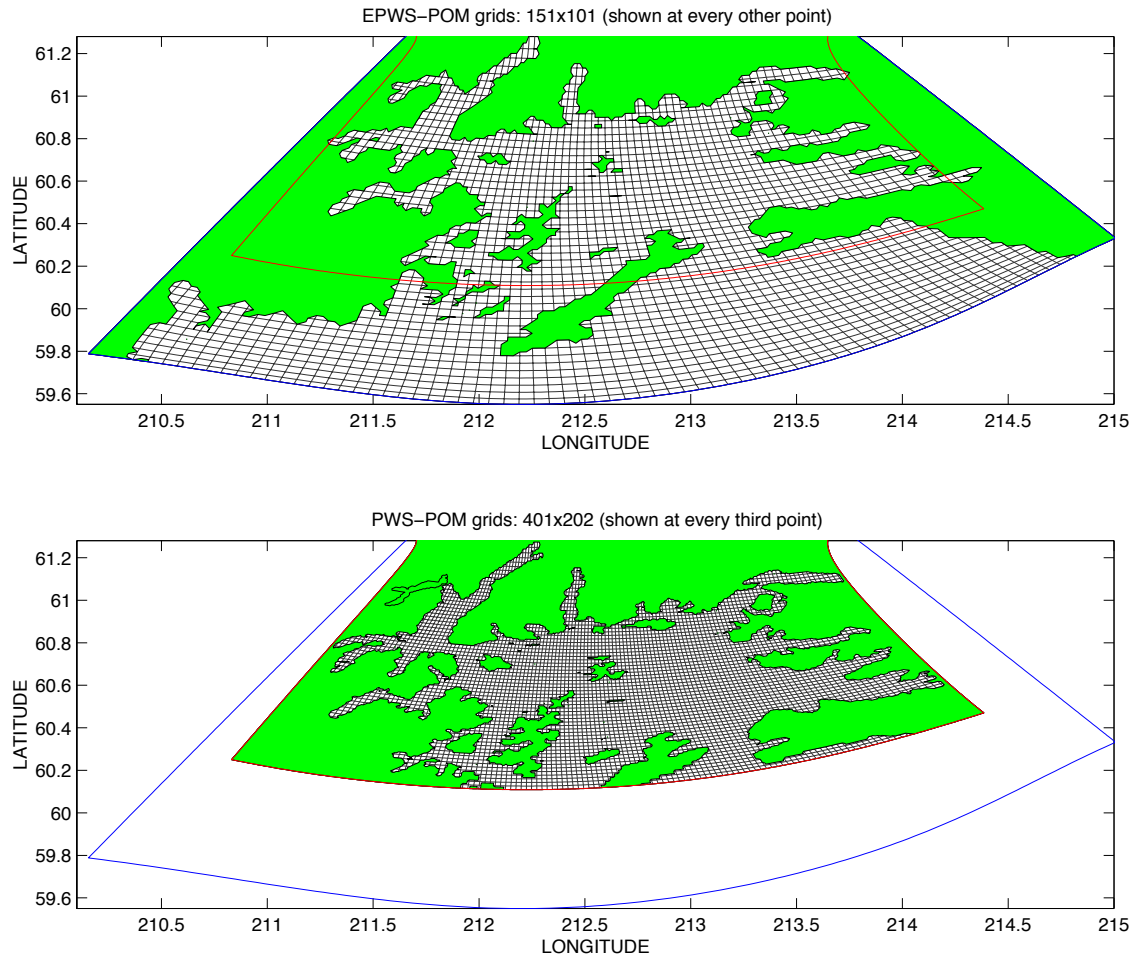


Figure 2.1: EPWS-POM (upper) and PWS-POM (bottom) grids

sizes is convenient for the development of one-way coupling between these two models, as explained below.

Previous observations (Vaughan *et al.*, 2001), and modeling studies with 15 σ -levels (Wang, *et al.*, 2001; Bang and Mooers, 2003), have demonstrated the complicated flow structures in both surface and bottom layers, especially at HE and MS. It is thus suggested that for a PWS circulation study, an effective numerical model should also have high-resolution in the vertical direction. After a set of sensitivity studies (as follows), 26 σ -levels in the vertical are utilized: six levels with logarithmic distribution near the surface ($< 30m$

deep) and two levels with logarithmic distribution at the bottom ($< 60m$ high), and 18 levels uniformly distributed between them. POM has only a few free numerical parameters; such as, HORCON and TPRNI. They will be tested for the optimal combination based on both previous modeling experience and a sensitivity study.

2.2.1 High-Resolution Topography in POM

While POM is well known for its accurate representation of bottom topography, thanks to its terrain-following σ -coordinates, the representation of the high-resolution coastline by horizontal curvilinear grids in POM still imposes a challenge, especially for the topographically complex PWS region. Normally, curvilinear coordinates have the disadvantage that the coastline that it follows must be relatively smooth (Fringer *et al.*, 2006). However, the so-called “masking” strategy, i.e., separating the “wet” grids with “dry” grids by a set of “masker” grids, to represent the sharply-varying coastline closely (*ibid*), is an effective option. This strategy becomes particularly useful with finer horizontal grid resolutions, when the variations of the coastline are comparatively less sharp. For instance, compared with EPWS-POM, PWS-POM depicts more details of the PWS coastline (Fig. 2.2). Side-by-side comparisons with a satellite image (from <http://maps.google.com>) indicate that PWS-POM is able to represent more realistic PWS coastline features (Fig. 2.2).

Inside PWS, a non-uniform topographic database (from Dr. Shari L. Vaughan) is used with an average horizontal resolution of *ca.* 100 *m*. Outside PWS, there is no such high-resolution topography database available, and instead, ETOPO2³¹ (from NOAA/NGDC/MGG)

³¹Source: <http://www.ngdc.noaa.gov/mgg/fliers/01mgg04.html>

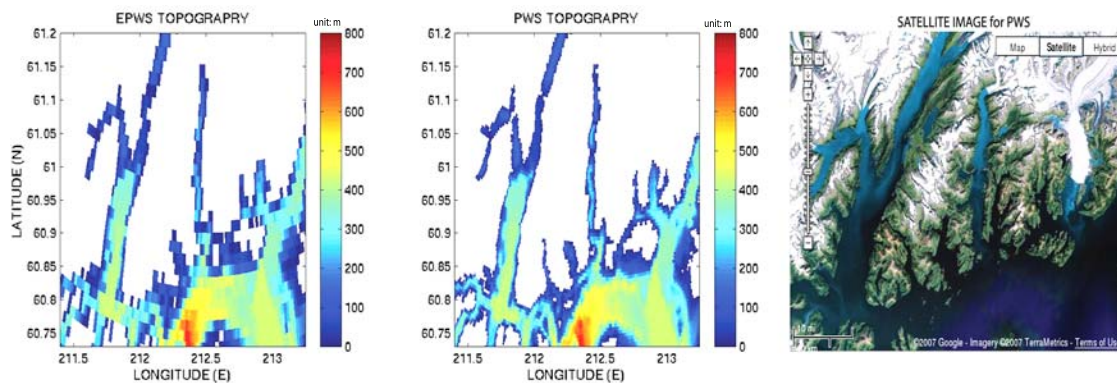


Figure 2.2: EPWS-POM (left), PWS-POM (middle) grid represented topography and coastline in the northeast PWS. For comparison, the satellite image (right) indicates the realistic coastline features in the same region (courtesy of Google Maps).

is used. One typical problem encountered during the high-resolution model topography processing is that direct interpolations from the topography database to model grids result in numerous, unreal, small “lakes” along the coastline. These spurious “lakes” may occupy as many as 50 grid points in PWS-POM horizontal grids (Fig. 2.3), and often devastate simulation results. A Fortran program³² has been developed to automatically remove these small “lakes”. The final model topography thus demonstrates a better agreement with the satellite image (Figs 2.2 and 2.3).

2.3 One-way Coupling

When the downscaling strategy between large-domain and small-domain models is invoked, the challenge of the one-way coupling scheme, whether from Global-NCOM to EPWS-POM or from EPWS-POM to PWS-POM, lies in that along the open boundaries their grid points, as well as the associated bottom topography, do not consistently coincide with each other. Thus, the momentum or heat flux transferred from one model to another is

³²downloadable from <http://epws-nfs.rsmas.miami.edu/codes/delake.f>

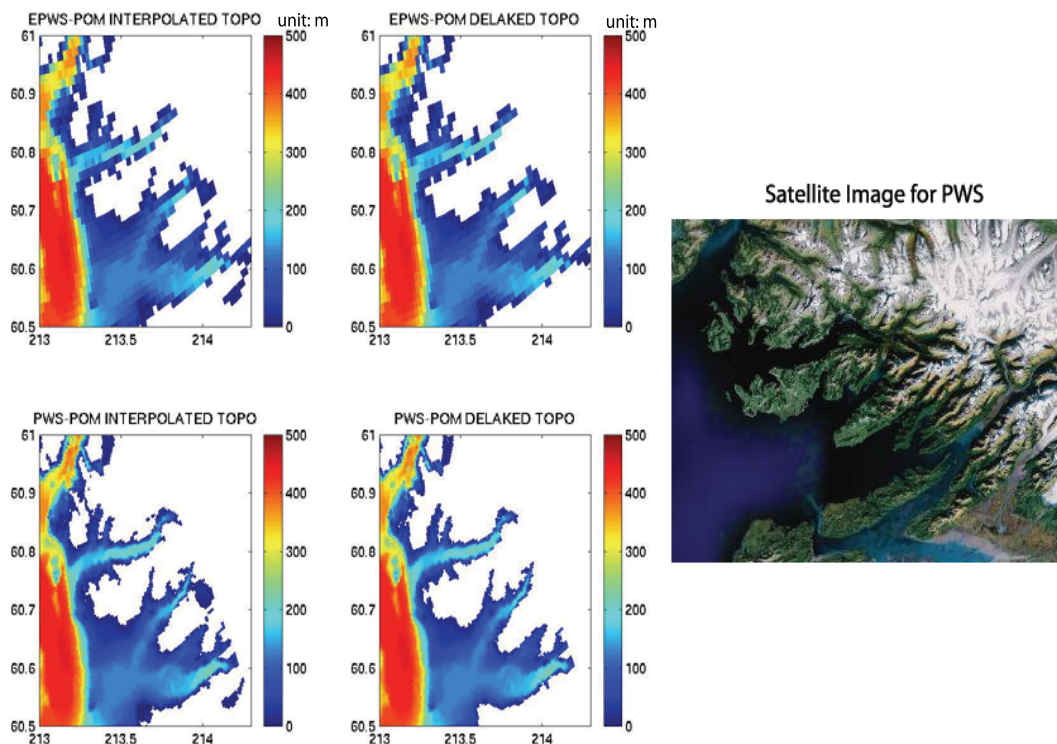


Figure 2.3: EPWS-POM (upper), PWS-POM (lower) grid represented topography and coastline in the east PWS, without (left) or with (middle) coastline refinement to remove the spurious “lakes”. For comparison, the satellite image (right) indicates the realistic coastline features in the same region (courtesy of Google Maps).

hard to conserve due to the interpolations used (Marchesiello, *et. al.*, 2001). For an ocean “weather” study with the maximum integration time of *ca.* 1 year, it is likely that the exact conservation properties are not critical (Fox and Maskell, 1995); and, consequently, it is feasible to sacrifice the exact conservation during one-way coupling in exchange for a smooth transition between two models.

2.3.1 From Global-NCOM to EPWS-POM

For the one-way downscaling coupling from Global-NCOM to EPWS-POM at the southern boundary, the first problem is that the global model topography is apparently inconsistent with the local model values (Fig. 2.4); at some locations, the discrepancy can be as large as

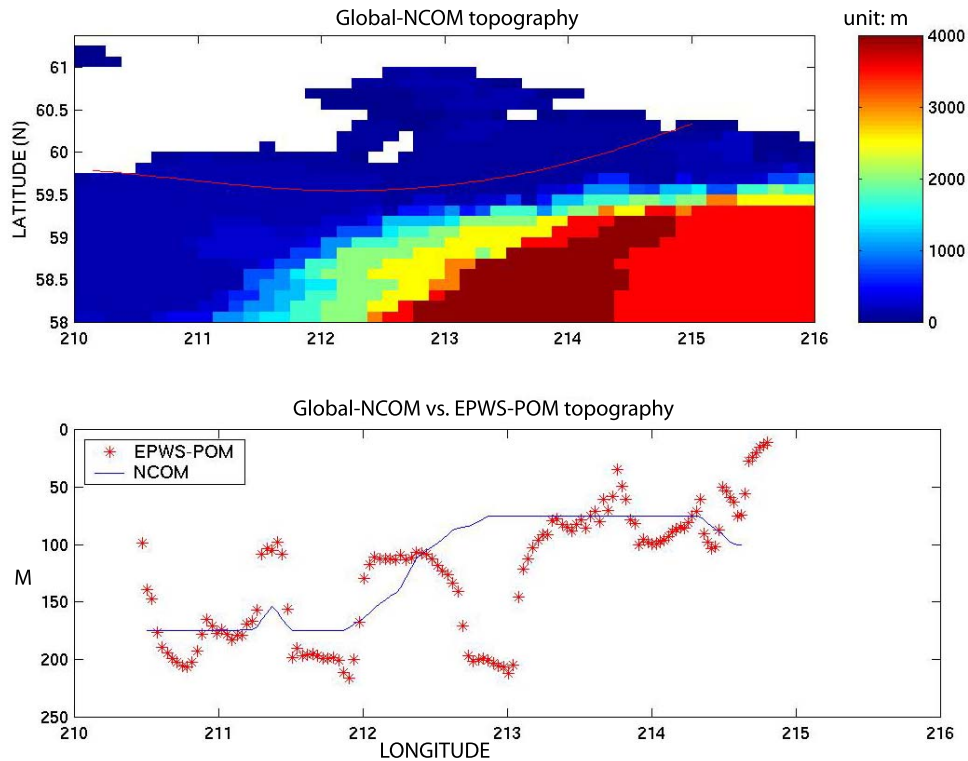


Figure 2.4: Global-NCOM topography in PWS, as well as on the continental shelf outside PWS (upper) with the superposition of EPWS-POM southern boundary (red solid line). Global-NCOM topography (lower) along the EPWS-POM southern boundary (blue solid line), via the simple 2-D interpolation, is greatly different from the local, high-resolution EPWS-POM topography (red asterisks).

150 *m* (for instance, 213E). An even larger difficulty comes from those EPWS-POM boundary grid points where the local water depth is greater than that of Global-NCOM, and thus, not enough information can be possibly provided from the global model to EPWS-POM OBCs. The simple solution is linear or spline extrapolation, which probably creates some physically unreasonable values near the bottom. Also, the total mass/momentum transport would not be conserved from Global-NCOM to EPWS-POM at the open boundary.

A more logical “estimator” would be a simple mapping method, which replaces the value of EPWS-POM bottom grid points by the bottom value from Global-NCOM, and then, linearly maps the Global-NCOM vertical profiles of horizontal velocities (U , V), temperature

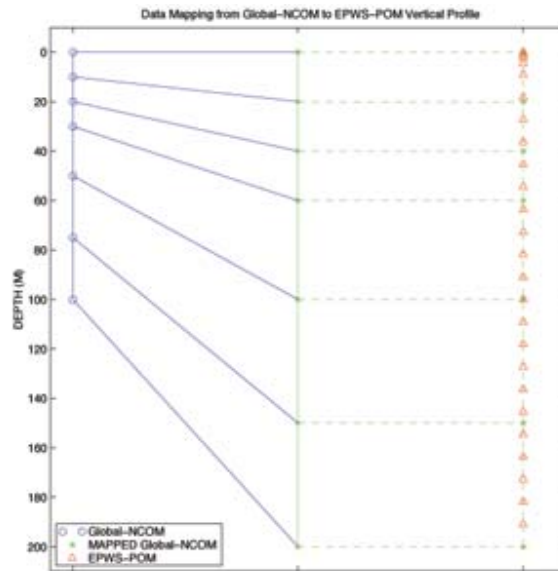


Figure 2.5: Diagram mapping Global-NCOM vertical profile to EPWS-POM σ -levels

(T) and salinity (S) to the EPWS-POM sigma-levels (Fig. 2.5). The big advantage of this mapping method is that it is guaranteed to not introduce unexpected inflow or outflow, as well as spurious cool and salty water, near the bottom at the EPWS-POM southern boundary. Also, if the total point volume transport, based on a single vertical profile of horizontal velocity from Global-NCOM, is zero, the mapped EPWS-POM vertical profile of horizontal velocity has the zero point volume transport, too.

However, the weakness of this mapping method is that the total volume transport from Global-NCOM to EPWS-POM at the open boundary is not conserved, and the discrepancy becomes larger when water depth difference between Global-NCOM and the corresponding EPWS-POM grid point is greater.

After interpolations and mapping from Global-NCOM data to vertical profiles along the EPWS-POM southern boundary, EPWS-POM barotropic variables (sea level and depth-averaged velocities) are coupled via a modified Flather radiation boundary condition (Flather radiation plus Roed local solution; Roed and Smedstad, 1984; Palma and Matano, 2000),

and baroclinic variables (depth-dependent velocity/temperature/salinity) are directly specified from Global-NCOM data.

2.3.2 From EPWS-POM to PWS-POM

There are many options available for coupling schemes between EPWS-POM and PWS-POM, once the topography discrepancy has been controlled for the model grid design. One attractive option is the Adaptive Grid Refinement method, which has been utilized in ROMS (Penven *et al.*, 2006). An alternative is the combination of the sponge layer and an appropriate radiation boundary condition, which can be relatively easily coded and installed into the original POM codes. An online one-way coupling is thus developed for the parallel runs of EPWS-POM and PWS-POM, which has the advantage that interactions between two model grids can be achieved at each time step, and is readily applicable for future development of a two-way coupling method.

Coupling Grids

As introduced previously, PWS-POM is embedded within EPWS-POM model domain but has its southern boundary open and placed near the entrance of HE and MS. The embedded grid of PWS-POM is refined from EPWS-POM grid with a constant grid size ratio of 1:3. An odd ratio gives easier and better implementation of numerical coupling for the staggered C-grid used by POM. For illustration, a simple schematic of embedded C-grid (Fig. 2.6) is plotted in an orthogonal coordinate system, with elevation/temperature/salinity/density points indicated as plus(+) signs and velocity points as upper-triangular(Δ) or circular(o) signs for the coarse or fine grids, respectively. With the usage of odd grid size ratio (1:3),

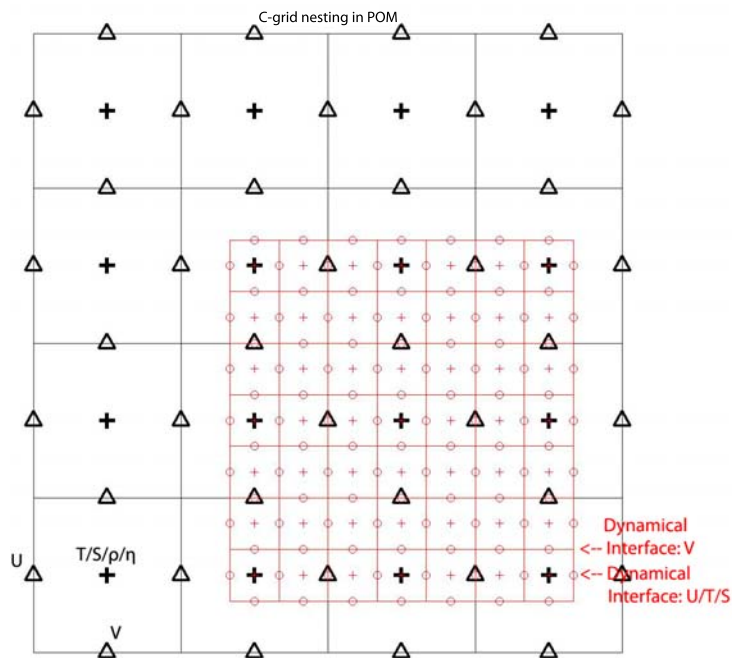


Figure 2.6: Diagram on coupling grids in an embedded C-Grid with a ratio of 1:3

all the variables at a coarse grid point within the embedded domain coincide with a fine grid point of the same type, and consequently the interpolations and interactions between grids are simplified (Spall and Holland, 1991).

The application of the embedded grids with one-way coupling from EPWS-POM to PWS-POM leads to additional efforts for grid “masking” when realistic PWS topography and coastlines are involved. For instance, what “masks” should be used in coupling grid points of fine resolution model (referred to as FRM hereafter) when the adjacent coarse resolution model (referred to as CRM hereafter) grid points are land/water interface? The question becomes more complicated when elevation and velocity data in C-grid do not coincide (Fig. 2.6). After a few numerical experiments, a simple rule-of-thumb turns out to be the most effective: at any land/water interface in CRM grids, the first FRM “wet”

grid point should always correspond to the “wet” point in CRM grids; in other words, no interpolations in FRM grids occur between the CRM land/water interface.

Although this “masking” strategy does not refine the FRM topography within the coupling grids, it has the advantage of ensuring the approximate (but not exact) conservation of mass/momentum transport, and of avoiding the complexity of possible extrapolations from the CRM to the FRM grids.

Coupling Procedure

Due to the nature of splitting barotropic and baroclinic modes in POM’s temporal integration, the external (barotropic) variables (elevation and depth-averaged velocities) are calculated with a much shorter (30 to 40 times) time step than for the internal (baroclinic) variables. It takes much longer to finish a corresponding internal mode integration for baroclinic variables (temperature/salinity/density/velocities). There is no interaction between EPWS-POM and PWS-POM at each external time step, and instead, barotropic variables in EPWS-POM are saved. At the end of each internal time step, the interaction between EPWS-POM and PWS-POM occurs; both barotropic and baroclinic variables are interpolated at the southern boundary of PWS-POM. Similarly modified Flather radiation OBCs are applied for PWS-POM barotropic variables, while baroclinic variables are directly specified as interpolated EPWS-POM values.

Due to its smaller grid size, PWS-POM has a shorter time step than EPWS-POM. For online coupling between two models, different time steps can thus be used for a faster integration. However, the different time steps in PWS-POM and EPWS-POM would result in temporal interpolations at each time step, as well as the additional requirement for data

matrix storage. Therefore, for the purpose of simplicity, the external time steps in both PWS-POM and EPWS-POM are set equal to 1 sec, and both models have a time step ratio of 30 between barotropic and baroclinic modes.

The coupling procedure proposed here is also not mass conserving. However, the method for the exact conservation of information at the interface of coarse grids and fine grids is normally time-consuming and more suitable for long-term integration, such as climate research. As mentioned previously, for an ocean “weather” study, exact mass conservation is probably not critical.

Lateral Sponge Layer

For limited-area models with one-way coupling, the purpose of a lateral sponge layer near the FRM open boundary is to impose a smooth transition of coupling variables from the CRM and to reduce the spuriously reflected outgoing gravity-inertial waves at the FRM open boundaries, using spatially varying sponge coefficients. Consequently, the CRM variables can be relaxed to the corresponding FRM variables without a spatially abrupt change in values, which is especially useful for coastal ocean modeling study where the one-way coupling between FRM and CRM often occurs in a topographically complex region with sharply-varying coastlines.

The sponge coefficients can be either specified empirically (Davies, 1976), determined optimally (Lehmann 1993), or obtained semi-analytically (Kar and Turco, 1995). All these studies suggest the effectiveness of a sponge layer for $n > 6$, where n is the number of FRM grid points away from the open boundary, and a better result can be obtained for $n = 12$ (Kar and Turco, 1995). After several testing experiments, an exponentially decreasing curve

of sponge coefficient values with $n = 7$ is efficient for the the sponge layer in the present one-way coupling study.

2.4 Internal Pressure Gradient Error/Hydrostatic Inconsistency

The σ -coordinate was introduced for the simulation of coastal ocean processes, which are coupled to the variable bottom topography. However, the internal pressure gradient error and the related “Hydrostatic Inconsistency” conditions within σ -level circulation models, for instance, POM, are a cause for concern, including for the topographically-complex, density-stratified PWS.

The internal pressure gradient error (Mellor *et al.*, 1994; Mellor *et al.*, 1998) occurs with steep “model-represented” topography and a strong background density stratification. When the horizontal pressure gradient term along σ -levels in the momentum equations involves the sum of two large terms of the same order but opposite sign, an unstable error often results, even with initially small errors in those two large terms. This sort of error can be largely reduced by (i) use of higher horizontal resolution since topography will be better resolved (Mellor *et al.*, 1998); (2) removal of the climatological mean (RMEAN) from the initial density field (Berntsen, 2002; Mellor, 2002); and (3) use of higher-order numerical integration schemes, for example, those developed in ROMS (Ezer, *et al.*, 2002). Also, numerical sensitivity studies for HORCON and TPRNI parameters in the Smagorinsky lateral viscosity in POM are conducted.

The “Hydrostatic Inconsistency” condition is a stringent requirement for grid size in σ -level numerical circulation models since it is not simply due to a horizontal discretization

error. Instead, the condition requires a cautious selection of the combination of horizontal and vertical grid sizes by imposing

$$\left| \frac{\sigma}{H} \frac{DH}{Dx} \right| \delta x < \delta \sigma \quad (2.7)$$

(Haney, 1991). For very shallow waters, it is nearly certain for any distribution of σ -levels to make δH within the adjacent grids the same order as H ; consequently, inequality (2.7) will be likely violated. Determination of whether the induced errors in very shallow water are large enough to invalidate the entire model solution, and whether the errors remain localized rather than spread to the whole model domain, requires more careful studies.

2.4.1 Sensitivity Studies

Both EPWS-POM and PWS-POM are tested to reduce the internal pressure gradient error to a tolerable level. In these sensitivity studies, horizontal grids are the same with all the open boundaries closed, which means that there is no flow through the boundaries. No external forcing is applied. Both models are started from rest for the barotropic and baroclinic experiments. In either case, there are no initial horizontal pressure gradients, which means that no motion should be generated when the model starts running. And thus, if any motion is produced, it must be due to numerical errors. For a σ -coordinate ocean model, most of these errors may result from the internal pressure gradient errors and the ‘‘Hydrostatic Inconsistency’’ condition for baroclinic experiments. Results from sensitivity studies (not shown) for EPWS-POM and PWS-POM are summarized below:

1. above all, the RMEAN value should be removed from the initial density field;

2. the default pressure gradient scheme in POM, *i.e.* subroutine BAROPG, rather than higher-order scheme such as 6-order scheme (Chu and Fan, 1997), should be used;
3. the default advection scheme, *i.e.*, the centered difference scheme provided in POM rather than the Smolarkiewicz iterative upstream scheme, is recommended;
4. the use of 26 σ -levels is appropriate for both EPWS-POM and PWS-POM;
5. for EPWS-POM, an optimal combination of HORCON and TPRNI is 0.1 and 0.05, respectively; and for PWS-POM, it is 0.3 and 0.01, respectively.

Therefore, all the subsequent EPWS-POM and PWS-POM simulations will follow these findings.

2.5 Model Initialization

Different from coarse resolution models, which may have a final state of “truly” steady circulation or dynamical equilibrium, the eddy-resolving ocean circulation models; such as, PWS-POM and EPWS-POM develop time-dependent mesoscale motions, and probably cannot lead to a final steady state (Soloviev, 1999). However, such model solutions can be expected to reach a statistical equilibrium where the eddy kinetic energy, *etc.*, is basically constant. Depending on their specific applications, EPWS-POM and PWS-POM are initialized in two different ways: the former, aiming at the general circulation patterns and interactions between the Sound and the continental shelf, is initialized from climatology, followed by a spin-up run; and the latter, aiming at the mesoscale or sub-mesoscale studies inside PWS, is initialized from EPWS-POM fields due to its embedded grid distribution within EPWS-POM grid. This simple initialization of PWS-POM can thus be conveniently

used for synoptic-scale assessment studies. For instance, if EPWS-POM simulations suggest the formation of eddies in the Sound, and PWS-POM can then be initialized and driven by EPWS-POM to closely monitor the evolution of these eddies.

2.5.1 EPWS-POM Initialization

To accelerate the convergence to a statistical steady state before simulations of interest, EPWS-POM is spun-up for a period long enough to exceed the memory of the initial state. This process is slow for the deep water circulation below the main thermohaline and thus, may require quite a long time (ca. 10 years; Drijfhout, 1994). The situation is different for the upper ocean, where a much shorter adjustment time is needed due to the presence of fast-propagating Poincare and other waves. During the spin-up period, the model undergoes a process of internal adjustment and the fine resolution allows the development of time-dependent motions on a scale of the internal Rossby radius of deformation.

There are two common strategies for numerical circulation model initializations; *i.e.*, use of climatology or a previous model run (Chassignet and Malanotte-Rizzoli, 2000). The horizontal resolution of standard climatological data, for instance, Levitus (1994) and GDEM (Generalized Digital Environmental Model) seasonal or monthly ocean profiles³³, is too coarse for typical small coastal ocean regions, such as PWS. Thus, interpolations or even extrapolations from these climatologies have to be invoked for much finer model grids in both the horizontal and vertical directions unless there are adequate historical data available to make a local climatology. Therefore, for the present EPWS-POM initializations, the previous model runs from EPWS/NFS are adopted, because (1) the assessment of EPWS/NFS

³³Source: <http://https://128.160.23.42/gdemv/gdemv.html>

efficiency (Chapter 1) indicates that EPWS/NFS probably represents well the main circulation features in PWS; (2) both the horizontal and vertical resolution of EPWS/NFS provide dense enough data fields inside the EPWS-POM model domain, although interpolations and adjustments are still unavoidable due to the inconsistency of topography among different models ; and (3) all the prognostic variables, including velocity, temperature, salinity, and sea surface height, are initialized in a physically and internally consistent way. On the other hand, the presence of the nowcast deep water in BH with significant seasonality (Fig. 1.39) suggests that the initialization of EPWS-POM should contain this deep water, for the subsequent numerical studies of deep water properties in PWS. Therefore, the EPWS/NFS daily-mean field in 01 SEP 2005 is used, when temperature/salinity/density profiles in BH are well stratified while during the remaining seasons, a temperature inversion occurs in PWS (Figs. 1.38 and 1.39).

After initialization, a one-year EPWS-POM spin-up run with relaxation to EPWS/NFS climatology is implemented. EPWS/NFS climatology is obtained as the temporal mean of SEP 2005 model outputs. The relaxation scheme is

$$\frac{\partial \vec{U}}{\partial t} = \vec{F}_u - \frac{1}{\tau_c}(\vec{U} - \vec{U}_c) \quad (2.8)$$

$$\frac{\partial \phi}{\partial t} = F_\phi - \frac{1}{\tau_c}(\phi - \phi_c) \quad (2.9)$$

where $\vec{U} = \vec{U}(u, v)$ and ϕ are the prognostic horizontal velocity and tracer (temperature or salinity), respectively, with $\vec{U}_c = \vec{U}_c(u_c, v_c)$ and ϕ_c representing the corresponding climatology. \vec{F}_u and F_ϕ contain all the others terms in the system of equations, and τ_c is the relaxation time which is chosen as one month as a common strategy. The relatively strong

nudging guarantees that after some period of time significantly longer than τ_c , the prognostic velocity and tracers in eddy-resolving EPWS-POM will be dynamically consistent with the EPWS/NFS climatology. The length of the spin-up period is 400 days.

The radiation boundary conditions are applied for both external and internal velocities during the EPWS-POM spin-up period. This method has the advantage that the normal velocity through the open boundary is adjusted automatically during the integration to ensure the net volume transport is approximately zero. At the end of the spin-up, EPWS-POM achieves a statistical equilibrium state (Figs. 2.7): the initial transition period, represented by a quick increase of the total kinetic energy inside the model domain, and volume transports through HE and MS, ends after *ca.* 80 days. Fluctuations in the time-depth plots of temperature in both BH and Central Sound quickly dampen after *ca.* 30 days.

2.5.2 Comments on Computation Time

The advance of modern computer technology enables advances in computational oceanography with higher spatial resolution but less computing time. The present EPWS-POM and PWS-POM run simultaneously on an HP workstation with Intel Itanium 2 dual-processor (4GB memory) and a Linux desktop with Intel Core 2 Duo dual-processor (4GB memory). Both computers have similar computing power with the same Intel Fortran Compiler (Version 9.0) installed. Since EPWS-POM and PWS-POM (both based on pom2k) are not optimized for parallel computing, one model run can only be supported by a single processor.

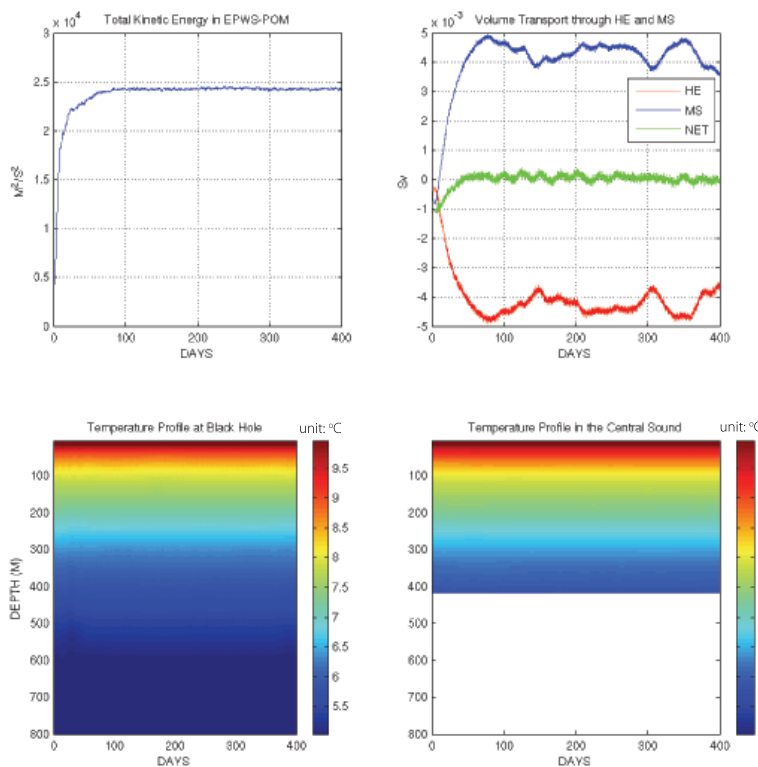


Figure 2.7: EPWS-POM spin-up: (a) total kinetic energy; (b) volume transport through HE and MS; time-depth plots of temperature in (c) BH and (d) Central Sound

The typical integration time for a one-day EPWS-POM run on one processor is 5 minutes, and nearly 400 minutes for a one-day EPWS-POM/PWS-POM coupled run. Therefore, it takes less than 2 days to finish a one-year spin-up run for EPWS-POM, and about 9 days to finish a one-month simulation of a coupled run.

2.6 Summary

Based on POM, two numerical implementations (EPWS-POM and PWS-POM) are configured for oceanographic studies in PWS, including horizontal and vertical grid distributions, high-resolution topography processing, and a one-way downscaling coupling scheme with an optional lateral sponge layer. The ratio of grid sizes between Global-NCOM and

EPWS-POM is *ca.* 5:1, and between EPWS-POM and PWS-POM is 3:1. For the purpose of minimizing the internal pressure gradient error, the optimal values of HORCON and TPRNI are determined to be 0.1, and 0.05, respectively, for EPWS-POM, and 0.3 and 0.01, respectively, for PWS-POM, after a series of sensitivity studies. The same studies also suggest that the optimal number of vertical σ -levels is 26 in both EPWS-POM and PWS-POM.

EPWS-POM is then initialized from EPWS/NFS fields in SEP 05 and spun-up for a 400-day period with relaxation to the EPWS/NFS climatology. After the spin-up, EPWS-POM horizontal kinetic energy achieves a statistical equilibrium. EPWS-POM is then ready for subsequent numerical studies on the response of PWS to external forcings.

Chapter 3

Response of PWS to Large-Scale Circulation (LSC)

As a small coastal sea, PWS is an integral component of the NGOA dynamical system, and naturally, under the influence of the Large-Scale Circulation (LSC) prevailing in the NGOA, especially the dominant flows along the coast. Over the shelf, the ACC is the most energetic flow along the Alaskan coast (Royer, 1998), and part of it flows through PWS with significant seasonal variability (Vaughan *et al.*, 2001). Other LSC features, such as mesoscale eddies and upwelling and downwelling events across the shelf affect PWS circulation, too.

3.1 Methodology

The LSC is the keystone of physical, chemical and biological oceanography and an important part of the Earth's climate system. It typically ranges in horizontal scale from hundreds to thousands of kilometers, and the carefully-implemented global- (Rhodes *et al.*, 2002) and basin-scale (Ezer and Mellor, 1997; Kara *et al.*, 2007) ocean models represent

well these dominant, LSC flows. Consequently, the PWS response to the LSC can be examined by numerical simulations of EPWS-POM and/or PWS-POM driven by the global- or basin-scale ocean models at the open boundaries.

This type of study becomes practical with the availability of data-assimilative, 1/8-degree Global-NCOM (Section 1.2) real-time products and its historical database since FEB 2005. The study starts via the one-way, down-scale coupling from Global-NCOM to EPWS-POM at the southern open boundary, with both barotropic (surface elevation and depth-averaged velocities) and baroclinic (velocity, temperature, and salinity profiles) variables used in the coupling scheme (Section 2.3). The integration time is chosen as a full year (2006). The focus is on phenomena with synoptic or seasonal variability, but no inter-annual variability will be studied here.

Before numerical simulations are made with EPWS-POM, the skill of Global-NCOM must be determined, to validate how well Global-NCOM represents the general circulation in the NGOA. After that, post-processed Global-NCOM data are prepared for two EPWS-POM numerical experiments; *i.e.*, the response to annual-mean and synoptic LSC variability. These experiments correspond to applications of Global-NCOM annual-mean and three-hourly fields, respectively, along the EPWS-POM open boundary. One PWS-POM experiment, driven by one-way coupling with EPWS-POM, will be conducted during the summertime for better simulation of mesoscale and sub-mesoscale circulations in PWS.

No other external forcings, *e.g.*, surface AP or winds, heating/cooling, runoff, and tides, are applied in both EPWS-POM and PWS-POM simulations in this Chapter. Upon finishing these experiments, the analysis of the simulation results will be focused on (1) mesoscale

variability in Central Sound, (2) the barotropic and baroclinic transports through HE and MS, and (3) deep water properties in PWS.

3.1.1 Verification of NCOM Performance in NGOA

NCOM topography over the PWS domain is significantly different from the high-resolution EPWS-POM topography (Fig. 2.4), which is common for global ocean models since they normally do not have enough horizontal resolution to resolve the geometric details of small coastal ocean domains. The validation of NCOM data with available observations has thus been conducted primarily over the shelf outside PWS.

NCOM nowcast CSL is compared with 40-hour low-passed tide gauge observation at Seward (Fig. 3.1): they are substantially correlated (COR=0.56 at zero lag with $rmse = 0.03$) and agree well with respect to the seasonal cycle. Better correlation (COR=0.60 at zero lag with $rmse = 0.01$) is obtained when the observed CSL is adjusted by local atmospheric pressure. However, NCOM nowcast CSL ($var = 4.9 \times 10^{-3} m^2$) is substantially less energetic than the observed values ($var = 3.6 \times 10^{-2} m^2$ and $1.2 \times 10^{-2} m^2$ for non-adjusted and adjusted CSL, respectively), which might contribute to the lack of enough low-frequency variability in EPWS/NFS CSLs (Fig. 1.11).

NCOM nowcast SST is compared with NDBC buoy observations at various locations: Seward, buoy 46061, 46076 and 46082 (Fig. 3.2). The seasonal cycles of observed SST are closely followed by the NCOM nowcast, resulting in nearly perfect correlations of COR=0.99 (zero lag) at all four location. Slightly better agreements are obtained at three buoy locations, where $rmse$ values between nowcast and observed time series are 1.0, 0.9, and 0.8, while at the land station (Seward), a $rmse$ value of 1.4 is obtained.

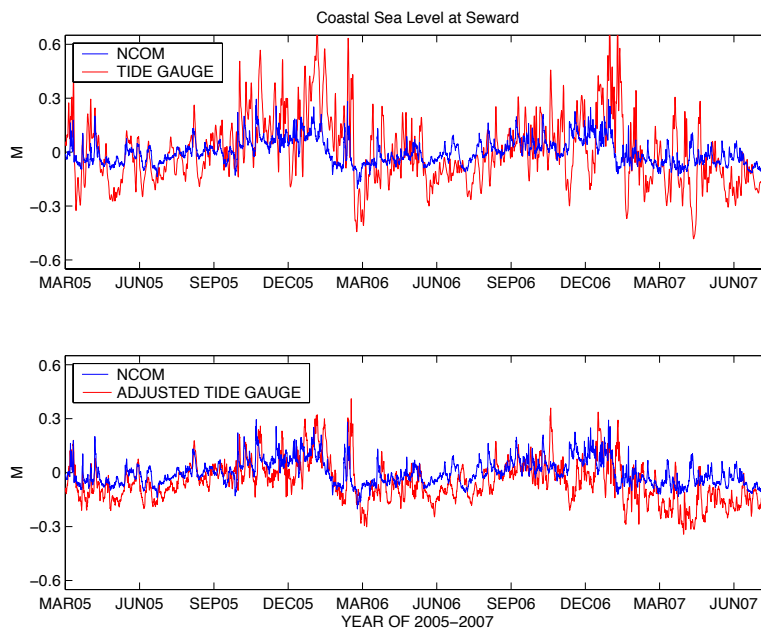


Figure 3.1: (upper) Two-year comparison of three-hourly Global-NCOM nowcast (blue) with 40-hr low-passed observed (red) coastal sea level at Seward. (lower) Comparison with observed adjusted sea level is also shown.

NCOM nowcast vertical temperature/salinity profiles are compared with observed CTD profiles at GAK1 (also see Section 1.3.5). Observed CTD profiles are downloaded directly from the GAK1 website³⁴ with data at depths of 15, 30, 60, 100, 150, 200, and 250 *m* between MAY 2005 and JUN 2006 (Fig. 3.3). For comparison, NCOM simulations during the same period are extracted at the standard NCOM output vertical levels of 10, 30, 50, 70, 100, and 150 *m*. Despite topographic mismatches in NCOM, both observed and nowcast temperature profiles exhibit the temperature inversion starting in DEC 2005, after substantial mixing and surface cooling, and the surface water becomes cooler than the deep water while remaining hydrostatically stable due to salinity stratification. Also, probably due to vertical mixing, the bottom water becomes warmer in NOV, DEC 2005 and JAN, FEB 2006 than the remaining year at GAK1, as both NCOM nowcast and CTD observations

³⁴<http://www.ims.uaf.edu/gak1/Plots/Deployment6.html>

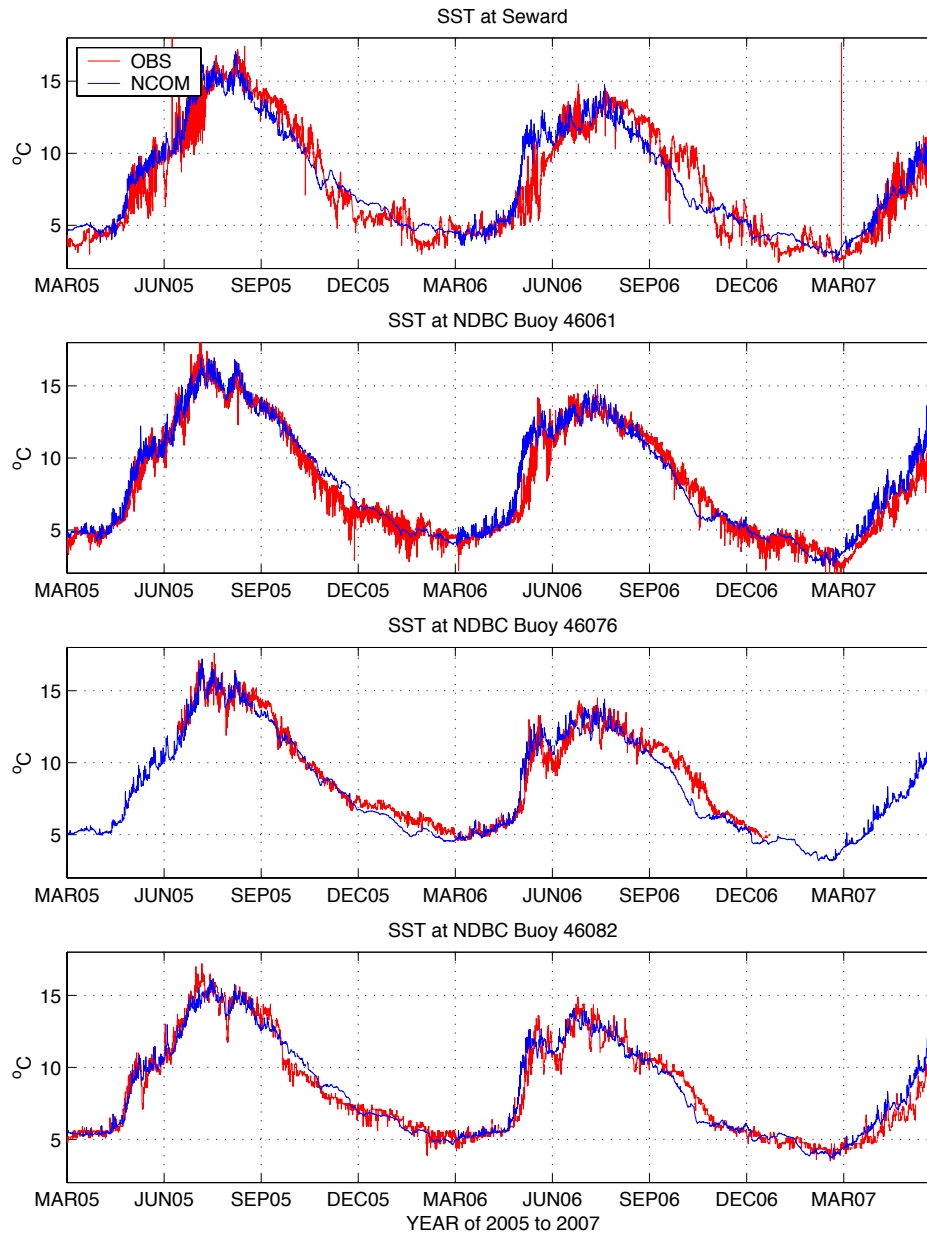


Figure 3.2: Two-year comparison of Global-NCOM nowcast (blue) and observed (red) sea surface temperature at Seward, NDBC buoy 46061, 46076 and 46082

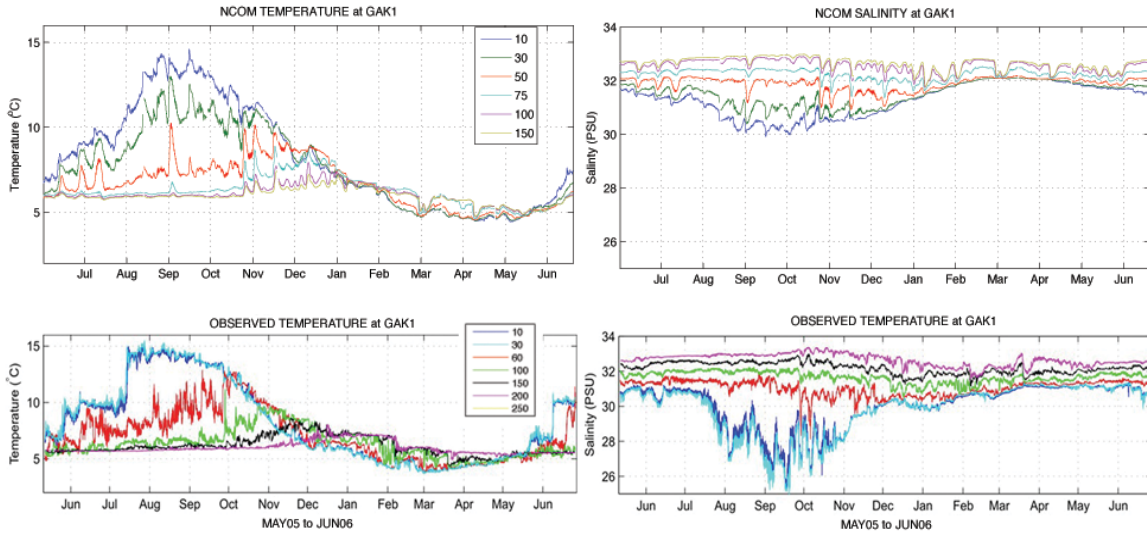


Figure 3.3: One-year comparison of Global-NCOM nowcast (upper) and observed (lower) temperature/salinity profiles at GAK1 between MAY05 and JUN06. Observed GAK1 T/S plots are directly obtained from GAK1 website and colors indicate nominal depth level: Near surface (blue & cyan), 60m (red), 100m (green), 150m (black), 200m (magenta) and 250m (yellow).

indicate. NCOM nowcast bottom water, however, is *ca.* 1°C warmer than the observed value. In the intermediate water (*ca.* 50 m depth), NCOM successfully simulates some observed synoptic events; for instance, at the beginning of AUG 2005 and the end of SEP 2005. On the other hand, NCOM fails to capture a significant surface heating and freshening event in the middle of JUL 2005, when the upper layer temperature (*ca.* 30 m) is increased by 5°C in a few days. Similarly, NCOM salinity profile compares well with the observed profile at GAK1. However, NCOM upper layer salinity is substantially saltier than observed during the second half of 2005 (MAY to DEC), by an average of 2 *ppt* and as much as 5 *ppt* in SEP 2005.

Following the previous work (Section 1.3.4), more investigations of Global-NCOM data are conducted along the EPWS/NFS open boundaries. As the most prominent circulation features along the Alaskan coast, the cyclonic ACC (within the inner shelf) and Alaska Current (further offshore) generally account for the nowcast cross-shelf SSH gradient (not

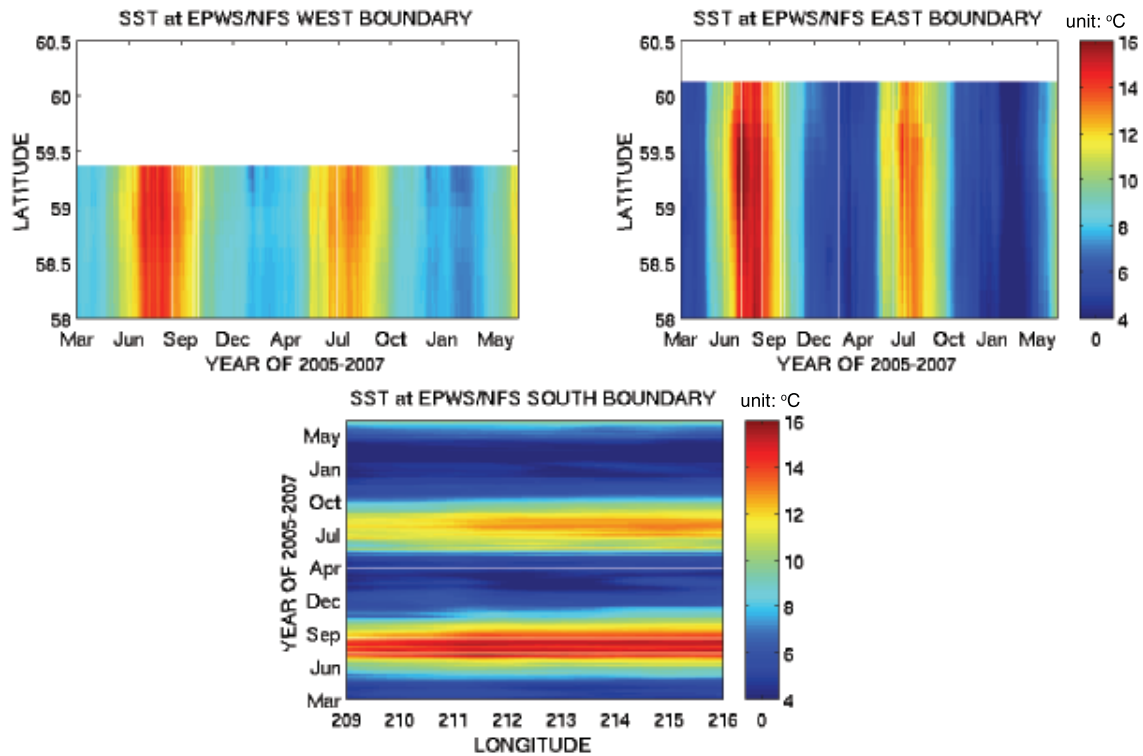


Figure 3.4: Two-year NCOM nowcast SST at EPWS/NFS eastern, western, and southern boundary

shown) due to geostrophic balance. The LSC seasonal variability in heating/cooling is well indicated in the Global-NCOM SST nowcast (Fig. 3.4). Surface currents, on the other hand, indicate a mixed nature of nowcast response to both LSC and surface forcing, since they contain more synoptic variations. Over the shelf break at the EPWS-POM eastern boundary, the dominant westward flow (ACC) occurs in the upper 100 *m*, and has a mean volume transport of *ca.* 0.2 Sv (Fig. 3.5). Eastward flows occur near the bottom in the NCOM mean field, and this undercurrent along the NGOA shelf break was obtained in a previous numerical study (Wu, 2003).

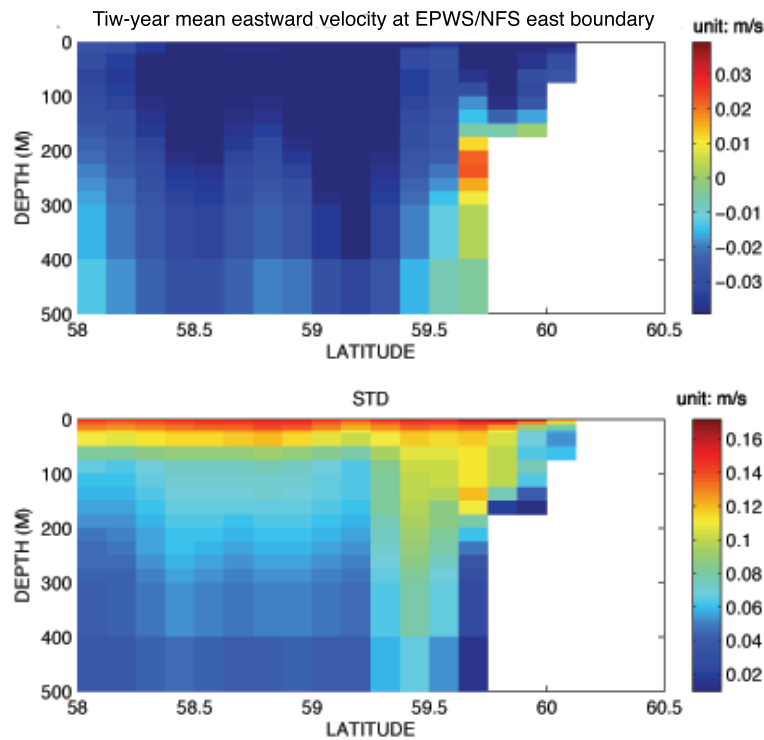


Figure 3.5: Two-year mean and *std* of eastward flow profile along the EPWS/NFS eastern boundary

3.2 Annual-mean LSC Response

The annual-mean LSC in NGOA is thus represented by the Global-NCOM mean field for the year of 2006, and applied as spatially-dependent, temporally-constant OBCs along the EPWS-POM southern boundary (Section 1.3.1). The first 50-day period is characterized by relatively large fluctuations in sea levels (Fig. 3.6) and a rapid increase of volume transport through HE and MS (Fig. 3.7). After *ca.* 100 days, sea levels at various locations over EPWS-POM domain are nearly constant in time, except over the western shelf outside PWS where sea level continues to decrease slightly and develops small fluctuations with a period of a few days. Coastal sea levels, including at three land stations (Cordova, Valdez and Seward), Central Sound and BH, tend to equilibrium values, while sea level fluctuations

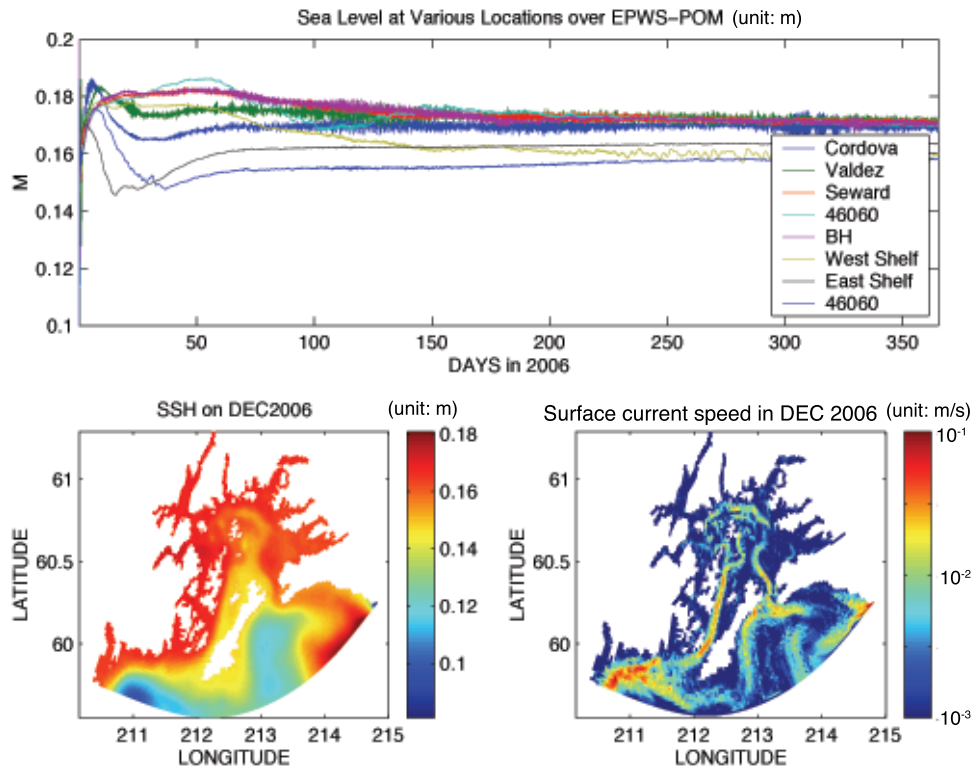


Figure 3.6: EPWS-POM simulated 1-yr sea levels at various locations (upper), along with SSH (bottom left) and surface current speed (bottom right) in DEC 2006

over the shelf outside PWS are relatively smaller (Figs. 3.6). The cross-shelf SSH gradient is geostrophically consistent with the pathway of the cyclonic-flowing ACC over the shelf.

The mean volume transport is exclusively in through HE and out through MS and very weak (*ca.* 0.02 Sv; Fig. 3.7), thus developing a through-flow circulation pattern in PWS. Considering that the mean geostrophic transport carried by the ACC is *ca.* 0.2 Sv (Niebauer *et al.*, 1994), only *ca.* 1/10 of ACC transport thus penetrates into PWS via HE and out via MS, developing a simple through-flow circulation pattern as the annual-mean LSC response. No persistent mesoscale eddies are identified inside the Sound (not shown).

The annual-mean baroclinic transport through MS is characterized by a well-defined two-layer structure: outflow in the upper 75 m and inflow below (Fig. 3.7). At HE, the annual-mean baroclinic transport demonstrates a more complex structure: for the upper

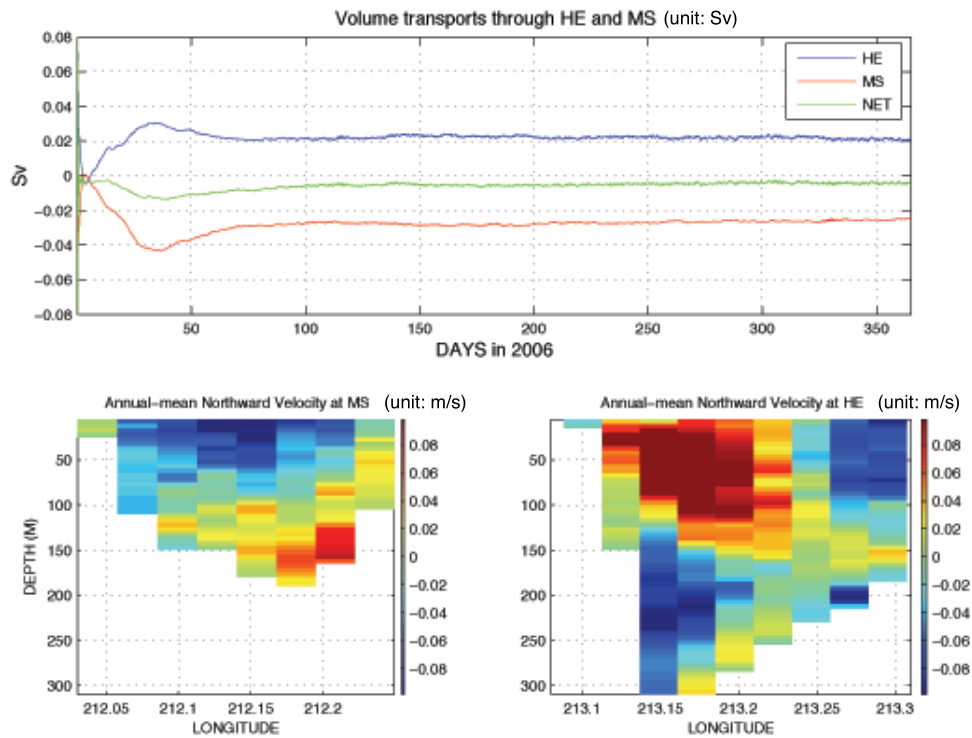


Figure 3.7: EPWS-POM simulated 1-yr volume transports through HE and MS (upper), along with annual-mean northward velocity at MS (bottom left) and HE (bottom right)

150 m, inflow occurs on the western side of HE, with outflow on the eastern side. Below 150 m, the flow is reversed from the layer above; i.e., outflow on the western side of HE and inflow on the eastern side.

The annual-mean LSC forcing substantially smooths the vertical temperature gradients at various locations, making PWS less temperature stratified (Fig. 3.8): initial surface warm water (*ca.* 10°C) gradually cools, sooner over the shelf than inside the Sound, and the deep water at BH (*ca.* 4.5°C) is replaced by warm water (6°C) at the beginning of JUL 2006.

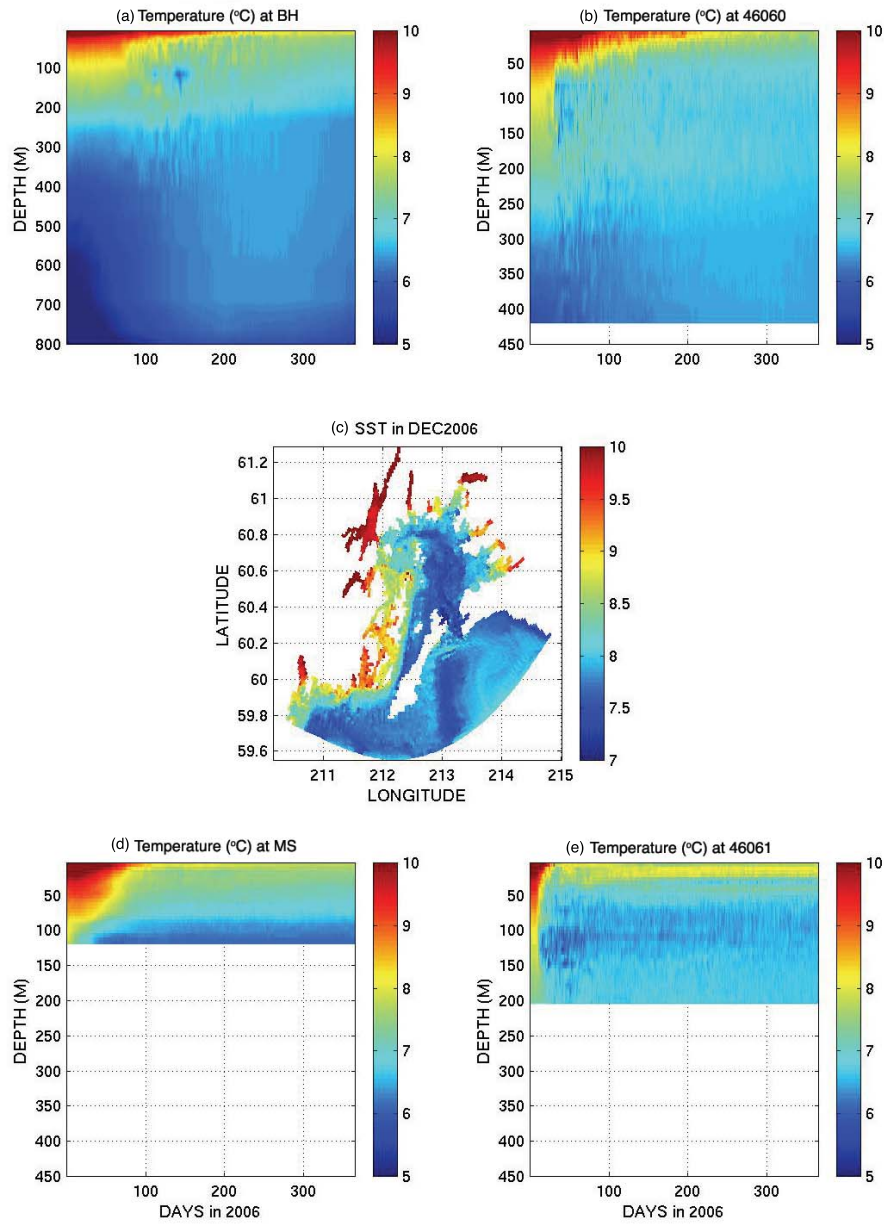


Figure 3.8: EPWS-POM simulated 1-yr time-depth plots temperature at (a) BH, (b) 46060, (d) MS, and (e) 46061, along with (c) map of SST in DEC 2006

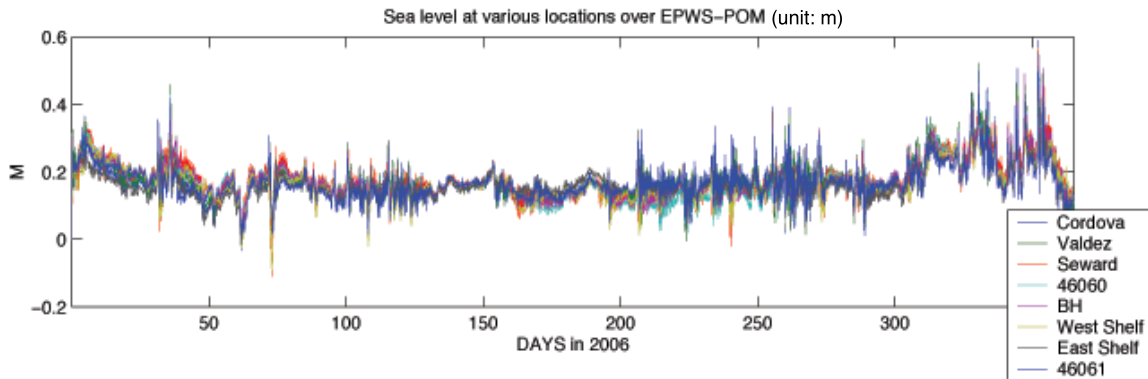


Figure 3.9: EPWS-POM simulated 1-yr sea levels at various locations

3.3 Synoptic LSC Response

With the introduction of synoptic forcing from OBCs, EPWS-POM simulated sea levels are substantially more energetic than those in the annual-mean LSC response (Fig. 3.9), but still lack enough variability, either inside the Sound or over the shelf, to account for the observed low-frequency sea level fluctuations at the tide gauges (Fig. 1.11). On the other hand, the HE and MS volume transports (Fig. 3.10) have similar variability as in EPWS/NFS (Fig. 1.23): they are significantly correlated ($COR=-0.97$ at zero lag) with reversed transport from time-to-time at both straits. The coherence pattern between HE and MS volume transports reveals the occurrence of a “transition band” (Section 1.3.6): highly coherent, generally out of phase, and nearly balanced for periods longer than *ca.* 30 hr, and partially coherent, generally in phase for periods less than *ca.* 5 hr. In the “transition band” of *ca.* 5 to 30 hr, HE and MS volume transports are less coherent and exhibit a rapid phase shift. The inertial peak at the period of *ca.* 13.8 hr in the volume transports power spectra (Fig. 3.10) is prominent, and two other peaks at periods of *ca.* 2.5 and 4 hr probably are indicative of seiches for PWS.

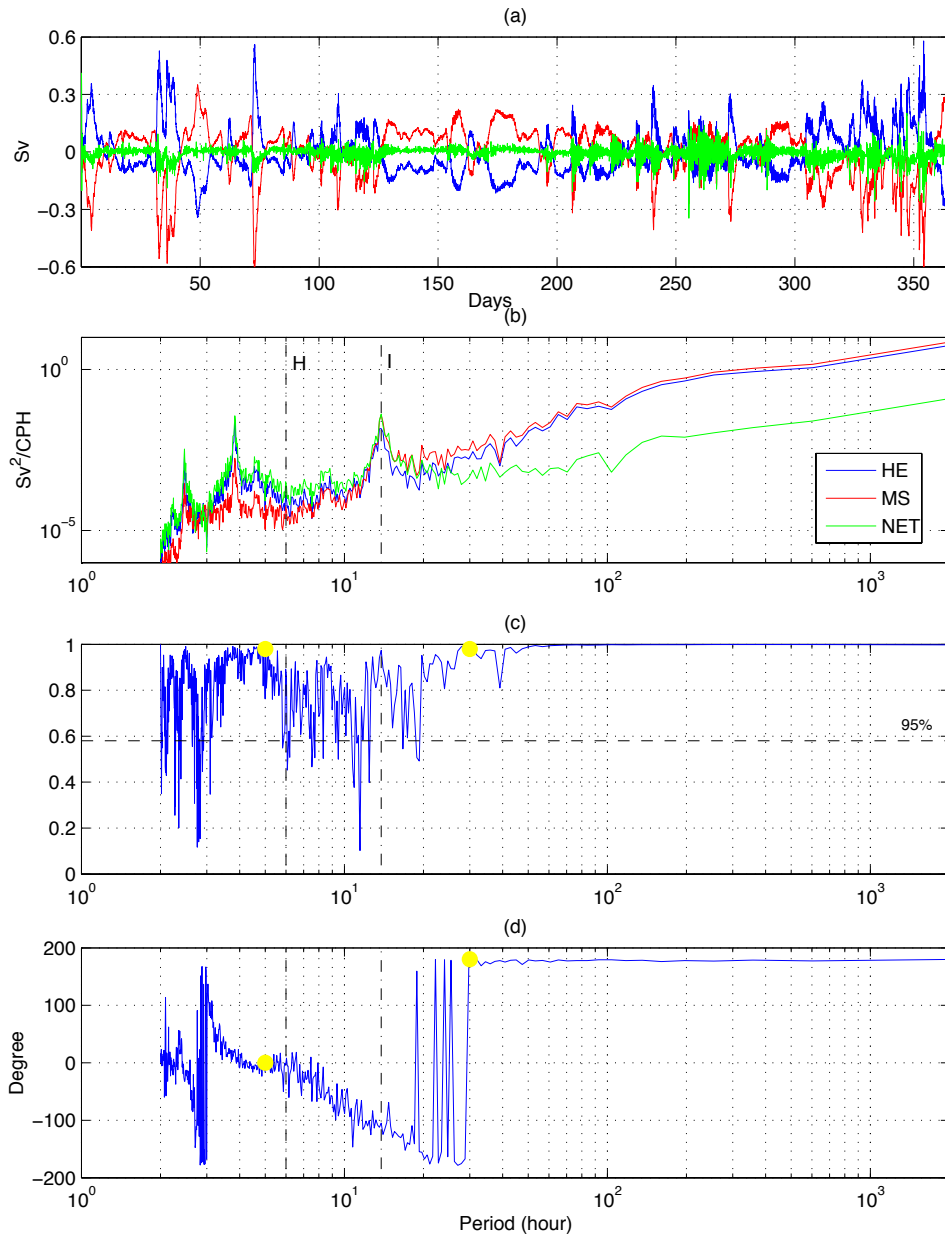


Figure 3.10: EPWS-POM simulated 1-yr (a) volume transports through HE (red) and MS (blue), as well as the net transport (green); (b) corresponding power spectra (DOF=10); (c) coherence squared between volume transports through HE and MS; and (d) phase. The transition band (solid yellow dots) of the coherence function is indicated. KEY: H, Helmholtz resonance period for PWS (*ca.* 6 hrs); I, inertial period (13.8 hrs).

In Central Sound, a well-developed cyclonic gyre (referred to as CG thereafter in this Chapter) occurs in AUG and SEP (Fig. 3.11). Detailed investigation³⁵(Fig. 3.12) indicates that this CG first appears in late JUL, and surface warm water penetrates into Central Sound via HE at that time (Fig. 3.13). During the next two months (AUG and SEP), the continuous intrusion of warm water within the HE surface inflow layer interacts with the CG until mid OCT. The position of the CG is not fixed in space, and instead, its position is associated with the strength and duration of the warm water intrusion through HE. The HE surface inflow weakens in SEP (Fig. 3.13), and the CG shrinks, and gradually dissipates in OCT when there is outflow. In comparison, strong surface inflow at HE occurs again in NOV and DEC but with a cool water intrusion into Central Sound, but, no cyclonic gyre appears during these months. The simulated monthly-mean SST pattern and baroclinic transport at HE and MS (Fig. 3.14) in NOV is very similar to those of APR, which suggests that the synoptic LSC response of PWS upper layer circulation may be appropriately defined as two dynamic sub-systems: the summer circulation during MAY to OCT, characterized by warm water intrusions due to HE surface inflow and warming of PWS surface water, and the winter circulation during NOV to APR, characterized by cool intrusion into PWS and cooling of PWS surface water. Correspondingly, during the summer circulation, weak inflow occurs in the MS surface layer, while during the winter circulation, the MS surface layer is dominated by strong outflow (Fig. 3.14).

Monthly-mean surface flows at both HE and MS are mostly geostrophically balanced with the cross-strait sea level gradient (Figs. 3.11, and 3.13, 3.14). At MS, strong bottom inflows ($> 0.1m/s$) occur throughout the year except in APR and NOV when the flow is

³⁵also see one-year SST animation from http://epws-nfs.rsmas.miami.edu/EPWS/ncoms_sst.mpeg

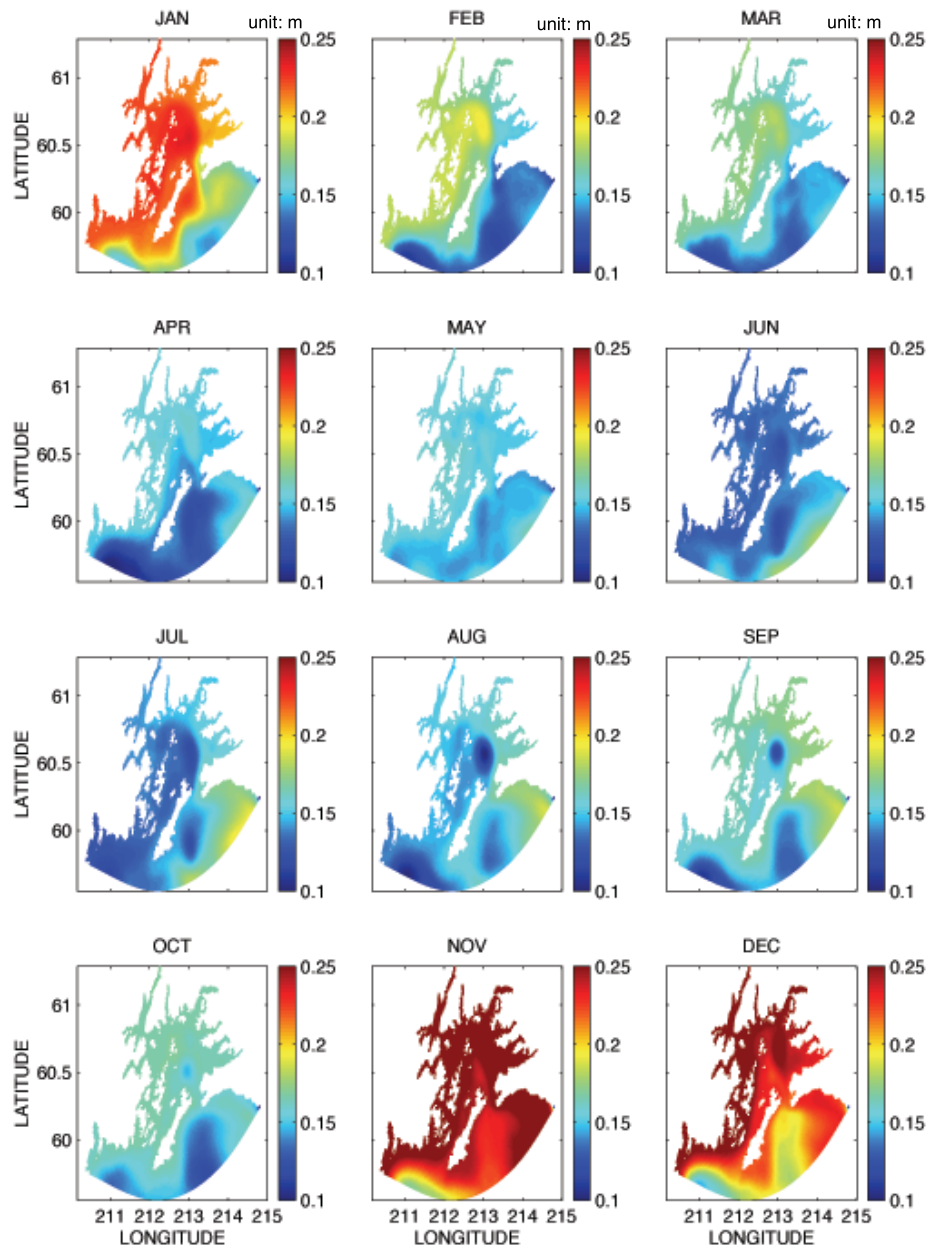


Figure 3.11: EPWS-POM simulated monthly-mean SSH

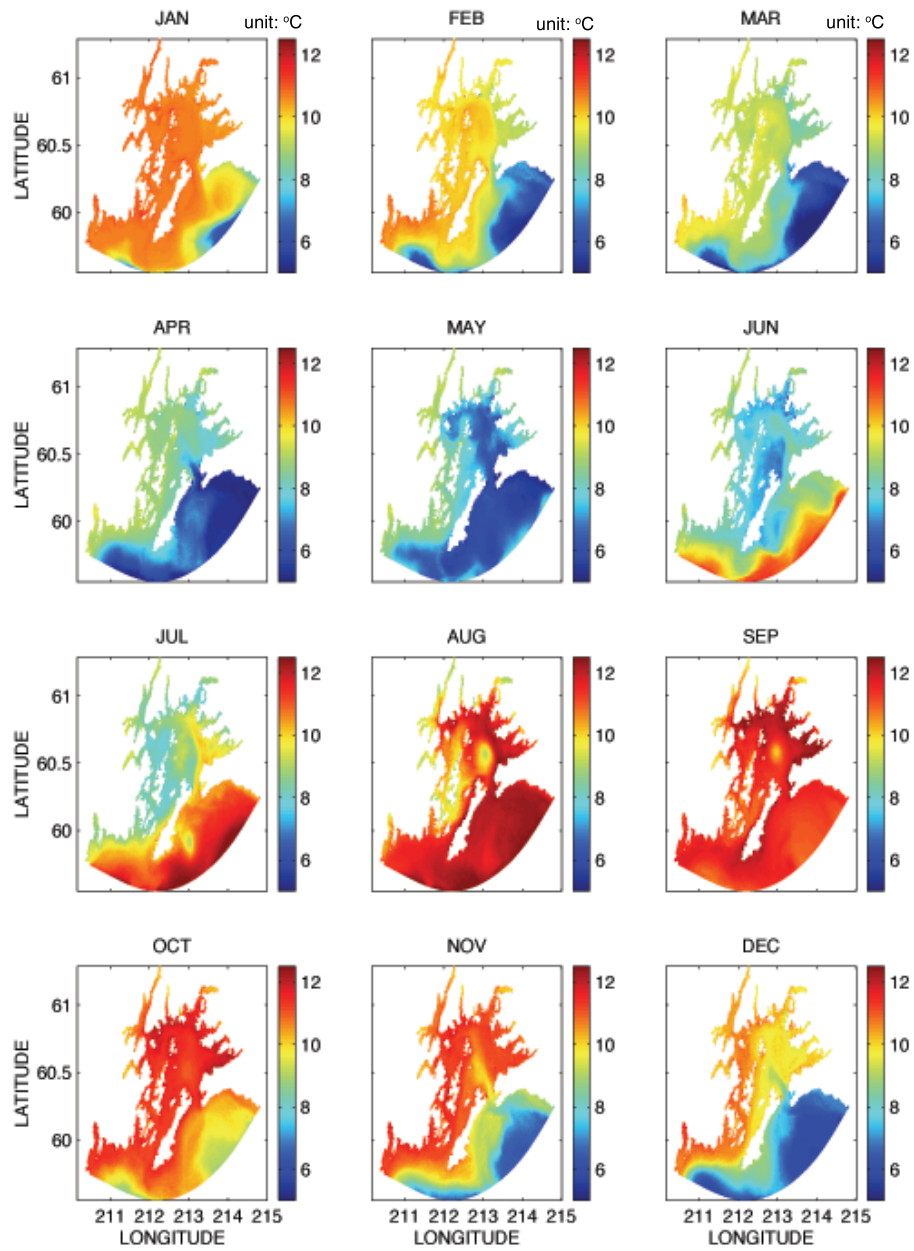


Figure 3.12: EPWS-POM simulated monthly-mean SST

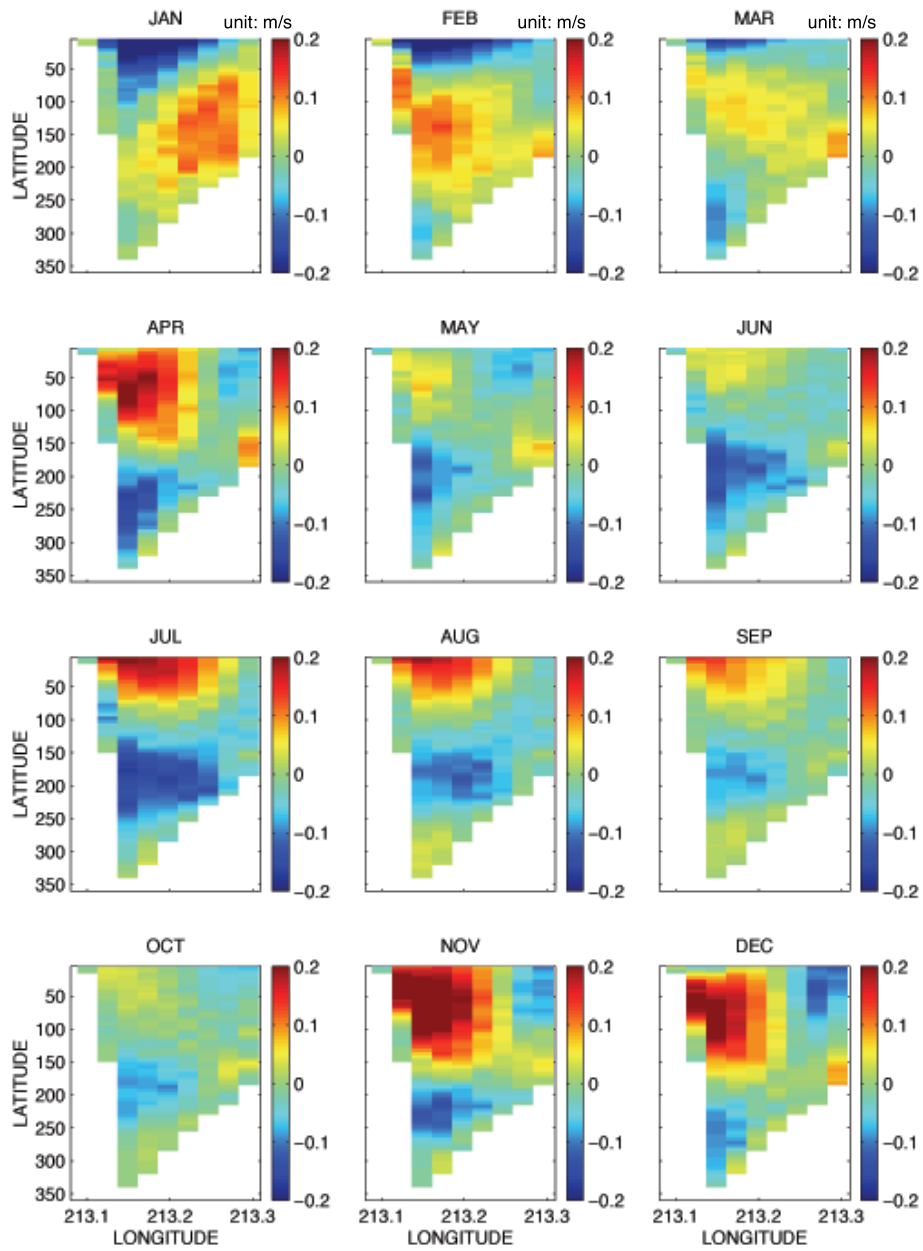


Figure 3.13: EPWS-POM simulated monthly-mean northward velocity transect through HE

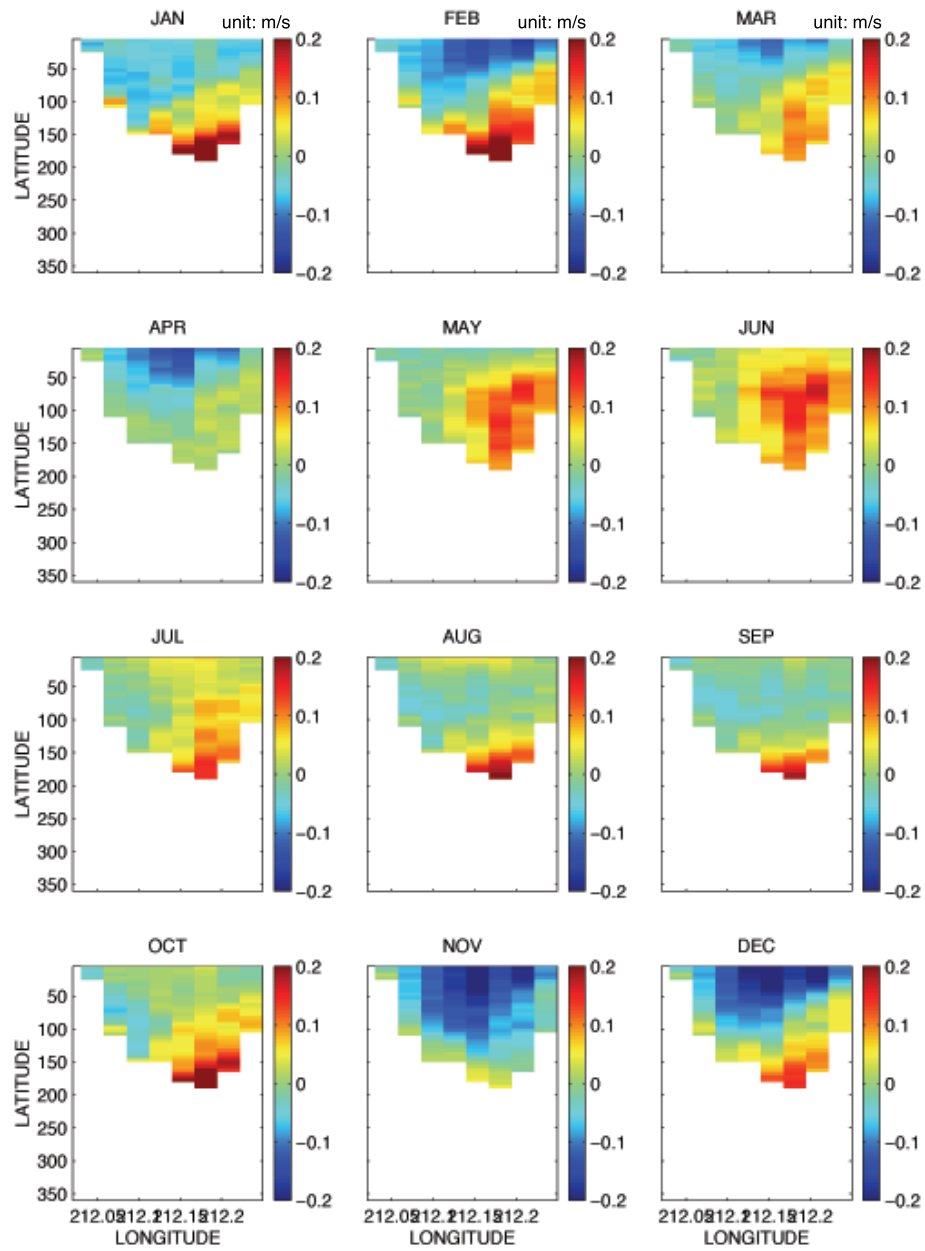


Figure 3.14: EPWS-POM simulated monthly-mean northward velocity transect through MS

relatively weak ($< 0.05m/s$). At HE, two-layer baroclinic flows dominate except in FEB and MAR when the well-defined three-layer flow occurs with inflow in the surface and bottom layers and outflow in the intermediate layer.

Cool ($< 5^\circ$) deep waters below the depth of 300 *m* at BH appear at the beginning of AUG, a few days after surface warm water intrusion into Central Sound in late JUL (Figs. 3.15). Approximately in mid-AUG, the cool water ($< 5^\circ$) also develops below 300 *m* in Central Sound. The surface cool water intrusion during MAY, as the temperature profiles at both 46060 (located in Central Sound) and 46061 (located at the entrance of HE) indicates, is probably related to the development of the deep water at both the BH and Central Sound.

3.3.1 Synoptic LSC Response in PWS-POM

Occurrence of the CG in Central Sound during AUG and SEP in EPWS-POM simulations is one of the most interesting and important dynamical features of the PWS response to synoptic LSC. Numerous observations, including satellite images (Fig. 1.3), Lagrangian field experiments (Cox. 2004), and cruise surveys (Vaughan *et al.*, 2001), have revealed the existence of the cyclonic gyre in Central Sound during these two months with year-to-year variability. No previous studies, however, have been conducted to understand the dynamical mechanism(s) associated with this prominent circulation feature in PWS. On the other hand, the pursuit of better understanding of the CG, along with its role in the seasonal transition of the circulation and stratification, imposes a demand for more exploration within the present numerical experiment.

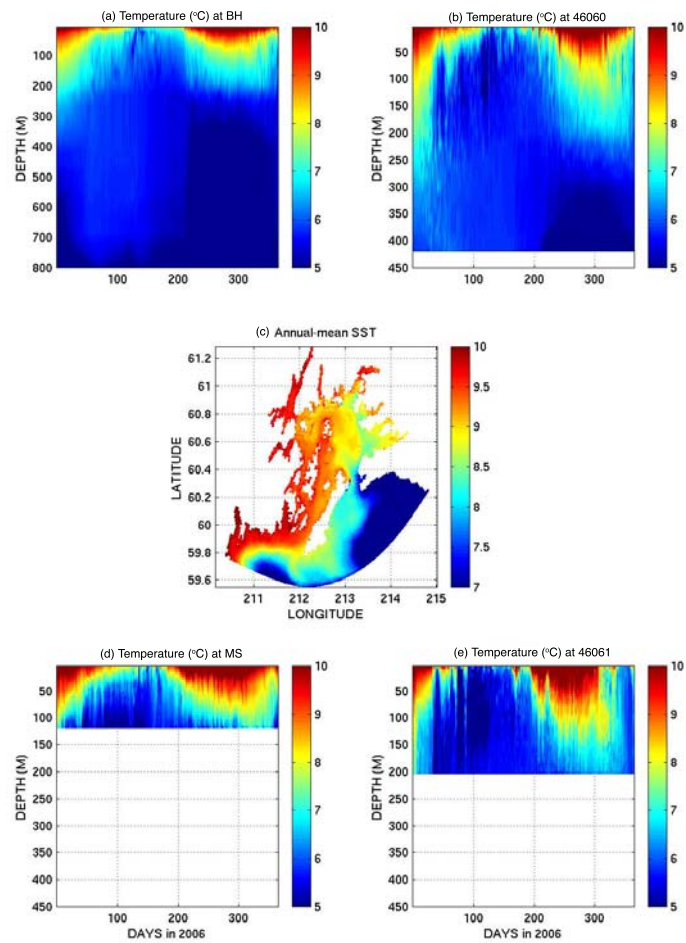


Figure 3.15: EPWS-POM simulated 1-yr time-depth plots of temperature at (a) BH, (b) 46060, (d) MS, and (e) 46061, along with (c) annual-mean SST

Based on EPWS-POM simulations, the radius of the CG is *ca.* 10 *km*, and varies during its evolution (Fig. 3.11). Thus, it may not be favorable to conduct further analysis with EPWS-POM results, primarily due to the limit of EPWS-POM horizontal resolution (*ca.* 1 *km*). Alternatively, the higher-resolution PWS-POM (*ca.* 300 *m* horizontal resolution in Central Sound; Section 1.2) is invoked here, aiming at a simulation with more detailed information about both the mesoscale and sub-mesoscale circulation.

The initial condition for PWS-POM, including both barotropic (depth-averaged velocity and sea level) and baroclinic ($u/v/w/t/s$) variables, is obtained from EPWS-POM results on 30 JUL. The RMEAN variable in EPWS-POM (climatological mean density from the EPWS-POM initial field) is transferred to the same variable in PWS-POM, which is fairly efficient in reducing the numerical errors in PWS-POM, based on several coupling experiments between the two models. The specific date of 30 JUL is selected for PWS-POM initialization in order to follow the CG formation from the very beginning. PWS-POM then runs for 30 days via one-way coupling with EPWS-POM (as in Section 1.3.2).

PWS-POM Performance

As expected, the CG, readily identified as the depressed surface level surrounded by cyclonic currents, is well developed in PWS-POM a few days after the initialization, and centered visually at the same location as in EPWS-POM with very similar size (Fig. 3.16). Surface current speed within the CG agrees well with the EPWS-POM value. On the other hand, PWS-POM differs slightly from EPWS-POM pattern at some other locations inside PWS; for instance, sea level in the northern Sound in PWS-POM is *ca.* 2 to 3 *cm* lower than those in EPWS-POM, while at BH, sea level is *ca.* 2 *cm* higher.

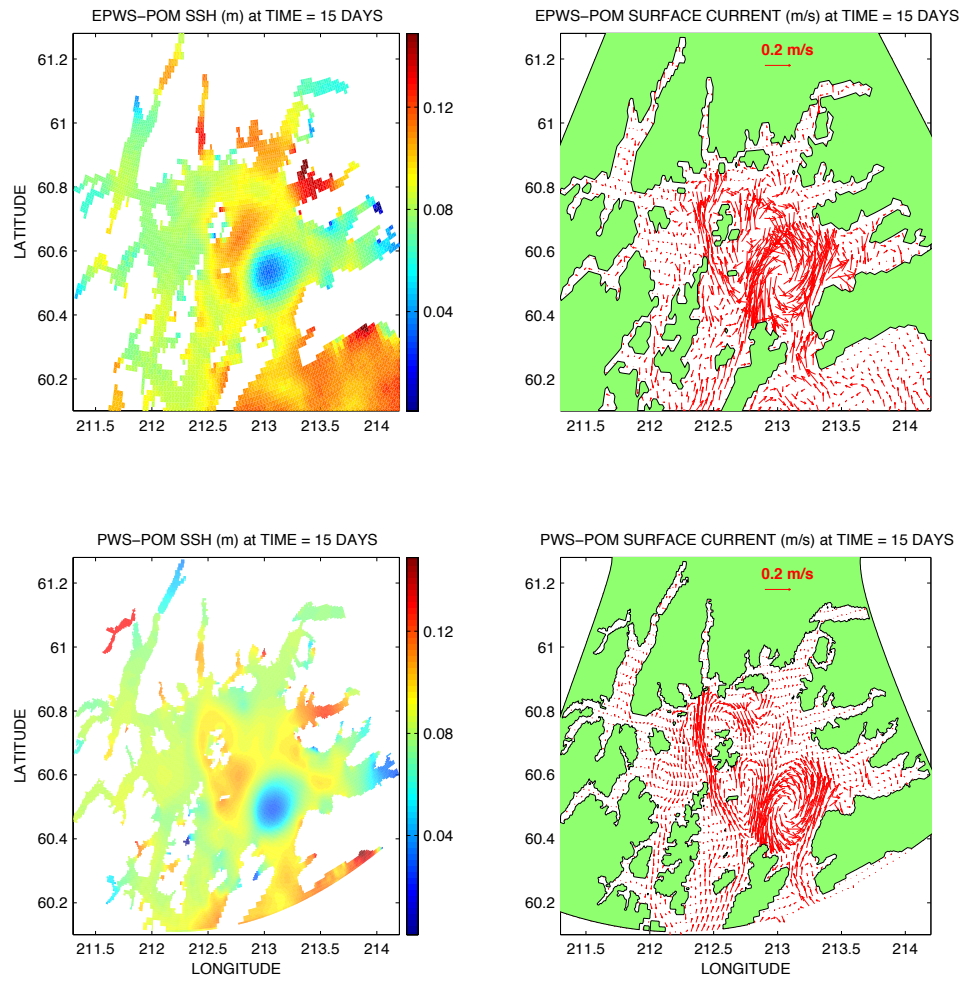


Figure 3.16: PWS-POM simulated SSH and surface current after 15 days, as well as the corresponding EPWS-POM fields at the same time

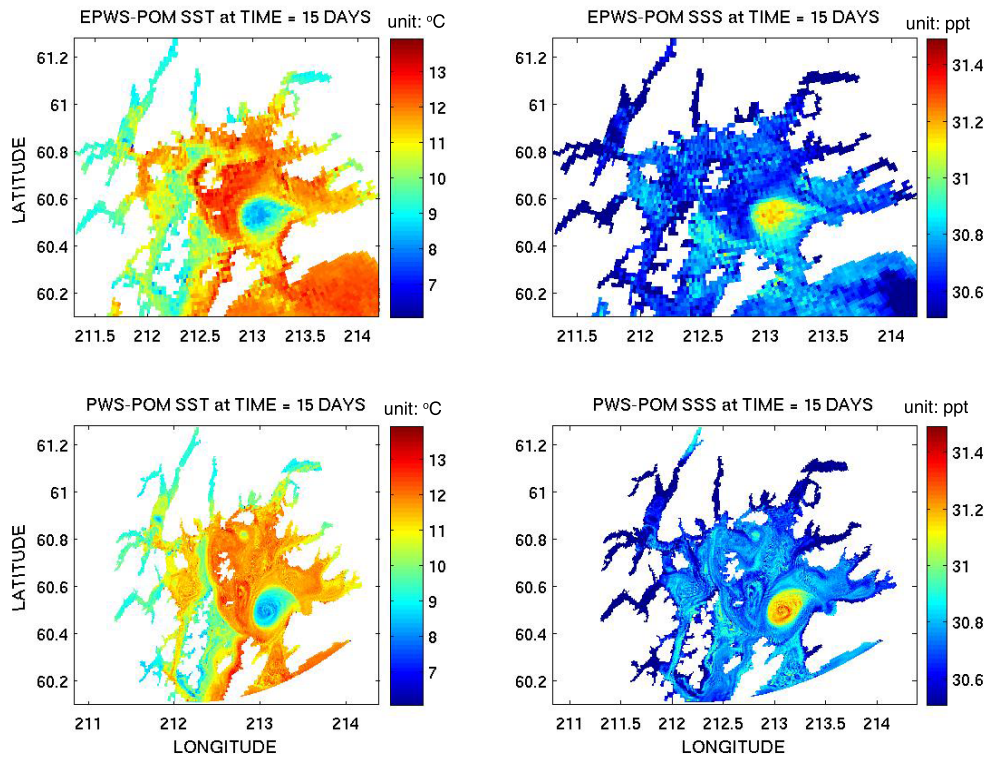


Figure 3.17: PWS-POM simulated SST and SSS after 15 days, as well as the corresponding EPWS-POM fields at the same time

Examination of SST and SSS after 15 days indicates that PWS-POM agrees well with EPWS-POM in regard to the general spatial pattern inside the Sound (Fig. 3.17). Interestingly, PWS-POM introduces much detail not only on the horizontal structure of the CG, but also for sub-mesoscale features at other locations. For instance, a small cyclonic eddy (*ca.* 2 km) exists near the coast of northern Central Sound, and a meridionally-elongated anticyclonic eddy adjacent to and located northwest of the CG, consisting of a horizontal dipolar eddy structure (Voropayev *et al.*, 2001), is also present. These mesoscale or sub-mesoscale features are not so clearly defined in EPWS-POM, apparently due to the limitation of grid resolution. Previous observational studies (Vaughan *et al.*, 2001) have also suggested the richness of sub-mesoscale eddies in PWS.

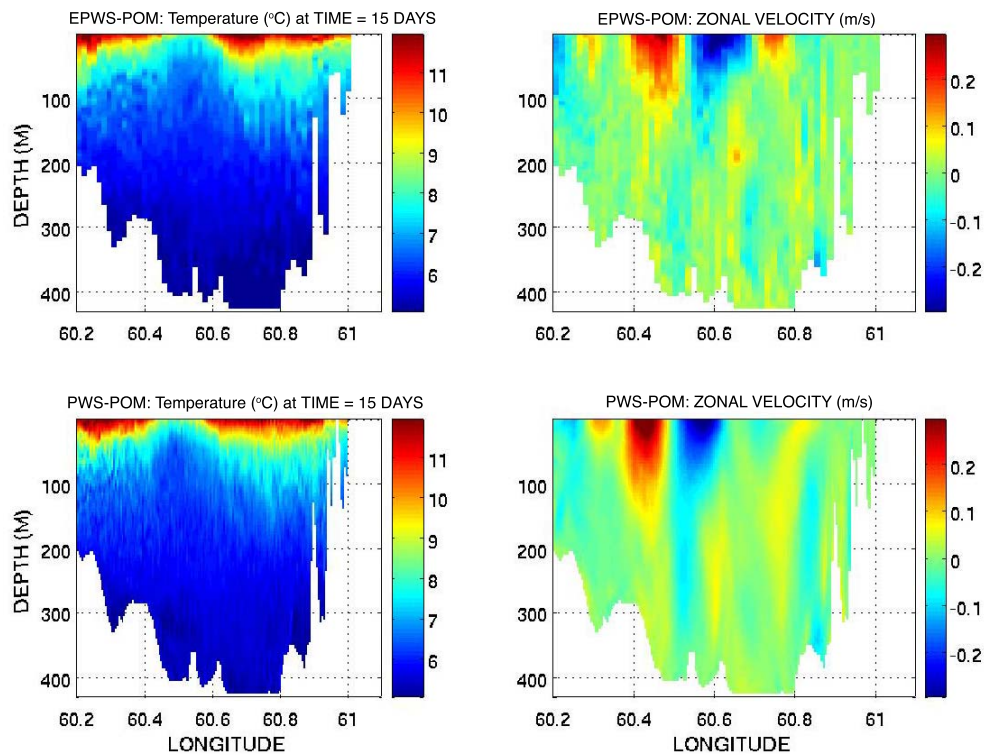


Figure 3.18: PWS-POM simulated temperature and normal velocity section in Central Sound after 15 days, as well as the corresponding EPWS-POM field during the same time

The CG is characterized by the surface doming of deep isopycnals in the center where the cool water (*ca.* 8°C) is displaced vertically more than 50 *m* to intersect the surface, as both EPWS-POM and PWS-POM indicate, with a meridional 2-D section across the center of HE extending to the coastline of northern PWS (Fig. 3.18). Examination of zonal velocities across this 2-D section indicates that the effect of the CG reaches at least as deep as 150 *m*, and probably to the bottom in PWS-POM (Fig. 3.18). Also, EPWS-POM significantly overestimates (*ca.* 0.2 m/s) a surface eastward flow in PWS-POM near 60.8N; since there are no observed current data readily available for validation, it is suggested that the difference is mainly attributed to the better representation of bottom topography and the coastline in PWS-POM.

Cyclonic Gyre in PWS-POM

Employing the high-resolution PWS-POM simulations, identification of the CG evolution in AUG with such properties as its location, size, and strength is readily conducted (Fig. 3.19). For oceanic gyres and eddies, sea level distribution is probably the most effective way to distinguish these mesoscale features from the general circulation pattern (Fig. 3.16). Other surface indicators, using characteristic currents and water temperature or salinity, can also detect their occurrence. To quantitatively locate the center of an oceanic gyre or eddy, these other variables normally yield non-unique results that require further interpretation. Therefore, the center of the CG is determined from the SSH pattern in Central Sound, where the location of the lowest sea level is selected as the CG center. As the subsequent calculation indicates, this method yields a unique value for the center of the CG during the entire simulation period. The thus-determined gyre center agrees well with the surface current pattern (Fig. 3.19). During AUG, the CG center moves along three well-defined circular paths with a general southeastward heading (Fig. 3.20). In the first few days of AUG (when the CG starts to develop and its center is not well defined from the SSH pattern), the CG center does not follow the circular paths. At the end of AUG, the CG returns to its original position.

The outer bound of the gyre is determined from the surface vorticity, based on the fact that within a cyclonic gyre the vorticity should always be positive. The simulated CG seems to closely follow this rule-of-thumb: associated with SST, the positive-vorticity area surrounding the SSH-determined gyre center represents well the position and extent of the CG (Figs. 3.19 and 3.21). On the other hand, due to the geometric constraints of both the bottom topography and the coast, as well as interactions with other mesoscale eddies,

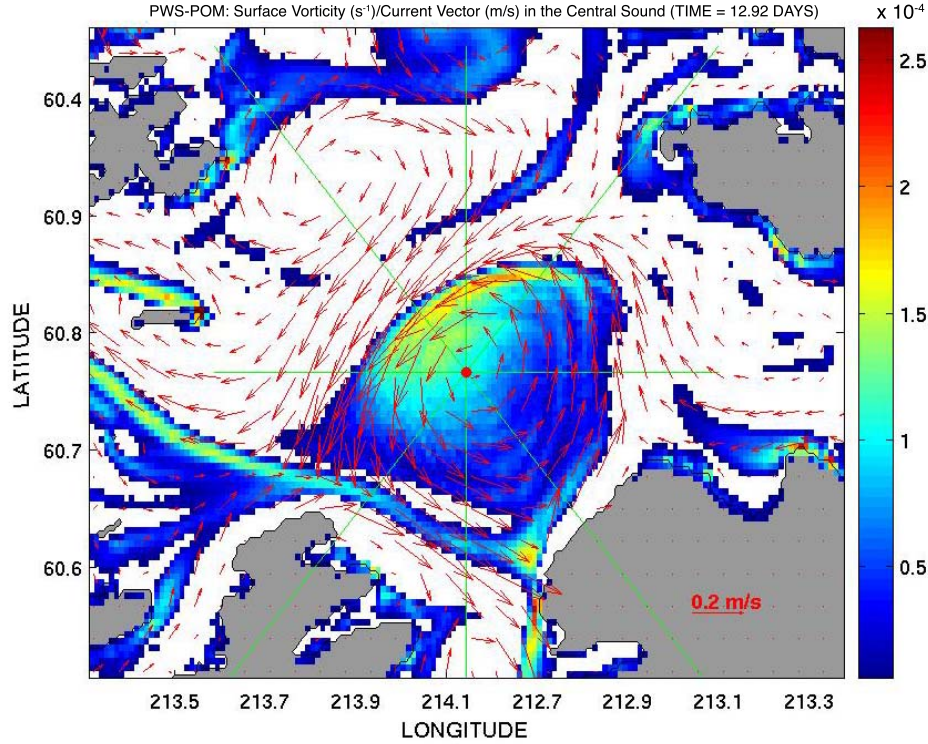


Figure 3.19: PWS-POM simulated surface current and vorticity in Central Sound. The example is randomly selected from PWS-POM simulations. The red dot marks the center of the CG. Notice that locations with negative vorticity have not been visualized for clarity.

the CG has an ellipse-like shape instead of a true circle. Consequently, the outer bound of the CG is quantitatively estimated as the interface between positive and negative surface vorticity along four different directions (green lines in Fig. 3.19), from which the semi-major and semi-minor axes of the CG are selected. The lengths of semi-major (a) and semi-minor axes (b) are calculated based on the distance between the CG center and the outer bound. These values are then used to obtain the surface area (πab) and eccentricity ($\epsilon = \sqrt{1 - \frac{b^2}{a^2}}$) of the ellipse-like CG.

In AUG, the CG covers a surface area ranging from *ca.* 250 to 550 km^2 , or can be conveniently defined as an equivalent radius of *ca.* 9 to 13 km based on the circle with the same area as estimated from the ellipse (Fig. 3.21). Considering potential errors in

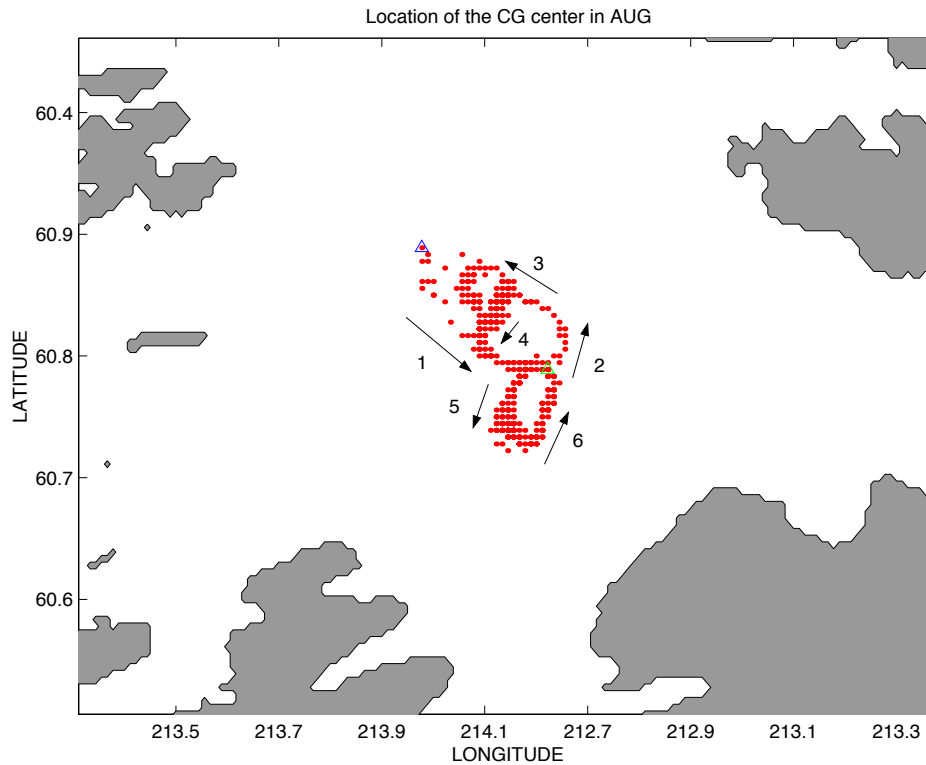


Figure 3.20: PWS-POM determined CG center and its path in AUG. Blue and green triangle marks indicate the initial and final positions of the CG center, respectively, and arrows are numbered to follow the movement of the CG center.

the estimate, the fairly consistent distribution of the CG radius between 9 and 13 *km* (about 80% of all CG surface area estimates; Fig. 3.22) suggests that surface vorticity is an efficient index to define the area of CG in the numerical simulations. The CG is significantly elongated from the shape of a circle during most of AUG (Fig. 3.22), since continuous estimates of the eccentricity indicate that the near-circular shape of CG (the eccentricity smaller than 0.2) occurs less than 20% of the time in AUG.

EPWS-POM and PWS-POM simulations lead to the speculation that the CG formation is connected with the surface inflow of warm water through HE. For instance, comparison between the CG movement and surface inflow at HE indicates that the general behavior of the CG meridional movement is sensitive to variations of inflow magnitude; e.g., the

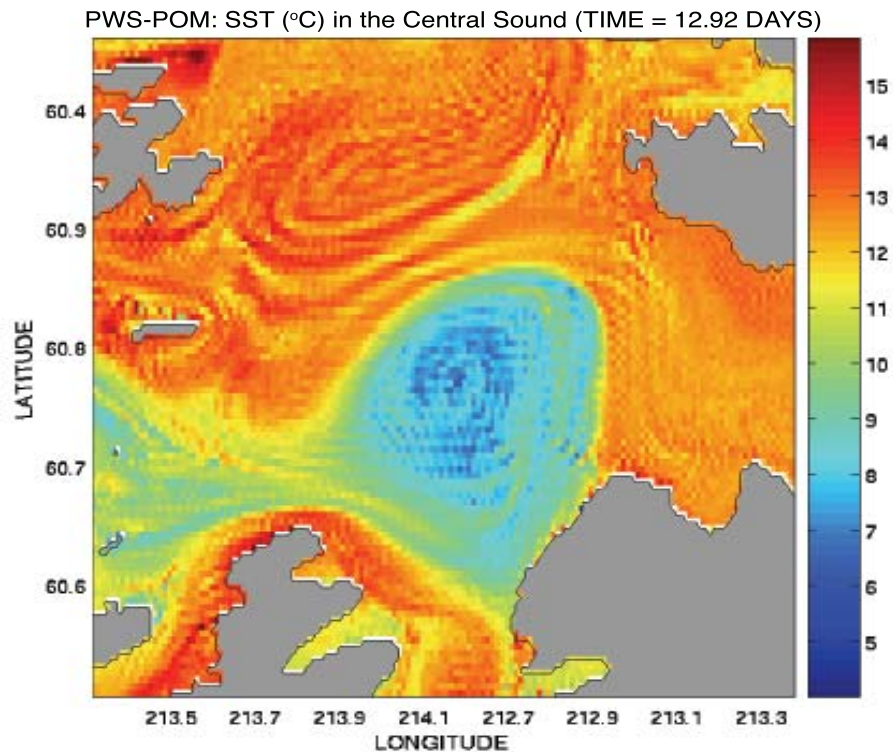


Figure 3.21: PWS-POM simulated SST at the same time as the surface current shown in Fig. 3.19

decrease of surface inflow velocity at HE in the beginning and between DAY 6 and 12 is followed by the southward movement of the CG with a lag of *ca.* 2 to 3 days, and similarly, northward movement of the CG occurs after the increase of HE inflow velocity between DAY 2 and DAY 4 and after DAY 13 (Fig. 3.23). The lagged response between the CG meridional movement and HE inflow variation is of particular interest since it clearly indicates the dependence of the former on the latter but not vice versa. In contrast, no significant dependence of the CG zonal movement on HE surface inflow is indicated.

The relations between the CG properties; e.g, coverage area, eccentricity, and maximum surface current speed, and the HE surface flow properties, i.e., northward velocity and temperature. Both the CG and HE flow variables are normalized by their standard deviations to facilitate the comparison. Except between DAY 12 and DAY 15, HE surface temperature

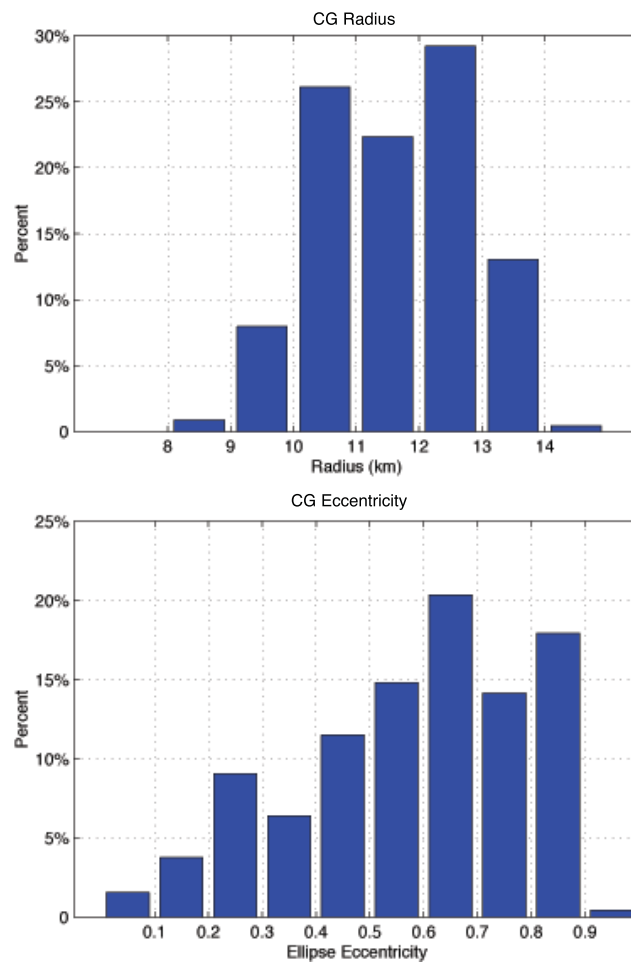


Figure 3.22: Histogram of PWS-POM simulated CG radius and eccentricity in AUG

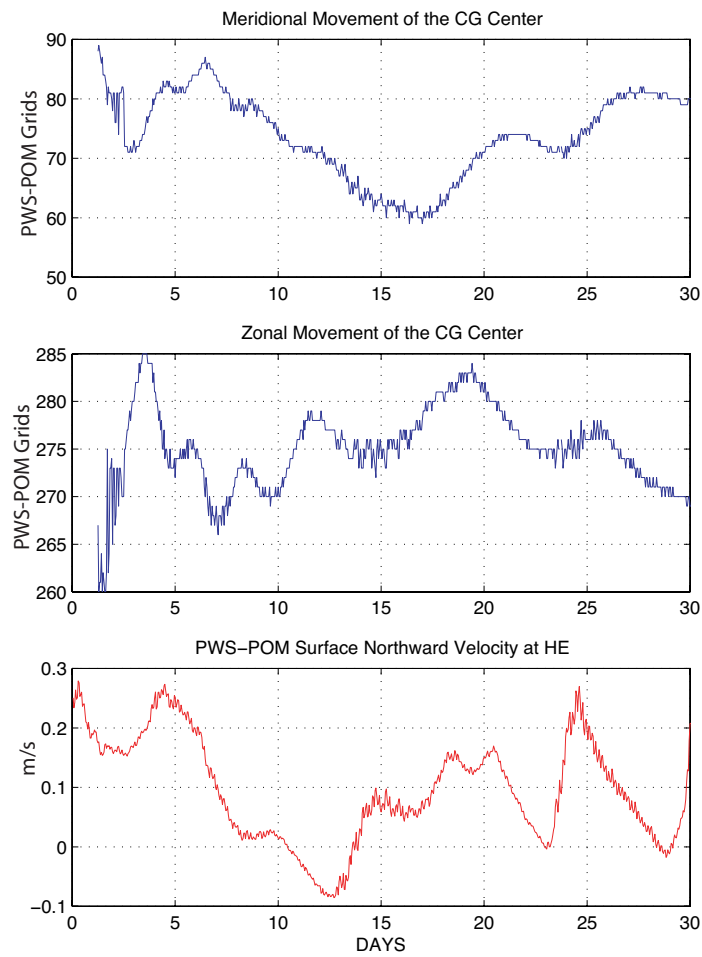


Figure 3.23: Comparison of the CG meridional and zonal movement with HE surface inflow velocity

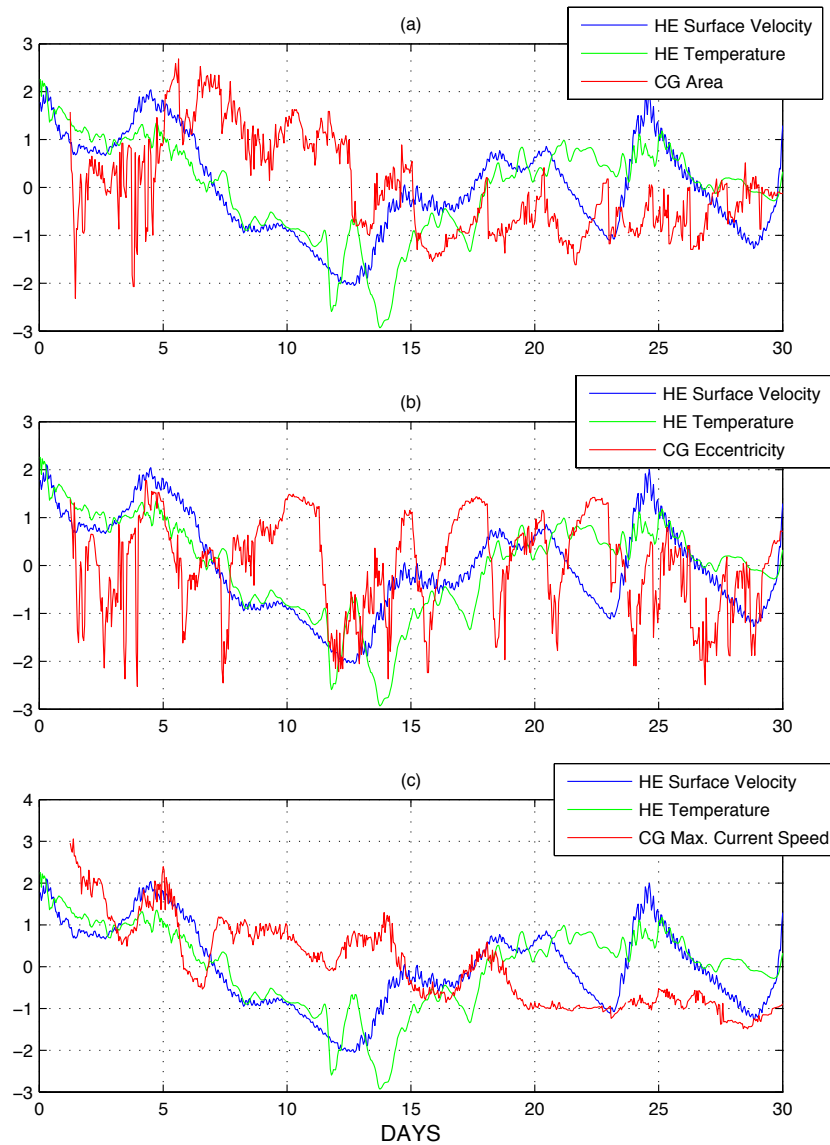


Figure 3.24: Comparison of CG (a) coverage area, (b) eccentricity, and (c) max. current speed with HE surface inflow and temperature

variations closely resemble surface northward velocity variations (Fig. 3.24). Similar to the CG meridional movement, the general behavior of variations on the CG area and maximum current speed is directly related to HE surface flow variations with normally less than 1-day lag, although the variability at shorter periods is significantly different.

3.4 Summary and Discussion

Both EPWS-POM and PWS-POM are used to study the PWS response to the LSC prevailing in NGOA with the latter model especially focused on the synoptic LSC response. Annual-mean or synoptic LSC variability is transferred to EPWS-POM via one-way coupling from the Global-NCOM field, and then, transferred to PWS-POM in a one-month simulation study.

After the initial adjustment period of *ca.* 50 days, the annual-mean LSC response of PWS is characterized by a well-established equilibrium state: the cross-shelf SSH gradient is geostrophically balanced by the cyclonically-flowing ACC, PWS circulation is a weak (*ca.* 0.02 Sv) through-flow pattern with HE inflow and MS outflow. A layered baroclinic flow structure is developed at both HE and MS with the time-independent OBCs.

In comparisons, as probably the most important external forcing for PWS circulation, synoptic LSC produces temporal variability of barotropic transports, and two-layer/three-layer baroclinic transport at HE and MS, as in EPWS/NFS. The “transition band” in the coherence pattern between HE and MS transport is found within the period band of *ca.* 5 to 30 hrs. As one of the most interesting and dynamically important features of the synoptic LSC response, a cyclonic gyre occurs during AUG and SEP in Central Sound. As is to be expected, this cyclonic gyre is characterized by cool water trapped in the center and upward doming of deep isopycnals. The development of the cyclonic gyre is associated with the surface inflow of warm water at HE. Additional investigations of detailed properties of this cyclonic gyre were conducted using PWS-POM, The results indicate that the cyclonic gyre can be most appropriately depicted as a ellipse with has an equivalent radius of *ca.* 10 km. The cyclonic gyre continuously evolves with time by varying its shape, size, location,

and maximum current speed. The gyre moves along three inter-connected closed circles in AUG with a general trend of southeastward movement. The meridional movement of the gyre responds to the HE surface flow velocity with a 2 to 3 day lag. Unlike the shape, general variations of the size and maximum current speed of the gyre closely follow HE surface flow variations.

Based on the similarity of the SST and surface circulation patterns in Central Sound between APR and NOV, as well as the baroclinic structures at HE and MS, the PWS upper layer response to synoptic LSC demonstrates two distinct patterns: the summertime circulation during MAY to OCT, and the wintertime circulation during NOV to APR. Below the depth of 300 *m*, the cool deep water appears at BH in late summer apparently a few days delayed from the arrival of surface warm water, and later (*ca.* 10 days), the cool deep water appears in the Central Sound.

Chapter 4

Response of PWS to Surface Atmospheric Forcing

The straits connecting a semi-enclosed sea with the open coastal ocean influence how the semi-enclosed sea responds to external forcing, including the surface atmospheric forcing. Consequently, some unique phenomena are thus introduced. Their properties and effects on the circulation inside PWS are studied in the present chapter.

4.1 Introduction

The well-known Inverse Barometer (IB) response of sea level to atmospheric pressure (AP) is often not realized in coastal ocean, due to dynamical effects of the shallow water depth and the coastline, which alter the simple relationship of 1 *cm* sea level decrease/increase corresponding to 1 *mbar* increase/decrease in the atmospheric pressure (Wunsch and Stammer, 1997). Density stratification also affects this simple relationship. The understanding of sea level fluctuations is crucial for accurate forecasts of sea surface height, proper corrections to satellite altimetry, and correctly distinguishing the different dynamical components in total sea level variations, for instance, those due to wind-driven and geostrophic flows and coastally trapped waves.

Atmospheric pressure fluctuations vary with position, time, frequency, and horizontal wavenumber. Consequently, a wide-range of physical phenomena are involved when studies of the ocean's response to AP are conducted (Gill, 1982). On a global scale, there is no oceanic response to the spatial mean over-ocean AP loading as a result of the high modulus of elasticity of water. In semi-enclosed seas, the spatially-varying AP may no longer account for the total AP loading forcing, and the basin-wide spatial-mean, time-dependent AP, as well as AP difference inside and outside the semi-enclosed seas, can produce observable effects due to the water exchange with the open ocean. One resulting phenomenon, which can be excited by other forcings as well, is the oceanic Helmholtz resonance owing to the oscillation of a water mass in the semi-enclosed basin. This geometry-dependent resonance in semi-enclosed seas is often energetic in non-tidal sea level fluctuations, and can be directly compared with classical Helmholtz resonators, like some small whistles and the ocarina.

The basic dynamical ideas are illustrated by the Candela model (Candela, 1991), a simple while illuminating 1-D, time-dependent barotropic model, which has been used to analyze how the mean sea level in a semi-enclosed sea responds to basin-wide uniform AP loading. This model has been utilized for the Mediterranean Sea (Candela, 1991), Black Sea (Ducet *et al.*, 1999), Red Sea (Sofianos, 2000) and Japan/East Sea (Lyu *et al.*, 2002). In the Red Sea application, this model was extended to include the local wind stress forcing and a two-layer response. From the Candela model, the resonant period of the system can be determined, which is described as a "Helmholtz-like" resonance, based on the similarity of its mathematical expression to that of the well-known Helmholtz resonators in musical acoustics. For the Mediterranean Sea, tidal energy and weather-band AP were considered as the possible energy sources for two resonant periods of 1.2 days and 5.6 days, corresponding

to the resonance of the entire basin through Gibraltar Strait, and that of the western and eastern basins through the Sicily Strait, respectively.

4.2 Observed and EPWS/NFS Simulated Response

The oceanic response to AP loading in a semi-enclosed sea is mainly focused on basin-wide averaged sea level fluctuations and barotropic/baroclinic transports through the strait(s) (Lyu and Kim, 2005). In the following studies, local AP is normally referred to the observation at NDBC buoy 46060 in Central Sound, while AP difference is obtained between inside and outside the Sound, represented by observations at NDBC buoys 46060 and 46061, respectively. These two buoys are separated by *ca.* 50 km. The power spectrum, along with the corresponding spectrogram, for the 10-year local AP over PWS (Fig. 4.1) reveals that although most of the energy is contained in the low-frequency band (*i.e.*, periods longer than 50 hrs), there are two prominent energetic peaks at periods of 8 and 12 hrs in the high-frequency band, representing mesoscale atmospheric variability and the well-known semi-diurnal atmospheric tide, respectively. For the AP difference, no energetic peaks occur at these two periods (Fig. 4.1).

Both the observed and EPWS/NFS simulated CSL power spectra (Fig. 1.12) suggest the possible presence of a barotropic Helmholtz resonance (referred as HR thereafter; Mooers *et al.*, 2007) peak near 6 hrs (another possibility is a shallow water tidal harmonic). Further investigation of the 10-year observed CSL response at Cordova to local AP (Fig. 4.2) indicates that the maximum gain magnitude occurs at two periods, 6 and 12 hrs. Associated with power spectra of local AP (Fig. 4.1), the 12-hr peak in the gain magnitude thus corresponds to a forced CSL response to the semi-diurnal atmospheric tide, and the 6-hr

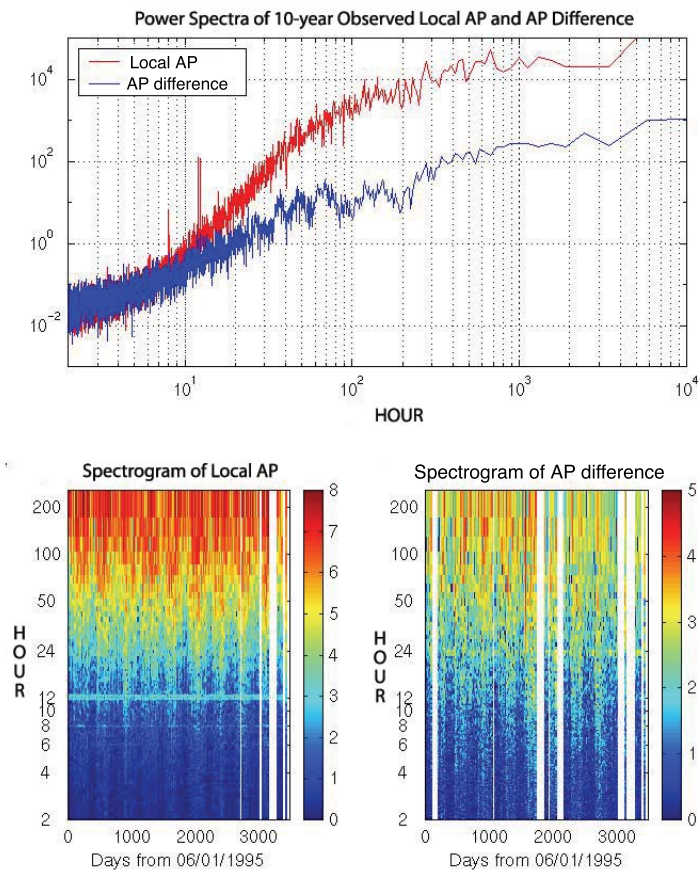


Figure 4.1: Power spectra, along with spectrograms, of 10-year observed local AP and AP difference over PWS. The spectrograms are obtained via a 512-point FFT window with a total of 328 degrees-of-freedom.

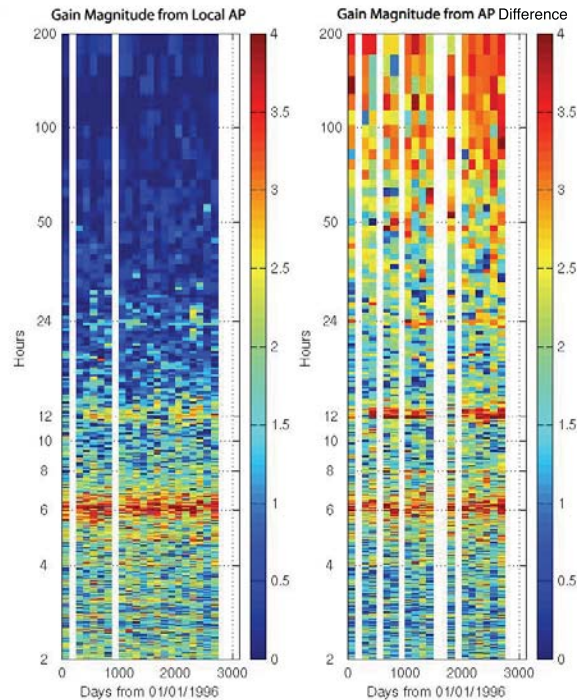


Figure 4.2: Spectrograms of 10-year observed CSL gain magnitude in Cordova to local AP (left) and AP difference (right)

peak is apparently the AP-excited HR response in PWS. Because the observed CSL gain has greater magnitude from local AP at a period of 6 hrs than that at a period of 12 hrs (Fig. 4.2), the CSL response at a period of 6 hrs reflects the resonant (Helmholtz resonance) response in PWS.

Due to the free surface in PWS, a basin-wide mean sea level response in PWS to AP can also be examined via the response of volume transports through the two straits, which is conveniently obtained from EPWS/NFS simulations (Section 1.3.6). The result indicates that HE and MS volume transports respond similarly to AP difference in gain magnitude (Fig. 4.3): their maximum gain occurs at periods of *ca.* 6 and 12 hr with similar peaks. For the net volume transport, the maximum gain in the response function occurs at the same periods, i.e., *ca.* 6 and 12 hr, with nearly the same order of magnitude. Associated

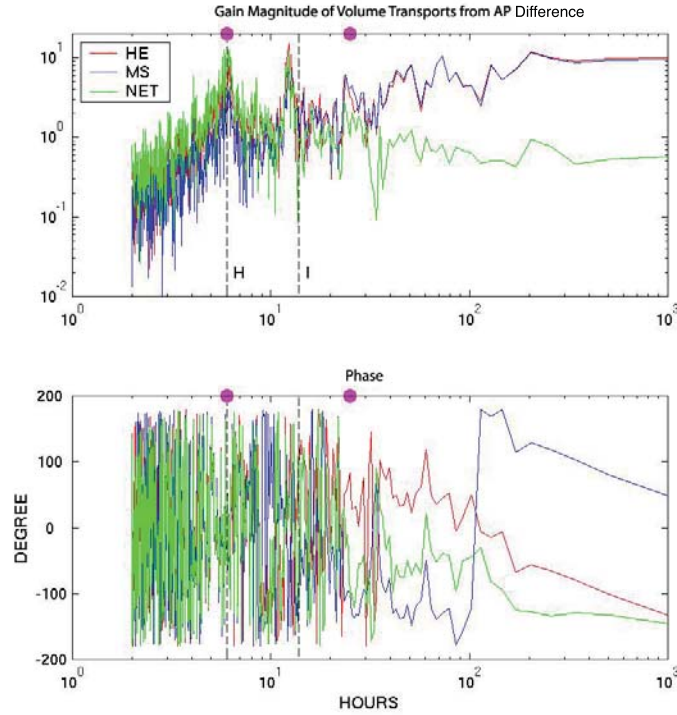


Figure 4.3: Gain magnitude and phase (DOF=10) of EPWS/NFS simulated volume transports to AP difference: HE (red), MS (blue), and net (sum of HE and MS transports; green). KEY: H, barotropic Helmholtz resonance period for IPWS (*ca.* 2.5 hrs); I, inertial period (13.8 hrs). Magenta dots indicate the location of transition band in coherence pattern between EPWS/NFS simulated HE and MS volume transports (Fig. 1.25).

with the barotropic HR period for PWS and the power spectra of the AP difference, these two peaks correspond to the periods of the HR (*ca.* 6 hr) and the semi-diurnal atmospheric tide (12 hr), respectively.

For periods longer than 30 *hr*, the gain magnitude curves of HE and MS transports are nearly identical, while the net volume transport gain is approximately constant but much weaker by over one order of magnitude. Based on the gain phase, the HE and MS volume transports are nearly 180° out-of-phase for periods longer than 30 *hr*. This result is consistent with the coherence and phase between HE and MS volume transports (Section 1.3.6).

Therefore, it is motivated to address the following questions “what is the physical significance of the 6-hr period in CSL and volume transport gain functions from AP?”, “what is the nature of the related ‘transition band’ between HE and MS volume transports (Section 1.3.6)?” “Is the two- or three-layer flow structure at HE and MS related to the transition band?”. Since the 6-hr period corresponds to the HR in PWS, the investigation starts with the basic physical principles governing the barotropic HR.

4.3 Barotropic Helmholtz Resonance

The theoretical background is introduced in this section, aiming at the physical interpretation of the simulated phenomena and establishing an analytical model for the general response of a semi-enclosed sea to AP.

4.3.1 Helmholtz Resonance in Musical Acoustics

“A Helmholtz resonator or Helmholtz oscillator is a container of air with an open hole (or neck or port). A volume of air in and near the open hole vibrates because of the springiness of the air inside.”³⁶ Examples of typical Helmholtz resonators include some small whistles, the air in the body of a guitar, and the ocarina. In these examples, the wavelength of the sound produced is much longer than the dimensions of the resonator, and thus, the relative pressure variations inside the volume of the resonator are neglected. For an idealized Helmholtz resonator (Fig. 4.4), if the air in the neck moves a small distance x into the bottle due to the initial disturbance, the air inside the bottle is compressed accordingly so that its volume that was previously V now becomes $V - Sx$. Consequently,

³⁶Source: <http://www.phys.unsw.edu.au/~jw/Helmholtz.html>

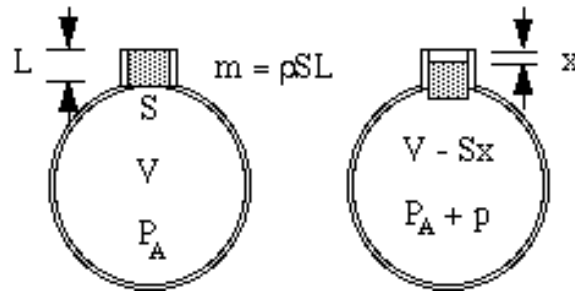
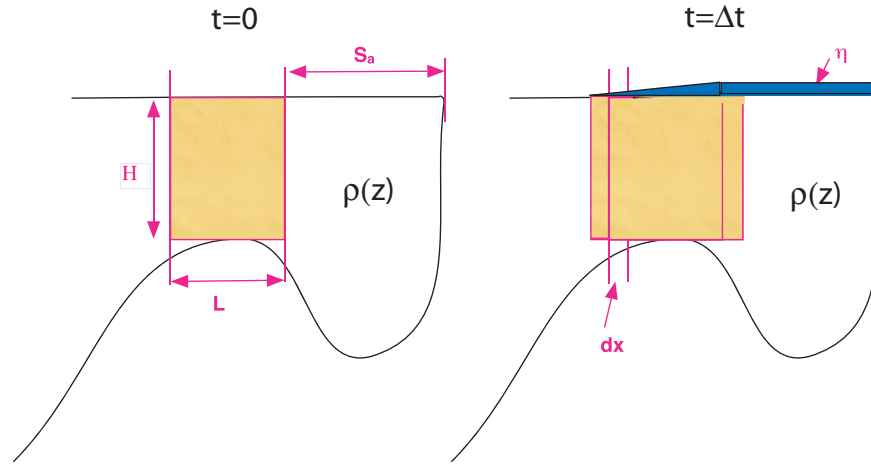


Figure 4.4: Schematic of a simple Helmholtz resonator (courtesy of <http://www.phys.unsw.edu.au/jw/Helmholtz.html>)

the pressure in the bottle increases from P_A to a higher value $P_A + p$. The increased pressure must force the air in the neck moving backward, and associated with the inertial of the air, the vibration motion develops and gives rise to sound. Quantitatively, if the neck has an effective length L and cross-sectional area S , the frequency of the HR is given as $f = \frac{c}{2\pi} \sqrt{\frac{S}{VL}}$ (Helmholtz, 1912), where c is the speed of sound in air.

4.3.2 Barotropic Helmholtz Resonance in Semi-enclosed Seas

Consider that the water in the strait moves into the semi-enclosed sea due to, for instance, a sudden increase of the offshore atmospheric pressure, and then, the mean surface level inside the semi-enclosed sea must rise a corresponding amount to conserve the total water volume inside, since the ocean water can be treated as incompressible. The increased surface level now must force the water in the strait out of the semi-enclosed sea, but, when it reaches its original position, its momentum carries it further outward. Therefore, in an idealized undamped situation, the water in the strait can oscillate back and forth, exactly as the air in the neck of a Helmholtz resonator does. The difference is that here, gravitational force of the fluctuating surface level inside the semi-enclosed sea, rather than the compressed air in the container, provides the restoring force when the resonance occurs (Fig. 4.5).



A simple oceanic Helmholtz resonator

Figure 4.5: Schematic of simple oceanic Helmholtz resonator in a semi-enclosed sea

The above analysis implicitly suggests that the HR normally occurs when its period is much longer than the corresponding periods of barotropic basin (seiche) modes, and is controlled by the geometry of the semi-enclosed sea, including the strait(s) connecting them to the open ocean (Candela, 1991; Lyu, *et al.*, 2002; Lyu and Kim, 2005). The oceanic HR thus relates the spatially mean sea level perturbation inside the semi-enclosed sea, as a response to surface pressure, wind or tidal forcing, with the transport through the strait(s).

Considering a semi-enclosed sea with a surface area of S , and with one strait connecting to the open ocean, the barotropic HR frequency, ω , is

$$\omega = \sqrt{\frac{gA}{SL}}, \quad (4.1)$$

(Candela, 1991) where g is the gravitational acceleration, A and L are the cross-sectional area and effective length of the strait (Note: ω is independent of the depth of the semi-enclosed sea and the Coriolis parameter). Similarly, for a semi-enclosed sea with n straits,

(Eq. 4.1) can be readily generalized (Lyu and Kim, 2005) as

$$\omega = \sqrt{\frac{g}{S} \sum_n \frac{A_n}{L_n}}, \quad (4.2)$$

where A_n and L_n are the cross-sectional area and effective length of the n th strait, respectively. For the real ocean, the effective length of the strait in the calculation of the HR period is longer than the geometric length (about twice for PWS), due to the open end effect that similarly occurs in the HR that arises in musical acoustics. The open end effect in the real ocean takes place when the external water body near both ends of the strait moves together with the water body inside the strait, which effectively extends the geometric length in the HR mechanics. In PWS, the period of the barotropic HR is *ca.* 6 hr based on observations (Fig. 4.2), simulation (Fig. 4.3), and theory (Eq. 4.2) with the correction of open end effect, as the values in Table 4.1 are applied. The period of the first barotropic (seiche) normal mode is *ca.* 1.4 hr, which justifies, *post hoc*, the requirement imposed in the calculation of the HR period.

The volume transport (Q) through the strait(s) is also constrained by the bottom friction ($\lambda_f Q$) and the geostrophic control ($\lambda_g Q$) (Toulany and Garrett, 1984). An estimate of the friction coefficients ($\lambda_f = \frac{C_0 U}{H}$, where C_0 is the drag coefficient, 2.5×10^{-3} ; U the characteristic along-strait mean flow speed, 0.1 m/s; H the depth of the strait, as in Table 4.1) for HE and MS yields the values of $1.25 \times 10^{-6} s^{-1}$ and $2.5 \times 10^{-6} s^{-1}$ (Table 4.2), respectively. Correspondingly, an estimate of the coefficient for geostrophic control ($\lambda_g = \frac{fW}{2L}$, where f is the Coriolis parameter, $1.3 \times 10^{-4} s^{-1}$; W the cross-sectional width of the strait, as in Table 4.1) yields the values of 3.6×10^{-5} and 4.3×10^{-5} (Table 4.2) for HE and

Table 4.1: Characteristics of the geometric values at HE, MS and PWS

Parameters	Description	Values
S	Surface Area of PWS	$1.0 \times 10^{10} m^2$
W_1	Width of HE	$1.0 \times 10^4 m$
H_1	Depth of HE	$200 m$
A_1	Cross-sectional area of HE	$2.0 \times 10^6 m$
L_1	Along-strait length of HE	$1.8 \times 10^4 m$
W_2	Width of MS	$2.0 \times 10^4 m$
H_2	Depth of MS	$100 m$
A_2	Cross-sectional area of MS	$2.0 \times 10^6 m$
L_2	Along-strait length of MS	$3.0 \times 10^4 m$
f	Coriolis parameter	$1.3 \times 10^{-4} s^{-1}$
C_D	Bottom drag coefficient	2.5×10^{-3}
U_0	Characteristic along-strait current speed	$0.1 m/s$ for HE and MS
ω^*	HR period without end effect correction	$4.2 hr$
ω	HR period with end effect correction	$5.8 hr$

Table 4.2: Estimated Friction (λ_f) and Geostrophic Control (λ_g) Coefficients at HE, MS*

	$\lambda_f (s^{-1})$	$\lambda_g (s^{-1})$	$\frac{\lambda_g}{\lambda_f}$
HE	1.25×10^{-6}	3.6×10^{-5}	29
MS	2.5×10^{-6}	4.3×10^{-5}	17

*: the friction coefficient is $\lambda_f = \frac{C_D U_0}{H}$, and the geostrophic control coefficient is $\lambda_g = \frac{fW}{2L}$, where C_D, U_0, H, f, W , and L are estimated as in Table 4.1.

MS, respectively. Thus, for both straits, geostrophic control is over one order of magnitude more significant than bottom friction, and has a characteristic period of about 2 days. Associated with the barotropic HR period (*ca.* 6 hrs) for PWS, the constraints of bottom friction and geostrophic control on the volume transport are probably not important.

4.3.3 Mean Sea Level Response of A Barotropic Semi-enclosed Sea

The application of barotropic Helmholtz resonance with respect to the presence of bottom friction leads to an applicable dynamical model to describe how the sea level of a barotropic semi-enclosed sea responds to AP. As (Eq. 4.2) indicates, the inclusion of multiple-straits ($n > 1$) for a semi-enclosed sea simply decreases the period of HR but does not change the basic physics. For simplicity, the following analysis is conducted with one strait considered, but the final conclusion is readily applicable to a multi-strait semi-enclosed sea.

Governing Equations

List of Parameters

t – time;

z – vertical coordinate;

x – along-strait coordinate;

g – gravitational acceleration;

Q – volume transport through the strait;

S – surface area of the semi-enclosed sea;

L – effective length of the strait;

A – cross-section area of the strait;

ρ_0 – background potential density;

P – subsurface pressure;

P_1 – averaged AP over open ocean;

P_2 – averaged AP over semi-enclosed;

η_0 – mean sea levels in the semi-enclosed sea;

ω_0 – barotropic Helmholtz resonant frequency (Eq. 4.1);

λ – linear friction coefficient;

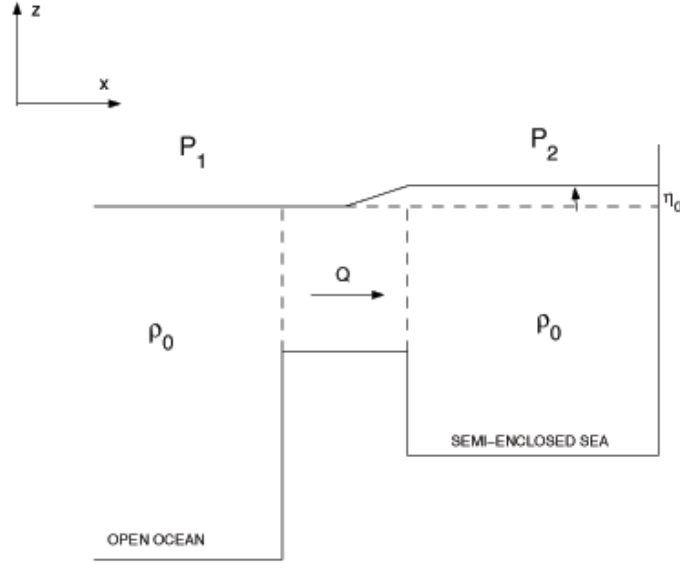


Figure 4.6: Schematic of Helmholtz resonance in a barotropic ocean

Application of conservation of mass to the water inside the semi-enclosed sea (Fig. 4.6) gives

$$\frac{\partial \eta_0}{\partial t} = \frac{Q}{S} \quad (4.3)$$

Application of conservation of momentum yields

$$\frac{\partial Q}{\partial t} = -\frac{1}{\rho_0} \frac{\partial P}{\partial x} - \lambda Q \quad (4.4)$$

where λ is the linear friction coefficient (Candela, 1991; Sofianos, 2000). Across the sea surface, continuity of pressure yields

$$P - \rho_0 g \eta = P_a \quad (4.5)$$

where P_a is local AP loading with vanishing time average and η the vertical displacement of the sea surface in the presence of the basic rest state due to AP loading (Wunsch and

Stammer, 1997). In the open ocean, subsurface pressure (P) would ideally be zero since sea level response is generally assumed to be IB.

In the semi-enclosed sea, non-IB response is expected due to various factors; such as, shallow water, and lateral boundaries (Wunsch and Stammer, 1997). Subsurface pressure is simply $P_2 + \rho_0 g \eta_0$. Therefore, subsurface pressure gradient differentiation term in (Eq. 4.4) (the first term on the right) can be treated as

$$-\frac{1}{\rho_0} \frac{\partial P}{\partial x} = -\frac{1}{\rho_0 L} (\rho_0 g \eta_0 + P_2) \quad (4.6)$$

where the along-strait pressure gradient ($\frac{\partial P}{\partial x}$) is approximated by the pressure difference divided by the effective length of the strait (Candela, 1991).

Using (Eq. 4.6), combination of (Eq. 4.3) and (4.4) leads to

$$\frac{\partial^2 \eta_0}{\partial t^2} = -\omega_0^2 (\eta_0 + \eta_a) - \lambda \frac{\eta_0}{\partial t} \quad (4.7)$$

where $\eta_a = \frac{P_2}{\rho_0 g}$ and $\omega_0 = \sqrt{\frac{gA}{SL}}$ are the equivalent dynamical height of AP and the barotropic Helmholtz resonance frequency (Eq. 4.1), respectively.

Given that the AP varies sinusoidally in time,

$$\eta_a = a_0 \sin(\omega t) \quad (4.8)$$

and the mean sea level responds as

$$\eta_0 = M \sin(\omega t + \phi) \quad (4.9)$$

Substitution of η_a and η_0 to (Eq. 4.7) yields the response magnitude of the sea level as

$$M = \frac{a_0\omega_0^2}{\sqrt{(\omega^2 - \omega_0^2)^2 + \lambda^2\omega_0^2}} \quad (4.10)$$

and the phase lag ϕ from AP is

$$\tan(\phi) = \frac{\lambda\omega}{\omega_0^2 - \omega^2} \quad (4.11)$$

The results (Fig. 4.7) indicate that the maximum gain of mean sea levels from the AP occurs at barotropic HR frequency with a 90 degree phase shift. The corresponding volume transport (Eq. 4.3) is

$$Q = SM\omega\cos(\omega t + \phi), \quad (4.12)$$

where M and ϕ are given in (Eq. 4.10) and (4.11), respectively. The volume transport thus has the maximum gain magnitude from AP forcing at barotropic HR frequency but with a 180 degree phase shift.

For frequencies higher than the barotropic HR frequency, there is little or no response in sea level with no phase shift, while for frequencies much lower than that, a perfect IB response occurs with a 180 degree out of phase shift (Fig. 4.7). This type of basin-wide sea level response pattern is generally consistent with observed pattern in PWS (Fig. 4.2); where the gain magnitude of observed CSL relative to AP is very small at high-frequencies but much greater at low-frequencies, while it is significantly larger at the barotropic Helmholtz resonance period (ca. 6 hr).

Hence, the basin-wide mean sea level response to AP of a barotropic semi-enclosed sea with bottom friction is analogous to the dynamic response of a classic forced-damping system, for instance, a forced spring oscillation (Goldstein *et al.*, 2002).

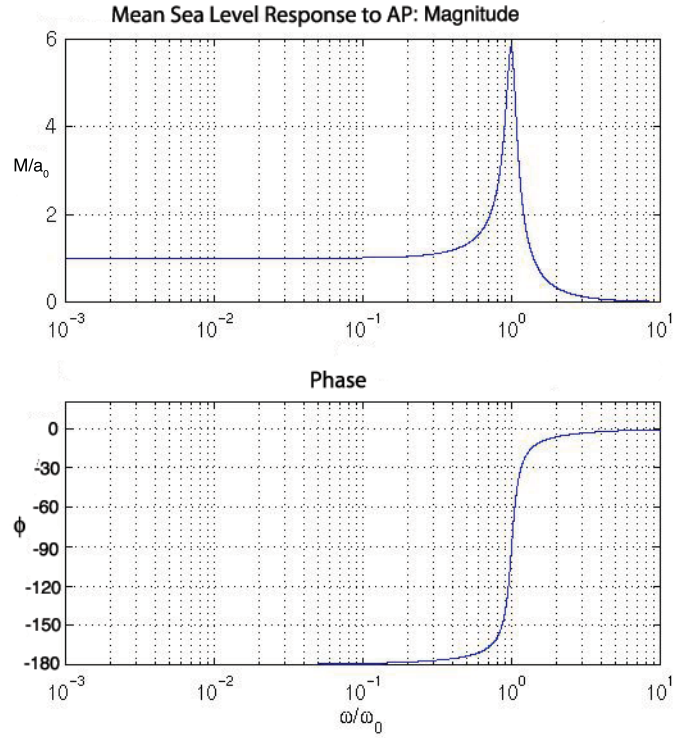


Figure 4.7: Response of mean sea level response to AP: a barotropic HR model ($\lambda = 1.0 \times 10^{-4}$)

4.3.4 Discussion on Barotropic Helmholtz Resonance

An analytical model has been constructed to study the response of a barotropic semi-enclosed sea to AP. The model successfully predicts that (1) the maximum gain in the HE and MS volume transports from AP occurs at the period of the barotropic Helmholtz resonance (*ca.* 6 hr); (2) for the barotropic ocean, the sea level response decreases and is in-phase with AP at higher frequencies, while it becomes increasingly constant and out-of-phase (inverted barometric) with AP at lower frequencies; However, more details on the properties of the transition band, cannot be obtained from the present HR models probably due to 1-D approximation used in (Eqs. 4.3 and 4.4) which might not be dynamically effective for interpreting 2-D horizontal circulation in PWS. The influence of baroclinic flow

structure through the strait is unclear, too. Hence, a series of numerical experiments are conducted; they also serve as validation for HR models used here.

4.4 Numerical Experiments

To gain insight into the physical mechanisms and parameters controlling the coherence and phase functions between the transports through HE and MS, several numerical experiments with atmospheric forcing (but without tidal forcing) for an idealized semi-enclosed sea are described. Influential time scales are likely to be of the same order as those for PWS: the inertial period of 14 hr, the Helmholtz resonance of 6 hr, and gravest barotropic or baroclinic seiches of the semi-enclosed sea of 0.5 and 10 hr, respectively. Similarly, influential space scales are likely to include the diameter of the semi-enclosed sea of *ca.* 100 km, the length, width, and depth of the straits of *ca.* 10 km, 10 km, 200 m, respectively, and the barotropic and baroclinic Rossby radii of deformation of *ca.* 450 and *ca.* 20 km, respectively. The Princeton Ocean Model (POM) is the “numerical engine” for EPWS/NFS, and it is also used in the idealized experiments described below (referred to as IPWS-POM hereafter).

4.4.1 Reference Experiment

For the reference case study, the idealized semi-enclosed sea is constructed in a rectangular shape of 50 km in the meridional direction and 50 km in the zonal direction, with a constant water depth of 400 m (Fig. 4.8). It is centered at 60N and the f-plane approximation is adopted. It is connected with the open ocean to the south via two straits, both of which have a length of 9 km, a width of 5 km and a depth of 200 m. (To relate readily to the realistic PWS, the eastern idealized strait is termed IHE, its western counterpart termed IMS, and

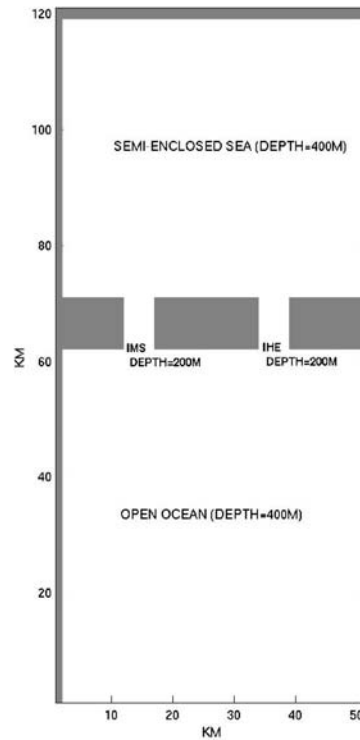


Figure 4.8: IPWS Reference Case model domain (IPWS) for an idealized PWS, open ocean, and two straits connecting them. For convenience, the lefthand strait is named as IMS, and the righthand strait as IHE.

the idealized semi-enclosed sea as IPWS.) The barotropic Rossby radius of deformation and barotropic HR period for IPWS are thus *ca.* 450 *km* and 2.5 hr, respectively. The open ocean is represented by another rectangular domain of 60 by 50 *km*, with a constant water depth of 400 *m*, subject to an open boundary in the south. In the horizontal, a uniform Cartesian grid is used with 1 *km* resolution. In the vertical, there are 11 uniformly-distributed sigma levels, and thus, the vertical resolution is 40 *m* for both IPWS and the open ocean, and 20 *m* inside the straits.

As a preliminary experiment, a barotropic (i.e., unstratified) case is run using IPWS-POM for the fluid initially at-rest, and the sea surface level. The model is then forced for 100 days by the AP, which is uniform over the open ocean and the semi-enclosed sea

individually, but with a pressure difference between these two sub-domains. The observed hourly pressure data at NDBC buoy 46061 (outside PWS) and 46060 (inside PWS) are used for the forcing (Fig. 4.9). Hence, the pressure gradient forcing only occurs along one row of gridpoints at the seaward mouth of IHE and IMS. As in EPWS/NFS, a modified Flather radiation boundary condition is applied along the southern boundary. After 100 days, the volume transports through the two straits are highly correlated ($r = 0.996$ at zero lag), and nearly identical with each other (Fig. 4.10). They are highly coherent and in phase for periods shorter than *ca.* 60 hr, and become less coherent and experience various phase changes (but no pi-radian out-of-phase relation) for periods longer than 60 hr. Hence, no well-defined in-phase, coherent/transition band/out-of-phase, coherent pattern occurs in the barotropic case. Examination of volume transport response to AP indicates that the maximum gain magnitude occurs at a period of *ca.* 2.5 hr, the barotropic HR period for IPWS (now shown).

The reference case starts with a two-layered, stably-stratified fluid ($\frac{\delta\rho}{\rho} = 1.4 \times 10^{-2}$, based on the summer stratification in Central Sound; the interface depth of 100 m is specified throughout the model domain. The corresponding baroclinic Rossby radius of deformation is *ca.* 23 km. It runs from rest and the same surface forcing as in the barotropic experiment is applied. After a 100-day integration, the time series of volume transport through the two straits (Fig. 4.11) are highly anti-correlated, ($r = -0.96$, at zero lag), and have a character similar to that of HE and MS transports simulated by the realistic EPWS/NFS. For example, the volume transport direction reverses in both straits with an irregular period varying from several to ten days. The volume transports through the two

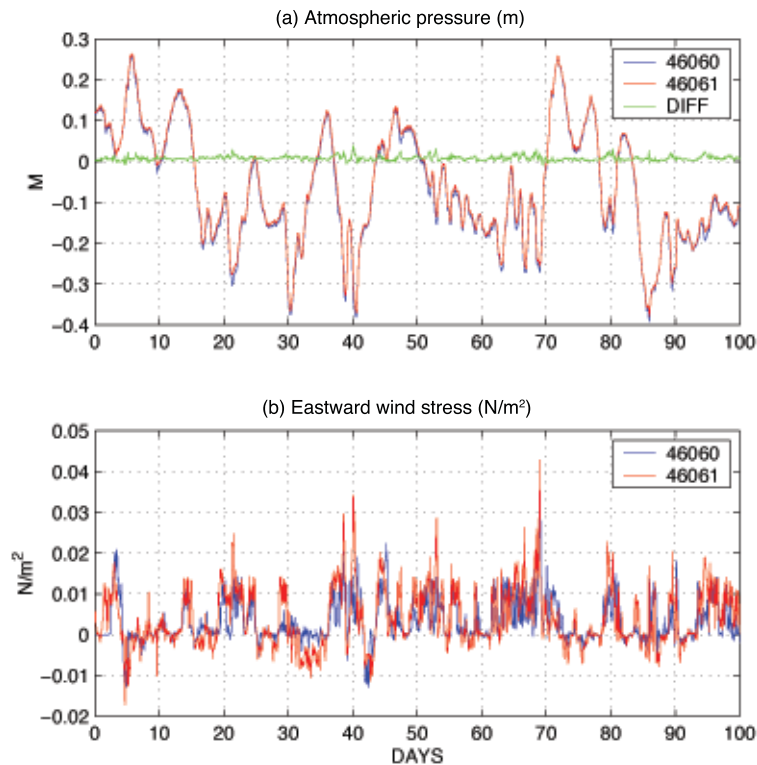


Figure 4.9: Atmospheric forcing for 100 days (1 JAN thru 10 APR 2005): (a) atmospheric pressure and (b) eastward wind stress at NDBC buoy 46060 (blue) and 46061 (red). The atmospheric pressure difference between 46060 and 46061 is indicated by green line in (a).

straits are perfectly coherent, out-of-phase, and nearly balanced with each other for periods longer than *ca.* 40 hr. At periods shorter than *ca.* 9 hr, the volume transports are also perfectly coherent, generally in-phase, and balanced by the time rate-of-change of the spatial-mean sea level inside PWS (not shown). For a transition period band between *ca.* 9 and 40 hr, the volume transports are partially coherent and experience a π -radian phase shift.

Investigation of the response function of IHE, IMS, and net volume transports to AP (Fig. 4.12) reveals similar results as in EPWS/NFS simulations: maximum gain magnitude occurs at a period of *ca.* 2.5 hr, the barotropic HR period for IPWS, and net volume transport gains are greater (less) than the IHE or IMS response for periods shorter than

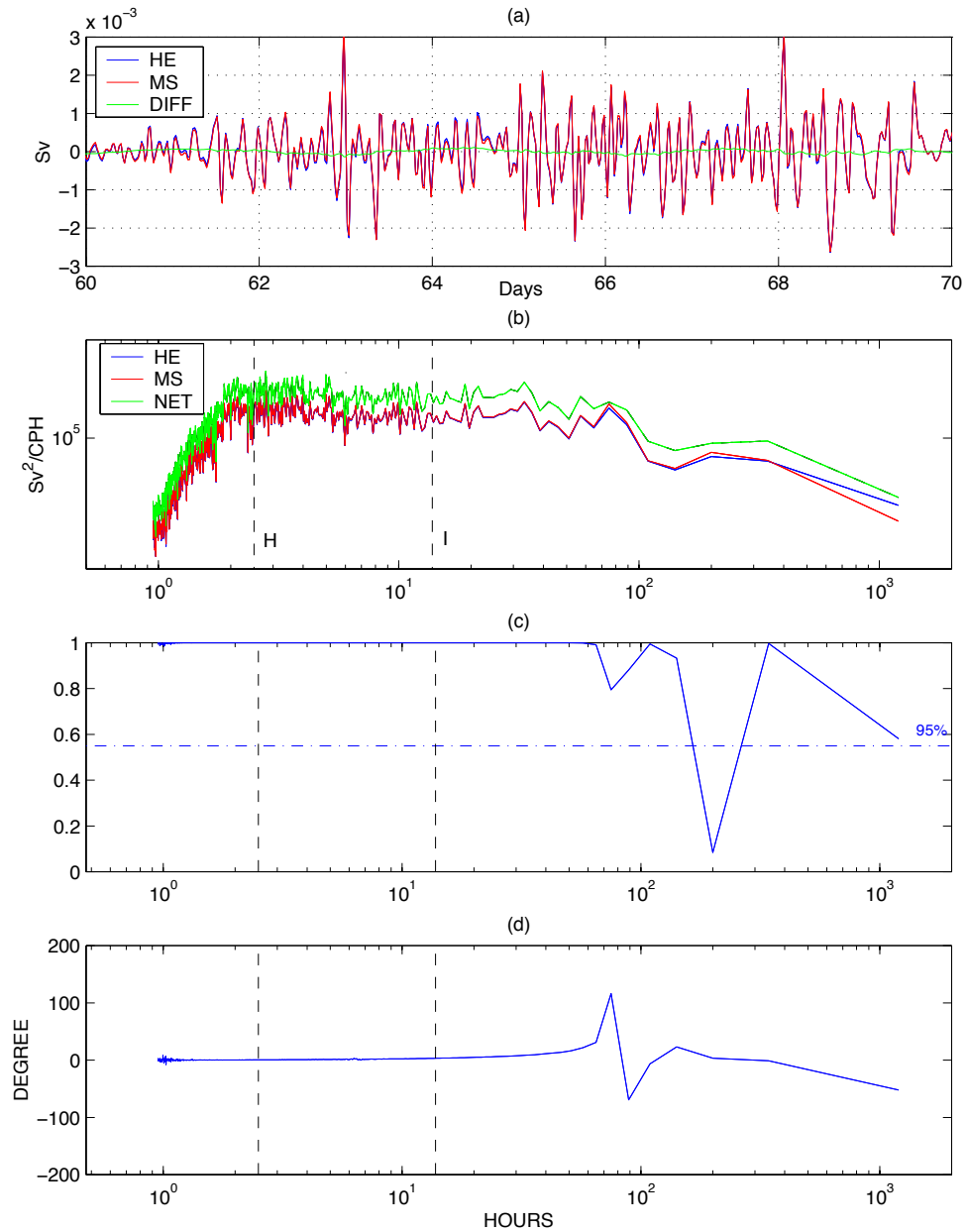


Figure 4.10: IPWS barotropic case: (a) simulated 10-day volume transports through IHE (red) and IMS (blue), as well as difference between IHE and IMS transport (green); (b) power spectra (DOF=10) for IHE (red), IMS (blue), and net volume transports (green); (c) coherence squared between volume transports through IHE and IMS; and (d) phase. KEY: H, barotropic Helmholtz resonance period for IPWS (*ca.* 2.5 hrs); I, inertial period (13.8 hrs).

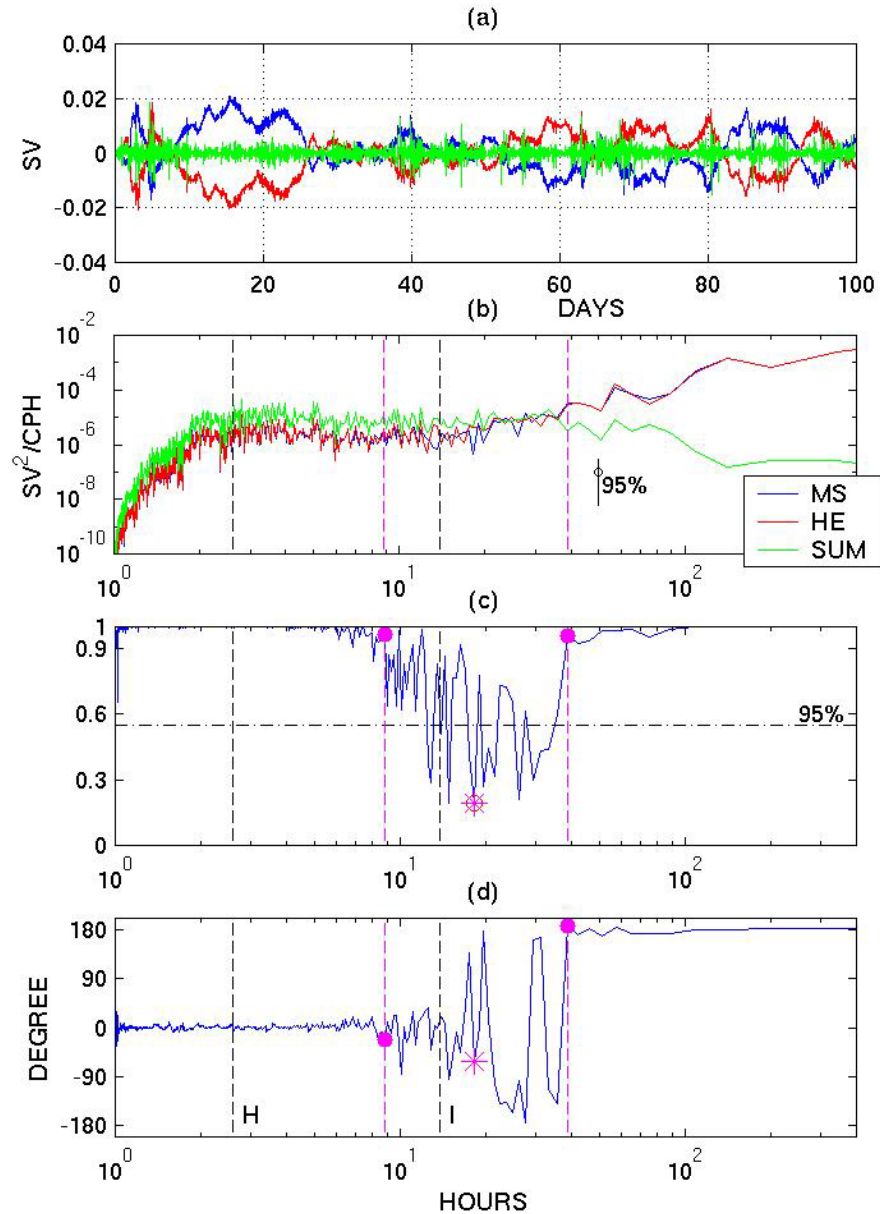


Figure 4.11: IPWS Reference Case: simulated 100-day (a) volume transports through IHE (red) and IMS (blue), as well as the net transport (green); (b) corresponding power spectra (DOF=10); (c) coherence squared between volume transports through IHE and IMS; and (d) phase. The transition band of the coherence function (solid magenta dots) is defined where the coherence squared is generally less than 0.9, and the minimum coherence squared (magenta star) is inside the transition band.

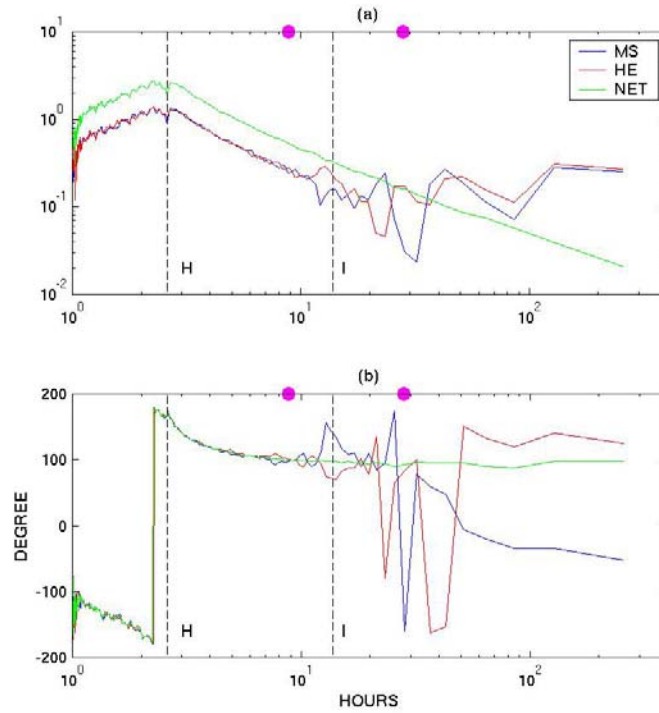


Figure 4.12: IPWS Reference Case: response of IHE (red), IMS (blue), and net (green) volume transports to atmospheric pressure forcing: gain (a) magnitude and (b) phase (DOF=10). The transition band (solid magenta dots) of the coherence function between IHE and IMS volume transports is indicated.

10 hr (longer than 40 hr). Other than for the period band of 10 to 40 hr, IHE and IMS gain magnitudes agree closely with each other. Furthermore, IHE, IMS, and the net volume transport has nearly identical gain phase curves for periods shorter than 10 hr, and for periods longer than 40 hr, net volume transports have nearly constant gain phase of *ca.* 100° . There exists a well-defined in-phase/high-frequency band, and an out-of-phase/low-frequency band, relationship between IHE and IMS volume transports.

There is a three-layer inflow/outflow/inflow structure in the mean meridional velocity field in both straits: inflow in both the surface layer (upper *ca.* 50 m) and the bottom layer (lower *ca.* 50 m), and outflow in the intermediate layer (*ca.* 50 to 150 m deep)(Fig. 4.13). At 100 m depth, however, there is a small inflow region on the western side of the both

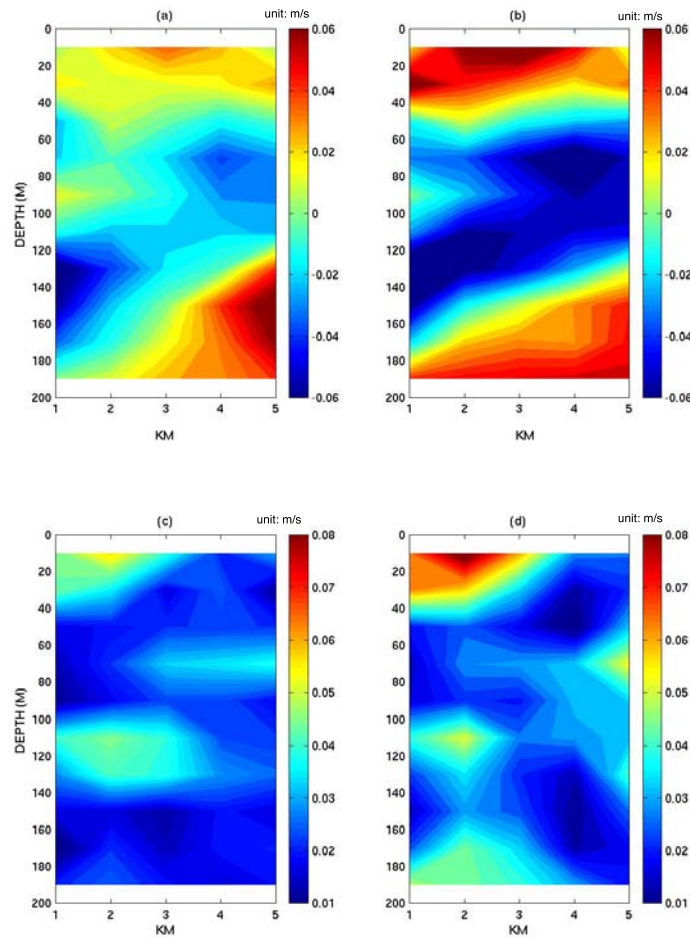


Figure 4.13: IPWS Reference Case 100-day mean northward velocity transect (m/s) at IMS and IHE (a, b), and the corresponding standard deviation transect (STD; c, d).

straits, corresponding to the position of the density interface. Typically, the magnitude of the horizontal shear of the northward velocity is *ca.* $0.1f$, especially in the bottom layer where maximum inflow occurs on the eastern side of the straits.

4.4.2 Effects of Density Stratification and Rotation Experiments

These numerical experiments, which differ from the reference case in the form and strength of density stratification and the magnitude of the Coriolis parameter, are designed to explore the relation between the transition band and the two most important geophysical fluid

dynamical variables: vertical density stratification and rotation. The results are summarized in Table 4.3, and indicate that (1) weaker stratification shifts the transition band to longer periods; for instance, the transition band occurs at *ca.* 30 to 80 hr with the smaller density jump in Exp. 1.2, compared with 9 to 40 hrs in the reference case; (2) changes in density interface depth substantially affect the transition band when it is less than the depth of the straits, while, when the density interface depth is deeper than the depth of the straits (or the water inside the strait is barotropic), the effect on the transition band is not obvious; and (3) the decrease of the Coriolis parameter slightly shifts the transition band to shorter periods; for instance, the transition band is shifted from between *ca.* 9 to 40 hrs to between *ca.* 4 and 28 hrs when the Coriolis parameter is decreased to *ca.* 1/100 of the original value. On the other hand, there is a close inverse relation (in a logarithmic scale) between the normalized (by the inertial period) transition band and the normalized (by the length of the strait) internal Rossby radius (Fig. 4.14). Since the slopes of the first-order curve fit for both the upper and lower transition band limits are nearly -1, there is a linear dependence of the normalized width of the transition band on the reciprocal of the normalized internal Rossby radius.

Table 4.3: Summary of Density Stratification and Rotation Experiments

	Reference	Exp 1.1	Exp 1.2	Exp 2.1 [§]	Exp 2.2 [§]	Exp 3.1	Exp 3.2	Exp 3.3	Exp 4.1	Exp 4.2	Exp 4.3	Exp 4.4
Depth of Interface (m)	100	~	~	N/A	N/A	40	200	300	100	~	~	~
Stratification ($\frac{\partial \rho}{\rho}$)	1.4×10^{-2}	1.0×10^{-2}	0.6×10^{-2}	9.0×10^{-3}	7.5×10^{-3}	1.4×10^{-2}	~	~	~	~	~	~
Coriolis Parameter	1.3×10^{-2}	~	~	~	~	~	~	~	1.0×10^{-3}	1.0×10^{-4}	1.0×10^{-5}	1.0×10^{-6}
Internal Rossby Radius# (km)	25	21	16	9	7	17	29	23	3.2	32	320	3200
Transition Band* (hr)	9~40	12~70	30~80	90~1000	90~1000	12~65	25~95	20~90	4~40	9~45	5~32	4~28
M.C.S.% (hr)	0.2 (18)	0.3 (24)	0.2 (42)	0.1 (150)	0.3 (150)	0.2 (25)	0.2 (45)	0.2 (38)	0.1 (30)	0.1 (15)	0.1 (10)	0.06 (6)

[§]: Continuously-stratified experiment, and N is given as the stratification value below

~: Same value as the reference case

#: Internal Rossby Radius is based on the physical parameters for PWS

*: Associated with a π -radian phase shift, the transition band subjectively corresponds to the period interval where the coherence squared is less than 0.9

‡: Minimum Coherence Squared (period)

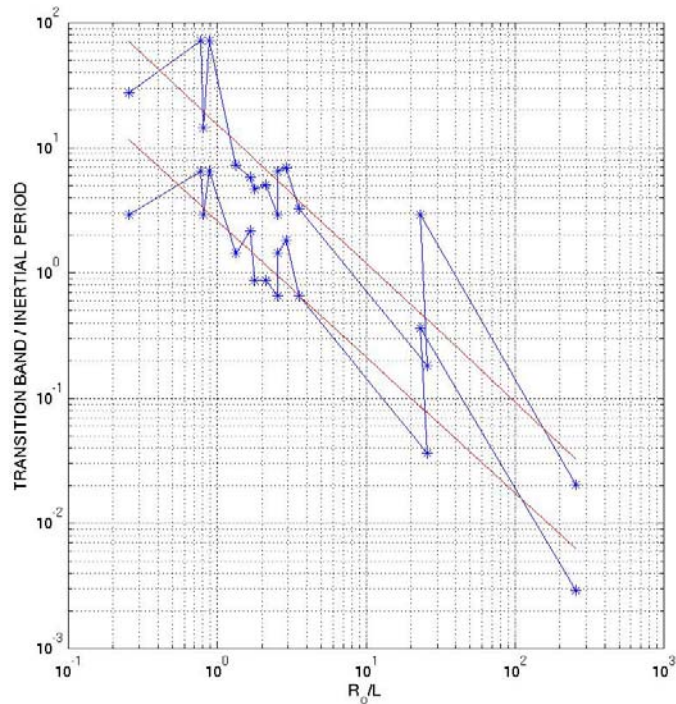


Figure 4.14: Normalized (by inertial period) upper and lower period bounds of transition band versus normalized (by strait length) baroclinic Rossby radius of deformation for the experiments documented in Table 4.3. The slopes of least-square fitted curves for the upper and lower period bounds are -1.01, and -1.09, respectively.

4.4.3 Effect of Domain Geometry Experiments

These numerical experiments are focused upon the effects of the geometric configuration of a semi-enclosed sea on the transition band, since results of the reference case suggest the importance of geometry-dependent HR. The length, width and position of the two straits are changed from experiment to experiment, and the water depth of the semi-enclosed sea and open ocean are varied too. The results (Table 4.4) indicate that (1) the general pattern of the coherence and phase functions between the IHE and IMS volume transports; e.g., coherent, in-phase/partially coherent, transition band/coherent, out-of-phase, is independent of the geometry of the ocean system consisting of the semi-enclosed sea, open ocean, and two

straits; (2) the width of the transition band is nearly independent of the geometry of the two straits, but varies with their relative location; (3) this width is unchanged when the depth of the semi-enclosed sea is doubled and halved; and (4) this width is also unchanged when the water depth in the open ocean is decreased to 200 *m*, but it narrows when the water depth is increased to 800 *m*.

Table 4.4: Summary of Domain Geometry Experiments

	Reference	Exp 5	Exp 6.1	Exp 6.2	Exp 6.3	Exp 7	Exp 8.1	Exp 8.2
Distance between He and MS (km)	20	10	~	~	~	~	~	~
HE (LxWxD; km, km, m)	9x5x200	~	~	~	1x1x200	~	~	~
MS (LxWxD; km, km, m)	9x5x200	~	9x5x120	9x5x80	1x1x200	~	~	~
IPWS (LxWxD; km, km, m)	50x50x400	~	~	~	~	50x50x800	~	~
Open Ocean (LxWxD; km, km, m)	60x50x400	~	~	~	~	~	60x50x800	60x50x200
Transition Band (hr)	9~40	12~65	9~45	9~40	7~40	8~40	4~18	9~40
Minimum Coherence Squared (hr)	0.2 (18)	0.1 (25)	0.05 (30)	0.05 (38)	0.02 (14)	0.15 (24)	0.05 (8)	0.2 (20)

~: Same value as the reference case

Table 4.5: Summary of Forcing Function Experiments

	Reference	Exp 9.1	Exp 9.2	Exp 10.1	Exp 10.2	Exp 10.3	Exp 10.4
Pressure	observed	halved	doubled	none	none	none	none
Wind	none	~	~	zonal	meridional	doubled	halved
Transition Band (hr)	9~40	12~50	6~28	3~5	3~7	3~7	3~7
Minimum Coherence Squared (hr)	0.2 (18)	0.2 (27)	0.2 (14)	0.2 (4)	0.2 (3.5)	0.1 (5.8)	0.2 (5)

~: Same value as the reference case

4.4.4 Effect of Forcing Functions Experiments

Forced by the doubled or halved AP forcing, and the doubled or halved surface wind (Fig. 4.9) stress (in both meridional and zonal components), these experiments (Table 4.5) reveal that (1) the general pattern of the coherence and phase functions between the IHE and IMS volume transports is independent of the forcing functions investigated; (2) the transition band occurs at shorter periods as the intensity of the atmospheric pressure increases, and vice versa (*i.e.*, a sign of nonlinearity) and (3) it occurs at much shorter periods (between *ca.* 3 and 6 hour) with wind stress applied, but is unchanged as the intensity of wind stress varies.

4.4.5 Summary of Numerical Experiments

A series of numerical experiments for idealized regimes have identified the characteristics of the transition band, and its dependence on such physical parameters as density jump and interface depth for two-layer stratification (or buoyancy frequency (N) for continuously-stratified cases) and rotation rate; geometry of the straits, semi-enclosed sea, and open

ocean; and surface forcing. The transition band depends on the baroclinic radius of deformation, with the periods increasing for both the upper and lower bounds and the bandwidth as the radius of deformation increases, which directly determines the location of the upper or lower period bound of the transition band.

4.5 Summary and Discussion

Motivated by the presence of a 6-hr peak in the response magnitude of CSL to AP, as well as the “transition band” in the coherence pattern between HE and MS volume transports, analytical models of oceanic HR have been established and utilized to interpret the barotropic HR and the related phenomena in PWS. Based on the numerical experiments, the location of the transition band is likely determined by the baroclinic radius of deformation for a semi-enclosed sea.

The transition band may also be associated with the baroclinic flow developed inside each strait. For instance, similar three-layered baroclinic mean flow structure; e.g., inflow in the surface and bottom layers and outflow in the intermediate layer, is found in both the EPWS/NFS simulations for the realistic PWS and the idealized reference experiment. This three-layered mean flow is probably related to the exchange flow experiencing hydraulic control (by internal wave modes) over a sill (Smeed, 2000). Either two-layer (Helfrich, 1995) or three-layer (Smeed, 2000) water mass/flow model can develop for hydraulic exchange flow, and both these models demonstrate the importance of time-dependent forcing, and geometric details of the strait. The difference, however, from the present study is evident: the three-layered velocity flow occurs even with two-layer stratification (e.g., reference experiment). On the other hand, the baroclinic transport is normally four to five times larger

than the corresponding barotropic transport, and thus, the highly variable circulation of PWS may be influenced to a significant degree by time-dependent, three-layered flow at the straits.

Chapter 5

Response of Prince Willam Sound to Surface Winds

The winds (and to some degree, the highly-correlated atmospheric pressure fluctuations), especially the alongshore component, produce vigorous motions, deeply affecting the primary circulation structures involving synoptic and seasonal time scales and spatial scales of a few hundred to a thousand kilometers in the coastal oceans (Kantha and Clayson, 2000). For a semi-enclosed sea such as PWS, studies of the response to the wind forcing impose a particularly interesting challenge, since a wide range of physical processes are involved in this small region, and which of these many processes dominate the PWS response due to the external wind forcing depends on a variety of factors.

5.1 Methodology

As introduced previously (Section 1.2), local terrain adds significant fluctuations to the general wind-field pattern over PWS; for instance, the mesoscale barrier winds and gap winds. These mesoscale features in the wind field may play significant roles in affecting local ocean circulation patterns, especially surface flows. And thus, for the purpose of mesoscale ocean circulation study, it may be unreasonable to apply a one-point observed

wind velocity (for instance, at NDBC buoy 46060 in Central Sound) as spatially uniform throughout the entire EPWS-POM domain.

Alternatively, the surface wind field from a mesoscale atmospheric model may be more appropriate. PWS-RAMS (Section 1.3.4), coupled to EPWS/NFS operationally, has provided hourly wind velocity at a horizontal resolution of 4 *km* since 2005. It also covers an area larger than the EPWS-POM domain, and thus, will be utilized for surface wind input for subsequent numerical studies in this chapter. Similar to the study of PWS response to LSC (Chapter 3), numerical integrations start with the same initial conditions, and run from 1 JAN 2006 for a full year. The simulation is driven by RAMS mesoscale winds only, and radiation OBCs are applied along open boundaries.

5.1.1 Verification of RAMS Surface Winds

RAMS winds agree well with observations at buoys 46060 and 46061 in 2005, and demonstrate a similar pattern of spatial coherence between these two locations (Section 1.3.4). In 2006, both RAMS winds and observations at 46060 indicate several significant synoptic events; for instance, the shift from northwestward (*ca.* 25 *m/s*) to southeastward (*ca.* 20 *m/s*) winds in FEB (Fig. 5.1). Another significant synoptic event in late NOV, characterized by strong southward wind of *ca.* 20 *m/s*, was predicted by RAMS but with a few days lag. Further verification of RAMS winds is conducted with the focus on the zonal wind component, since it is related to coastal upwelling and downwelling processes over the shelf, and is, presumably, important for the water exchange between PWS and the shelf.

In 2006, based on monthly statistics of duration of wind direction, both RAMS predicted and buoy observed zonal winds at 46060 indicate that downwelling-favorable (westward)

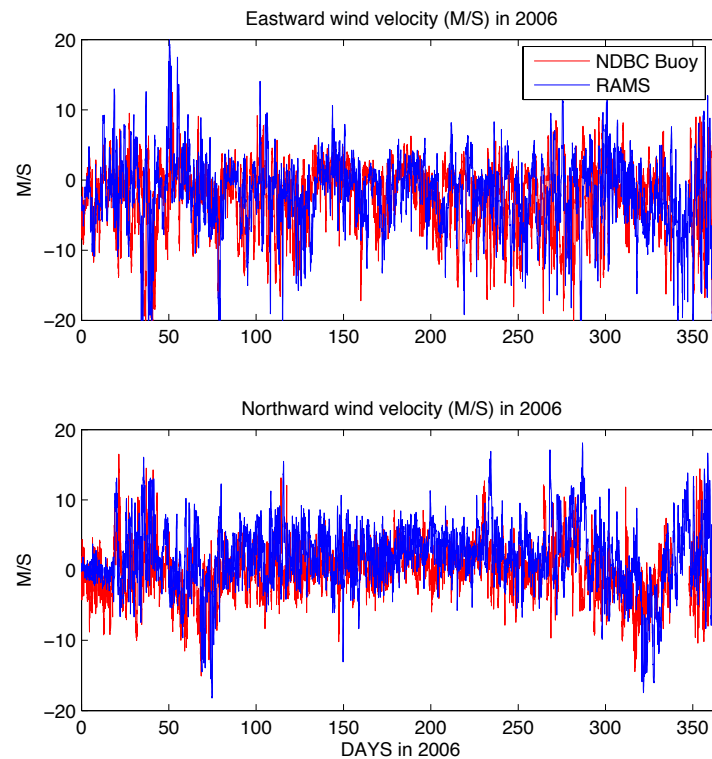


Figure 5.1: One-year (2006) comparison between RAMS simulated and NDBC buoy observed wind velocities at buoy 46060

winds are dominant in all months, more so during the winter than during the summer (Fig. 5.2). Compared with observations, RAMS produces slightly more frequent (*ca.* 2% to 5%) upwelling-favorable (eastward) winds in each month, except MAY, JUN and JUL.

This simple picture based on monthly statistics becomes more complicated when a closer investigation is conducted for each week (Fig. 5.3). During the 8th, 9th, 20th, 21st, 22nd, 24th, 26th, 27th week, upwelling-favorable winds are more dominant in the observations, and the 27th week (JUL) is characterized as a period when upwelling-favorable winds blow persistently. In RAMS, the same eight weeks are dominated by simulated upwelling-favorable winds. But RAMS seems to produce more of these “upwelling-favorable weeks”, as in the 13th, 16th, 30th, 34th, 41th, 43th and 44th week, which disagrees with the observations (Fig. 5.3). Hence, one must be cautious when the synoptic response of

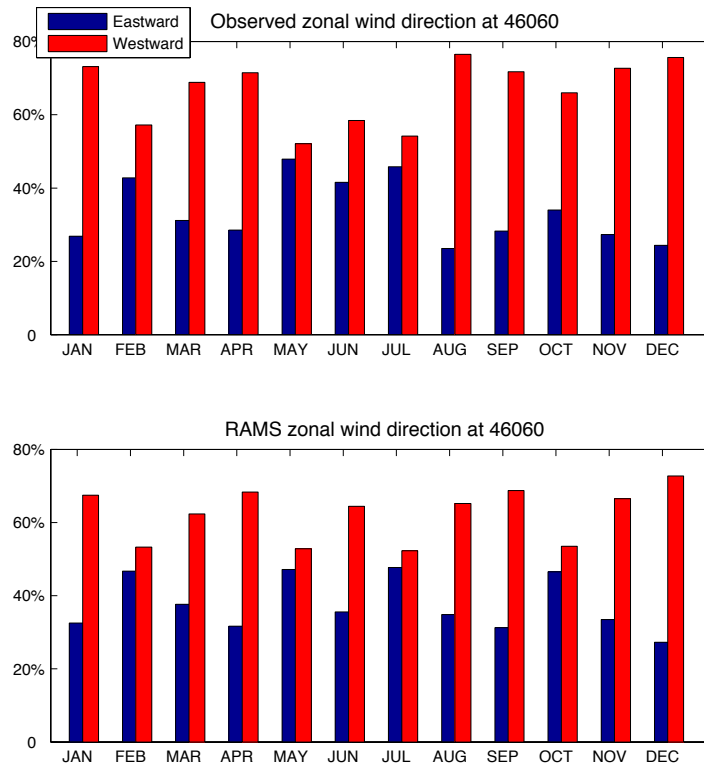


Figure 5.2: Monthly histogram on buoy observed and RAMS simulated zonal winds at 46060

PWS to surface winds is examined during these weeks (e.g.,13th, 16th, 30th, 34th, 41th, 43th and 44th week).

5.2 Response to RAMS Surface Winds

PWS sea level response to RAMS mesoscale winds is fairly small, only a few centimeters throughout EPWS-POM domain, except during periods when strong winds blow for a few days. For instance, sea level variation at Seward can reach 0.15 *m* in FEB (Fig. 5.4) when RAMS wind speed in Central Sound is usually over 20 m/s. Annual-mean SSH field is characterized by two cyclonic eddies over the shelf, and a cyclonic eddy and an anticyclonic eddy in the Central Sound. Examination of monthly-mean SSH in Central Sound confirms the occurrence of anticyclonic eddies in MAY, JUN, JUL, and OCT (Fig.

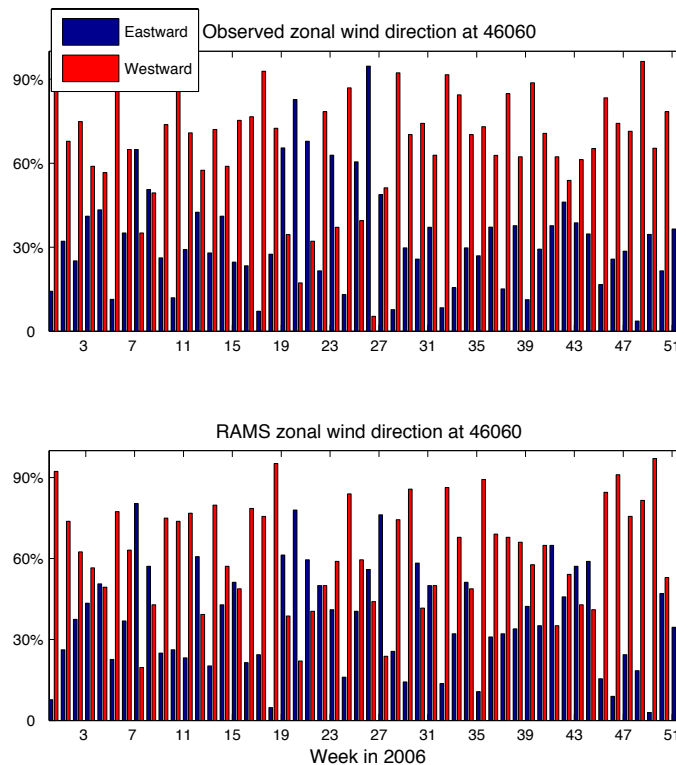


Figure 5.3: Weekly histogram on buoy observed and RAMS simulated zonal winds at 46060

5.5). The maximum annual-mean surface current (*ca.* 0.6 m/s) occurs at HE and the channel connecting BH and the fjord in northwest PWS (Fig. 5.4), both of which are relatively deep and narrow.

RAMS wind-driven volume transports are dominantly in through HE and out through MS with significant correlation ($\text{COR}=-0.98$ at zero lag; Fig. 5.6). This pattern was reversed mainly in JAN, JUN and NOV, and occasionally during some short periods (*ca.* few days) in other seasons. The maximum volume transport through HE is *ca.* 0.13 Sv , and compared with synoptic LSC response (Fig. 3.10), RAMS winds apparently produce less energetic variations in HE and MS volume transports (Fig. 5.6). A “transition band” between *ca.* 5 to 20 hrs can be roughly defined in the coherence pattern between HE and MS volume

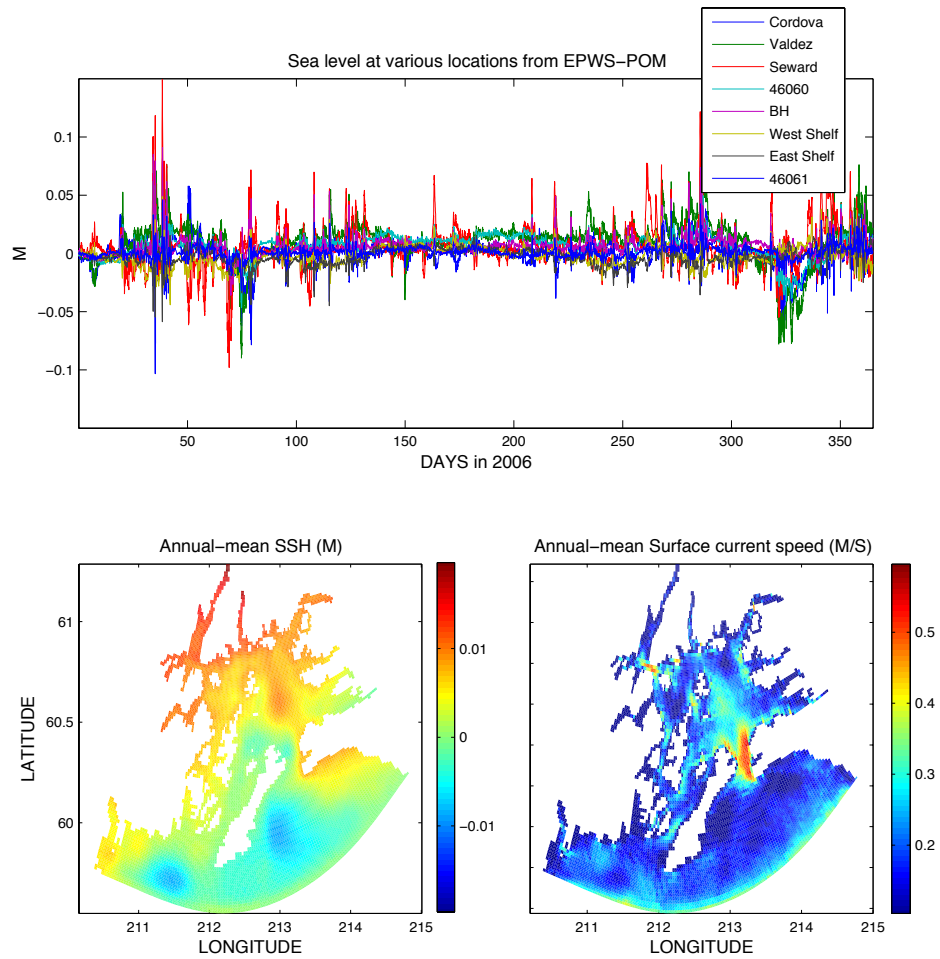


Figure 5.4: EPWS-POM simulated 1-yr sea levels at various locations (upper), along with annual-mean SSH (bottom left) and surface current speed (bottom right)

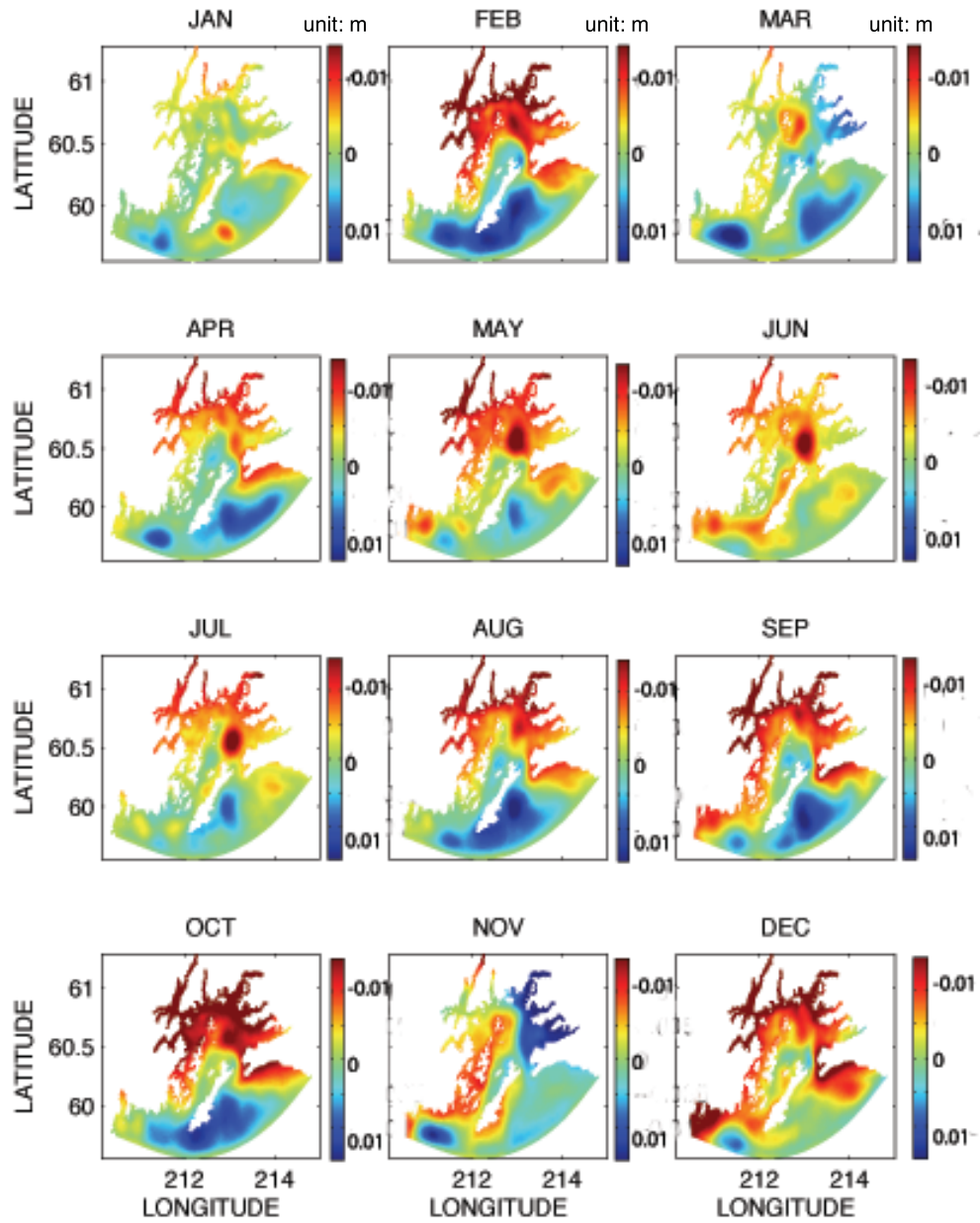


Figure 5.5: EPWS-POM simulated monthly mean SSH

transports; except at the period of 5 hr, HE and MS volume transports are generally not in-phase (Fig. 5.6).

Examination of the vertical structure of monthly mean northward velocity across MS transect indicates predominant two-layered flow structures, surface outflow (for the upper 150 *m*) and bottom inflow, with normally small flow speed (less than 0.05 *m/s*) in each layer. (Fig. 5.7). This pattern is reversed in JAN, JUN, and JUL when surface inflow (for the upper 50 *m*) occurs above weak bottom outflow. In DEC, a three-layered flow is developed at MS with inflow in surface and bottom layers and outflow in the intermediate layer. At HE, one of the most prominent features in monthly-mean northward velocity transects is vigorous bottom inflow throughout the year (Fig. 5.8), similarly as demonstrated by EPWS/NFS (Fig. 1.30). Well-defined layered flows develop in NOV (two-layer) and DEC (three-layer).

Monthly-mean SST response to RAMS winds is fairly weak, and varies mostly within 10°C and 11°C (Fig. 5.9). In Central Sound, in response to strong northwestward winds in FEB (Fig. 5.1), the 10°C isotherm at 46060 was displaced downward for *ca.* 50 *m*, and subsequently followed by upward displacement of *ca.* 40 *m* in early MAR (Fig. 5.10) due to a strong southwestward wind (*ca.* 20 *m/s*). This type of isotherm response to strong surface winds also occurs at BH, where the deep water (< 5°C) is affected with the corresponding upward and downward displacements of the 5°C isothermal by *ca.* 20 *m*. Surface doming of the isotherm in the Central Sound in NOV is apparently associated with strong southward winds during the same period (Fig. 5.9). In contrast to the synoptic LSC response, no cool water (< 5°C) inflow occurs through HE and MS (Fig. 5.10), and the cool deep water seemingly resides at BH with little seasonal variability.

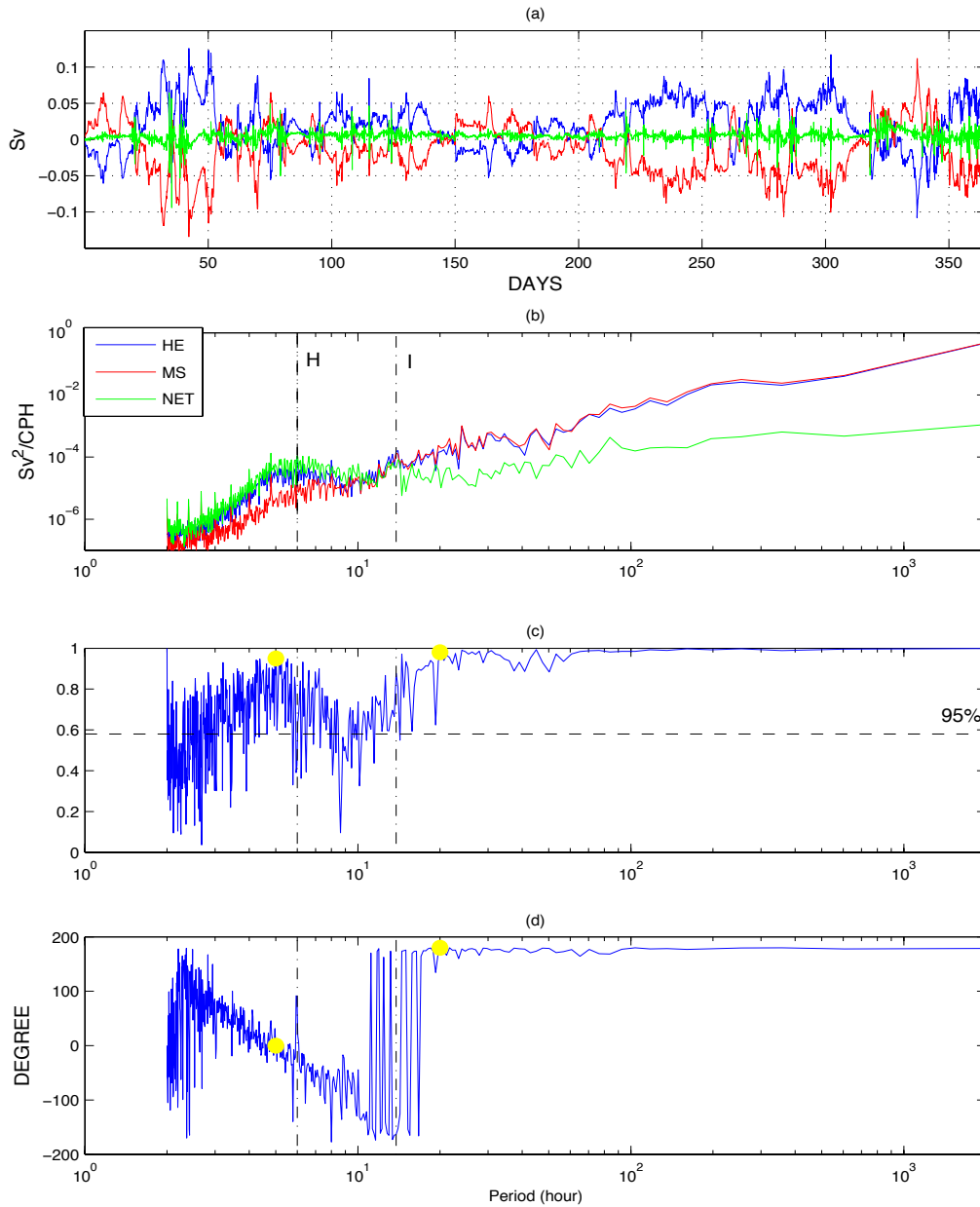


Figure 5.6: EPWS-POM simulated 1-yr (a) volume transports through HE (red) and MS (blue), as well as the net transport (green); (b) corresponding power spectra (DOF=10); (c) coherence squared between volume transports through HE and MS; and (d) phase. The transition band (solid yellow dots) of the coherence function is indicated. KEY: H, Helmholtz resonance period for PWS (*ca.* 6 hrs); I, inertial period (13.8 hrs).

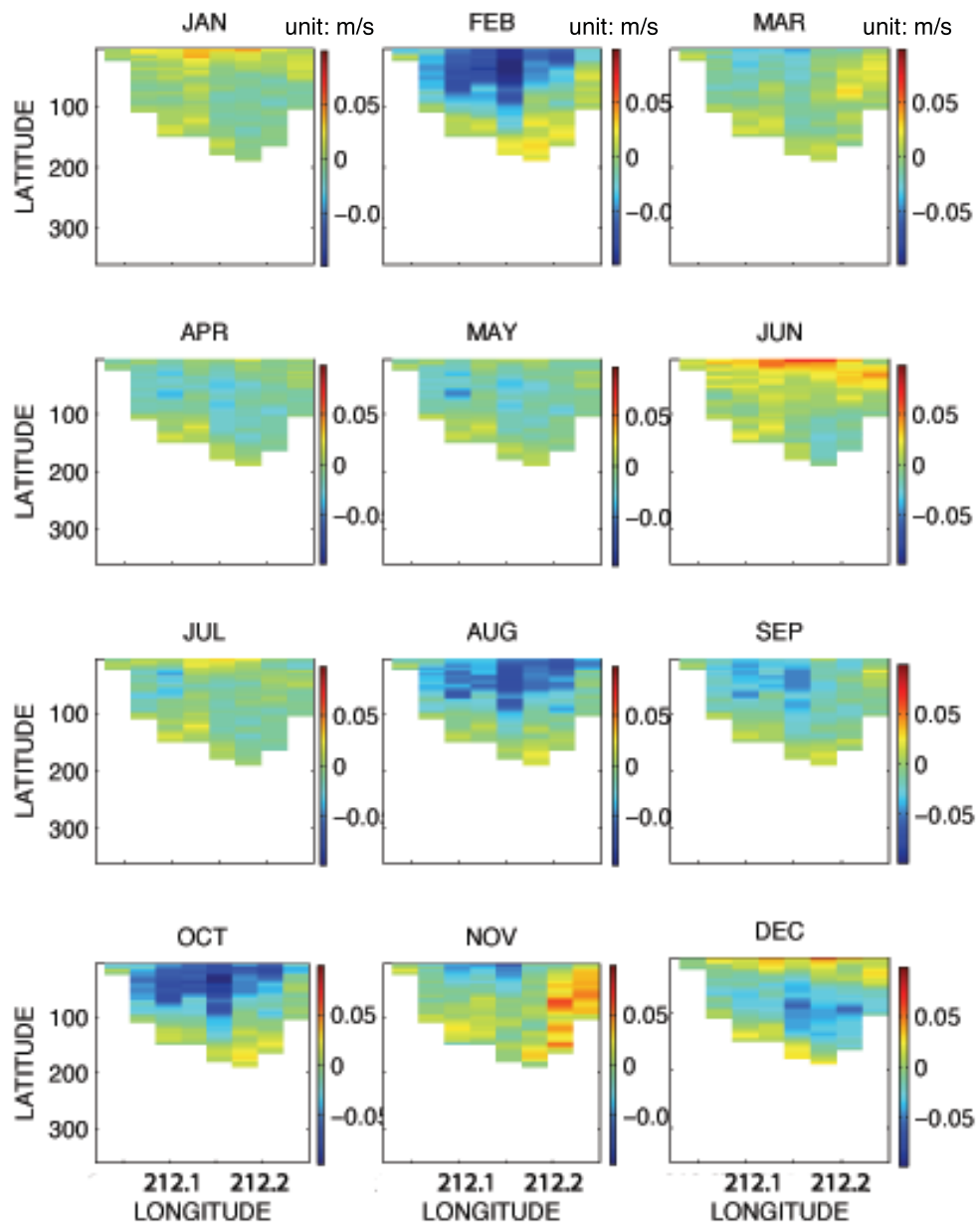


Figure 5.7: EPWS-POM simulated monthly mean northward velocity transect at MS

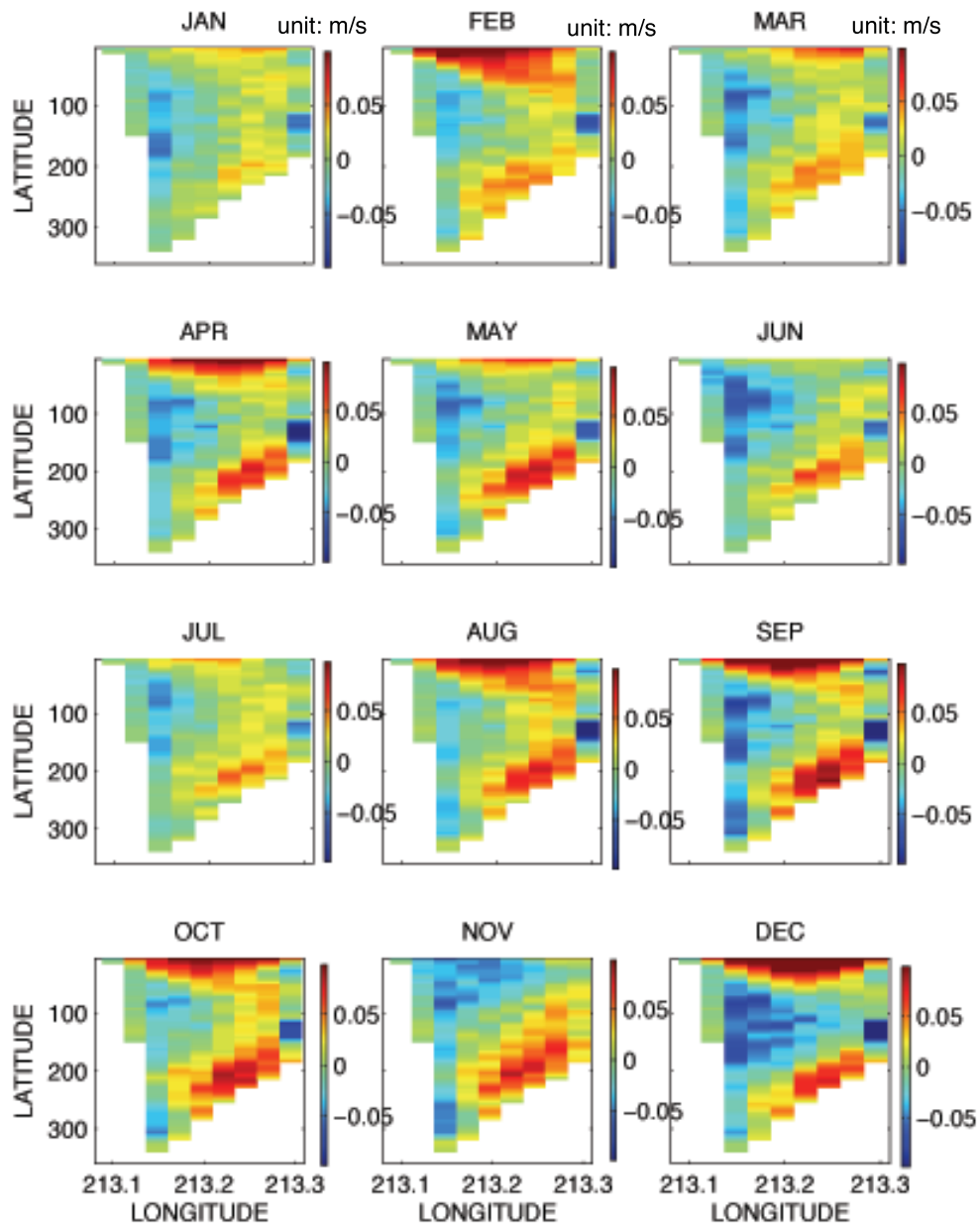


Figure 5.8: EPWS-POM simulated monthly mean northward velocity transect at HE

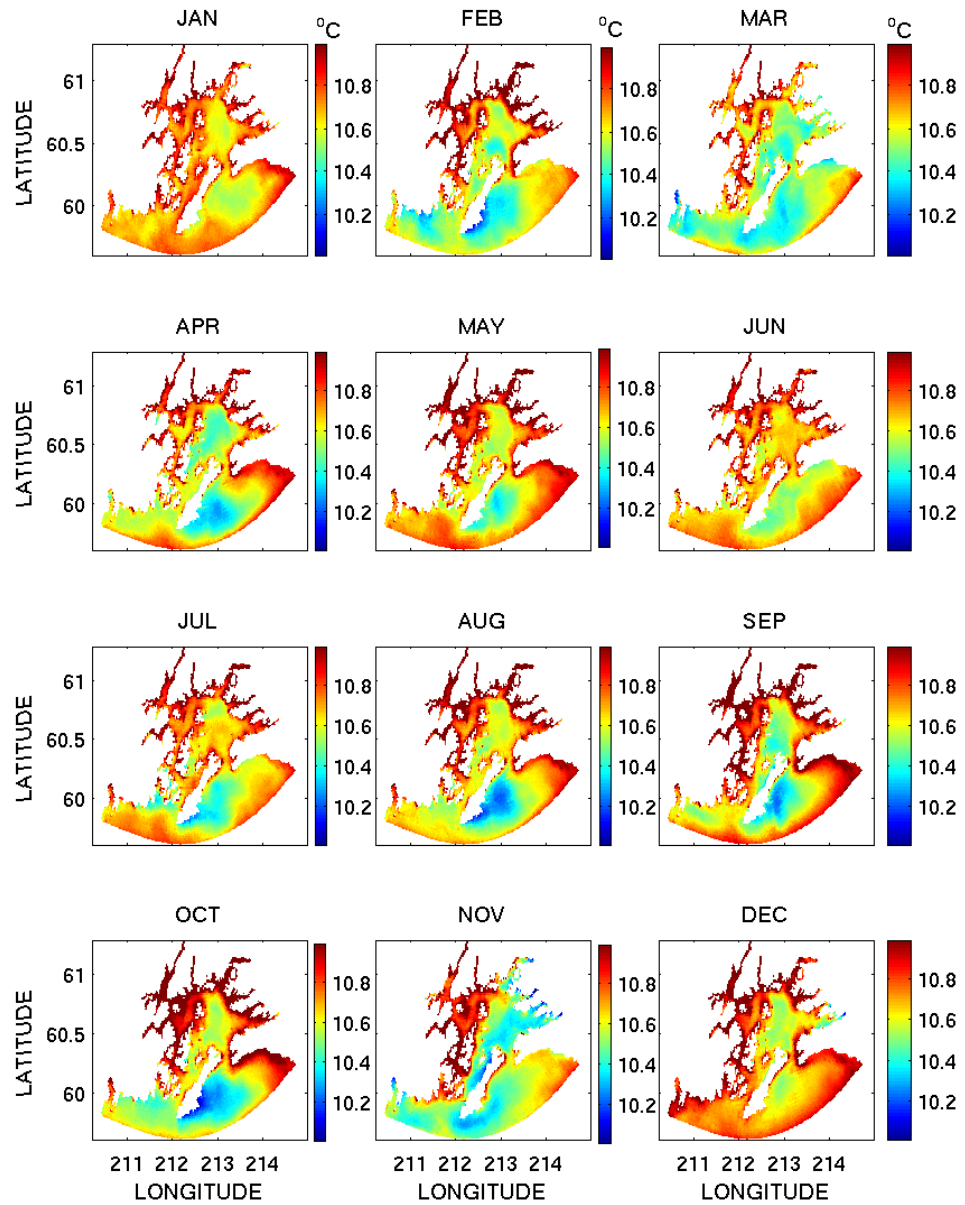


Figure 5.9: EPWS-POM simulated monthly mean SST

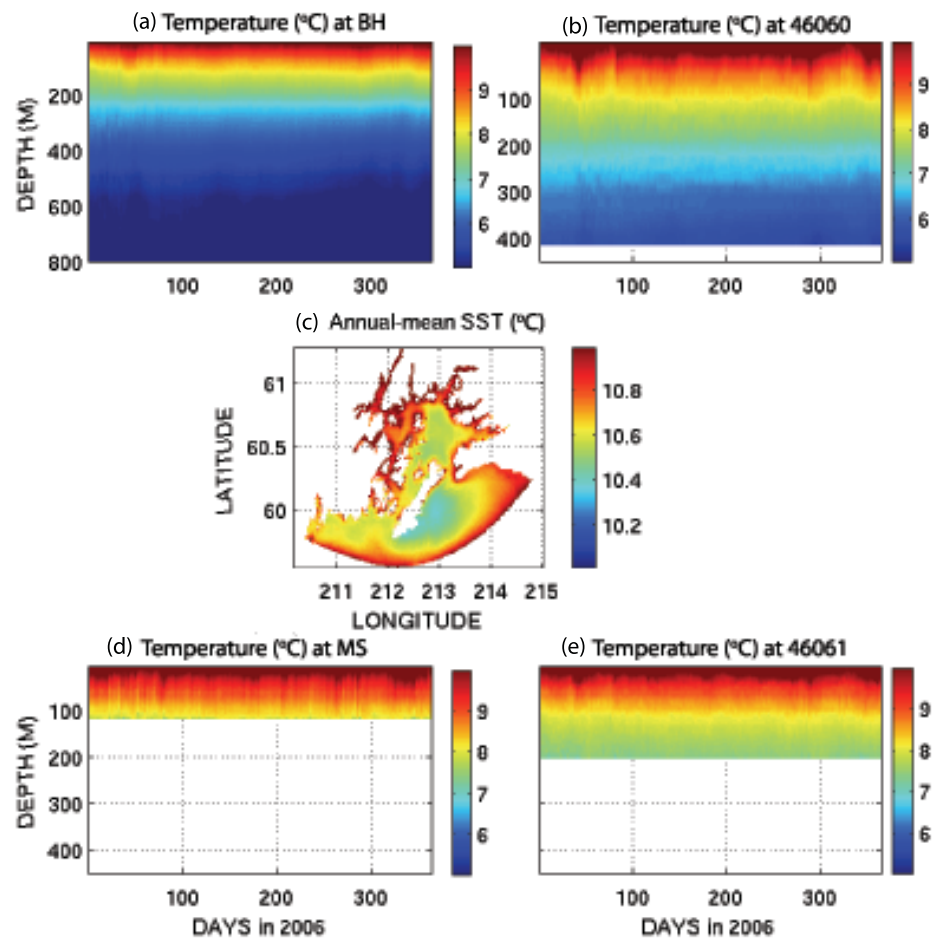


Figure 5.10: EPWS-POM simulated 1-yr temperature time-depth plots at (a) BH, (b) 46060, (d) MS, and (e) 46061, along with (c) annual-mean SST

5.2.1 Wind-Driven Mesoscale Circulation in PWS

The most noticeable mesoscale circulation response to RAMS winds is the residence of an anticyclonic gyre in Central Sound in MAY, JUN, and JUL (Fig. 5.5). While in other seasons, continuous monitoring of surface currents³⁷ indicates that transient anticyclonic eddies occur in Central Sound from time to time, and normally, these eddies “survive” for less than 10 days. For instance, one of these anticyclonic eddies was generated on 11 MAR near the northern PWS coast (Fig. 5.12) when RAMS surface wind speed in Central Sound was usually moderate (*ca.* 5 m/s; Fig. 5.11). The eddy grew and translated southward during the next two days under relatively strong northward surface winds (*ca.* 10 m/s) on 12 MAR and much weaker southward winds (*ca.* 2 m/s) on 13 MAR. On 14 MAR, RAMS surface winds were initially southward (*ca.* 5 m/s) and then nearly northward with relatively strong wind speed (*ca.* 10 m/s), and the eddy became a dominant anticyclonic gyre in the northern Central Sound with a radius of *ca.* 10 km and a maximum surface current of *ca.* 0.2 m/s. The gyre then quickly dissipated on 15 MAR, and disintegrated the next day under moderate northeastward surface wind (*ca.* 5 m/s) in Central Sound. Strong surface outflow occurred at both HE and MS during the presence of the anticyclonic eddy (Fig. 5.12). Compared with the cyclonic gyre with similar size in AUG as a synoptic LSC response (Fig. 3.18), this wind-driven anticyclonic eddy was more surface-trapped: the velocity signature of anticyclonic eddy was confined within the upper 100m, and the vertical displacements of the isotherms were less than 20 m (Fig. 5.13). These transient

³⁷also see one-year animation of RAMS wind-driven surface current at http://epws-nfs.rsmas.miami.edu/EPWS/rams_ssu.mpeg

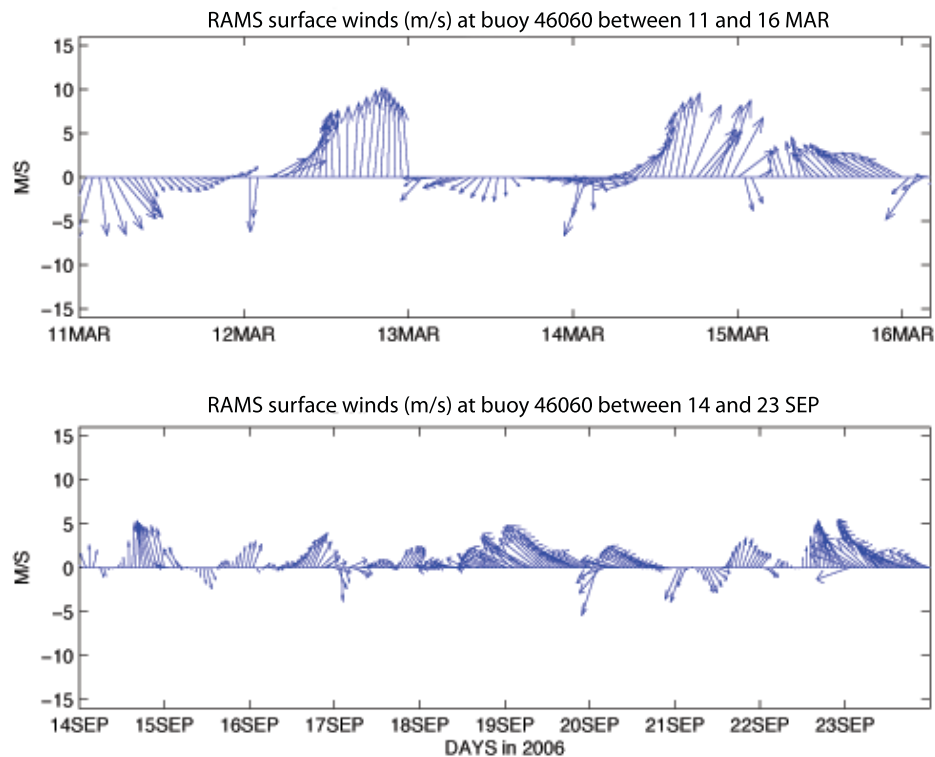


Figure 5.11: RAMS surface winds at 46060 between 11 MAR and 16 MAR, and between 14 SEP and 23 SEP

(ca. four inertial periods) anticyclones were not quasi-geostrophic eddies but near-inertial motions.

Another anticyclonic eddy seemingly experienced two stages of a life cycle: the eddy was generated between 14 SEP and 15 SEP when strong surface inflow occurred at HE (ca. 0.2 m/s; Fig. 5.14) and RAMS surface wind was predominantly northward with moderate wind speed (ca. 5 m/s; Fig. 5.11). The eddy translated northwestward with a radius of ca. 5 km afterwards under relatively weak RAMS surface winds (ca. 3 to 4 m/s). During translation of this anticyclonic eddy on 16 and 17 SEP, an adjacent, smaller cyclonic eddy was generated in the southwest quadrant. Probably associated with strong surface inflow at HE (ca. 0.2 m/s) and a predominant northwestward wind (ca. 8 to 10 m/s) on 18 and 19 SEP (Fig. 5.11), the anticyclonic eddy radius shrank, and the cyclonic eddy could not

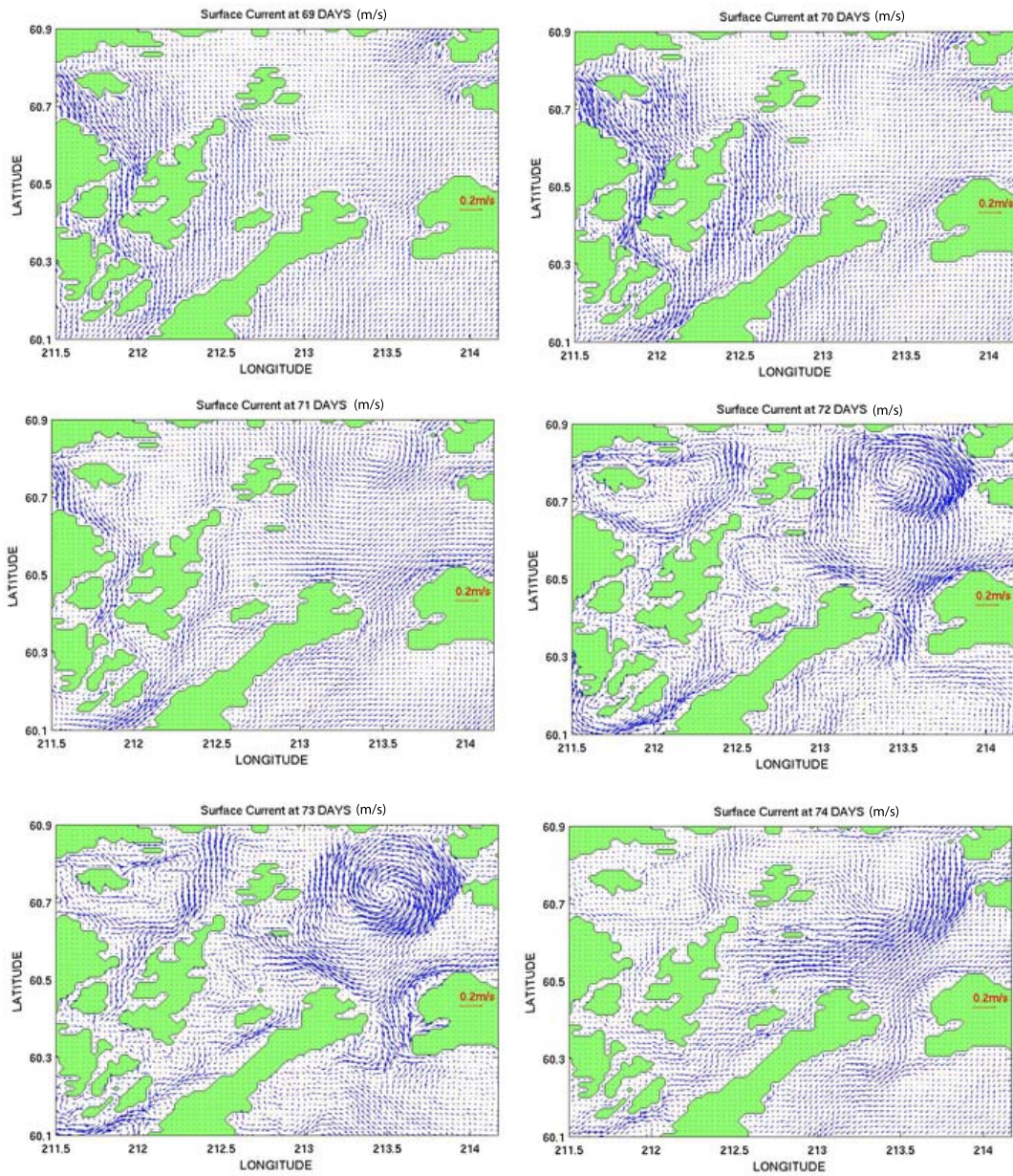


Figure 5.12: EPWS-POM simulated surface current in Central Sound between 11 MAR and 16 MAR

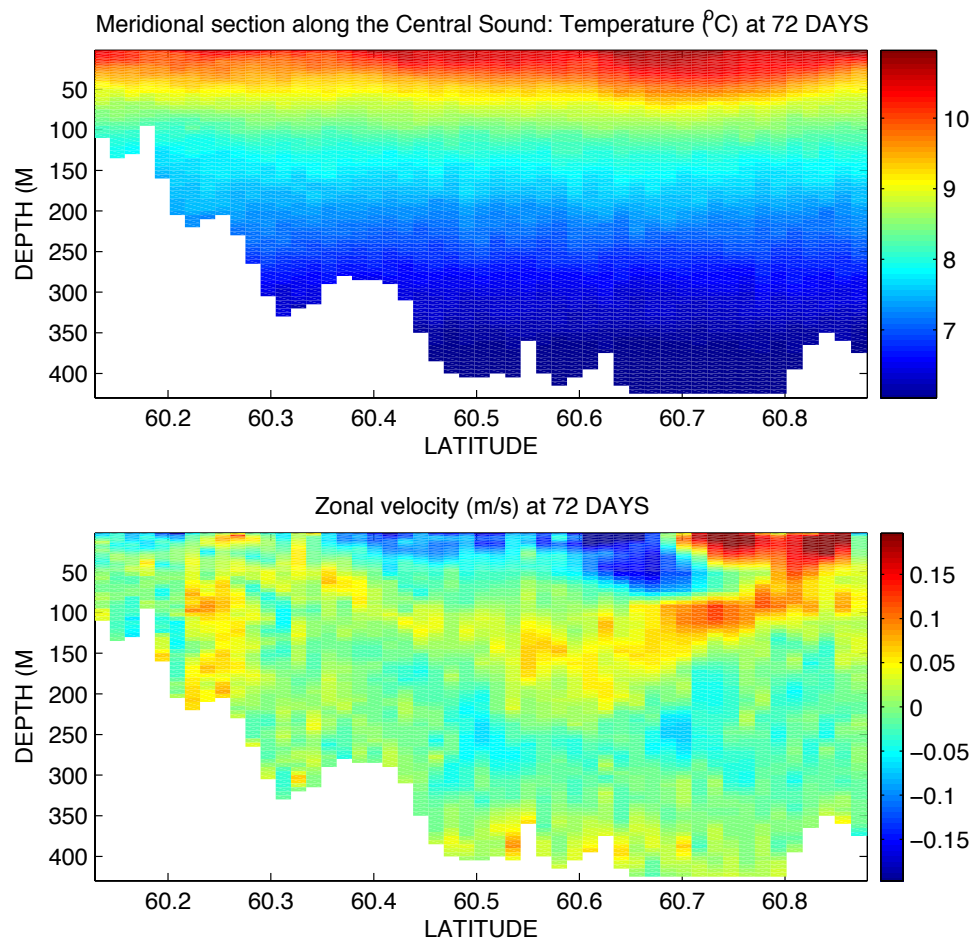


Figure 5.13: EPWS-POM simulated meridional section across Central Sound: (a) temperature and (b) zonal velocity

be recognized within the surface current field, and then, both eddies seemed to disintegrate on 19 SEP (Fig. 5.14). Nearly two days later on 21 SEP when the RAMS surface wind was initially southwestward (*ca.* 3 *m/s*), two eddies appeared in the surface current field and apparently shifted northwestward from the previous eddies (Fig. 5.15). They continued to translate northwestward on 22 SEP when HE surface inflow was weaker. On 23 SEP, with the presence of strong HE surface inflow and dominant northwestward wind (*ca.* 8 *m/s*), both eddies disintegrated permanently when approaching Naked Island. Again, these transient anticyclones were not quasi-geostrophic eddies but near inertial motions, which are commonly forced the synoptic winds in PWS.

5.3 Summary and Discussion

RAMS mesoscale winds are used in EPWS-POM simulations to investigate PWS response to surface wind forcing. During a one-year (2006) simulation period, the sea level response is generally small except when strong surface winds are blowing. In Central Sound, mesoscale circulation is dominated by anticyclonic eddies: these quasi-geostrophic eddies may reside for months, as in MAY, JUN and JUL, while in other seasons, anticyclones can be generated at different locations and normally persist for several days as near inertial motions.

Wind-driven volume transports are dominantly in through HE and out through MS with reversed flow mainly in JAN, JUN and NOV. The maximum barotropic volume transport is *ca.* 0.13 Sv, significantly smaller than the maximum value (*ca.* 0.6 Sv) in volume transport response to synoptic LSC. Except in DEC, predominant two-layer flows, e.g., surface outflow over bottom inflow, develop at MS. At HE, vigorous bottom inflow occurs throughout the

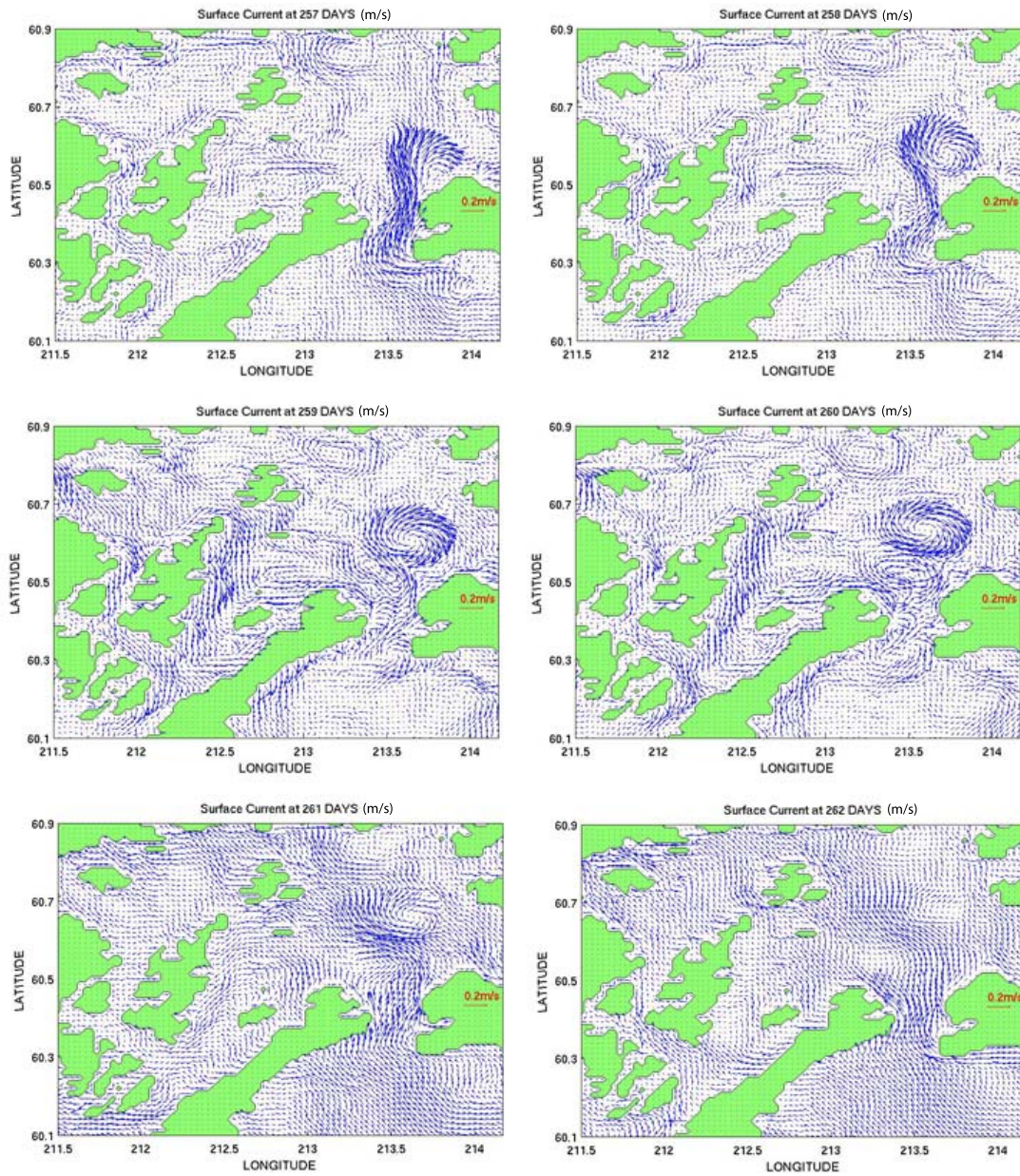


Figure 5.14: EPWS-POM simulated simulated surface current in Central Sound between 14 SEP and 19 SEP

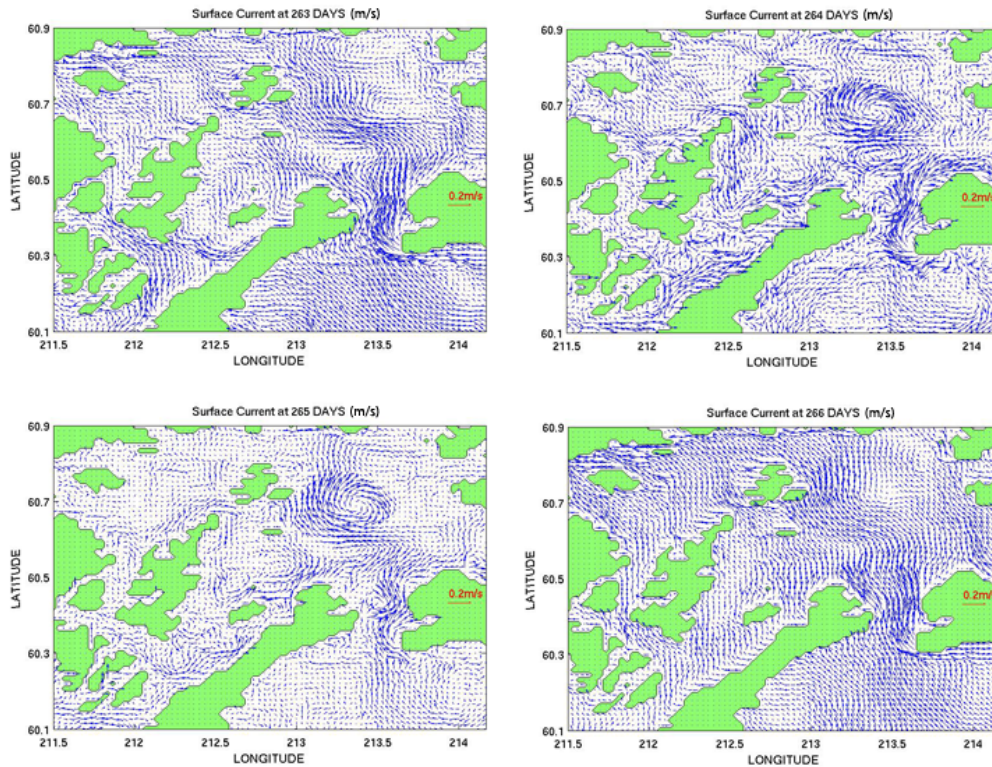


Figure 5.15: EPWS-POM simulated simulated surface current in Central Sound between 20 SEP and 23 SEP

year, and well-defined layered flows develop in NOV and DEC. In DEC, three-layer flows are prominent at both HE and MS.

Upper layer isotherms in PWS are displaced upward or downward with respect to strong northward or southward winds. The vertical displacement is as large as *ca.* 50 m in FEB and NOV when RAMS surface wind speed was over 20 m/s. The cool deep water ($< 5^{\circ}C$) at BH is not significantly affected by RAMS mesoscale winds, and no such deep water is developed in Central Sound.

Chapter 6

Response of Prince William Sound to Tides

As one of the most prominent phenomena in coastal oceans, the tides, including vertical motion of coastal sea levels and horizontal motion of tidal currents, have been well-known for centuries. Coastal regions are the most important dissipation zones for tidal energy (Egbert and Ray, 2000). The dissipated tidal energy, partially via breaking of internal waves of tidal period or internal tides, drives turbulence and mixing, which helps to redistribute water properties and influence ocean circulation (Garrett, 2003). Consequently, nutrients and dissolved gases are also redistributed, affecting biological productivity in coastal oceans.

Tidal motions are energetic in PWS; the tidal height is normally 3 *m* along the coast (for instance, Fig. 1.10), and the tidal current is as strong as 1.5 *m/s* in channels and nearshore regions (Gay and Vaughan, 2001). Interactions between tides and topography-complex, density-stratified PWS are regarded as a source for the production of internal tides, and upon the breaking of these internal tides, substantial mixing throughout the water column occurs, especially over the topography with critical slopes (Ivey and Nokes, 1989). ADCP-observed and EPWS/NFS-simulated M2 vertical profiles of horizontal tidal currents in Central Sound suggest propagation of internal tides (Fig. 1.19). No systematic

studies on internal tides in PWS, however, have yet been conducted partly because there are not many suitable sub-surface observations available allowing field investigations on the generation, propagation, and dissipation of internal tides. On the other hand, due to the sensitivity of internal tides to the shape/slope of sea bottom, numerical investigations may fail to accurately represent observed tidal currents unless topographic variations can be sufficiently resolved (Holloway and Merrifield, 1999).

As a preliminary study, high-resolution EPWS-POM is utilized to investigate some basic properties of barotropic and baroclinic tides in PWS, and the annual tidal energy budget is estimated via the present numerical investigation.

6.1 Methodology

POM has been widely used to simulate both barotropic and baroclinic tides in coastal oceans (Blumberg and Kantha, 1985; Foreman, 1995; Galperin and Mellor, 1990a, 1990b; Holloway, 1996; Petrucio *et al.*, 2002), and reasonable accuracy has been obtained in simulating both sea levels and tidal currents. Inclusion of density stratification in 3-D numerical simulations significantly improves the representation of tidal current ellipses in coastal regions; for instance, off Northern British Columbia (Cummins and Oey, 1997).

Similar to prior numerical studies (Chapters 3 and 5), EPWS-POM starts with the same initial condition on 01 JAN 2006 and runs for one year. For better introduction of tidal motions into EPWS-POM as OBCs, a separate 2-D tidal model is implemented, covering the area slightly larger than the EPWS-POM domain (Fig. 6.1). Based on POM, this 2-D tidal model is incorporated with the realistic coastlines, and forced by eight tidal constituents (amplitudes and phases), namely, four major semi-diurnal constituents (M2,

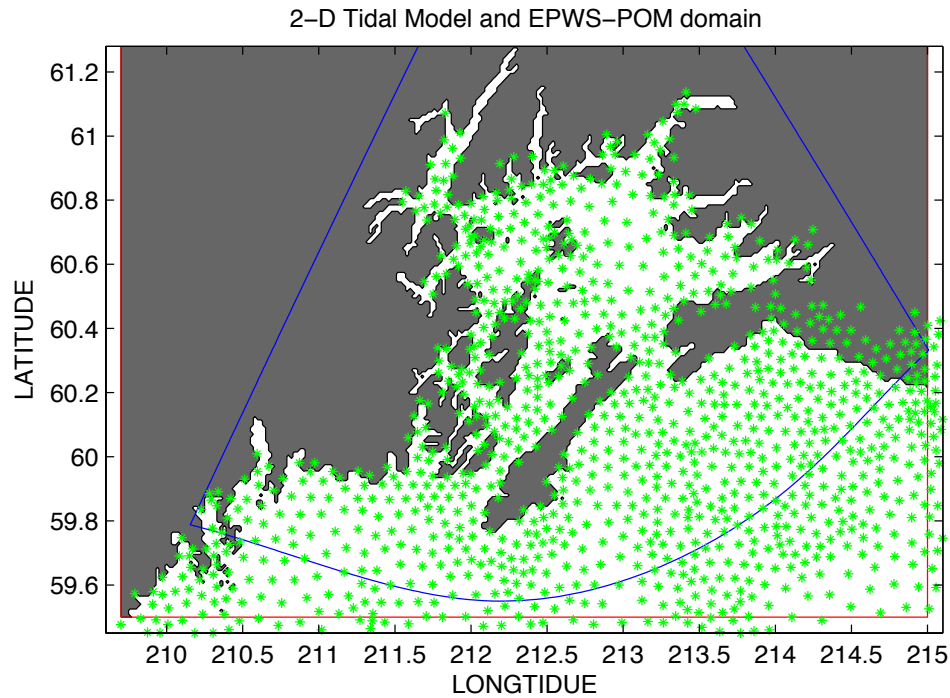


Figure 6.1: Domain of the 2-D tidal model (red lines) and locations of available tidal constituents (green stars) based on a North Pacific tidal model. For comparison, EPWS-POM domain is also indicated (blue lines).

S2, N2, K2) and four major diurnal constituents (K1, O1, P1, Q1). These tidal constituents are obtained from a high-resolution, data-assimilative North Pacific tidal model (Foreman *et al.*, 2000) and interpolated to the open boundaries of the 2-D tidal model. No other external forcings (LSC/AP/winds/surface heating/cooling, *etc.*) are imposed for the present tidal simulations.

The initial conditions of the 2-D tidal model are obtained from EPWS/NFS sea levels and depth-averaged currents on 1 JAN 2006. Then, it is run for the full year of 2006, and provides sea level fluctuations and barotropic currents along EPWS-POM open boundary every 12 minutes. Both sea levels and currents are specified since previous experience with EPWS/NFS suggests that, compared with PWS/NFS results, better simulation of baroclinic tidal currents in Central Sound in EPWS/NFS (Figs. 1.19 and 1.20) is achieved

Table 6.1: *rmse/std* of EPWS/NFS, the 2-D tidal model, and EPWS-POM simulated CSLs at tide gauges (unit: *m*)

	EPWS/NFS	2-D Tidal Model	EPWS-POM
Cordova	0.78/1.20	0.27/1.08	0.29/1.20
Valdez	0.64/1.02	0.24/1.07	0.24/1.16
Seward	0.58/1.16	0.22/0.97	0.22/1.02

Table 6.2: Cross-correlations (at zero lag) between EPWS/NFS, the 2-D tidal model, and EPWS-POM simulated CSLs compared with tide gauges

	EPWS/NFS	2-D Tidal Model	EPWS-POM
Cordova	0.85	0.98	0.97
Valdez	0.84	0.98	0.98
Seward	0.85	0.98	0.98

due to specification of both tidal height and current at EPWS/NFS open boundaries. No other external forcings are imposed for the present EPWS-POM simulation.

6.2 Response of PWS to Tides

With the annual-mean removed, EPWS-POM simulation of observed CSLs at three tide gauges (Cordova, Seward and Valdez; Fig. 6.2) has *STDs* of 1.20, 1.16, and 1.02 *m*, with *rmse* of 0.29, 0.24, and 0.22 *m* and cross-correlations of 0.98, 0.97, and 0.98, respectively. Compared with the 2-D tidal model and EPWS/NFS (Section 1.3.5), EPWS-POM achieves nearly the same performance for CSLs as the 2-D tidal model does, and it is a substantial improvement over EPWS/NFS (Tables 6.1 and 6.2).

In Central Sound, EPWS-POM simulation of horizontal currents is generally in phase with ADCP observations, except for northward component near the bottom (Figs. 6.3 and 6.4). At a depth of 25 *m*, simulated currents are significantly less energetic, and apparently due to the occurrence of cyclonic gyre in Central Sound in AUG, large fluctuations of

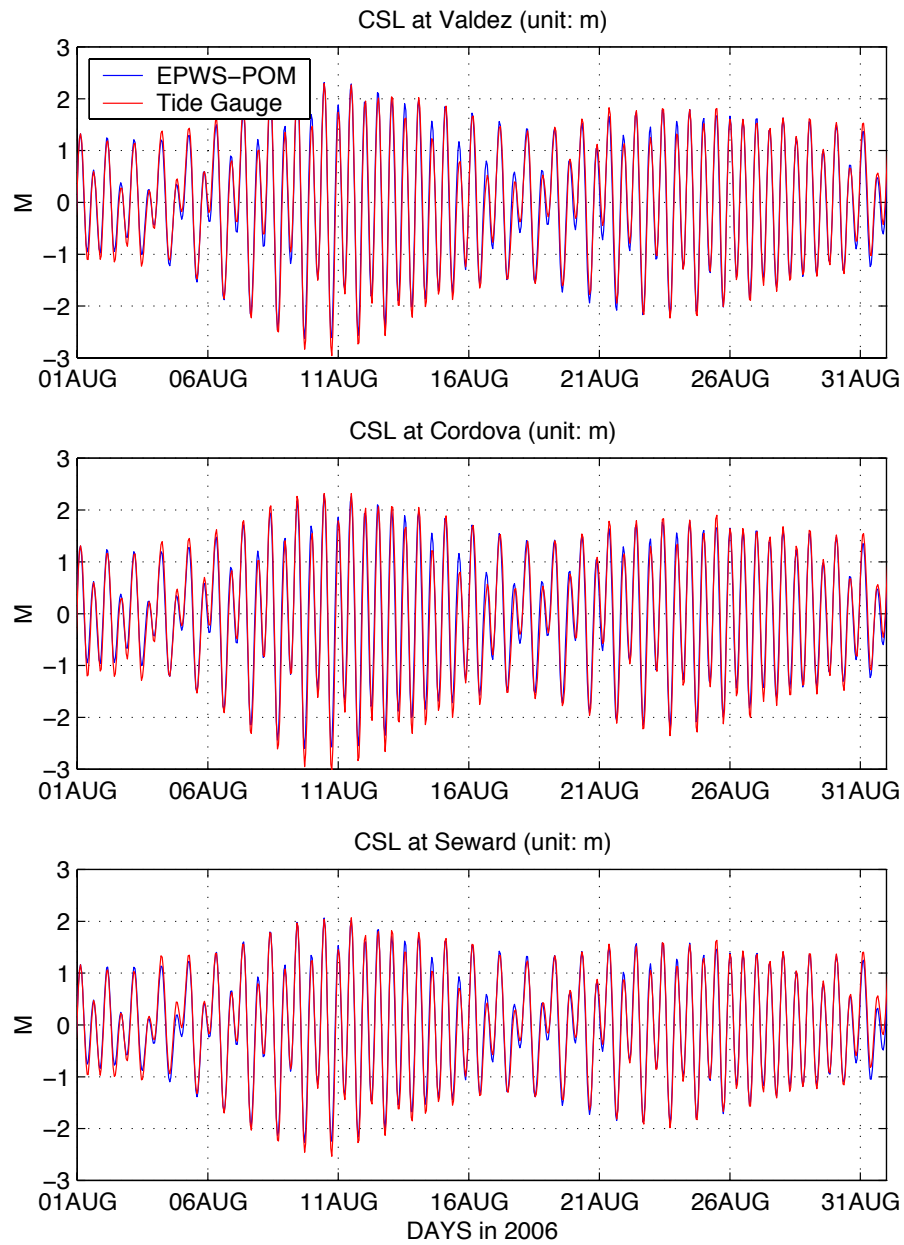


Figure 6.2: One-month comparisons of EPWS-POM simulated (blue) and tide gauge observed (red) CSLs at Cordova, Valdez and Seward

observed currents (ca. 0.5 m/s) are absent in EPWS-POM. Below 100 *m*, EPWS-POM-simulated and ADCP-observed currents have similar variability; for instance, at depths of 200 *m* and 368 *m*, EPWS-POM eastward velocities closely agree with observations between 09 and 14 AUG (Fig. 6.3). However, EPWS-POM-simulated northward velocity at a depth of 368 *m* are nearly 180° out-of-phase with the observed value (Fig. 6.4).

The cool deep water ($< 5^{\circ}C$) at BH is absent in JUN (Fig. 6.5), and no such deep water is developed at 46060. Furthermore, SST at both BH and 46060 are cooler, accompanying a ca. 20 *m* upward displacement of 8° isotherm at the end of 2006. The apparent vertical mixing of temperature in PWS may be related to the dissipation of incoming tidal energy, as discussed further in the next section.

Tide-driven volume transport at HE is more energetic than at MS, and cross-correlation between simulated HE and MS volume transports is 0.89 at zero lag (Fig. 6.6). The maximum cross-correlation is 0.98 at 12-hr lag. At semi-diurnal tidal periods, HE and MS volume transports are highly-coherent and in-phase, while at diurnal tidal periods, they are highly-coherent but out-of-phase (Fig. 6.6). There is no well-defined “transition band” in the coherence pattern between volume transports. Across HE, annual-mean northward velocity transect is characterized by strong bottom inflows (ca. 0.1 m/s; Fig. 6.7). Overall, no vigorous layered flows are developed at both HE and MS.

Within a semi-diurnal tidal period, a maximum speed of ca. 0.5 *m/s* in surface tidal currents occurs at HE and MS (Fig. 6.8). Strong tidal current (ca. 0.3 *m/s*) also occurs in the channel southwest of Naked Island. In Central Sound, typical surface tidal currents are less than 0.2 *m/s*.

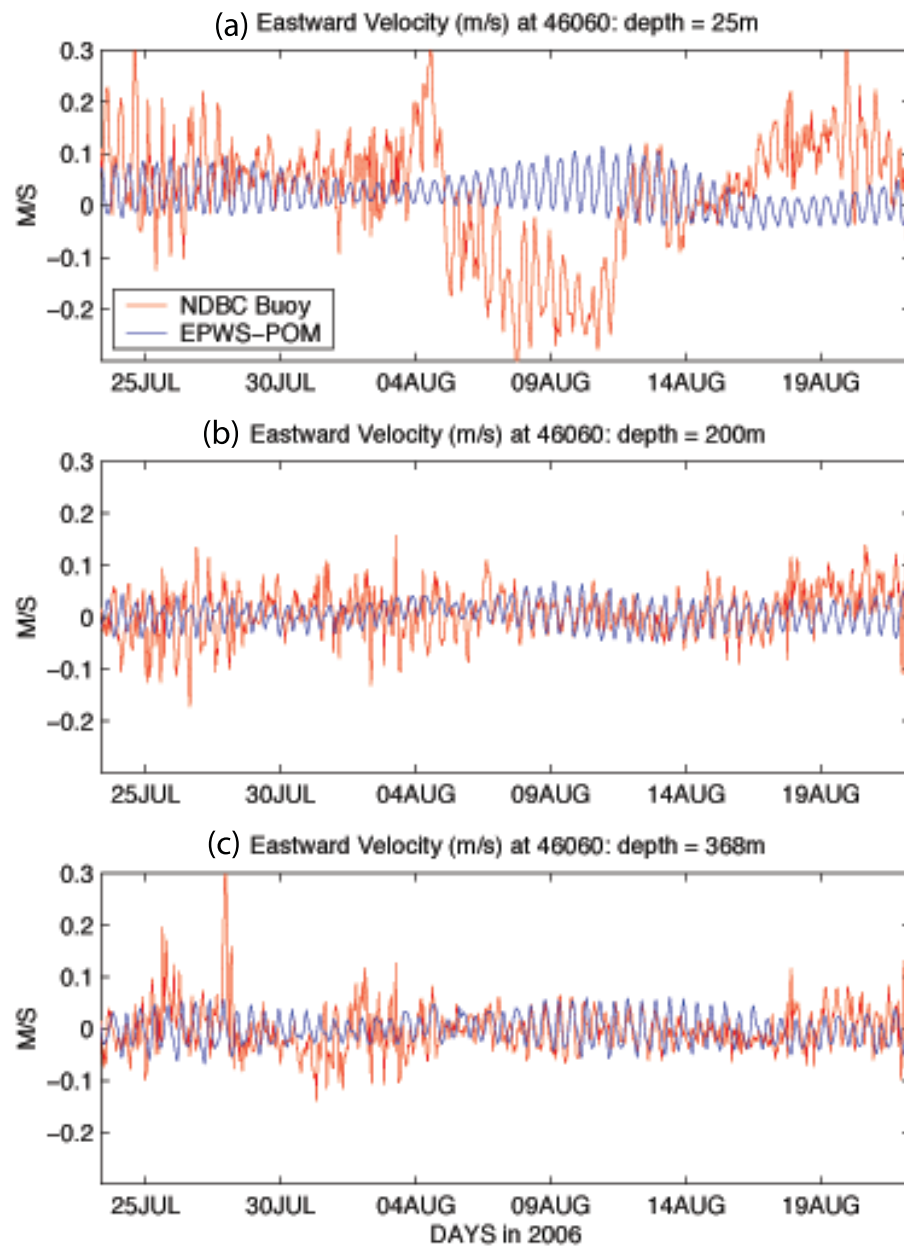


Figure 6.3: One-month (24 JUL to 23 AUG) comparisons of EPWS-POM simulated (blue) and ADCP observed (red) eastward velocity at 46060: (a) 25 m; (b) 200 m; and (c) 368m. Observed velocity is obtained from ADCP deployment during the same month in 2005

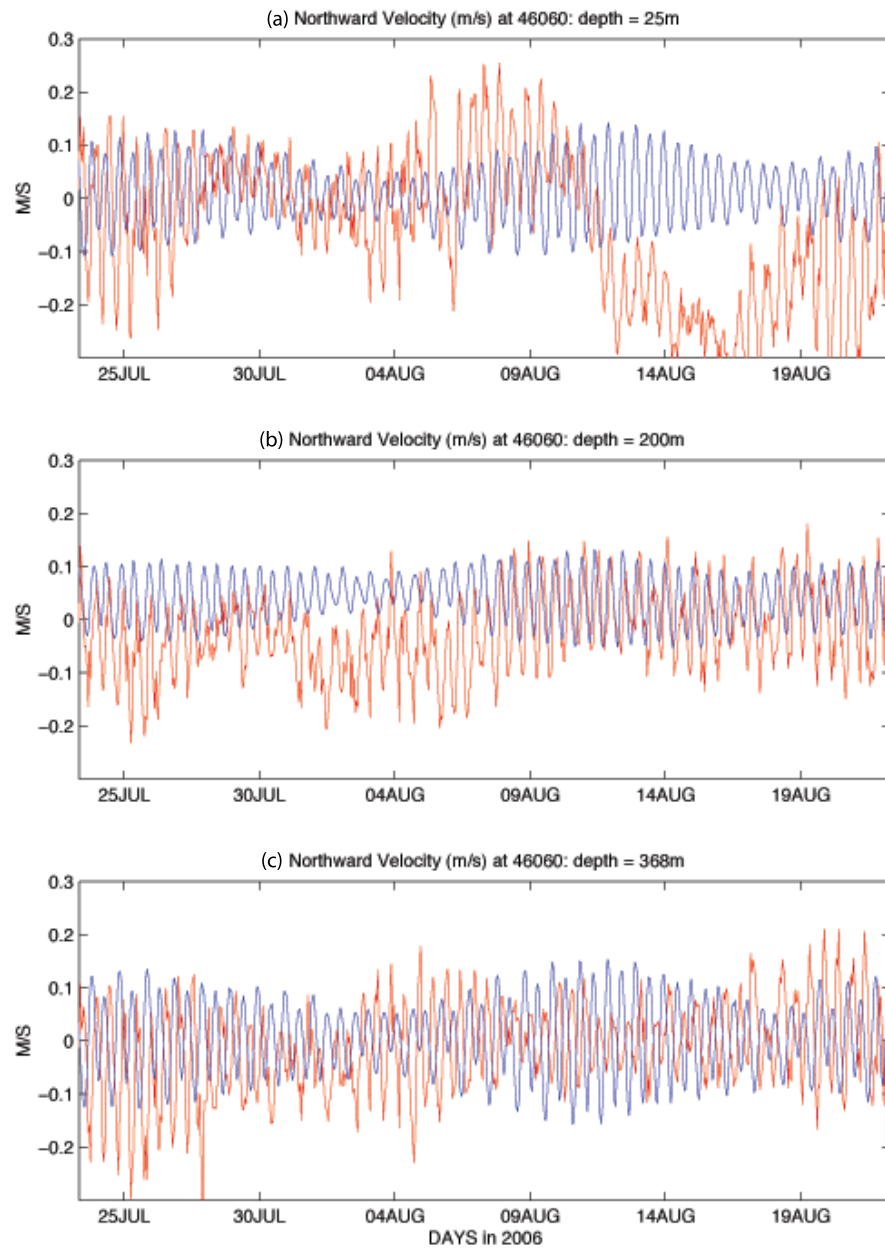


Figure 6.4: One-month (24 JUL to 23 AUG) comparisons of EPWS-POM simulated (blue) and ADCP observed (red) northward velocity at 46060: (a) 25 m; (b) 200 m; and (c) 368m. Observed velocity is obtained from ADCP deployment during the same month in 2005

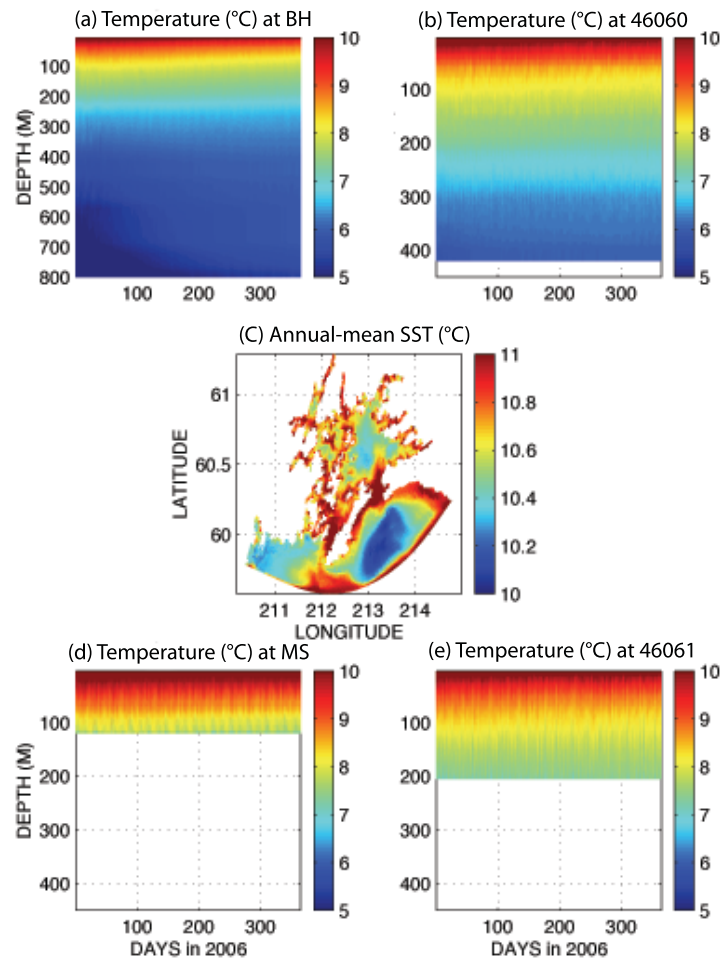


Figure 6.5: EPWS-POM simulated 1-yr temperature time-depth plots at (a) BH, (b) 46060, (d) MS, and (e) 46061, along with (c) annual-mean SST

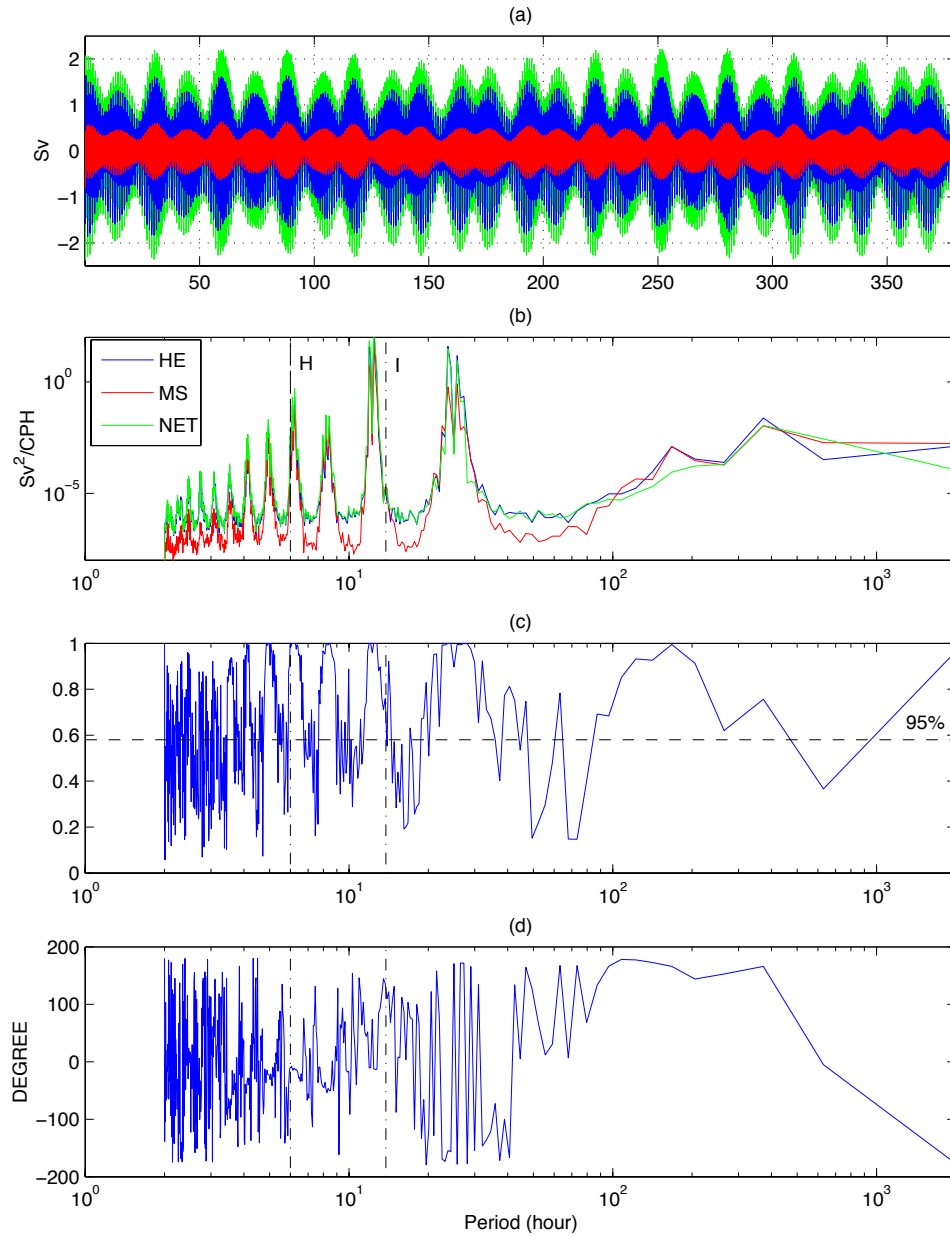


Figure 6.6: EPWS-POM simulated 1-yr (a) volume transports through HE (red) and MS (blue), as well as the net transport (green); (b) corresponding power spectra (DOF=10); (c) coherence squared between volume transports through HE and MS; and (d) phase. KEY: H, Helmholtz resonance period for PWS (*ca.* 6 hrs); I, inertial period (13.8 hrs).

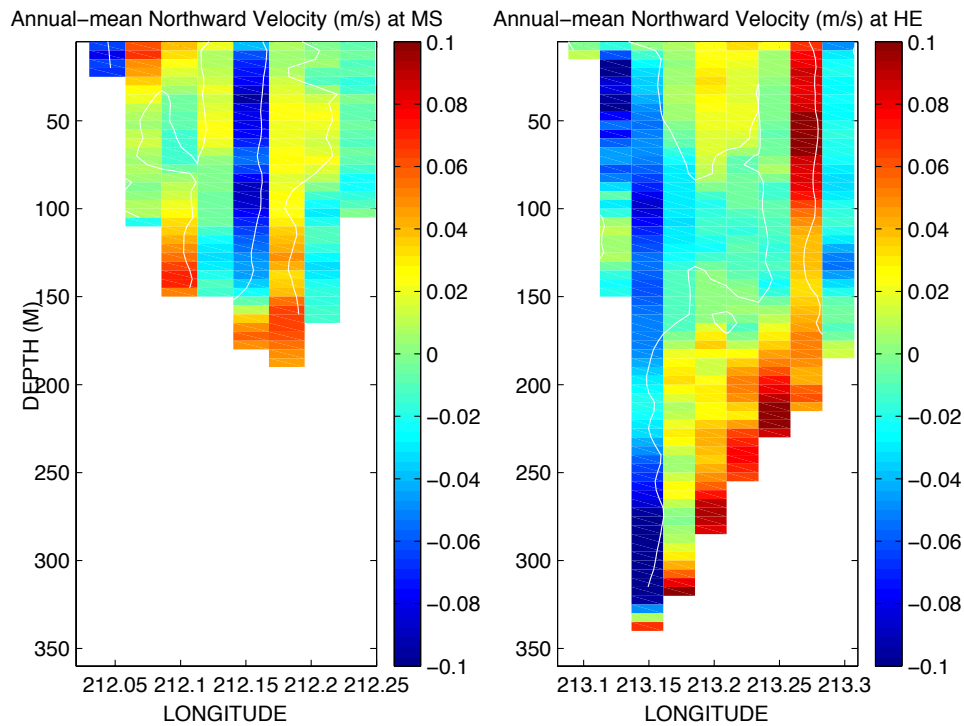


Figure 6.7: EPWS-POM simulated annual-mean northward velocity transect at MS and HE

6.3 Tidal Energy Flux and Dissipation

Numerical circulation models are widely used to examine tidal energy flux and dissipation in the coastal oceans (Holloway, 1996; Zhong and Li, 2006; Pereira and Castro, 2006). The dissipated tidal energy is one of the most important mechanisms for turbulent mixing over the shelf or inside estuaries. As a semi-enclosed sea, PWS exchanges water mass and energy with the open ocean via HE and MS, and thus, it is convenient to firstly examine the total amount of tidal energy flux through these two straits. Then, the spatial distribution of tidal energy dissipation in PWS will be investigated.

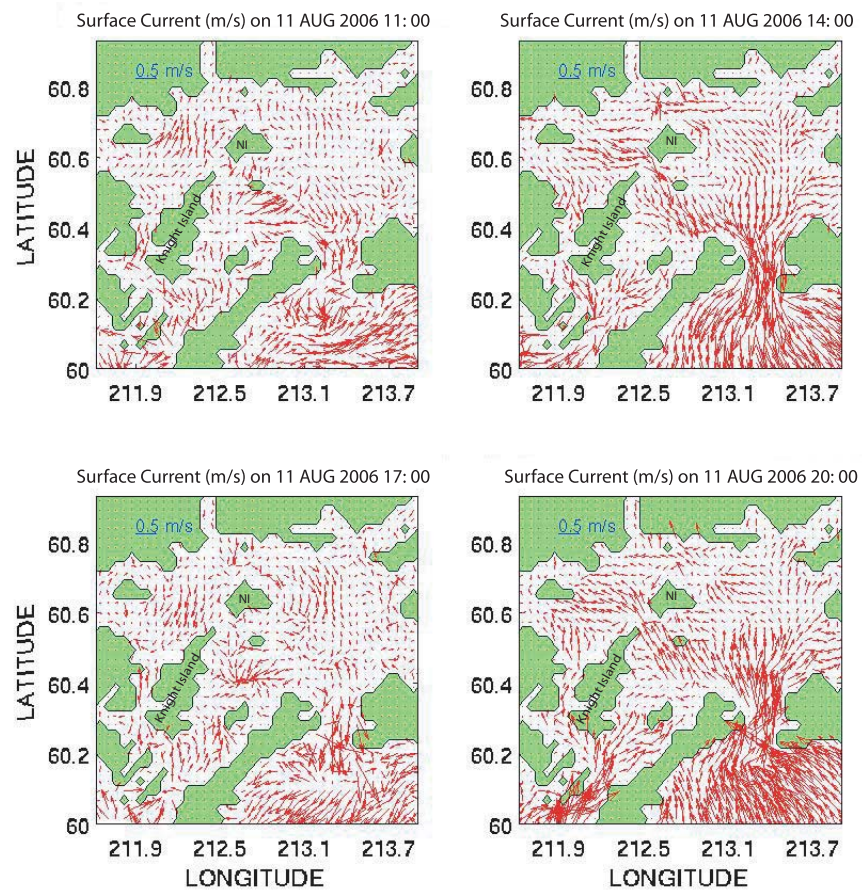


Figure 6.8: EPWS-POM simulated surface current in PWS on 11 AUG 2006

Associated with barotropic tidal motion, the mean energy flux normal to a control volume (V) with a lateral surface (S) over a tidal period are given as

$$\vec{F} = \int \int \left\langle \left(p + \rho_0 \frac{u^2 + v^2}{2} \right) \vec{u} \cdot \vec{n} \right\rangle dS, \quad (6.1)$$

(Gill, 1982), where the angle brackets denote the time average, and p is dynamic pressure, ρ_0 the reference density (1025 kg/m^3), u, v instantaneous depth-averaged horizontal velocity components, and $\vec{u} \cdot \vec{n}$ the depth-averaged velocity normal to the surface (S). The kinetic energy (i.e., the second term on right-hand side) contribution to the energy flux is normally two orders of magnitude smaller than the potential energy flux, and will be neglected in the subsequent calculation (Zhong and Li, 2006). Therefore, the depth-integrated energy flux per unit length through each strait is approximately

$$\vec{F} = \rho_0 g H \langle \vec{u} \eta \rangle, \quad (6.2)$$

where H is the water depth, η the sea level fluctuation, and \vec{u} the depth-averaged along-strait velocity. Based on one-year tide-driven EPWS-POM simulation, integration of (Eq. 6.2) across HE and MS yields that the annual-mean tidal energy fluxes entering PWS are *ca.* 750 MW ($1 \text{ MW} = 1.0 \times 10^6 \text{ Watt}$) through HE and *ca.* -495 MW through MS, respectively. Therefore, the net amount of annual-mean tidal energy flux entering PWS is *ca.* 255 MW.

The negative energy flux through MS suggests that for a multi-strait semi-enclosed sea, each strait may play a totally different role with respect to direction of tidal energy flux. One question though is “how is the role of each strait determined?”, or more specifically, “how does the negative energy flux occur at MS?” On the one hand, (Eq. 6.2) indicates that

opposite directions of energy flux through HE and MS occur only when either (i) depth-averaged velocities (or proportionally, volume transports) or (ii) sea level fluctuations, but not both (i) and (ii), at these two straits are out-of-phase. On the other hand, since the present EPWS-POM simulation is driven by tides only, it is reasonable to assume that the majority of the depth-averaged throughflow variability at HE and MS is associated with different tidal constituents. Therefore, as the coherence pattern between HE and MS volume transports indicates (Fig. 6.6), the out-of-phase relationship between volume transports driven by the diurnal tides contributes to the occurrence of the negative energy flux through MS when energy flux through HE is positive. A 12-hr lag for the maximum correlation between HE and MS volume transports also indicates the out-of-phase relationship between diurnal-tides related variability.

The estimated total tidal energy flux entering PWS is of the same order of magnitude as in the Chesapeake Bay, where a total of 188 MW tidal energy is found entering the Bay mouth (Zhong and Li, 2006). And significantly larger energy flux at HE, *e.g.*, 750 MW vs. 188 MW, is predominantly related to greater water depth (*ca.* 200 *m*) and larger tidal height (*ca.* 2 *m*) in the strait (Eq. 6.2) while the water depth and tidal height at the Bay mouth are *ca.* 30 *m* and 0.5 *m*, respectively.

Dissipation of tidal energy inside PWS is examined based on the integration of the energy equation (Gill, 1982),

$$\begin{aligned}
 Diss_e &= \int \int \int \rho_0 < [\frac{\partial}{\partial z}(uK_M \frac{\partial u}{\partial z}) + \frac{\partial}{\partial z}(vK_M \frac{\partial v}{\partial z})] > dV \\
 &- \int \int \int \rho_0 < K_M [(\frac{\partial u}{\partial z})^2 + (\frac{\partial v}{\partial z})^2] > dV \\
 &- \int \int \int \rho_0 < A_M [(\frac{\partial u}{\partial x})^2 + (\frac{\partial u}{\partial y})^2 + (\frac{\partial v}{\partial x})^2 + (\frac{\partial v}{\partial y})^2] > dV \quad (6.3)
 \end{aligned}$$

where K_M and A_M are the vertical and horizontal kinematic viscosity, respectively. The three terms on the right-hand side represent tidal energy dissipation due to bottom turbulence energy, horizontal diffusion, and vertical diffusion, respectively. The first term can be further simplified as

$$\begin{aligned} \int \int \int \rho_0 \left\langle \left[\frac{\partial}{\partial z} \left(u K_M \frac{\partial u}{\partial z} \right) + \frac{\partial}{\partial z} \left(v K_M \frac{\partial v}{\partial z} \right) \right] \right\rangle dV &= \int \int \langle \vec{u}_s \cdot \vec{\tau}_s - \vec{u}_b \cdot \vec{\tau}_b \rangle dS \\ &= - \int \int \rho_0 C_D \langle |\vec{u}_b|^3 \rangle dS \quad (6.4) \end{aligned}$$

(Zhong and Li, 2006) where it is assumed that the surface stress ($\vec{\tau}_s$) is zero since no surface wind is applied, and bottom stress ($\vec{\tau}_b$) is obtained via a logarithmic bottom boundary layer with a bottom roughness height of 0.01 m and quadratic bottom friction coefficient (C_D). The bottom velocity (\vec{u}_b) is approximated as the corresponding values at the EPWS-POM σ -level closest to the bottom.

In POM, the bottom friction coefficients (C_D), horizontal kinematic viscosity (A_M), and vertical kinematic viscosity (K_M) are readily available during model implementation and integrations; for instance, horizontal kinematic viscosity (A_M) is determined by the Smagorinsky diffusivity with the HORCON parameter, and vertical kinematic viscosity (K_M) is determined by embedded second moment turbulence closure sub-model (Mellor, 1973; Mellor and Yamada, 1982). The integrations in (Eq. 6.3 and 6.4) are conducted at each grid point, and over the water column for the horizontal and vertical diffusion terms, and then, averaged over the one-year simulation period. As a result, the simulated annual-mean tidal energy dissipation (Fig. 6.9) indicates that most of the tidal energy is dissipated

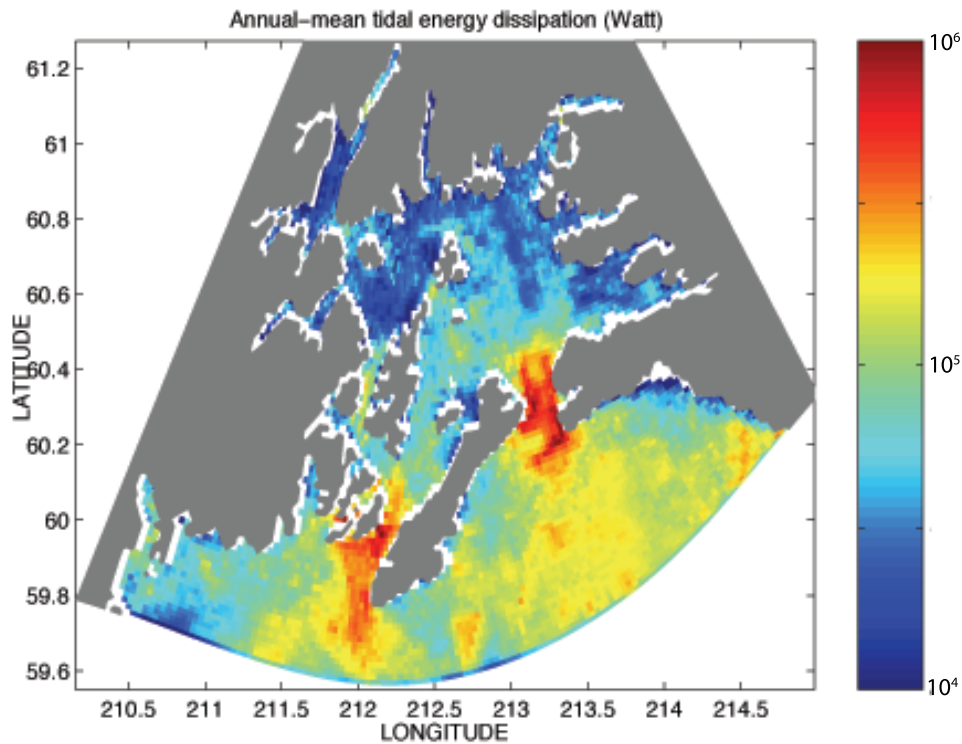


Figure 6.9: EPWS-POM simulated annual-mean tidal energy dissipation

at HE and MS, where interactions between the tidal currents and abrupt topographic variations probably generates turbulent eddies and results in high energy dissipation. The secondarily important dissipation region is the continental shelf outside PWS, while inside the Sound, much less tidal energy is dissipated presumably due to relatively deeper water and smaller tidal currents.

The total amount of annual-mean tidal energy dissipation in PWS is *ca.* 243 MW, which is *ca.* 12 MW less than the total incoming tidal energy flux via HE and MS. This discrepancy amounts to *ca.* 5% error and is probably due to the approximation to bottom velocities, numerical inaccuracy when velocity gradient terms in (Eq. 6.3) are computed, and to spatial integration discrepancies. Thus, a better agreement may be achieved if the bottom velocities are more accurately obtained via a logarithmic boundary layer approximation.

6.4 Baroclinic Tidal Energy Flux

The energy content of the internal tides is estimated to be 0.3% of the global barotropic tidal energy using an analytical model (Baines, 1982). Over large-scale mid-ocean ridges such as the Hawaiian Ridge, 8% of the barotropic tidal energy is transferred to baroclinic tides (Dushaw *et al.*, 1995). Observations over Mendocino Escarpment in the eastern North Pacific indicate that 3% of the barotropic tidal energy is converted to internal tides (Althaus *et al.*, 2003). General estimates for baroclinic energy are normally in the range of 1% to 10% (Wunsch 1975) of the barotropic tidal energy over steep topography. In the coastal ocean, baroclinic tidal energy varies with the season, depending on density stratification (Holloway, 1996). In PWS, due to limited observational evidence of baroclinic tidal energy, numerical simulation by EPWS-POM is used instead, as a preliminary study with focus on the spatial distribution of barotropic energy conversion to baroclinic tides.

Baroclinic tidal energy conversion can be examined as the horizontal energy flux transported by the internal tide velocity field over a tidal period, as

$$\vec{F}_{bc} = \frac{1}{T} \int \int p' \vec{u}' dt dz, \quad (6.5)$$

(Legg, 2003) where p' is the perturbation pressure and u' is the baroclinic perturbation velocity. p' is defined as the fluctuation component of the dynamic pressure relative to the background “mean” field (Brickman and Loder, 1993) and satisfies $\int p' dz = 0$ to obtain the perturbation pressure associated with internal tides only (Legg, 2003). u' is defined as $u - u_{bt}$ where u is the total velocity from the present baroclinic model run and u_{bt} the barotropic tidal velocity obtained from another model run with no density stratification but

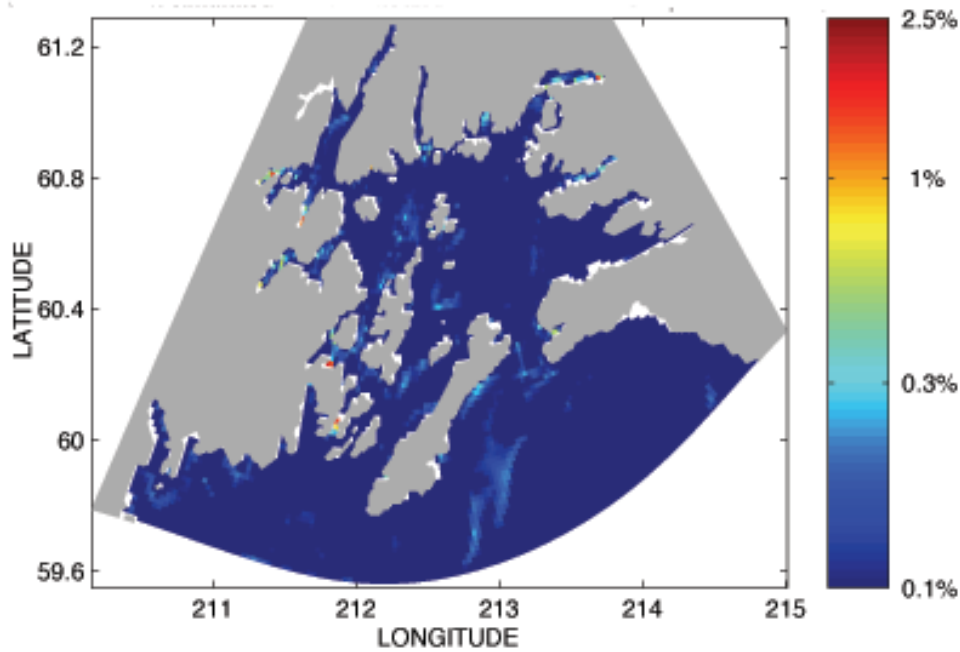


Figure 6.10: Ratio between EPWS-POM simulated annual-mean baroclinic and barotropic tidal energy flux

with identical tide forcing and topography (Holloway, 1996; Legg, 2003). Based on a one-year EPWS-POM simulation, (Eq. 6.5) is vertically integrated over the water column at each grid point to obtain the annual-mean baroclinic tidal energy flux in PWS. Associated with the annual-mean barotropic tidal energy flux (Eq. 6.2), conversion from barotropic to baroclinic tidal energy is less than 1% in most of PWS, while inside some narrow channels and small fjords, as much as *ca.* 2.5% of the barotropic tidal energy is converted to baroclinic tidal energy (Fig. 6.10). Since the generation of internal tides heavily depends on density stratification (Ivey and Nokes, 1989; Holloway, 1996), the present estimates of tidal energy conversion in PWS may change significantly when seasonal variability of density stratification is incorporated.

6.5 Summary and Discussion

The PWS response to tides has been investigated via two POM-based numerical implementations: a 2-D tidal models and 3-D baroclinic EPWS-POM. Incorporated with realistic topography, the 2-D tidal model covers a domain slightly larger than EPWS-POM, and is forced by four major semi-diurnal and four major diurnal tidal constituents from another high-resolution, data-assimilative North Pacific tidal model (Foreman *et al.*, 2000). The 2-D tidal model is then run for the year of 2006 and provides tidal heights and barotropic tidal currents along EPWS-POM open boundaries every 12 minutes. Forced by the 2-D tidal model, the one-year EPWS-POM simulated CSLs achieve substantial improvement, *e.g.*, better correlations and smaller *rmse* with observed CSLs, compared with EPWS/NFS at three tidal gauges. In Central Sound, EPWS-POM simulated and ADCP observed currents have similar variability except for the upper 100 *m*. However, the out-of-phase discrepancy between simulated and observed northward velocity near the bottom may be attributed to the lack of seasonal variations of density stratification, especially of the deep water development, in the EPWS-POM simulation. Based on the temperature time-depth plots in Central Sound and BH, it is thus suggested that the tides probably do not contribute to seasonal variability of the deep water in PWS.

A well-defined “transition band” is not found in the coherence pattern between simulated HE and MS volume transports, and no vigorous layered flows are developed at both straits. A 12-hr lag occurs in maximum correlation between volume transports, which is attributed to highly-coherent but out-of-phase relationship at diurnal tidal periods.

Based on the EPWS-POM simulation, the net annual-mean tidal energy flux entering PWS is *ca.* 255 MW, with incoming energy flux of *ca.* 750 MW though HE and outgoing

energy flux of *ca.* 495 MW through MS. The different roles played by HE and MS with respect to tidal energy flux are probably due to the out-of-phase diurnal tidal constituents at these two straits. A total of *ca.* 243 MW annual-mean tidal energy is dissipated inside PWS, with HE and MS identified as the most important tidal energy dissipation regions. The total dissipated energy in PWS differs by *ca.* 12 MW (or a 5% error) from the total incoming tidal energy flux (*ca.* 255 MW), and is probably due to approximations made during numerical computation. The annual-mean conversion from barotropic tidal energy to baroclinic tidal energy is less than 1% in most of PWS, but inside some narrow channels and small fjords, as much as *ca.* 2.5% barotropic tidal energy is converted to baroclinic tidal energy. These conversion rates, however, may change significantly when seasonal variations of density stratification and circulation are incorporated into the numerical simulations.

Chapter 7

Summary and Conclusions

Ever since early 2001, the quasi-operational ocean nowcast/forecast systems for Prince William Sound (PWS/NFS, and its successor EPWS/NFS beginning in early 2005) have improved our understanding of synoptic and general ocean circulation patterns in this small semi-enclosed sea. On the other hand, the multi-year experience with PWS/NFS and EPWS/NFS initially motivated the present dissertation research when new, challenging phenomena were revealed during a comprehensive assessment of the performance of these NFSs (Chapter 1; Mooers *et al.*, 2007). For instance, the so-called transition band in the coherence pattern between HE and MS volume transports, the seasonal changes between two-layer or three-layer velocity transects across HE and MS, the transient cyclonic and anticyclonic eddies and gyres in Central Sound, and the annual variability of salty, cool water near the bottom of Black Hole, raised new questions.

Associated with the purpose of the dissertation (Chapter 1), four POM-based numerical model implementations, *viz.*, EPWS-POM (Chapter 2), PWS-POM (Chapter 2), IPWS-POM (Chapter 3), and a 2-D tidal model (Chapter 6), along with an analytical Helmholtz resonance model (Chapter 3), were designed. With the horizontal resolution of *ca.* 1 km and 26 vertical σ -levels, EPWS-POM is readily coupled with data-assimilative Global-NCOM

and mesoscale RAMS, and utilized as the modeling backbone to simulate a wide range of physical processes in PWS. Embedded within EPWS-POM grids with a constant horizontal grid size ratio of 1:3, PWS-POM achieves higher horizontal resolution of *ca.* 300 *m.* Focused on mesoscale and sub-mesoscale circulations inside the Sound, PWS-POM is initialized from EPWS-POM field, and nested within EPWS-POM via a one-way, online coupling scheme. IPWS-POM is uniquely designed for an idealized two-strait, small semi-enclosed sea and used to (1) examine the results from the analytical Helmholtz resonance model, and (2) gain insight into the physical mechanisms and parameters controlling barotropic and baroclinic transports through HE and MS. Driven by eight tidal constituents from a data-assimilative North Pacific tidal model (Foreman *et al.*, 2000), the 2-D tidal model is implemented to incorporate tidal motions into EPWS-POM simulation via open boundaries.

Through use of all these models, the dissertation is aimed at addressing the PWS response to specific external forcings; *e.g.*, large-scale circulation (LSC) in NGOA (Chapter 3), atmospheric pressure (AP; Chapter 4) and mesoscale surface winds (Chapter 5), and tides (Chapter 6). Other forcings, for instance, surface heating/cooling, fresh water runoff along PWS coast, and evaporation/precipitation, are likely significant to PWS circulation as well. However, due to either research priority or perceived relative importance to PWS response, forcings other than those considered here will instead be treated in future studies.

The PWS response to LSC is investigated mainly via a one-year (2006) EPWS-POM simulation driven by annual-mean or synoptic data-assimilative Global-NCOM field. With time-independent annual-mean LSC imposed, PWS general surface circulation is characterized by a simple through-flow pattern (Niebauer *et al.*, 1994; Deleersnijder *et al.*, 1998), *i.e.*, a portion of the ACC enters PWS through HE and transits the Sound from east to

west before exiting through MS and rejoining the ACC. In this simple circulation picture, two-layer flows are developed at both straits. The introduction of time-dependent, synoptic variability of LSC greatly changes the through-flow circulation pattern in PWS: HE inflow volume transport is reversed mainly during summertime (MAY to AUG) and occasionally for a few days during other seasons. Two-layer flow dominates HE and MS baroclinic transport response to time-dependent LSC variability, while three-layer flow is present at HE in FEB and MAR, normally with weak bottom inflow velocity. Mesoscale circulation response to synoptic LSC is characterized by a persist cyclonic gyre in Central Sound in AUG and SEP, as found in observations (Cox. 2004; Vaughan *et al.*, 2001). While in other seasons, either cyclonic or anticyclonic eddies occur. The cyclonic gyre is further investigated via one-month (AUG) PWS-POM simulation, which reveals that the gyre is more accurately depicted as an ellipse with an equivalent radius of *ca.* 10 km, and its evolution is apparently affected by HE surface inflow. Time-dependent LSC greatly affects the deep water development in PWS, and seasonal variability of the deep water in Central Sound and BH is probably related to cool water intrusion via HE in MAY. Furthermore, synoptic LSC response suggests that the deep water in Central Sound is transported from BH.

The PWS response to AP is investigated via combination of the analytical Helmholtz resonance model and a series of IPWS-POM simulations. For a barotropic ocean, sea level response to AP similarly to a classic Helmholtz resonator with the maximum gain at the period of barotropic Helmholtz resonance. Density stratification introduces the transition band in the coherence pattern between HE and MS volume transports. The characteristics of the “transition band” depend on various physical parameters, including the ratio between baroclinic Rossby Radius and the length of the straits. Baroclinic transports respond to

AP by vigorous three-layer flows with the transport through each layer significantly larger than the corresponding barotropic transport,

The PWS response to surface wind is investigated via one-year (2006) EPWS-POM simulation driven by RAMS mesoscale winds. Wind-driven volume transports are dominantly in through HE and out through MS. And, consistent with the seasonal cycle of the local weather system, volume transports are significantly larger in fall and winter (*ca.* 0.1 *Sv*) than in spring and summer (*ca.* 0.05 *Sv*). Strong inflow (*ca.* 0.1 *m/s*) occurs near the bottom of HE in 2006, and no well-defined layered flow is developed in wind-driven HE baroclinic transport except in NOV and DEC. In Central Sound, anticyclonic eddies dominate the wind-driven induced mesoscale circulation. These eddies can last as quasi-geostrophic gyres for months, as in MAY, JUN and JUL; while in other seasons, anticyclones are generated and dissipated typically within a week as near-inertial motions.

The PWS response to tides is investigated via a one-year (2006) EPWS-POM simulation driven by the 2-D tidal model. Based on the simulation, tides do not affect seasonal variability of the deep water in PWS, but substantial vertical mixing of temperature and salinity in Central Sound and BH is probably due to dissipated tidal energy. The total annual-mean tidal energy flux entering PWS is *ca.* 255 MW, with incoming energy flux of *ca.* 750 MW through HE and outgoing energy flux of *ca.* 485 MW through MS. The different roles played by HE and MS with respect to direction of tidal energy flux are presumably attributed to the out-of-phase relationship of along-strait diurnal tidal current at these two straits. A total amount of *ca.* 243 MW annual-mean tidal energy is dissipated inside PWS with *ca.* 5% error from the total tidal energy flux entering PWS presumably due to approximations made for computation of velocity gradient terms in discrete numerical grids. HE

Table 7.1: Some aspects of PWS response to external forcings

External Forcing	Max. Barotropic Transport (Sv)	Transition Band	Baroclinic Flow	Dominant Eddies (Central Sound)
LSC	0.6	5-30	two/three layers	cyclones (AUG-SEP)
AP	0.02	9-40	three layers	N/A
Winds	0.13	5-20	two/three layers	anticyclones (MAY-JUL)
Tides	2.0	N/A	largely barotropic	N/A

and MS are the most important tidal energy dissipation regions. Annual-mean conversion from barotropic to baroclinic tidal energy flux is less than 1% in most of PWS, while as much as 2.5% of the tidal energy is converted into internal tides in some small fjords and channels along the PWS coast.

In conclusion, far from a simple through-flow circulation, the PWS general circulation presents a much more complicated pattern along with vigorous exchange flow between PWS and the shelf. Further comparisons between some aspects of PWS response to external forcings (Table 7.1) indicates that except for tides, LSC contributes most significantly to barotropic/volume transports, followed by surface winds. And also except the tides, LSC, AP and winds are all associated with the occurrence of the “transition band” between HE and MS volume transports, and with the development of the layered baroclinic flow at HE and MS. Mesoscale circulation in Central Sound is substantially affected by both LSC and surface winds. On the other hand, AP and tides are less important for the development of mesoscale eddies in PWS.

Finally, specific answers to the questions in Chapter 1 can be provided as below,

- (1) **What causes the seasonal change from two-layer mean flow at HE and MS in the wintertime to three-layer mean flow for the remainder of the**

year?

EPWS/NFS simulation suggests that the seasonal change in buoyancy over the shelf and PWS is the dominant factor controlling the seasonal transition of two-layer/three-layer baroclinic flows at HE. Numerical studies of HE and MS baroclinic transport response to external forcings indicate that except for tides, both large-scale circulation and mesoscale winds contribute significantly to the development of two-layer/three-layer flows. Seasonal variability of these layered flows can thus be caused by large-scale circulation and mesoscale winds via seasonal changes in the stratification.

- (2) **Why does a large cyclonic gyre occur in PWS in late summer, while in other seasons the predominant circulation pattern in central PWS may be either cyclonic or anticyclonic?**

The large cyclonic gyre in PWS in late summer (AUG and SEP) is associated with the intrusion of warm, fresh surface water via HE in JUL. In other seasons, the presence of either cyclonic or anticyclonic eddies in Central Sound is attributed to both large-scale circulation and mesoscale winds.

- (3) **Considering that the sills just outside the two main entrances impede the entry of the deeper NGOA coastal waters into PWS, and that the seasonal heating/cooling, freshening/salinification, and stratification of PWS are strong factors, what controls the formation, properties, and variability of the PWS deep water?**

Seasonal variability of the deep water in PWS is significantly affected by large-scale circulation in NGOA, and is presumably related to the cool water intrusion

through HE in MAY. The deep water in Central Sound is likely transported from BH, but not vice versa. In comparison, both mesoscale winds and tides may contribute insignificantly to the formation and development of the deep water in PWS.

- (4) **What is the nature of the PWS response to synoptic atmospheric forcing? In particular, what is the nature of the flow in the so-called transition band in the coherence and phase patterns between HE and MS volume transports?**

As a small semi-enclosed sea, barotropic PWS responds to AP similarly to a classic Helmholtz resonator. Density stratification is likely the only factor determining the occurrence of the “transition band” in the coherence pattern between HE and MS volume transports. The characteristics of this “transition band” directly depend on the ratio between baroclinic Rossby radius and the lengths of the straits.

- (5) **Associated with the complex bottom topography and density stratification, how are the tides dissipated inside PWS? What is the PWS’s annual tidal energy budget?**

Annual-mean tidal energy flux entering PWS is *ca.* 255 MW, and HE and MS the most important regions for tidal energy dissipation. In most of PWS, less than 1% of the barotropic tidal energy is converted into baroclinic tides.

Bibliography

- Althaus, A.M., E. Kunze, and T.B. Sanford, 2003: Internal tide radiation from Mendocino Escarpment. *J. Phys. Oceanogr.*, 33, 1510-1527.
- Baines, P.G., 1982: On internal tide generation models, *Deep Sea Res.*, 29, 307-338.
- Bang, I. and Kowalik, Z., 1994: A numerical modeling study on the interannual variability in the Gulf of Alaska. *Journal of Korean Society of Coastal and Ocean Engineers*, 6, 298-308.
- Bang, I. and Mooers, C.N.K., 2003: The influence of several factors controlling the interactions between Prince William Sound, Alaska, and the Northern Gulf of Alaska. *J. Phys. Oceanogr.*, 33, 19-36.
- Bang, I., Vaughan, S.L. and Mooers, C.N.K., 2005: Initial steps toward validation of a seasonal cycle simulation for Prince William Sound circulation (flow and mass) fields. *Cont. Shelf Res.*, 25, 901-934.
- Barron, C. N., Kara, A. B., Martin, P. J., Rhodes, R. C. and Smedstad, L. F., 2006: Formulation, implementation and examination of vertical coordinate choices in the Global Navy Coastal Ocean Model (NCOM). *Ocean Modelling*, 11 (3-4), 347-75.
- Berntsen, J., 2002: Internal pressure errors in Sigma-Coordinate Ocean Models. *J. Atmos. Oceanic Tech.*, 19, 1403-1414.
- Blumberg, A.F. and Kantha, L.H., 1985: Open boundary conditions for circulation models. *J. Hydraulic. Eng.*, 111, 237-255.
- Blumberg, A.F. and Mellor, G.L., 1987: A description of a three-dimensional coastal ocean circulation model. In: *Heaps, N.S. (Ed.), Coastal and Estuarine Science 4: Three-Dimensional Coastal Ocean Models*, Vol. 18, American Geophysical Union, Washington, DC, 1-16 pp.
- Bond, N.A. and Macklin, S.A., 1992: Aircraft observations of offshore-directed flow near Wide Bay, Alaska. *Mon. Wea. Rev.*, 121, 150-61.

- Bond, N.A. and Stabeno, P.J., 1998: Analysis of surface winds in Shelikof Strait, Alaska, using moored buoy observations. *Weather and Forecasting*, 13, 547-59.
- Candela, J., 1991: The Gibraltar Strait and its role in the dynamics of the Mediterranean Sea. *Dyn. Atmos. Oceans.*, 15, 267-300.
- Chassignet, E.P. and Malanotte-Rizzoli, P., 2000: Ocean circulation model evaluation experiments for the North Atlantic basin. *Special issue of Dyn. Atmos. Oceans*, 32, 155-432.
- Chu, P.C., and Fan, C.W., 1997: Sixth-order difference scheme for sigma coordinate ocean models. *J. Phys. Oceanogr.*, 27, 2064-2071.
- Cooney, R.T., Allen, J.R. Bishop, M.A., Eslinger, D.L., Kline, T., Norcross, B.L., Mcroy, C.P., Milton, J., Olsen, J., Patrick, V., Paul, A.J., Salmon, D., Scheel, D., Thomas, G.L., Vaughan, S.L. and Willette, T.M., 2001: Ecosystem controls of juvenile pink salmon (*Onchorynchus gorbusha*) and Pacific herring (*Clupea pallasii*) populations in Prince William Sound, Alaska. *Fish. Oceanogr.*, 10 (Suppl. 1), 1-13.
- Cox, W. 2004: The Prince William Sound 2004 Lagrangian Field Experiment. *Technical Report*. Oil Spill Recovery Institute (OSRI).
- Crawford, W.R. and Whitney, F.A., 1999: Mesoscale eddy swirl with data in Gulf of Alaska, *Eos Trans. AGU*, 80(33), 365-370.
- Cummins, P.F. and Oey, L.-Y., 1997: Simulation of barotropic and baroclinic tides off northern British Columbia. *J. Phys. Oceanogr.*, 27, 762781.
- Davies, H.C., 1976: A lateral boundary condition formulation for multi-level prediction model. *Quart. J. Roy. Meteor. Soc.*, 102, 405-418.
- Deleersnijder, E., Wang, J. and Mooers, C.N.K., 1998: A two-compartment model for understanding the simulated three-dimensional circulation in Prince William Sound, Alaska. *Cont. Shelf. Res.*, 18, 279-287.
- Dodimead, A.J., Favorite, F. and Hirano, T., 1963: Review of oceanography of the subarctic Pacific Region. Salmon of the North Pacific Ocean. *Bull. Int. N. Pac. Fish. Comm.*, 13, 195 pp.
- Drijfhout, S., 1994: Heat transport by mesoscale eddies in an ocean circulation model. *J. Phys. Oceanogr.*, 24, 353-369.
- Ducet, N., Le Traon, P.Y. and Gauzelin, P., 1999: Response of the Black Sea mean level to atmospheric pressure and wind forcing. *J. Mar. Sys.*, 22, 311-27.
- Dushaw, B.D., Worcester, P.F., Cornuelle, B.D., Howe, B.M., and Luther, D.S., 1995: Baroclinic and barotropic tides in the central North-Pacific Ocean determined from long-range reciprocal acoustic transmissions. *J. Phys. Oceanogr.*, 25, 631-647.
- Egbert, G. D. and Ray, R. D., 2000: Significant dissipation of tidal energy in the deep ocean inferred from satellite altimeter data. *Nature*, 405, 775778.

- Ezer, T. and Mellor, G.L., 1997: Simulations of the Atlantic Ocean with a free surface sigma coordinate ocean model, *J. Geophys. Res.*, 102, 15647-15657.
- Ezer, T., Arango, H. and Shchepetkin, A.F., 2002: Developments in terrain-following ocean models: intercomparisons of numerical aspects. *Ocean Modelling*, 4, 249-67.
- Foreman, M.G., 1995: Tide removal requiring a dynamical interpretation. In: Lynch, D.R., Davies, A.M. (Eds.), *Quantitative Skill Assessment for Coastal Ocean Models*. American Geophysical Union, pp. 224239.
- Foreman, M.G., Crawford, W.R., Cherniawsky, J.Y., Henry R.F. and Tarbotton. M.R., 2000. A high-resolution assimilating tidal model for the northeast Pacific Ocean. *J. Geophys. Res.*, 105, 28629-28652.
- Fox, A.D. and Maskell, S.J., 1995: Two-way interactive nesting of primitive equation ocean models with topography. *J. Phys. Oceanogr.*, 25, 2977-2996.
- Fringer, O. B., McWilliams, J.C. and Street, R.L., 2006: A New Hybrid Model for Coastal Simulations. *Oceanography*. 19 (1), 46-59.
- Galperin, B. and Mellor, G.L., 1990a: A time-dependent, three-dimensional model of the Delaware Bay and River. Part I: Description of the model and tidal analysis. *Estuarine, Coastal and Shelf Sci.*, 31, 231-253.
- Galperin, B. and Mellor, G.L., 1990b: A time-dependent three-dimensional model of the Delaware Bay and River. Part II: Three-dimensional flow fields and residual circulation. *Estuarine, Coastal and Shelf Sci.*, 31, 255-281.
- Garrett, C., 2003: Mixing with latitude. *Nature*, 422, 477-478.
- Gay, S.M.III and Vaughan, S.L., 2001: Seasonal hydrography and tidal currents of bays and fjords in Prince William Sound, Alaska. *Fish. Oceanogr.*, 10(Suppl. 1), 159-193.
- Gill, A.E., 1982: *Atmosphere-ocean Dynamics*. Academic Press, San Diego, Calif.
- Goldstein, H., Poole, C.P., and Safko, J.L., 2002: *Classical Mechanics (3rd Edition)*, Addison Wesley, ISBN 0-201-65702-3.
- Haney, R.L., 1991: On the pressure gradient force over steep topography in Sigma Coordinate Ocean Models. *J. Phys. Oceanogr.*, 21, 610-19.
- Helfrich, K. R., 1995: Time-Dependent Two-Layer Hydraulic Exchange Flows. *J. Phys. Oceanogr.*, 25, 359-373.
- Helmholtz, H.L.F., 1912: On the Sensations of Tone as a Physiological Basis for the Theory of Music, Fourth Edition, Longmans, Green, and Co.
- Holloway, P.E., 1996. A numerical model of internal tides with application to the Australian north west shelf. *J. Phys. Oceanogr.*, 26, 2137.
- Holloway, P.E. and Merrifield, M.A., 1999: Internal tide generation by sea mounts, ridges, and islands. *J. Geophys. Res.*, 104, 25937-25951.

- Ivey, G.N. and Nokes, R.I., 1989: Vertical mixing due to the breaking of critical internal waves on sloping boundaries, *J. Fluid Mechanics*, 204, 479-500.
- Jin, M-B. and Wang, J., 2004: Interannual variability and sensitivity study of the ocean circulation and thermohaline structure in Prince William Sound, Alaska. *Cont. Shelf Res.*, 24, 393-411.
- Johnson, W.R. and Royer, T.C., 1986: A comparison of two current meters on a surface mooring. *Deep Sea Res.*, 33, 1127-38.
- Johnson, W.R., Royer, T.C. and Luick, J.L., 1988: On the seasonal variability of the Alaska Coastal Current. *J. Geophys. Res.*, 93, 12423-12437.
- Kantha, L.H. and Clayson, C.A., 2000: *Numerical Models of Oceans and Oceanic Processes*. Academic Press, San Diego, 940 pp.
- Kar, S.K. and Turco, R.P., 1995: Formulation of a lateral sponge layer for limited-area shallow-water models and an extension for the vertically stratified case. *Monthly Weather Review*, 123, 1542-1559.
- Kara, A. B., Metzger, E. J., Hurlburt, H. E., Wallcraft, A. J., and Chassignet, E., 2007: An eddy-resolving ocean model for the Pacific Ocean: Par 1: Deep convection and its relation to SST anomalies. *J. Geophys. Res.*, submitted.
- Large, W.G. and Pond, S., 1981: Open ocean momentum flux measurements in moderate to strong winds. *J. Phys. Ocean.*, 11, 324-36.
- Lehmann, R., 1993: On the choice of relaxation coefficients for Davies' lateral boundary scheme for regional weather prediction models. *Meteor. Atmos. Phys.*, 52, 1-14.
- Legg, S., 2003: Internal Tides Generated on a Corrugated Continental Slope. Part I: Cross-Slope Barotropic Forcing. *J. Phys. Ocean.*, 34, 156-173.
- Linder, C.A. and Gawarkiewicz, G., 1998: A climatology of the shelf break front in the Middle Atlantic Bight. *J. Geophys. Res.*, 103, C9, 18,405-23.
- Liu, H., Olsson, P. Q., Volz, K. P., and Yi, H., 2006: A climatology of mesoscale model simulated low-level wind jets over Cook Inlet and Shelikof Strait, Alaska. *Estuarine, Coastal and Shelf Science*, 70, 551-66.
- Lyu, S.J., Kim, K. and Perkins, H.T., 2002: Atmospheric pressure-forced subinertial variations in the transport through the Korea Strait. *Geophys. Res. Lett.*, 29, NO. 9, 10.1029/2001GL014366.
- Lyu, S. J., and Kim, K., 2005: Subinertial to interannual transport variations in the Korea Strait and their possible mechanisms, *J. Geophys. Res.*, 110, C12016.
- Macklin, S.A., Lackmann, G.M. and Gary, J., 1988: Offshore-directed winds in the vicinity of Prince William Sound, Alaska. *Mon. Wea. Rev.*, 116, 1289-301.
- Mellor, G.L., 1973: Analytic prediction of the properties of stratified planetary surface layers. *J. Atmos. Sci.*, 30, 1061-1069.

- Mellor, G.L., 2002: *User' Guide for a Three-Dimensional, Primitive Equation, Numerical Ocean Model*. Princeton University, 41 pp.
- Mellor, G.L., Ezer, T. and Oey, L.Y., 1994: The pressure gradient conundrum of sigma coordinate ocean models. *J. Atmos. Oceanic. Technol.*, 11, 1126-1134.
- Mellor, G.L., Oey, L.-Y. and Ezer, T., 1998: Sigma coordinate pressure gradient errors and the seamount problem. *J. Atmos. Oceanic Technol.*, 15, 1122-31.
- Mellor, G.L. and Yamada, T., 1982: Development of a turbulence closure model for geophysical fluid problems. *Reviews of Geophysics and Space Physics*, 20, 851-875.
- Melsom, A., Meyers, S.D., Hurlburt, H.E., Mezger, E.J. and O'Brien, J.J., 1999: ENSO effects on Gulf of Alaska eddies. *Earth Interactions*, 3, 1-30. (Available at <http://EarthInteractions.org>)
- Mooers, C.N.K. and Wang, J., 1998: On the implementation of a three-dimensional circulation model for Prince William Sound, Alaska. *Cont. Shelf. Res.*, 18, 253-277.
- Mooers, C.N.K., Wu, X. and Bang, I., 2007: Performance of a nowcast/forecast system for Prince William Sound, Alaska *Cont. Shelf. Res.*, accepted.
- Muench, R.D. and Heggie, D.T., 1978: Deepwater exchange in Alaskan subarctic fjords, in *Estuarine Transport Processes*, edited by B. Kjerfve, *Belle W. Baruch Libr. Mar Sci.*, 7, 239-267.
- Murray, C.P., Morey, S.L. and O'Brien, J.J., 2001: Interannual variability of upper ocean vorticity balances in the Gulf of Alaska. *J. Geophys. Res.*, 106, 4779-91.
- Niebauer, H.J., Royer, T.C. and Weingartner, T.J., 1994: Circulation of Prince William Sound, Alaska. *J. Geophys. Res.*, 99, 14113-14126.
- Okkonen, S.R., Jacobs, G.A., Metzger, E.J., Hurlburt, H.E. and Shriver, J.F., 2001: Mesoscale variability in the boundary currents of the Alaska Gyre. *Cont. Shelf Res.*, 21, 1219-36.
- Okkonen, S.R., Weingartner, T.J., Danielson, S.L., Musgrave, D.L. and Schmidt G.M., 2003: Satellite and hydrographic observations of eddy-induced shelf-slope exchange in the northwestern Gulf of Alaska. *J. Geophys. Res.*, 108, 3033-3042.
- O'Connor, W.P., Bromwich, D.H. and Carrasco, J.F., 1994: Cyclonically forced barrier winds along the Transantarctic Mountains near Ross Island. *Mon. Wea. Rev.*, 122, 137-50.
- Overland, J.E. and Hiestler, T.R., 1980: Development of a synoptic climatology for the northeast Gulf of Alaska. *J. Appl. Meteor.*, 19, 1-14.
- Palma, E.D. and Matano, R.P., 2000: On the implementation of open boundary conditions for a general circulation model: the three-dimensional case. *J. Geophys. Res.*, 105, 8506-27.
- Parish, T., 1982: Barrier winds along the Sierra Nevada mountains. *J. Appl. Meteor.*, 12, 925-930.

- Penven, P., Debreu, L., Marchesiello, P. and McWilliams, J.C., 2006: Evaluation and application of the ROMS: 1-way embedding procedure to the central California upwelling system. *Ocean Modelling*, Vol. 12, 157-87.
- Pereira, A.F. and Castro, B.M., 2006: Internal tides in the Southwestern Atlantic off Brazil: observations and numerical modeling. *J. Phys. Oceanogr.*, 37, 1512-1526.
- Petruncio, E.T., Paduan, J.D. and Rosenfeld, L.K., 2002: Numerical simulations of the internal tide in a submarine canyon. *Ocean Modelling*, 4, 221-248.
- Pielke, R.A., Cotton, W.R., Walko, R.L., Tremback, C.J., Lyons, W.A., Grasso, L.D., Nicholls, M.E., Moran, M.D., Wesley, D.A., Lee, T.J., and Copeland, J.H., 1992: A comprehensive meteorological modeling system – RAMS. *Meteor. Atmos. Phys.*, 49, 69-91.
- Putins, P., 1966: The sequence of baric pressure pattern over Alaska. Studies on the meteorology of Alaska. First Interim Report, Environmental Data Service, ESSA, Washington, DC, 57 pp.
- Ray, R.D. and Mitchum, G.T., 1997: Surface manifestation of internal tides in the deep ocean. *Prog. in Oceanogr.*, 40, 135-62.
- Reed, R.K. and Schumacher, J.D., 1986: Physical oceanography. In: *The Gulf of Alaska, Physical and Biological Resources*. D.W. Hood and S.T. Zimmerman (eds). Alaska Office, Ocean Assessments Division, NOAA, Alaska, pp. 655.
- Reynolds, T.L. and DeCola, E., 2001: Prince William Sound Meteorological Workshop, Final Proceedings. Oil Spill Recovery Institute, Cordova, AK.
- Rhodes, R.C., Hurlburt, H.E., Wallcraft, A.J., Barron, C.N., Martin, P.J., Metzger, E.J., Shriver, J.F., Ko, D.S., Smedstad, O.M., Cross, S.L. and Kara, A.B., 2002: Navy Real-Time Global Modeling Systems, *Oceanography*, 15, 29-43.
- Roed, L. P. and Smedstad, O. M., 1984: Open boundary conditions for forced waves in a rotating fluid. *SIAM J. Sci. Stat. Comput.*, 5, 414-426.
- Royer, T.C., 1975: Seasonal variations of waters in the Northern Gulf of Alaska. *Deep Sea Research*, 22, 403-416.
- Royer, T.C., 1979: On the effect of precipitation and runoff on coastal circulation in the Gulf of Alaska. *J. Phys. Oceanogr.*, 9, 555-63.
- Royer, T.C., 1981: Baroclinic transport in the Gulf of Alaska. II. Fresh water driven coastal current. *J. Mar. Res.*, 39, 251-266.
- Royer, T.C., 1982: Coastal fresh water discharge in the northeast Pacific. *J. Geophys. Res.*, 87, 2017-2021.
- Royer, T.C., 1998: Coastal processes in the northern North Pacific. in *The Sea*, Vol. 11, *The Global Coastal Ocean: Regional Studies and Syntheses*. A.R. Robinson and K.H. Brink, eds. John Wiley & Sons, Inc. 395-414.

- Royer, T.C., Hansen, D.V. and Pashinski, D.J., 1979: Coastal flow in the Northern Gulf of Alaska as observed by dynamic topography and satellite tracked drogued drift buoys. *J. Phys. Oceanogr.*, 9, 785-801.
- Royer, T.C., Vermersch, J.A., Weingartner, T.J., Niebauer, H.J. and Muench, R.D., 1990: Ocean circulation influencing the *Exxon-Valdez* oil spill. *Oceanography*, 3, 3-10.
- Rudnick, D.L., Boyd, T.J., Brainard, R.E., Carter, G.S., Egbert, G.D., Gregg, M.C., Holloway, P.E., Klymak, J.M., Kunze, E., Lee, C.M., Levine, M.D., Luther, D.S., Martin, J.P., Merrifield, M.A., Moum, J.N., Nash, J.D., Pinkel, R., Rainville, L. and Sanford, T.B., 2003: From tides to mixing along the Hawaiian Ridge. *Science*, 301, 355-57.
- Schmidt, G.M., 1977: The exchange of water between Prince William Sound the Gulf of Alaska. *Master's thesis*, 116 pp., University of Alaska, Fairbanks.
- Schumacher, J.D., Stabeno, P. and Roach, A.T., 1990: Volume transport in the Alaska Coastal Current. *Cont. Shelf. Res.*, 9, 1071-83.
- Simmons, H.L., 1996: Estimation of freshwater runoff into Prince William Sound using a digital elevation model. *Master's thesis*, University of Alaska Fairbanks, 78 pp.
- Smeed, D.A., 2000: Hydraulic control of three-layer exchange flows: application to the Bab al Mandab. *J. Phys. Oceanogr.*, 30, 2574-2588.
- Sofianos, S., 2000: Circulation and water mass formation in the Red Sea, and the exchange with the Indian Ocean. *Dissertation*, University of Miami.
- Soloviev, M.A., 1999: Assessment of mesoscale eddy parameterizations for coarse resolution ocean models. Ph.D. Dissertation. MIT/WHOI, 99-14.
- Smagorinsky, J., 1963: General circulation experiments with the primitive equations I: The basic experiment, *Monthly Weather Review*, 91(3), 99-164.
- Spall, M.A. and Holland, W.R., 1991: A nested primitive equation model for oceanic applications. *J. Phys. Oceanogr.*, 21, 205-220.
- Spiegel, E.A. and Veronis, G., 1960: On the Boussinesq approximation for a compressible fluid. *Astrophys. J.*, 131, 442-447.
- Tabata, S., 1982: The anticyclonic, baroclinic eddy off Sitka, Alaska, in the northeast Pacific Ocean. *J. Phys. Oceanogr.*, 12, 1260-82.
- Thomson, R.E. and Gower, J.F.R., 1998: A basin-scale oceanic instability event in the Gulf of Alaska. *J. Geophys. Res.*, 103, 3033-40.
- Toulany, B. and Garrett, C., 1984: Geostrophic control of fluctuating barotropic flow through straits. *J. Phys. Oceanogr.*, 14, 649-655.
- Vaughan, S.L., Mooers, C.N.K. and Gay III, S.M., 2001: Physical variability in Prince William Sound during the SEA study (1994-98). *Fish. Oceanogr.*, 10 (Suppl. 1), 58-80.

- Voropayev, S. I., Smirnov, S. A., and Brandt, A., 2001: Dipolar eddies in a stratified shear flow. *J. Fluid Mech.*, Vol. 13, Issue 12, 3820-3823.
- Wang, J., Jin, M.-B., Musgrave, D.L. and Ikeda, M., 2004: A hydrological digital elevation model for fresh water discharge into the Gulf of Alaska. *J. Geophys. Res.*, 109, C07009, doi:10.1029/2002JC001430.
- Wang, J., Jin, M., Patrick, E.V., Allen, J.R., Eslinger, D.L., Mooers, C.N.K. and Cooney, R.T., 2001: Numerical simulations of the seasonal circulation patterns and thermohaline structures of Prince William Sound, Alaska. *Fish. Oceanogr.*, 10 (Suppl.1), 132-148.
- Weingartner, T.J., Finney, B., Haldorson, L., Stabeno, P., Napp, J., Strom, S., Brodeur, R., Dagg, M., Hopcroft, B., Hermann, A., Hinckley, S., Royer, T.C., Whittedge, T., Coyle, K., Kline, T., Lessard, E., Haidvogel, D., Farley, E. and Lee, C., 2002: The Northeast Pacific GLOBEC Program: Coastal Gulf of Alaska. *Oceanography*, 15, 30-35.
- Weingartner, T.J., Danielson, S.L. and Royer, T.C., 2005: Freshwater variability and predictability in the Alaska Coastal Current, *Deep-Sea Research Part II-Topical Studies in Oceanography*, 52, 169-191.
- Williams, W.J., Weingartner, T.J. and Hermann, A.J., 2007: Idealized three-dimensional modeling of seasonal variation in the Alaska Coastal Current. *J. Geophys. Res.*, 112, C07001, doi:10.1029/2005JC003285, 2007.
- Wilson, J.G. and Overland, J.E., 1986: Meteorology. In *The Gulf of Alaska Physical Environment and Biological Resources*, D.W. Hood and S.T. Zimmerman, eds., OCS Study MMS86-0095. Minerals Management Service, Springfield, Va., pp. 31-54.
- Woodruff, S.D., Diaz, H.F., Elms, J.D., and Worley, S.J., 1998: COADS Release 2 data and metadata enhancements for improvements of marine surface flux fields. *Phys. Chem. Earth*, 23, 517-526.
- Wu, X., 2003: Assessment of a North Pacific data-assimilating ocean circulation model as a means for down-scaling to a higher-resolution, extended Prince William Sound circulation model. *Master's thesis*, University of Miami, 120 pp.
- Wu, X., Mooers, C.N.K. and Bang, I., 2007: An Assessment and Demonstrations of a Now-cast/Forecast System for the Prince William Sound, Alaska. *in preparation*
- Wunsch, C., 1975: Internal tides in the ocean. *Rev. Geophys. Space Phys.*, 13, 167-182.
- Wunsch, C. and Ferrari, R., 2004: Vertical mixing, energy and the general circulation of the oceans. *Annu. Rev. Fluid Mech.* 36, 281-314.
- Wunsch, C. and Stammer, D., 1997: Atmospheric loading and the oceanic inverted barometer effect, *Rev. Geophys.*, 35(1), 79107.
- Zhong, L. and Li, M., 2006: Tidal energy flux and dissipation in the Chesapeake Bay. *Cont. Shelf. Res.*, 26, 752-770.

VITA

Xinglong Wu was born in Tongshan, Hubei Province in the People's Republic of China, on August 1st, 1979. His happy childhood was spent with his parents, Yougong Wu and Caichai Xu, who, although they never obtained the opportunity to enter college, are aware of the value of knowledge. He received his elementary education at Tongshan Shiyan Elementary School and his secondary education at Tongshan No.1 High School. In September 1997 he entered the Department of Ocean Science and Engineering of Zhejiang University, from which he graduated with the B.E. degree in June 2001.

In August 2001 he was admitted to the Graduate School of University of Miami where he was granted the M.S. degree of Master of Science in August 2003 and the Ph.D degree in MAY 2008.

Permanent Address: Tongshan Fushiping Corporation, Nanshi Road,

Tongshan, Hubei, P.R. China, 437600